SENSITIVITY OF A SQUARE CYLINDER WAKE TO ORIENTATION AND OSCILLATION IN THE INTERMEDIATE REYNOLDS NUMBER REGIME

A Thesis Submitted
In Partial Fulfilment of the Requirement
for the Degree of
Doctor of Philosophy

by

Sushanta Dutta

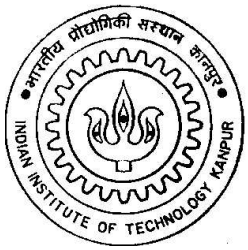

to the

DEPARTMENT OF MECHANICAL ENGINEERING
INDIAN INSTITUTE OF TECHNOLOGY, KANPUR
INDIA

March 2006

Abstract

Flow over a square cylinder leads to exceedingly complex fluid flow patterns in the wake. The flow field is characterized by a series of transitions with increasing Reynolds number. Additional complexity is developed when the cylinder is oscillated, either parallel (*inline*) or normal (*transverse*) to the main flow direction. Starting from a steady laminar condition, flow evolves to become unsteady at a Reynolds number of around 50, followed by periodic vortex shedding. With further increase in Reynolds number, flow becomes three dimensional even for a nominally two dimensional geometry at a Reynolds number of around 180. In the intermediate range of Reynolds numbers, namely 300-600, a chaotic state of the wake has been reported. At much higher Reynolds numbers (say > 5000) flow is everywhere three dimensional and turbulent. Much of the previous research on bluff body flows has focused on the circular cylinder geometry. Flow over a square cylinder is also a fundamental problem of interest to engineering. The fact that the point of separation is fixed for square geometry leads to significant differences in the flow structure when compared to a circular cylinder.

In the present work, the wakes of stationary and oscillatory square cylinders in the intermediate range of Reynolds number have been studied. For a stationary cylinder, the effect of cylinder orientation (i.e. the incidence angle with respect to the incoming flow direction) has been studied. Inline oscillations of the cylinder at zero incidence angle have been considered. The Reynolds number chosen for study is in the range of $90 \leq Re \leq 610$. The flow field has been investigated via experiments. Both spatial and temporal flow fields have been studied using particle image velocimetry (PIV) and hotwire anemometry (HWA), the former providing flow visualization images as well. The experimental technique and results have been validated against the data available in the literature and other established experimental techniques for measuring flow parameters. Measurements of PIV and hotwire anemometry have been compared against each other. Particle traces have been recorded as images to improve the basic understanding of the flow distribution.

Stationary square cylinder

For this configuration, the flow field has been characterized in terms of the time-averaged velocity field, instantaneous flow structure and overall flow parameters. Two different aspect ratios (AR=16 and 28) and four cylinder orientations (θ=0, 22.5, 30 and 45^o) have been considered. Quantities reported include Strouhal number, drag coefficient, time-averaged velocity field, stream traces, vorticity, turbulence intensity, centerline velocity recovery, power spectra, kinetic energy budget and flow visualization. Important results to emerge from the present study are the following: All flow parameters are seen to be affected by the cylinder orientation. A minimum in drag coefficient occurs at 22.5^o. At this orientation the Strouhal number is a maximum. For orientations other than 0 and 45^o, the wake is asymmetric. The v-velocity profile clearly brings out the wake asymmetry. The roll up of the shorter shear layer governs wake unsteadiness and hence Strouhal number. The loss of symmetry of the wake increases the transverse velocity, increases the base pressure and lowers drag. This factor is counter-balanced by an increase in blockage itself, but the minimum in the drag coefficient at an orientation of 22.5^o confirms that the former has an overall stronger influence at small cylinder angles. Stronger three dimensionality of the flow field at this angle additionally contributes to higher base pressure and lower drag.

Drag coefficient and Strouhal number are seen to be strong functions of aspect ratio for the range of Reynolds number studied. Strouhal number increases with an increase in aspect ratio while drag coefficient decreases with an increase in aspect ratio. For both aspect ratios, a minimum in drag coefficient is found at 22.5^o. For this orientation, Strouhal number is a maximum. The centerline recovery of streamwise velocity is greater for the higher aspect ratio cylinder (AR=28) when compared to low aspect ratio (AR=16). The size of the recirculation bubble is lower at the higher aspect ratio and explains the above trends in Strouhal number and drag coefficient.

The visualization pictures show that the separation distance between the alternating K*á*rman vortices is a function of both aspect ratio and cylinder orientation. The multiple modes in the power spectra indicate the modification of vortex shedding process and appearance of secondary vortical structures. From secondary flow visualization images it is seen that the flow three dimensionality is stronger for AR=16 compare to AR=28.

Drag coefficient and Strouhal number show only a weak dependence on Reynolds number. However, the flow structure is strongly affected. The velocity fluctuations (in particular, the peak values) generally increase with Reynolds number. The flow visualization images show the effect of Reynolds number clearly. Flow becomes increasingly three

dimensional as Reynolds number increases. Power spectra also show quasi-periodicity in flow unsteadiness at higher Reynolds numbers. This is seen in the form of multiple peaks in the spectra; hence energy is transferred across discrete harmonics other than that of vortex shedding. The maximum in the streamwise velocity fluctuation at the cylinder centerline doubles over the Reynolds number range of Re=165 to 595.

Effect of in-line cylinder oscillations

Flow past a square cylinder oscillated in the streamwise direction is investigated at zero angle of incidence. Two Reynolds numbers (Re=170, 355) have been considered for study. An aspect ratio of 28 has been selected for experiments. The effect of forcing frequency and amplitude of oscillation have been independently brought out. A limited study at an aspect ratio of 16 has also carried out at Re=175.

A strong effect of forcing frequency in the near-wake flow field is uniformly to be seen in the measured data. The recirculation length and formation length reduce substantially with an increase in frequency and directly diminish the time-averaged drag force acting on the cylinder. The instantaneous vorticity contours show the shear layer elongation to be a minimum before separation; hence the longitudinal wavelength of the shed vortices reduces. The time-averaged vorticity contours show that with an increase in frequency, the large scale vortices move closer to the cylinder. Their concentration near the cylinder leads to higher magnitudes of vorticity. The RMS values of velocity fluctuations cluster around the cylinder as well. By a mechanism of improved mixing, they can result in pressure equalization and a further reduction in drag coefficient. The extent of influence depends on the frequency of oscillation with respect to the vortex shedding frequency of the stationary cylinder configuration.

The effect of amplitude of oscillation on the flow details has been studied when the forcing frequency is kept constant at the vortex shedding frequency of the stationary cylinder. The time-averaged flow field shows a nominal effect of increase in amplitude but the instantaneous flow field changes significantly with amplitude. The time-averaged velocity profiles show asymmetry with increase in the perturbation amplitude. Asymmetry is also seen in the contours of RMS velocity. The peak value of RMS velocity increases with amplitude. The peak RMS value also moves upstream with an increase in the amplitude. The effect of increasing the amplitude at a given frequency leads to a reduction of the length of the recirculation bubble and the vortex formation region.

Contents

List of Figures

List of Tables

Nomenclature

B	edge of the square cylinder, m
L	length of the square cylinder, m
W	width of the test section, m
AR	aspect ratio, L/B
A	amplitude of oscillation, m
BR	blockage ratio, B/W
C_D	drag coefficient based on the average upstream velocity and B, = drag per unit length/ $\frac{1}{2}\rho U^2 B$.
f	frequency of vortex shedding, Hz
f_o	vortex shedding frequency of stationary cylinder Hz
f_{ex}	frequency of oscillation, Hz
t	time
Re	Reynolds number based on cylinder diameter, $\rho U B/\mu$
St	Strouhal number, fB/U
u	x-component velocity, m/s
v	y-component velocity, m/s
U	upstream velocity, m/s
W	width of the test section, m
x, y	dimensionless coordinates from the cylinder center scaled by B
x	coordinate along the flow direction
y	coordinate transverse to the flow direction
z	dimensionless coordinate parallel to the cylinder axis
X, Y, Z	dimensional coordinate from the cylinder center, m
V_r	reduced velocity, U/Bf_{ex}
KC	Carpenter number, $2\pi A/B$

Greek Symbols

μ	dynamic viscosity, kg/sec-m^2
ν	kinematic viscosity, m^2/sec
ρ	density, kg/m^3
ω_z	span-wise component of the vorticity scaled by U/B.
ω_x, ω_y	secondary components of the vorticity scaled by U/B.
λ_z	spanwise wavelength of secondary vortices, m
τ	delay time, sec.
θ	cylinder orientation angle, degree

Subscripts

CL	wake centerline
rms	root mean square

Chapter 1

Introduction

Bluff body wakes have been the subject of extensive investigation in view of their applications to wind engineering, hydrodynamics, aerodynamics and electronics cooling. Such wakes display characteristics that are distinct to the object shape, Reynolds number and distance from the object itself. At high Reynolds numbers, the wake structure is complex owing to unsteadiness and turbulence. In the lower range of the Reynolds number, recent studies show that the flow field, along with unsteadiness, is complex owing to three dimensionality even in nominally two dimensional geometries. Bluff body cross section that are often employed are circular and rectangular (especially, square). Between the two, the circular geometry has received considerable attention compared to rectangular. For square/rectangular cross-sections, the orientation with respect to the mean flow is another important parameter.

The vortex shedding frequency and more generally, the wake behavior depends on different aspects of the flow field such as the end conditions, blockage ratio of the flow passage, upstream turbulence level and the aspect ratio of the bluff body (Figure 1.1). In certain context, the flow complexity can be exploited for attaining varying degrees of control. If the bluff object is rectangular in cross section, the wake is determined primarily by flow separation initiated at its corners. The wake thus obtained shows sensitivity to aspect and blockage ratios, and Reynolds number. This may, however, not be sufficient to alter significantly the flow pattern.

The ability to actively or passively manipulate a flow field to effect a desired change is of immense technological importance. Modification and control of the flow can be employed to reduce the intensity of the wake in order eliminate flow induced oscillation and to reduce drag experienced by the object. A variety of techniques are available to control the flow field. These are classified as active and passive control. In passive control

the geometry or the configuration of the bluff body is modified to get the desired change in flow structure (Figure 1.2). No external energy is required for this type of control. Active flow control is a very recent topic of research as it required understanding of the coherent flow structures that can be manipulated according to requirements. For active techniques external energy is required to bring the desirable changes in flow structure. It may be implemented by using an independent external disturbance or a feedback-signal control system. When there is no feedback, it is called an open loop system, while with feed back, it is a closed loop system. Depending upon the direction of motion with respect to the flow direction, the oscillation may be transverse or in-line. In most of the flow applications, transverse oscillation is applied to counteract the instantaneous transverse force due to vortex shedding. Yet, there are situations where we encounter in-line oscillation (Figure 1.4) such as the damaging vortex induced oscillation of trash racks and of piles in tidal waters. Here, the wave and current induced forces on offshore structures need to be determined when the structure experiences in-line oscillations. With the understanding the coherent structure in fluid flow and its role in determining fluid forces active, a control strategy can be effectively applied, in principle, for reducing flow-induced forces.

In a passive control system, the geometry of the object with respect to the flow direction is manipulated to get the desired effect. Preliminary studies show that a large variation in the flow field is possible if the object motion is driven by the unsteadiness of the wake. To implement this strategy, the active flow control system will consist of sensors, actuators and a PC-based controller.

1.1 Flow over a Square Prism

Flow past a bluff body, in particular a square cylinder has attracted researchers due to its practical application on one hand and interesting flow details, on the other. Flow past a square cylinder replicates flow past a circular cylinder in terms of instability (Figure 1.5) and transition phenomena. The separation mechanism, the subsequent shedding frequency and the aerodynamic forces differ from that of a circular cylinder. Unlike a circular cylinder where the separation point varies with Reynolds number, the separation point is fixed for a square cylinder at the leading or trailing edge. Consequently, the fluid forces are insensitive to Reynolds number. This result is not applicable for low Reynolds number flow particularly in the transition range of Reynolds number. Furthermore, the width of the wake behind the cylinder is at-least one diameter whereas it is less than the

cylinder diameter for a circular cylinder. Hence, the square cylinder is more of a bluff body than a circular cylinder.

A large number of investigations have been performed on a circular cylinder at low as well as high Reynolds number. Very few investigations have been reported for a square cylinder at low and intermediate Reynolds numbers. At low Reynolds numbers, aspect ratio and end conditions are important parameters along with blockage and free stream turbulence. An additional parameter for the square cross-section of the cylinder is incidence angle to the main flow. The flow separates at a fixed point on the square cylinder, at its corners. By changing the cylinder orientation, flow separation can be made asymmetric, thus changing the overall flow pattern.

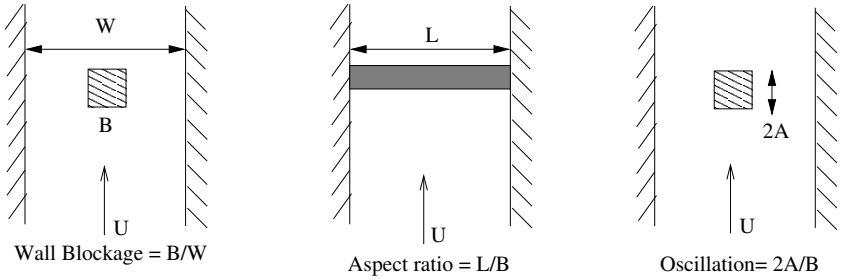

Figure 1.1: Disturbing parameters for flow past a square cylinder: blockage, aspect ratio and cylinder oscillation.

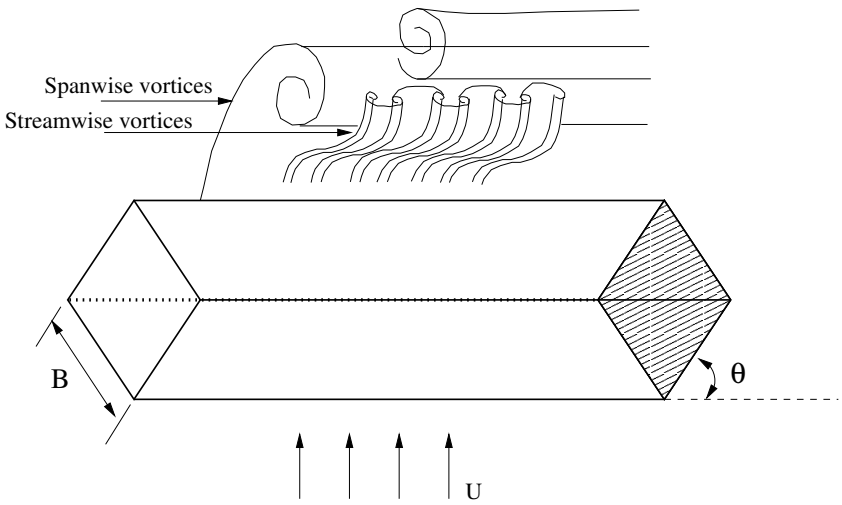

Figure 1.2: Vortices in the wake of a cylinder oriented at an angle to the incoming flow.

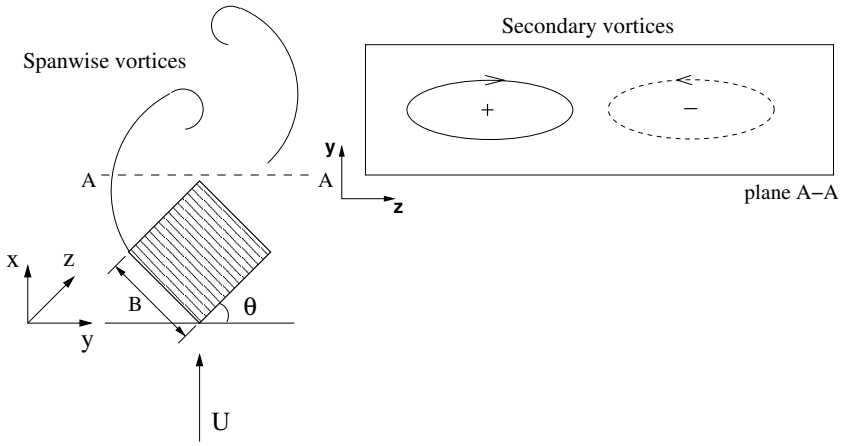

Figure 1.3: Flow past a square cylinder oriented to the incoming flow and the associated vortices.

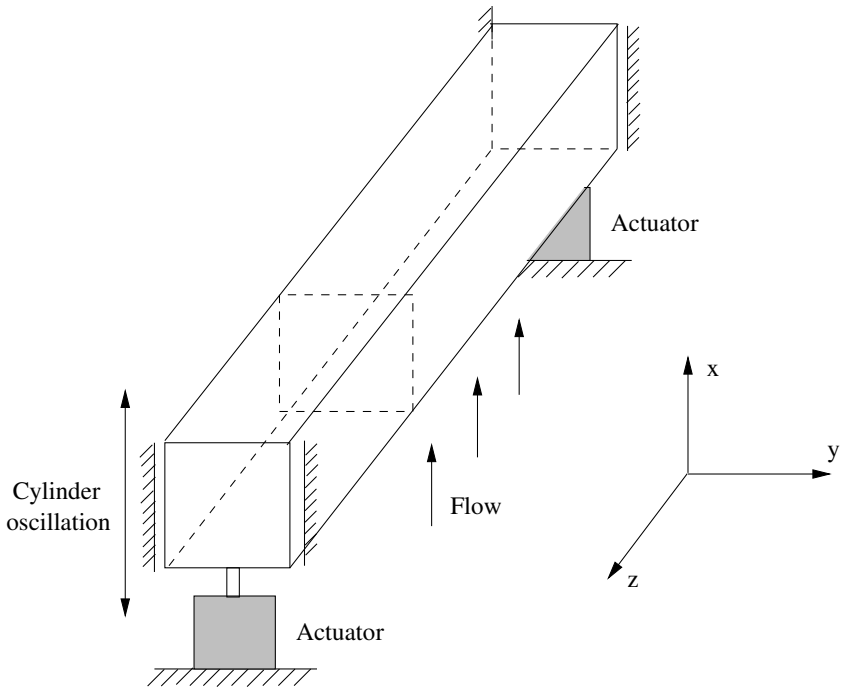

Figure 1.4: Schematic drawing of inline oscillation of a square cylinder created by an electromagnetic actuator.

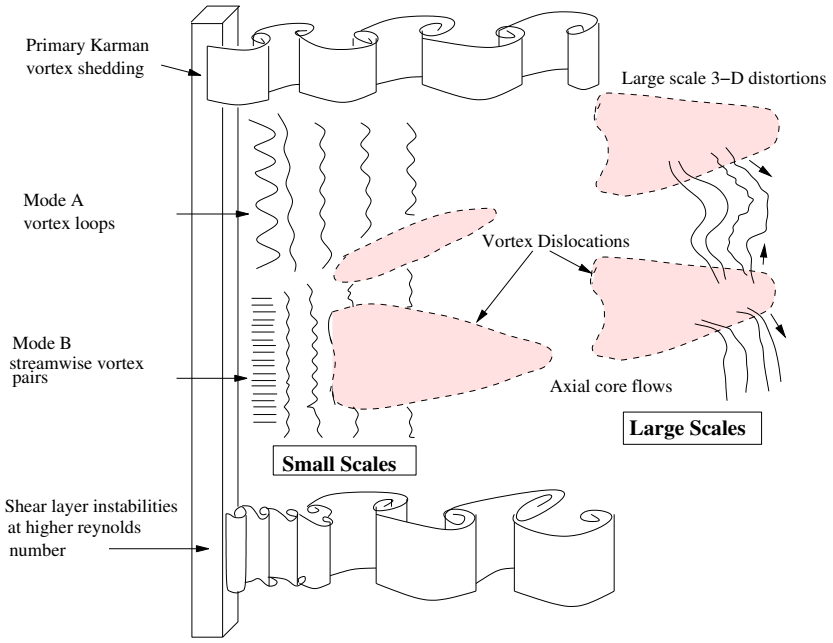

Figure 1.5: Summary of instability patterns in the wake of a square cylinder.

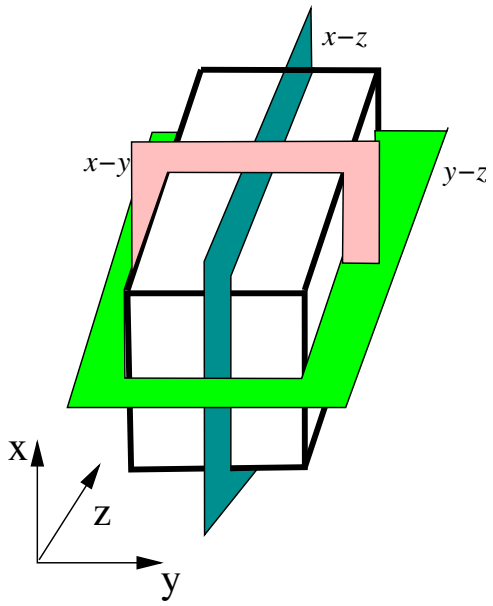

Figure 1.6: Definition of three planes around the cylinder where measurements were performed.

1.2 Objectives of the Present Work

In the present study flow past a prism of square cross-section has been considered. Experiments with stationary as well as oscillating cylinders in the intermediate range of Reynolds number have been conducted. The influences of cylinder orientation, aspect ratio and cylinder oscillation have been examined. The objective here is to explore the sensitivity of the wake to these external parameters. This knowledge will enable control of the wake pattern and hence quantities such as forces acting on the object. For a stationary cylinder, the flow field is affected by changing the cylinder orientation with respect to mean flow direction. In experiments with oscillation, the cylinder is given a prescribed motion in terms of frequency and amplitude in the direction of the approaching flow. The objective of the present research is to contribute in fundamental terms to the understanding the flow physics for a particular range of Reynolds numbers.

The present investigation is concerned with the intermediate Reynolds number range of 100-600. The flow field has been explored experimentally using Particle image velocimetry (PIV), Hotwire anemometry (HWA) and flow visualization. The cylinder is turned through certain specified angles and its influence on the wake pattern is examined. When the wake is actively controlled, the cylinder is given prescribed oscillations using an electromagnetic actuator. The PIV technique has been used to obtain the spatial flow field. For recording temporal details, hotwire anemometry has been used. Flow visualization has been carried out with the PIV camera (but a low inhomogeneous particle concentration). The focus of the research is directed towards the control of flow structure of the near-wake of the cylinder ($x \leq 10$) and the measurement of important global parameters such as drag coefficient and Strouhal number.

1.3 Thesis Organization

Subsequent chapters of the present thesis have been organized in the following sequence. Chapter-2 presents a literature review related to the different aspect of the flow past a square cylinder, circular cylinder, oscillating cylinder and the particle image velocimetry (PIV). The experimental setup and associated instrumentation are discussed in Chapter-3. The procedure for data reduction along with uncertainty analysis and validation of experimental procedure are presented in Chapter-4. Chapter-5 deals with the results of the present research for a stationary cylinder and related interpretations. The chapter is divided in three sections, namely, effect of orientation, effect of aspect ratio, and effect

of Reynolds number. In Chapter-6, results have been presented for flow past a cylinder with oscillation. The effect of frequency and amplitude have been separately considered. Chapter-7 summarizes the major conclusions of the present study and scope for future work.

Chapter 2

Literature Review

The literature related to flow past a prism of square cross-section is reviewed here[1]. Other bluff body cross-sections such as circular and rectangular are also discussed, though only for comparison. The discussion pertains mainly to experiments reported in the literature, while numerical data is included for comparison, where appropriate. Flow past a square cylinder resembles that of a circular cylinder as far as instabilities are concerned. But the separation mechanism and the consequent dependence of the shedding frequency and the aerodynamic forces on the Reynolds number differ significantly. These differences show up clearly in the flow properties of the near-wake. The separation points are fixed at the leading corners for a square cylinder. It is also possible for the flow to re-attach on the surface and separate again at the rear corners of the cylinder, a trend seen at high Reynolds numbers. For a circular cylinder, the point of separation depends on Reynolds number; in addition it may fluctuate about a mean position. Despite these differences, the disturbed flow behind these bluff bodies share certain similarities. The flow is characterized by the variation of local velocity in term of magnitude, direction and time. Common features include formation of a recirculation bubble in the near wake, a clear vortex shedding mechanism, center-line recovery of velocity and its fluctuations, and statistical features that are geometry independent in the far-wake.

The literature review has been presented in the following sequence : (i) Flow over circular cylinder, (ii) Flow over square cylinder, (iii) Cylinder oscillation and (iv) PIV technique. The summary from the literature review leading to the objective of the thesis has been presented in closure section.

[1]The phrase *square cylinder* will also be used to indicate this geometry.

2.1 Flow over a Circular Cylinder

The circular cylinder geometry has been extensively studied in the literature. In fact, the current knowledge of bluff-body wakes stems from the research on flow past a circular cylinder. In the following discussion, the phrase *low* Reynolds number refers to the range 1-40, *intermediate* to the range 100-400 and *high* to the range 10^5 and higher. The Reynolds number referred here is based on the average incoming velocity and the cylinder diameter. The focus of the present thesis is towards the intermediate range of Reynolds numbers.

Perry *et al.* (1982) studied flow past a circular cylinder using different flow visualization techniques. The vortex shedding phenomena and other salient features of the flow field were discussed on the basis of flow visualization images (Figure 2.1). From instantaneous streamline patterns, the authors showed that a closed cavity forms behind the cylinder at low Reynolds numbers. With an increase in Reynolds number, vortex shedding is initiated, the closed cavity behind the cylinder becomes open and instantaneous *alleyways* permit fluid flow into the cavity. Vorticity convected into the cavity is eventually squeezed out.

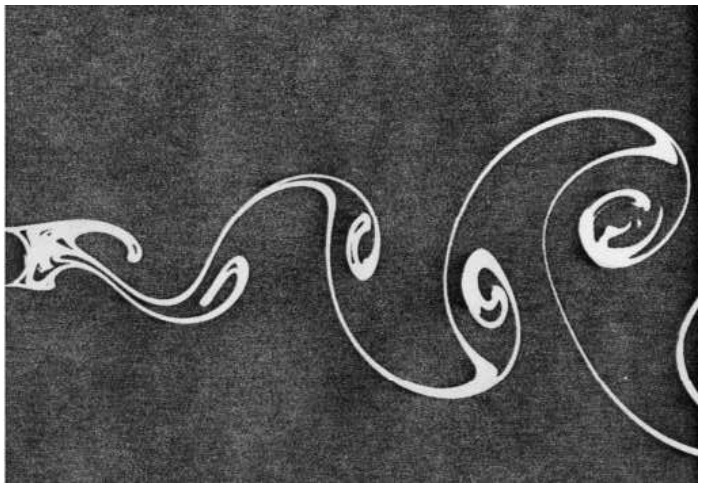

Figure 2.1: Flow visualization behind a circular cylinder (Perry *et al.* (1982))

.

Konig *et al.* (1990) studied the Strouhal-Reynolds number relationship for circular cylinder when the wake is laminar. The authors showed that the frequency laws change with a change in the end conditions. They have made measurements for three end conditions (end cylinder, end plate and cylinder terminated at the test cell walls). They recorded a discontinuity in the Strouhal number-Reynolds number curve for these end

conditions. The highest possible shedding frequency was measured when the vortex axes were parallel to the cylinder. When the shedding angle became slanted, the frequency was lower. The lowest frequency was seen to correspond to the largest possible angle of about 23^o when the cylinder is terminated at the wall. The shedding frequency was also found to be lower near the endplate when compared to cylinder centerline.

Lee and Budwig (1991) studied the effect of aspect ratio[2] for a circular cylinder at low Reynolds numbers using flow visualization and hotwire anemometry. For aspect ratios greater than 60 and without end modification, the authors found a discontinuity in the Strouhal number value in the Reynolds number range ($64 < Re < 130$). The discontinuity was related to the end condition, wherein a strong stabilization effect on the wake was seen for a small aspect ratio cylinder. The time-averaged wake profiles showed an increase in the wake-width with a reduction in the aspect ratio.

Stäger and Eckelmann (1991) studied the effect of end-plates on the shedding frequency of circular cylinders in the intermediate range of Reynolds numbers. Near the end plate, the shedding frequency was found to be lower than at midspan. The end-effect faded away with an increase in Reynolds number. The authors measured the power spectrum of velocity both at the mid-plane of the cylinder as well as near the end plate using a hotwire probe. It was shown that the end-effect faded away at mid-plane particularly at the higher end of the Reynolds number range.

Szepessy and Bearman (1992) experimentally studied the effect of aspect ratio for flow past a circular cylinder at high Reynolds number ($8\times10^3 < Re < 1.4\times10^5$). Moveable end-plates were used to vary the aspect ratio of the cylinder from 0.25-12. The wake in the central region of the cylinder was seen to be two-dimensional due to the presence of end plates. Within a certain range of Reynolds numbers of the study, a substantial increase in lift coefficient was seen for a reduction in aspect ratio, reaching a maximum for an aspect ratio of unity. The shedding frequency was seen to correlate closely with the fluctuating lift force. The shedding frequency diminished at smaller aspect ratios.

Karniadakis *et al.* (1992) numerically studied three dimensionality and transition to turbulence in the wake of a circular cylinder. The authors reported that the wake undergoes a rapid transition to a chaotic three-dimensional state at a Reynolds number of 500 starting from a laminar two-dimensional state at a Reynolds number of 200. The route followed to the chaotic state was of the period-doubling type.

Norberg (1994) studied the effect of aspect ratio for flow past a circular cylinder

[2]namely, the length-to-diameter ratio

over a wide range of Reynolds numbers. The range was large enough to cover laminar, transition and ultimately turbulent flow. In the laminar range, the critical Reynolds number for onset of vortex shedding was found to be a constant for aspect ratios larger than 40. However it is delayed for lower aspect ratios. At aspect ratios larger than 100, the Strouhal number was independent of aspect ratio. The author found a bi-stable flow pattern switching between regular vortex shedding and irregular flow in the intermediate range of Reynolds numbers. The results obtained in their study are in good agreement with the later study of Williamson (1996).

Wu *et al.* (1994) reported an experimental study for flow past a circular cylinder using Particle Image Velocimetry (PIV). The authors investigated the near wake structures around the cylinder through quantitative measurements of velocity and vorticity on transverse plane $(x - z)$ at a Reynolds number of 525. This longitudinal vortices (ω_y) were found to be stronger than spanwise vortices (ω_z). This result is possible when the longitudinal vortices are stretched by spanwise vortices as per the vortex stretching mechanism. The authors obtained streamlines by integrating the velocity signal which shows spiral motion at the vortex center. The spiral motion is indicative of flow three dimensionallity i.e. flow motions are out of the measurement plane.

Mansy *et al.* (1994) carried out an experimental investigation of flow over a circular cylinder for a wide range of Reynolds numbers. Laser velocimeter was used as a tool for detecting the small-scale structures and three dimensional disturbances in the near wake. The three dimensional structures were found to be the strongest close to the cylinder during the formation of primary vortices. The authors measured the wavelength in the spanwise direction from the autocorrelation function. As the wake develops in the downstream direction, it was found that the large-scales are amplified while the small scales are attenuated. The spanwise wavelength decreased continuously as $\mathrm{Re}^{-0.5}$ over the Reynolds number range of 300-22000.

Lin *et al.* (1995) studied the near wake structure of a circular cylinder using PIV for a Reynolds number range of 10^3-10^4. The authors examined both instantaneous and time-averaged velocity fields, streamline topology and vorticity distribution. Modes of large scale vortical structure with patterns of small scale Kelvin-Helmoltz vortical stuctures facilitated physical interpretation of the vortex formation length. The latter is often used as a criterion for linking the flow pattern to the loading coefficients.

Williamson (1996) and Zdravkovich (1997) reviewed the dynamics of flow past a circular cylinder in the intermediate range of Reynolds number. Three dimensionality

and transition phenomena were discussed in detail. For the Reynolds numbers studied, the flow details are susceptible to end conditions. It controls the wake pattern across the complete span. The vortex shedding patterns are either oblique or parallel to the cylinder axis in the laminar regime. A major reason for flow three-dimensionality in nominally two dimensional geometry is *vortex dislocation*, a phenomenon elaborated by Williamson (1996). Other phenomena which trigger three-dimensionality include oblique shedding. The transition of the wake behind bluff objects at intermediate Reynolds numbers is thus characterized by the presence of secondary vorticity.

Brede *et al.*(1996) conducted a PIV study for flow past a circular cylinder at Reynolds numbers between 160-500. Two modes of secondary vortices with different wavelengths were observed from the cross-stream velocity data. The origin and flow topology of the two modes (A and B) of vortices were found to be different. Two distinct flow instability mechanisms were responsible for the three dimensional structures. The A-mode arose from the instability of the braid region between Kárman vortices due to centrifugal forces. The B-mode was possibly related to the instability of the separated shear layer. The authors also measured the strength of the three-dimensional streamwise vortical structures in terms of their circulation and monitored their evolution along the streamwise direction.

Soria *et al.* (1996) investigated the near wake flow structure of a circular cylinder using a video-PIV technique. A time-accurate spatial cross-correlation of the recorded PIV images and analysis was developed. Experiments were conducted in a water tunnel for two Reynolds numbers (769 and 875) with hollow microsphere (Q-CEL 570). Two different planes were imaged. The study showed the peak longitudinal vorticity ($\omega_{y_{\max}}$) to be equal to 25-50 % of that of the spanwise peak vorticity ($\omega_{z_{\max}}$). The flow visualization images revealed that three dimensionality was a result of an influx of high velocity fluid from upstream into the stagnant near-wake region.

Prasad *et al.* (1997) studied the shear layer instability of the wake of a circular cylinder and the effect of end conditions. The authors carried out experiments using hotwire anemometry and flow visualization over a range of aspect ratios. The instability mechanism was found to depend on the mode of vortex shedding. The authors developed an emperical relationship between the shear layer frequency and Reynolds number. The intermittency of shear layer fluctuations was also confirmed which is due to random streamwise movement of the transition point in the shear layer. The fluctuation was not due to transverse motion of the shear layer as previously proposed.

Williamson (1998) studied flow past a circular cylinder at low Reynolds numbers. The author discussed the existence of discontinuity in the Strouhal number-Reynolds number relationship for laminar vortex shedding. The physical mechanism causing this discontinuity was identified as the oblique shedding mode. By manipulating the end conditions, parallel shedding could be obtained. In turn, it led to a continuous relationship between Strouhal number and Reynolds number. The data agreed with that for oblique shedding when tranformed as S_o=$S_\theta/\cos\theta$ (where S_θ is the Strouhal number corresponding with the oblique shedding angle θ). The relationship agreed well with other experiments as well.

Sung *et al.* (2003) studied the near wake vortex motion for flow past a circular cylinder at low Reynolds numbers. The authors discussed the flow topology from time resolved PIV data obtained at different planes. The plane-wise information was used to reconstruct the three dimensional flow field. The critical point theory was used to determine the location of the saddle point. The convection velocity of the K*á*rman and secondary vortices was evaluated from the trajectory of the vortex center.

In summary, the literature reviewed above shows that three dimensionality is a prominent feature of flow past a circular cylinder in the intermediate Reynolds number regime, at low as well as high aspect ratios. Three dimensionality arises from oblique shedding of vortices and formation of streamwise vortices. The flow field frequently undergoes transition at specific Reynolds numbers when a fundamental change in flow pattern is observed. Most of the experiments reported were conducted using either flow visualization, PIV or hotwire anemometry.

2.2 Flow over a Square Cylinder

Flow past a square cylinder resembles that of a circular cylinder as far as instabilities are concerned. The separation mechanism and the consequent dependence of aerodynamic forces and Strouhal number on the Reynolds number differ significantly. The separation points are fixed for a square cylinder, either at the leading edge or the trailing edge, depending on Reynolds number. The width of the wake for the square cylinder is about one diameter just behind the cylinder, though for a circular cylinder, it is less than a diameter. Consequently, the vortex formation region is significantly broader and longer for a square cylinder when compared to the circular. In the following section, the literature on (1) the effect of Reynolds number on flow past cylinders of square and rectangular

cross-sections and (2) the effect of orientation of the square cylinder with respect to the mean flow are reviewed.

2.2.1 Effect of Reynolds number

Okajima (1982) studied flow past rectangular cylinder for a wide range of Reynolds number (70 to 2×10^4) and width-to-height ratios. Hotfilm and hotwire anemometry were used for measurements. The flow pattern changed abruptly with a change in the width-to-height ratio of the cylinder. The dependence of Strouhal number on Reynolds number for different cross sections was brought out in the study. Later, Okajima (1990) carried out further numerical simulation using finite difference and the discrete vortex methods to get a better insight of the flow characteristics. The simulation showed the existence of a critical range of Reynolds numbers where Strouhal number changes are accompanied by a drastic change in the flow pattern.

Davis *et al.* (1984) conducted two dimensional simulation and experiments in the intermediate range of Reynolds number. Two different blockages ($B/H = 16.67$ and 25%) and aspect ratios of 0.6, 1.0 and 1.7 were used for numerical simulation. For experimental investigation the aspect ratio was 63. A good agreement between experimental and numerical results in terms of drag coefficient and Strouhal number was obtained. The inlet velocity condition and the blockage were found to play an important role in the measurements. The flow visualization images showed three dimensionality of the flow field for the range of Reynolds number studied.

Durao *et al.* (1988) studied flow behind the square cylinder using LDV at Re=14000. The highest velocity fluctuation was seen to be located in the shear layer surrounding the recirculation bubble. The energy associated with trubulent fluctuations was about 40% of the total energy near the highest velocity fluctuation zone. The importance of the turbulent and non turbulent motion around bluff body were thus highlighted. Along with LDV measurements the authors also conducted flow visualization using fluoroscent dye.

Lyn *et al.* (1995) carried out two-component LDV measurements in the wake of a square cylinder in a water tunnel at a Reynolds number of $21,400$. The phase-averaged velocity statistics was obtained in the near wake and base region of the cylinder. The authors made a quantitative comparison of length, velocity scale and vortex celerities with that of a circular cylinder. The experiments brought out the differences between the base region and the near wake on one hand and the relationship between the flow

topology and the turbulence distribution on the other.

Bearman (1997) reviewed the wake behind two and three dimensional bluff bodies of various shapes. The emphasis was on vortex formation and the near-wake dynamics. It was seen for bluff bodies that flow separation is induced at positions where the velocity at the edge of the boundary layer is higher than the free stream velocity. This results in the generation of high circulation which in turn leads to a high time-averaged drag. The near-wake was also seen to experience instabilities including vortex dislocation. A variation in the frequency of vortex shedding in the spanwise direction was seen. The study also showed that the instantaneous flow field is quite different from the time-averaged.

Sohankar *et al.* (1999) studied flow past a square cylinder at intermediate Reynolds number using 2D and 3D DNS[3]. Two aspect ratios (6 and 10) and blockage of 5.6% were considered. The study showed two modes of instability, namely A and B in the wake transition process as seen for a circular cylinder (Williamson, 1996). For a square cylinder a low frequency pulsation in the transitional Reynolds number was also present. A substantial increase in the intensity of secondary vortical structures and circulation level in the near wake was detected. The drag coefficient and Strouhal number variations with Reynolds number were opposite to those of a circular cylinder. Specifically for a square cylinder, Strouhal number decreases and the time-averaged drag coefficient increases with Reynolds number. The authors discussed the detailed flow structure and three dimensional transition phenomena from numerical data.

Robichaux *et al.* (1999) numerically studied the instability of three dimensional flow behind a square cylinder. The authors used Floquet stability analysis to extract different three dimensional modes. A new mode of instability, called *mode S* was observed along with modes A and B. This mode is absent for a circular cylinder flow. Mode S is a rare occasion where a two dimensional flow with T period undergoes a period doubling bifurcation by becoming unstable to three dimensional disturbances.

Saha *et al.* (2003a) performed three dimensional numerical simulation for flow past a square cylinder at low and intermediate Reynolds numbers. The authors discussed the spatial evolution of vortices and transition to three dimensionality behind a square cylinder at zero angle of incidence. Two modes of secondary vortex structures in the transition zone were discussed in terms of their influence on Strouhal number and the time-averaged drag coefficient. The transitional route to three dimensionality exhibited

[3]direct numerical simulation

an intermittent low frequency modulation. Transition phenomena in the wake of a square cylinder was found to be similar to circular, except for a shift in Reynolds number.

Luo *et al.* (2003) studied transition phenomena of a square cylinder using flow visualization and hotwire anemometry. The authors found two transition modes and the corresponding range of Reynolds numbers for these transitions. The transition phenomena of square and circular cylinders were compared with each other. Modes A and B were present for both cases but there were differences in spanwise wavelength and Reynolds number at which the respective transitions occured. The spanwise wavelength was larger for a square cylinder for both modes when compared to the circular. No hysteresis was detected for the square cylinder in the transition to mode A instability while it is present for a circular cylinder. These experiments indirectly confirm many of the wake transitions of a square cylinder as reported by Saha *et al.* (2003a).

The above review shows that the cylinder of square cross-section shares many of the transitional features of the circular cylinder in the intermediate range of Reynolds number. There are points of difference as well. The onset of three dimensionality even in high aspect ratio cylinders was a feature shared by the two cross-sections. Specialized, high accuracy numerical simulation is confirming many of the experimentally observed phenomena.

2.2.2 Effect of incidence angle

One of the earliest studies on this subject is that of Vickery (1966) who measured the fluctuating lift and drag forces on a long square cylinder at different incidence angles. The effect of turbulence level in the incoming flow was considered. The author used strain-gauge dynamometer and pressure guage for his study. The magnitude of the fluctuating lift of a square cylinder was found to be considerably higher than that of a circular cylinder. There was marked influence of large scale turbulence in the incoming flow on steady and dynamic forces. The most significant influence was found at small angles of attack ($\alpha < 10^o$) where base suction pressure reduced substantially with about 50% reduction in the fluctuating lift forces.

Obasaju (1982) used hotwire anemometry to study the effect of cylinder orientation at a high Reynolds number ($= 4.74 \times 10^4$). Five cylinder orientation, namely 0, 10, 13.5, 20 and 45^o were considered. A reduction in drag coefficient and a sharp rise in Strouhal number was seen at an angle close to 13.5^o. The author attributed this result to the shear layer reattachment over one of the edges of the cylinder. The author also calculated the

vortex strengths at various locations along the cylinder span.

Igarashi (1985) experimentally studied fluid flow and local heat transfer from a square prism at incidence for Reynolds numbers in the range of 1.1×10^4 to 5.3×10^4. For different cylinder orientations, the author correlated the fluctuating pressures on various surfaces with the local Nusselt number distribution. Empirical corelations of average Nusselt number as a function of Reynolds number and cylinder orientations were also reported.

Knisely (1990) experimentally recorded Strouhal number data of flow past a rectangular cylinder with side ratios of $0.04 - 1$ and angles of incidence between 0^o to 90^o. Reynolds number was set in the range of $7.2 \times 10^2 <$Re$< 8.1 \times 10^4$ for both water and wind tunnel study. The force coefficients showed a strong dependence on the angle of attack. An optimum incidence was identified where the load bearing capacity of the structure is the highest. A sharp rise in Strouhal number was seen at a small angle of incidence. The angle at which reattachment of the separated shear layer occurred was a function of the side ratio.

Tamura and Kuwahara (1990) performed 2D and 3D simulation of flow past a square cylinder at a high Reynolds number (Re=10^4). Four aspect ratios and two inclination angles (0 and 15^o) were considered for the study. Result revealed major differences in the results of 2D simulation with respect to 3D. The time and cylinder-averaged drag and lift coefficients were found to be smaller in 3D simulation when compared to 2D. The authors explained these differences in terms of the flow structure, namely streamlines and vorticity contours.

Norberg (1993) presented a comprehensive database of Strouhal numbers for rectangular cylinders of various side ratios (1-5), incidence angles (0-90^o) and Reynolds numbers (400-3×10^4). Measurements were carried out using a hotwire anemometer. In addition, lift coefficient, drag coefficient and moment coefficients were correlated with the incidence angle[4]. For intermediate angles, Strouhal number and drag coefficient were found to be nearly constant when based on the projected dimension of the cylinder.

Sohankar *et al.* (1998) performed a numerical simulation of flow past a square cylinder in the Reynolds number range of 200-455 for different cylinder orientations. In the range of incidence angles considered ($0 < \theta < 45^o$), the onset of vortex shedding occurred within the critical Reynolds number interval of 40 to 55[5]. Results for forces,

[4]also called, angle of attack

[5]Here, Re is based on the projected dimension of the cylinder cross-section.

moments and the Strouhal number were reported by the authors. The effect of blockage ratio was brought out in the study.

Chen and Liu (1999) experimentally studied flow past a square prism at incidence for a wide range of Reynolds number ($2000 - 2.1 \times 10^4$). Hotwire sensor and pressure transducer were used in the study. Strouhal number showed a sharp increase at an angle around 13^o. The pressure distribution around the cylinder showed a definite trend for all the Reynolds numbers studied. For lower Reynolds numbers, the pressure recovery was weak and the shear layer reattachment was less firm when compared to high Reynolds numbers. The maximum in Strouhal number occurred at relatively higher angle for low Reynolds numbers.

Dutta *et al.* (2003) experimentally investigated flow past a square cylinder at different cylinder orientations for three different Reynolds numbers (1000, 5000 and 10000). The authors used a two wire hotwire anemometer and flow visualization in a smoke tunnel for their measurements (Figure 2.2). A definite trend was observed in Strouhal number and Drag coefficient with respect to the cylinder orientations. The drag coefficient reduced and Strouhal number increased with incidence angle. A minimum in drag coefficient was observed at 22.5^o with a corresponding maximum in Strouhal number. The decay of velocity fluctuation showed a strong dependence on cylinder orientation and was the slowest at 45^o.

Oudheusden *et al.* (2005) studied the vortex shedding characteristics a square cylinder at incidence using PIV. Reynolds numbers considered were 4000, 10,000 and 20,000. The authors used proper orthogonal decomposition to reconstruct phase-averaged flow field from time uncorrelated data. The effect of incidence on vortex formation was brought out from the POD analysis. For a cylinder at incidence, the pattern of individual POD modes were found to be different. A good match of experimental data with LES simulation of other authors was to be seen. For a cylinder at an angle of incidence, a striking difference in vortex formation from the upper and lower sides of the body showed the importance of phase angles in vortex formation.

Literature review shows that dynamics of wakes of cylinders oriented with respect to the mean flow is a topic of current research. Issues such as recirculation length, recovery of velocity, decay of velocity fluctuations, vorticity interatcions, and three dimensionality have not been conclusively established. The complexity of the flow patterns in the intermediate range of Reynolds numbers is realized for cylinders at an angle of incidence as well.

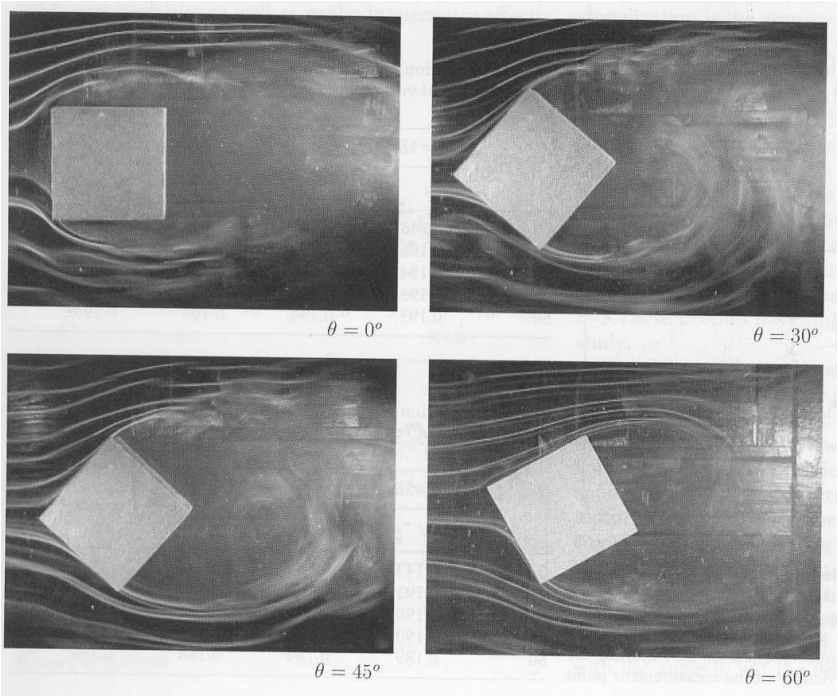

Figure 2.2: Smoke visualization behind a square cylinder at incidence (Dutta *et al.* (2003))

.

2.3 Cylinder Oscillation

Both active and passive control of flow past a bluff body can be achieved by manipulating its near wake structure. For a fixed cylinder, vorticity production arises from the adverse pressure gradient on the cylinder surface. Additional vorticity production mechanism comes into play for an oscillating cylinder. The surface motion now contributes to tangential component of fluid acceleration. Different techniques are available for active control of the near wake. Forced oscillation, acoustic excitation, and flexibly mounted cylinder are a few examples. The basic difference between forced oscillation and flexibly mounted cylinder is that for the latter, fluid-structure coupling can occur in either direction[6]. In forced oscillation of a rigid cylinder, surface motion defines and hence controls fluid motion. For this reason, forced cylinder oscillations are being effectively used as an active control strategy of bluff body wakes.

Tanida *et al.* (1973) experimentally studied the stabilty of a circular cylinder oscillating in a uniform flow over a range of Reynolds number ($40 < Re < 10^4$). Both inline and transverse oscillations for single cylinder and those in tandem were considered. The

[6]structure→ fluid, or fluid→structure

authors reported both fluctuating lift and drag forces for the configurations considered. The lift and drag forces were measured using strain gauges. For the tandem arrangement, no vortex shedding occurred below a particular spacing between cylinders, the minimum value depending on the Reynolds number. In the case of a single cylinder, the synchronization frequency is the Strouhal frequency for transverse oscillation whereas it is twice the Strouhal frequency for longitudinal oscillation. For both inline and transverse oscillations, the fluctuating lift and drag forces were found to be a maximum in the middle of the synchronization range.

Griffin *et al.* (1976) studied the wake of a circular cylinder oscillating in-line with the incident steady flow at Re=190. Vortex shedding was synchronized with the oscillation frequency set at twice the shedding frequency. Two distinct modes of vortex street were observed (Figure 2.3). In one experiment, two vortices of opposite sign were shed for one cycle of cylinder motion. In another, one vortex was shed for each cycle of oscillation. The longitudinal and lateral spacing of the vortices were seen to depend on the oscillation frequency and amplitude. Griffin *et al.* (1991) again reviewed the lock-on phenomena for both in-line, transverse and rotational oscillation of a circular cylinder placed in steady incoming flow. The effect of sound on vortex lock-on was also studied. The effect of amplitude and frequency of cylinder oscillation on the near-wake vorticity structure and base pressure coefficient were discussed.

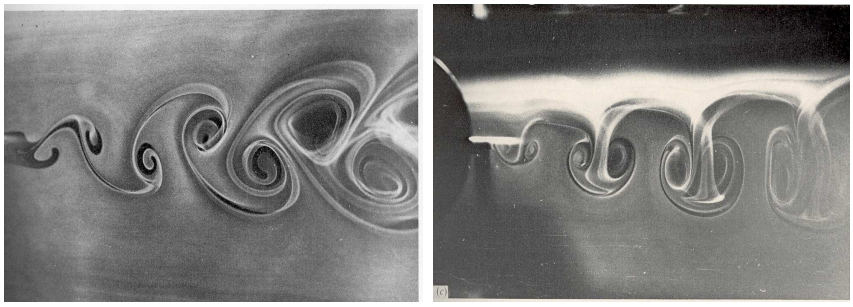

Figure 2.3: Flow visualization behind a stationary and oscillating (inline) cylinder at Re=190. (f/f_o=1.88, amplitude=0.2 D), after Griffin *et al.* (1976)

.

Sarpkaya (1979) reviewed vortex induced oscillation of circular cylinder in considerable detail. The author considered both transverse and longitudinal oscillations. The effect of oscillation amplitude, frequency, and Reynolds number on Strouhal number, lock-in phenomena, lift and drag coefficients, and base pressure were discussed. The effect of the vortex shedding mechanism on the added mass component and reduced velocity were presented. For inline oscillations, the lock-in frequency was found to be

twice the Strouhal frequency. For transverse oscillaions, it was found to be equal to the Strouhal frequency[7]. The amplitude of alternating forces was one order of magnitude less for inline oscillations when compared to the transverse. Sarpkaya (2004) again reviewed free and forced oscillations of circular cylinders and categorized fundamental aspects the wake behaviour.

Zdravkovich (1982) studied synchronization phenomena of flow unsteadiness with object motion for flow past a circular cylinder. The author analyzed the timing of vortex shedding in relation to cylinder displacement from flow visualization images. The study revealed that in the synchronization range, the increase in fluctuating forces had a simple fluid mechanical origin. The oscillating cylinder imposed not only its frequency to the wake behind it but also the timing of vortex shedding. In the lower region of the synchronization range, the vortex formed on one side of the cylinder was shed when the cylinder was near to the maximum amplitude on the opposite side. This timing suddenly changed in the upper synchronization range where the vortex with the same circulation sign as before was shed when the cylinder reached the maximum amplitude in the mean flow direction.

Bearman (1984) studied vortex shedding phenomena from an oscillating bluff body under conditions of free and forced vibrations. An increase in the correlation length was seen for an oscillating cylinder compared to the stationary. The degree of correlation was found to depend on the shape of the object cross-section. The lock-in phenomenon changed with the amplitude of oscillation. The relationship of the phase of instantaneous forces to cylinder position was brought out.

Ongoren *et al.* (1988) studied near wake flow structures arising from an transversely oscillating cylinder over a Reynolds number range of 584 to 1300 with the hydrogen bubble visualization technique. The authors studied three different geometries (circular, triangular and square) over a wide range of frequencies from subharmonic to super-harmonic. The study showed a distinct phase relationship between body motion and vortex shedding for the three harmonic ranges. Specifically, two fundamental types of lock-in are to be seen (Figure 2.4). At a frequency one half of the Strouhal frequency, a subharmonic form of lock-in takes place whereby the shed vortex is always from one side of the body. At frequencies near the Strouhal frequency the classical form of lock-in takes place as vortices are shed alternately from the body to form a K*á*rman vortex street. The after-body plays a significant role in phase shifting. Objects with short afterbody have a larger phase shift when compared to relatively larger afterbody, for example a

[7]namely, that corresponding to vortex shedding from a stationary cylinder

square cylinder. The phase shift results in the switch of the initially formed vortices from upper to lower side and *vice-versa*.

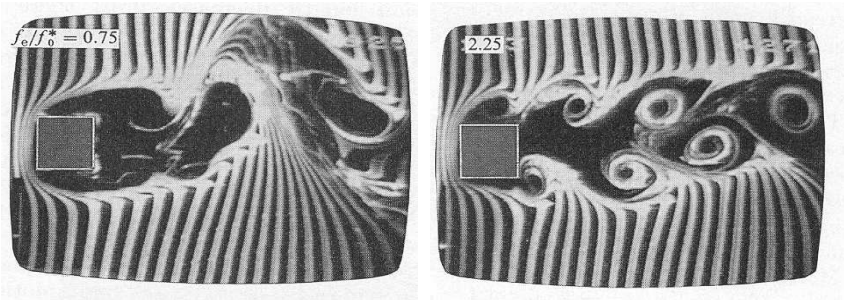

Figure 2.4: Near wake flow visualization over a square cylinder oscillating in transverse direction as a function of cylinder oscillation. Ongoren *et al.* (1988).

Zdravkovich (1988) conducted flow visualization experiments for an oscillating cylinder of circular and semicircular cross sections. The main objective of the study was to correlate the timing between vortex shedding and cylinder displacement in the synchronization range. Two types of oscillation were considered, namely forced and free. The following major conclusions were arrived at from the study (i) The vortex formed on one side of the cylinder is shed when the cylinder is near the maximum amplitude on the opposite side. (ii) The vortex formed on one side of the cylinder was shed when the cylinder was near its maximum displacement on the same side.

Roussopoulos (1993) studied feedback control of vortex shedding for flow past a circular cylinder at an intermediate Reynolds number using flow visualization and hotwire technique. A loudspeaker was used as an actuator and the hotwire sensor as control. The wake unsteadiness could be controlled for upto 10 times the Reynolds number at the onset of vortex shedding. Vortex suppression was not possible if the control sensor was located too far downstream of the cylinder, even when the sensor could clearly detect the shedding. Also, suppression was not possible if the feedback loop was highly tuned to the shedding frequency. The control transfer function played a significant role in triggering instability mechanism. A local control for a long span body did not help to control the whole-span shedding. In some regions along the span, shedding was unaffected by the controller action.

Gu *et al.* (1994) and Lu *et al.* (1996) studied the timimg of vortex formation for a transversely oscillating circular cylinder. Respectively, experiments and numerical simulation were used by the authors. Experimental study was done using PIV and

PTV at low and high Reynolds number (Re=185 and 5000). Numerical study was a 2D simulation at Re=185, 500 and 1000. With an increase in the excitation frequency, the vortices moved closer to the cylinder until a limiting position was reached and the vortices switched to the opposite side of the cylinder. This result was seen in both numerical and experimental investigations. The vortex switching mechanism and the flow topology matched quite well in the two studies.

Tao *et al.* (1996) reported a fascinating feedback experiment with a hotwire probe, wherein flow visualization was conducted using a dye injection technique for flow past a circular cylinder. The flow visualization images clearly showed complete vortex suppression and enhancement for various feedback conditions (Figure 2.5). The authors used a phase shifter, amplifier and dynamic shaker for modifying the flow conditions. Experiments showed suppression of vortex shedding for upto 25 % of Reynolds number above the critical value.

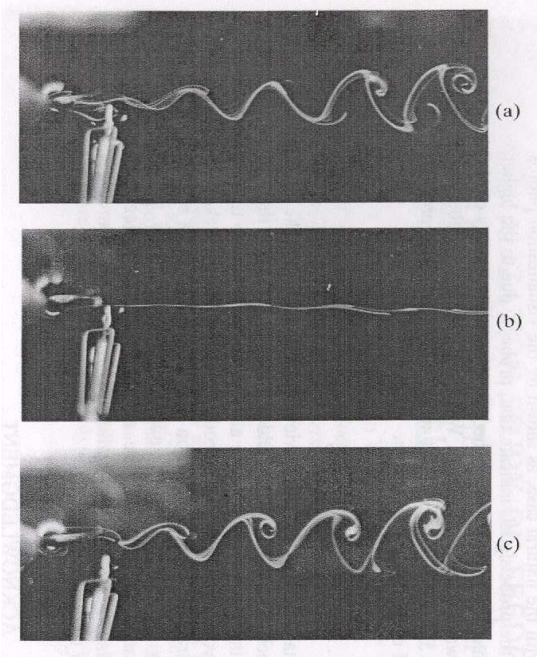

Figure 2.5: Flow visualization with feed back control, after Tao *et al.* (1996)

Blackburn *et al.* (1999) performed a two dimensional numerical simulation of flow past a transversely oscillating cylinder at a Reynolds number of 500 and a fixed amplitude of 0.25, while the frequency ratio was varied. The authors justified their assumption of two dimensionality by stating that the flow became increasingly periodic under oscillation conditions. The authors could replicate the phase switching phenomena observed earlier in a number of experiments. It was concluded that phase switching was

due to a change of sign of mechanical energy transfer between the cylinder and the flow field. The results suggested that the discontineous switch in phase of vortex shedding was due to competition between two modes of vorticity production.

Okajima *et al.* (1999) performed visualization experiments to study flow induced in-line oscillations for circular as well as rectangular cylinders of different side ratios. The authors categorized the excitation frequencies in two regimes based on the reduced velocity defined as $V_r = U/f_n d$. The lower range of reduced velocity ($1.6 < V_r < 2.25$) was called the first excitation region and the higher range of reduced velocity ($2.6 < V_r < 3.6$) was called the second excitation region. From flow visualization images it was confirmed that in-line oscillation is very much sensitive to the shape of the body. For a circular cylinder, symmetric vortex shedding is realized due to wake breathing at the first excitation range. On the other hand, alternate vortex shedding in seen in the second excitation range. For rectangular cylinders, the shedding process depends largely on the shape of the after-body.

Krishnamoorthy *et al.* (2001) studied near wake phenomena behind an oscillating circular cylinder. Experiments were conducted in a water tunnel using dye visualization in the Reynolds number range of 1250-1500. The amplitude of cylinder oscillation was fixed and the frequency of oscillation varied. At the lower excitation frequency in the lock-in regime (referred to as the 2P mode), the authors observed two pairs of vortices shed from the cylinder per cycle of cylinder oscillation. When a critical excitation frequency crossed the lock-in regime, one pair of vortices was shed from the cylinder (the 2S mode). For excitation frequency higher than the fundamental locked-in regime, the authors found that the wake pattern quickly relaxed to the usual Karmán mode.

Cetiner *et al.* (2001) studied lock-in and loading phenomena for a circular cylinder for streamwise forced oscillations with respect to the mean flow direction over a wide range of Reynolds number (405< Re< 2482). Particle image velocimetry was used for the study. The authors correlated the vortex pattern with the force coefficients. The authors showed that the lock-in phenomenon is possible for streamwise oscialltions as it is in transverse oscillations of the cylinder. The inter-relationship between forces, near-wake vorticity and streamlines pattern came out from the study. The degree of lock-in was identified for a range of Keulegan-Carpenter numbers.

Carberry *et al.* (2001) studied various wake modes of an oscillating cylinder and the forces generated when the cylinder is oscillated at and around the Karmán frequency. The interaction between the natural instabilities of the wake and forced oscillation was

seen to play an important role in determining the forces. The lift force is intrinsically dependent on the symmetry of the near-wake structure. With an increase in the frequency ratio, the amplitude of the lift force increases and simultaneously the mode of vortex shedding changes from 2P to 2S. The wake behaviour changes abruptly when the frequency ratio is close to unity. The wake transition phenomena was captured by the authors in terms of the lift phase and amplitude.

Jeon *et al.* (2001) studied the forced oscillation of a circular cylinder with two degrees of freedom using PIV. Both transverse and streamwise oscillations were included. The authors used a 2D traversing mechanism to facilitate both streamwise and transverse movement of the cylinder. Streamwise oscillation was seen to primarily change the phase of shedding. Changing the relative phase of shedding caused a corresponding change in the phase of the lift force. This is because energy transfer between the body and the wake is sensitive to the relative phase between the force and body motion. The phase of the streamwise motion was seen to control even the sign of energy transfer. The most dramatic change in flow structure was seen when streamwise motion added with transverse motion. The 2P mode of vortex shedding completely disappeared.

Guilmineau *et al.* (2002) studied flow over an oscillating circular cylinder with numerical simulation. Both in-line and transverse oscillations were studied at low Reynolds numbers (Re=100 and 185) with varying frequency ratios. The amplitude of oscillation was 20% of the cylinder diameter. The authors calculated parameters such as drag coefficient, Strouhal number, vorticity contours, streamlines and velocity profiles and showed a good match with experimental results reported in the literature.

Konstantinidis *et al.* (2003) studied the near wake characteristics of a circular cylinder for a periodically perturbed approach flow. Laser Doppler velocimeter was used for measurements in a water tunnel. A wide range of Reynolds numbers, mostly in turbulent flow regime was considered. The main aim of the study was to find the effect of superimposed velocity fluctuation on wake characteristics. The fluctuations, wave length of the vortex street, vortex formation length, and recirculation bubble length are parameters measured in the experiments. An important finding of the study is that at relatively low amplitudes, the flow perturbations can cause a strong modification of the wake structure comparable to that of cylinders oscillating with a high amplitude.

Zhang *et al.* (2003, 2004) studied the control mechanism of vortex shedding for a spring loaded square cylinder whose top surface was pertubed using peizo actuator (THUNDER). Both closed loop and open loop studies showed a reduction in the time-

averaged drag coefficient. The study revealed that closed loop control was more advantageous when compared to the open loop system. The open loop system depends on perturbation frequency. It can suppress vortex shedding or structural vibration only if it is outside the synchronization range. Within the synchronization range the open loop control enhances vorex shedding and hence, the structural vibration. On the other hand, the feedback signal from the flow suppresses vortex shedding by adjusting the phase of the forcing signal.

Yang *et al.* (2005) numerically studied flow past a transversly oscillating rectangular cylinder in channel flow. The authors captured flow details for a Reynolds number of 500. It was concluded that the wake pattern is dominated by the oscillations of the cylinder. The presence of lock-in state implies similar vortex entrainment for rectangular cylinders as for circular. There are, however, basic differences between the oscillating circular cylinder and a square cylinder.

Nobari *et al.* (2005) did numerical simulation using the finite element method for flow past an oscillating circular cylinder for Reynolds numbers upto 300. Both transverse and inline oscillations were studied for various frequencies and amplitudes. For cross flow oscilltaion, lock-in occurred near the shedding frequency. It occurs at twice the shedding frequency for inline oscillations. The effect of the oscillation parameters on the time-averaged drag coefficient was discussed. The authors compared the results of their numerical simulations with experimental data and found a good match. Lock-in phenomena and secondary vortex shedding due to the increased amplitude were observed in experiments as well as simulation.

Zhang *et al.* (2005) studied flow past a stationary cylinder with a perturbation of its top surface at a Reynolds number of 7400. The authors used closed loop control with PID controller to perturb the surface using piezo-ceramic actuators. The flow field was investigated using PIV, LIF, LDA and a hotwire probe. The study showed that when the surface perturbation and the force due to vortex shedding are in phase, there is an enhancement in the strength of the shed vortex, and consequently an increase in the fluctuating lift and drag coefficient. When they are in opposed phase, there is a weakening of vortex shedding and a reduction in the fluctuating forces.

Nishihara *et al.* (2005) studied the effect of streamwise oscillation on wake pattern and fluid dynamic forces of a circular cylinder in a water tunnel using LDV and flow visualization. The authors identified two ranges of the reduced velocity ($V_r = U/f_n d$), where distinct flow phenomena are observed. In the lower range ($V_r < 2.5$) symetric vortex

shedding was to be seen, while in the higher range ($V_r > 2.5$) alternate vortex shedding was realized. The added mass and damping coefficients due to cylinder oscillation were calculated and a definite relation between time-averaged drag coefficient and the added damping coefficient was found. The authors observed a well organized alternate shedding pattern when the forcing frequency was twice the natural shedding frequency. The added damping coefficient reached its maximum, along with the time-averaged drag coefficient. The damping effect originated from the relative velocity between the fluid particles and the cylinder surface.

2.4 PIV Technique

Particle Image Velocimetry (PIV) has emerged as a powerful tool[8] for velocity field measurement in the study of bluff body wakes. The velocity field can be analyzed to recover vorticity maps on selected planes around the object. A complete review of this technique was first given by Adrian (1991). The theory of PIV is also well-covered in a chapter of the edited book by Goldstein (1997). In view of the importance of the development, however, literature on PIV is briefly reviewed here.

Keane and Adrian (1990) carried out Monte-Carlo simulation to determine the experimental parameters that would yield optimal performance of the PIV system. The authors recommended the following criteria: (i) The number of particles per interrogation area should be at least 15, (ii) The particle image displacement in the direction perpendicular to the light sheet (out of plane displacement) should be less than 1/4 (pixel) or light sheet thickness. (iii) The inplane displacement of the particle images should be about or less than 1/4 of the interrogation area size, (iv) The velocity gradient over the interrogation area should be at most 5% of the mean velocity. These recommendations are now widely followed in all PIV measurements.

Willert and Gharib (1991) described particle image velocimetry when interfaced with a computer. They derived expressions for cross-correlation based on FFT of PIV images. They implemented this method in a real flow field and identified the flow structures. Various aspects of image capturing, parameter setting for image analysis and related errors were discussed. The real strength of digital particle image velocimetry (DPIV) is the fact that the images can be captured in real time, viewed and then batch-processed.

[8] essentially over the past decade

Westerweel (1994) introduced a statistical model that describes the occurrence of spurious vectors in PIV data. Three post-interrogation procedures, namely global mean, local mean and local median tests were compared to optimize the performance of PIV evaluation. Predicted performances agreed very well with the artificially generated PIV images. Out of these three, the local median test was found to be most efficient.

Boillot *et al.* (1996) calculated the optimized pulse separation time (Δt) in cross-correlation based PIV measurements. Different parameters that affect the choice of Δt for accurate correlations are random error, acceleration error, gradient error, bias error and tracking error. The selection of the time separation between laser pulses can significantly impact the random error and acceleration error. Random error arises from noise during recording of the flow seeded with tracer particles and subsequent interrogation of the particle images. Acceleration error arises from the approximation of the local Eulerian velocity based on small particle displacement. It is seen that random error decreases with an increase in particle displacement ($=\Delta x$). The acceleration error increases with an increase in Δx. The authors reported an optimum separation time that minimizes the resultant error. The result was confirmed against Monte Carlo simulation.

Stanislas and Monnier (1997) discussed practical aspects of PIV image recording. Starting from proper selection of laser light source, generating light sheet and imaging the particles with CCD camera and the selection of proper optics have been discussed. Different errors arising from optical components used for PIV have been reported. Optical aberration is one such shortcoming which needs proper selection of optics. Particle image size is another important factor. The light scattered by particles is based on Mie theory and the intensity profile depends on particle size. There is a limitation on particle size for approximation of intensity field as Gaussian. The intensity profile of a particle image is a strong function of refractive index of the particle.

Melling (1997) presented the choice of seeding and tracer particles in both liquid and gaseous media. The scattering properties of seeding particles, and proper selection of the particle size and diameter for different flow conditions were discussed. The basic criterion of seeding particle selection is that it should follow the main flow without any velocity lag. This requirement can be established by assuming the seeding particles to be spherical and solving the corresponding equation of motion. If external forces such as gravitational, centrifugal and elctrostatic are negligible, then the particle path of a suspended particle is influenced by the particle shape, diameter, density and fluid viscosity.

Adrian (1997) discussed the dynamic ranges of velocity and spatial resolution of PIV. The criteria leading to an optimum design of a PIV system for a given experiment was discussed. The most important consideration is to match the size of a typical particle image with the resolution of the recording medium. The author showed that there is an optimum magnification which maximises the dynamic range of imaging. Reducing the magnification also increases the depth of field, increases the field of view and also increases the dynamic spatial range. The disadvantage of reducing the magnification is that it reduces the dynamic velocity range.

Huang *et al.* (1997) quantified the measurement error in PIV as mean-bias and RMS errors. A fundamental source of these errors is the correlation scheme used. Other sources of errors arise from the peak finding scheme and noise within the particle images. The peak finding scheme is used to locate the correlation peak with sub-pixel accuracy. The authors have compared two schemes, namely, cross correlation (CC) and particle image pattern matching (PIPM) to estimate the errors. The error in PIPM is one order smaller when compared to CC. The authors introduced a peak-normalization method that reduces the error level of CC to that of PIPM.

Rockwell (2000) gave a comprehensive review of the strength of PIV imaging for interpretation of unsteady separated flow. The identification of coherent structures in complex flow phenomena in terms of vorticity and their interpretation using tools such as POD and wavelets were seen to give better insight of the flow field. With advances in image analysis, the author concluded that it is possible to identify and assess the dynamics of coherent structures.

2.5 Closure

From the above survey of the published literature, it is to be seen that extensive studies have been carried out on different aspect of cross-flow past fixed and oscillating circular cylinders. Flow past cylinder of square cross-section has not been studied in such a great detail. Quite a few peculiarities emerge in the low and transitional ranges of Reynolds number. These aspects of flow past a square cylinder remain unexplored. In view of the possibility of using arrays of ribs of square cross-sections (fixed as well as moving) for flow control applications, the square cylinder geometry emerges as one of fundamental importance.

The transitional behavior (both spatial and temporal) for square cylinder differ

from that of circular cylinder due to difference in flow separation mechanism. There is very little understanding on this important aspect of flow field. The effect of inlet turbulence, effect of shear on the wake structure, and the route to chaos have not been studied in detail. The generation mechanism of the random components which are otherwise believed to be universal in nature seems to depend on the large scale structure. There is no check on the validity of two dimensional simulation for a practically three dimensional flow fields at intermediate Reynolds numbers.

As far as forced oscillations are concerned, no systematic study has been reported to understand clearly the flow physics. It is a new and an important topic due to its direct relevance for practical applications. Much of the literature is on trasverse oscillations. Very few studies have been reported for inline cylinder oscillations.

The present study is an attempt to understand flow phenomena at low and transitional Reynolds number of a square cylinder. An experimental study has been carried out with PIV and hotwire anemometry to understand both spatial and temporal characteristics of the flow fields of stationary and oscillating square cylinders. The study is restricted to inline oscillations of the cylinder. Two aspect ratios have been investigated. The Reynolds number consider in the present study range from 100 to 600.

Chapter 3

Apparatus and Instrumentation

Introduction

A setup for conducting experiments where wake properties of a square cylinder can be studied has been constructed as a part of the present thesis. The setup resembles a low speed wind tunnel, though smaller in the overall size. It is a vertical test cell made of Plexiglas with two optical windows, one for laser sheet and the other for recording images by the CCD camera. The working fluid is air and the direction of overall fluid motion is in the vertically upward direction. Particle Image Velocimetry (PIV) and Hotwire Anemometry (HWA) have been primarily used for velocity measurements. Flow visualization study has been carried out at low seeding density in the PIV setup. The cylinder is oscillated with the help of an electromagnetic actuator. This chapter describes details of the experimental hardware, including instruments and auxiliary equipment used in the present study. The validation results for proper PIV technique implementation, flow parallelism and turbulence intensity of the test cell and the effect of end plates have been discussed.

3.1 Experimental Setup

A schematic drawing of the experimental setup is shown in Figure 3.1. It comprises the following components: flow circuit, traversing mechanism for hotwire measurements, laser (pulsed), CCD camera, seeding arrangement for PIV measurements, and data acquisition system. The free-stream velocity approaching the cylinder has been determined using a pitot-static tube connected to a micro-manometer. The micro-manometer has a resolution of 0.001 mm of H_2O; it translates to an error in Reynolds number of about ± 2. The details of the test cell are discussed in the following section and the PIV and

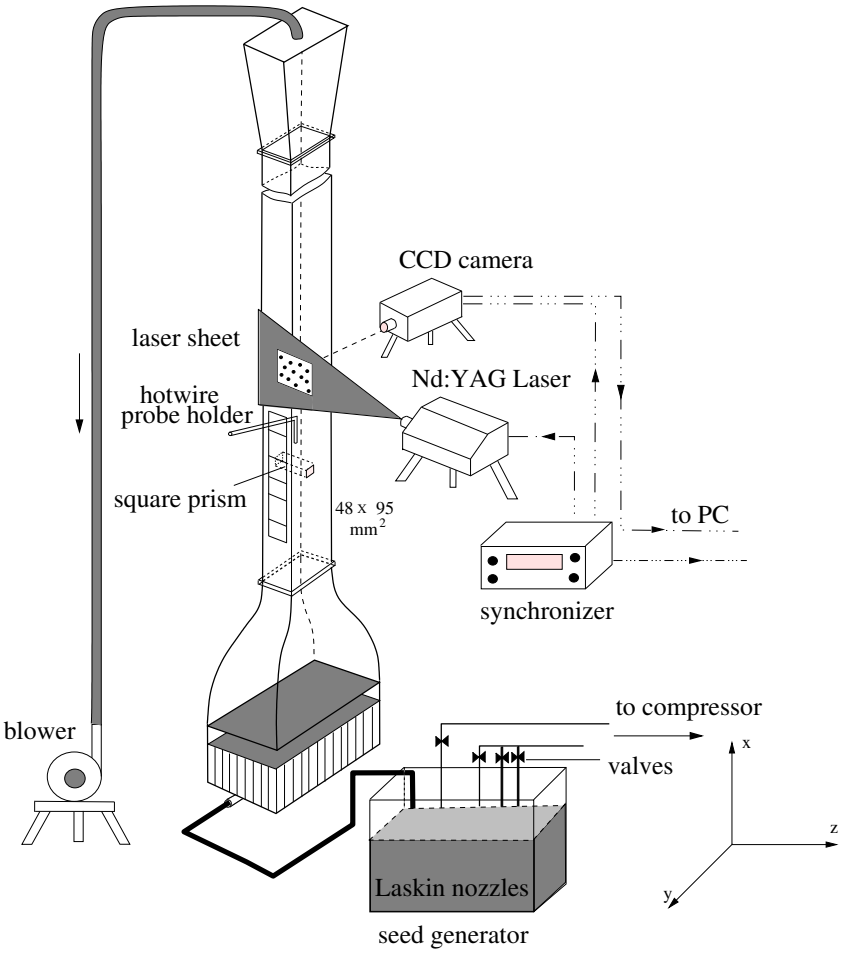

Figure 3.1: Schematic of the experimental setup.

HWA technique have been presented in the following section.

3.1.1 Test cell

Experiments have been performed in a vertical open-loop airflow system. The cross-section of the active portion of the test cell (to be called the *test section*) is 9.5×4.8 cm^2 with an overall length of 2 m. The active length of the test section where wake measurements have been carried out is 0.3 m. A contraction ratio of 10:1 ahead of the test section has been used. Prisms of square cross-section (3-4 mm edge) have been used for experiments as square cylinders. They are made either of Plexiglas or brass and carefully machined for sharp edges. Each cylinder is mounted horizontally with its axis perpendicular to the flow direction. It is supported along the two side walls for fixed cylinder experiments and mounted on actuators for oscillating cylinder experiments,

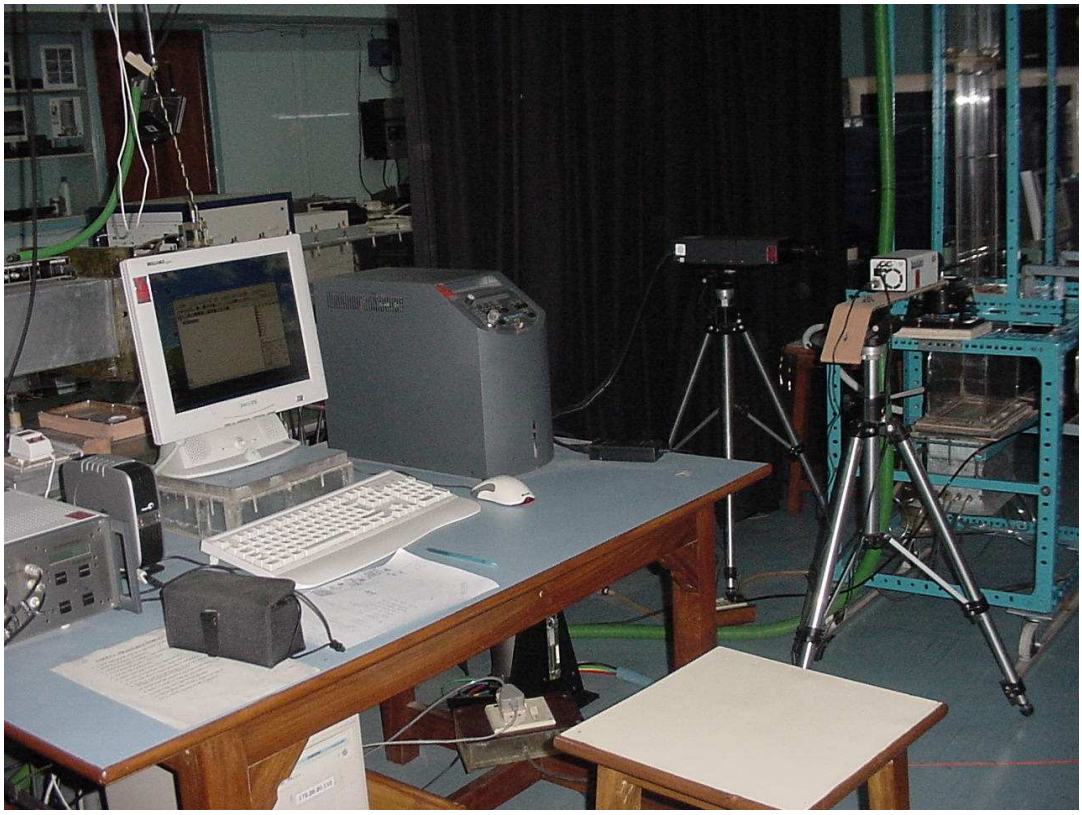

Figure 3.2: Picture of the PIV setup used for the present experiments.

Figure 3.13. Two different L/D ratios (also called *aspect ratios*) of 16 and 28 have been utilized in the experiments. The two aspect ratio was realized depending on the alignment of the cylinder axis with respect to test section sides. The corresponding blockages are 0.03 and 0.06 respectively. The effect of blockage seen to be negligible also mentioned in the literature, Zdravkovich [192]. With reference to Figure 3.1, the x-axis is vertical and aligned with the mean flow direction. The z-axis coincides with the cylinder axis and the y-axis is perpendicular to both x and z.

Flow in the test section was set up by a small fan (*Wolf*) driven by a single phase motor[1]. The suction side of the fan was used to draw the flow from the test cell. The power supply to the blower was from an online uninterrupted power supply unit (*Uniline*)to ensure practically constant input voltage to the motor. For better control of the voltage setting, particularly at low fan RPM and hence at low flow rates, the output of the UPS was stepped down via two variacs connected in series. In turn, this had the effect of minimizing the velocity fluctuations in the approach flow. The free stream turbulence level in the approach flow was quite small and it was found to be less than

[1]Names in italics indicate the make of the device.

(a) (b)

(c)

Figure 3.3: PIV components: (a) CCD Camera (b) Nd-YAG laser (c) Synchronizer.

the background noise of the anemometer ($< 0.05\%$). Flow parallelism in the approach flow was better than 98% over 95% of the width of the test cell. The validation of the test cell is discussed in a later section of the present chapter.

The flow to the test cell goes through three parts, namely the settling chamber, a honeycomb section and a contraction cone. Fine screens are mounted in the settling chamber for reducing the turbulence level of flow entering the test section. The contraction ratio of the contraction cone in area units is 10:1. The contraction cone reduces the spatial irregularities in the velocity distribution and helps in the decay of turbulence intensity by proper stretching of the vortices. The function of the honeycomb is to straighten the flow by damping the transverse components of velocity, and to reduce the turbulence level by suppressing the turbulence scales that are larger than the size of a honeycomb cell. The screens are used to suppress the small disturbances generated at the outlet tips of the honey comb. Proper mesh size gradation has been utilized by examining the diameter of the elements of the honeycomb, and hence the length scale of the vortices generated. Specifically, two screens, one with a coarse grid (10 per cm^2) and

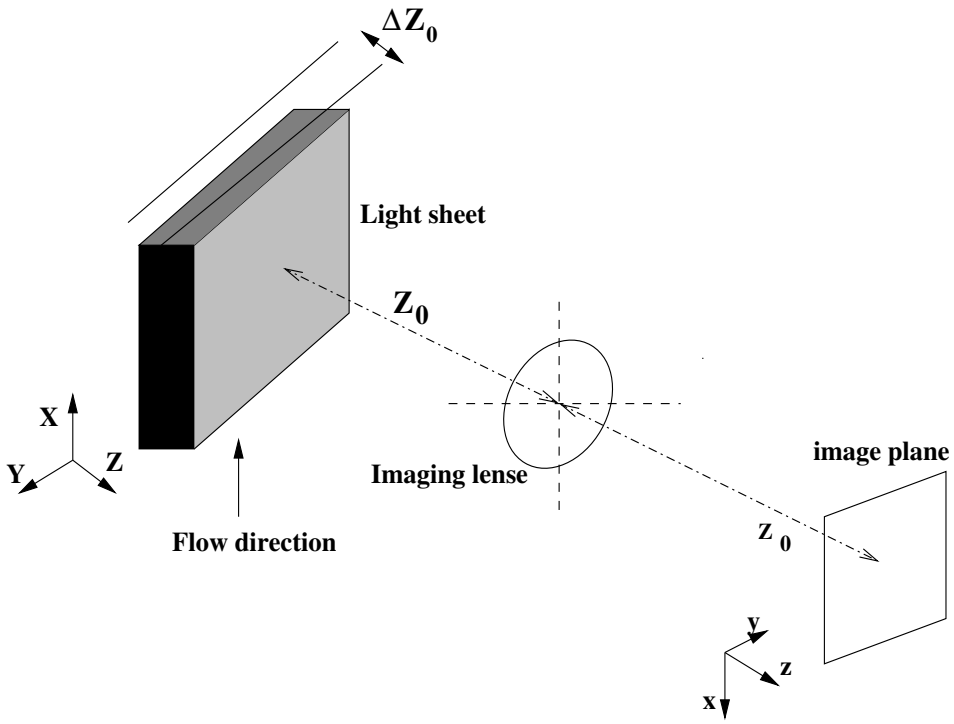

Figure 3.4: Imaging system for PIV.

Figure 3.5: Picture of the Laskin nozzle seed generator.

the other with a fine grid (100 per cm^2) have been used in the test cell. The distance maintained between the mesh and honeycomb has been selected by trial and error, to

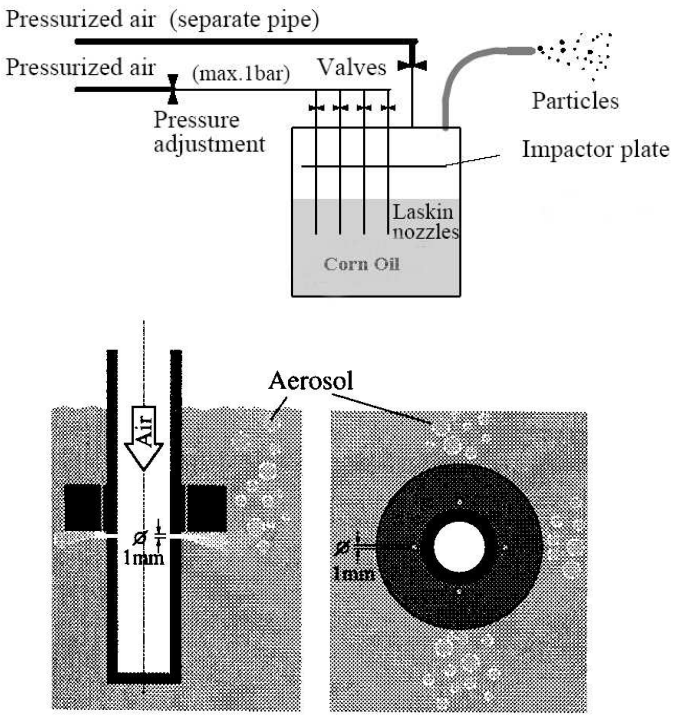

Figure 3.6: Schematic of the Laskin nozzle used for the seeding generation.

ensure that the smoothest possible flow approaches the square cylinder. Stable velocities in the range of $0.5 - 3$ m/s could realized in the test section . These values correspond to Reynolds number range $100 - 700$ for the cylinder sizes referred earlier. A seeding arrangement is fitted prior to the honeycomb for PIV measurements.

3.2 Particle Image Velocimetry

Traditionally, quantitative measurements of fluid velocity have been carried out using a pitot-static tube and hotwire anemometry. Both these techniques require insertion of a physical probe into the flow domain. This process is intrusive and can alter the flow field itself. In addition, measurements are averages over a small representative volume. The probe has to be physically displaced to various locations to scan the entire region of interest. The development of cost-effective lasers led to the development of Laser Doppler velocimeter (LDV) that uses a laser probe to enable non-intrusive velocity measurements. Velocity information by LDV however, is obtained point-wise similar to that of the pitot-static tube and the hotwire probe. Particle image velocimetry (PIV) is the state-of -the-art technique for velocity measurement in experimental fluid mechanics.

Original contributions towards its development were made by Adrian (1991), Gharib (1991), Melling (1997), and Westerweel (1997). The most important advantage of PIV is that it is a non-intrusive technique and gives the spatial details of the flow field over a plane of interest. There is some flexibility in the choice of the measuring plane. The measurement process can be repeated in time to yield temporal evolution of the flow field. The ability to make global velocity measurements makes PIV a special tool in experimental fluid mechanics.

With PIV, it is possible to acquire practically instantaneous velocity fields with high spatial resolution[2]. The spatial resolution is limited by the thickness of the laser sheet and the choice of the interrogation spot during analysis. The latter is about 8 or 16 pixels, and hence the smallest length scale that can be detected depends on the size of the pixel, and hence the spatial resolution of the camera. Depending on the camera speed, a time series of images can be recorded during experiments. The ensemble average of the instantaneous velocity vectors yields the time-averaged velocity field. This includes zones of reversed flow that cannot be dealt with by hotwire and pitot probes. Once the velocity field is obtained, other quantities such as vorticity, strain rates and momentum fluxes can be estimated. With developments in lasers, camera and high speed/low cost computers it is now possible to use PIV regularly for research and have industrial applications. Details of PIV image analysis are presented in Chapter 4.

The picture of the PIV setup is shown in Figure 3.2 and the photograph of important hardware of PIV is shown in Figure 3.3. In the present experiments, PIV measurements were carried out at selected planes perpendicular and parallel to the cylinder axis. A double pulsed Nd:YAG laser (*New Wave*) of wavelength $\lambda = 532$ nm, and 15 mJ/pulse with a maximum repetition rate of 15 Hz per laser head was used. The light sheet had a maximum scan area of 10×10 cm^2. The sheet thickness was about 1 mm to minimize the effect of the out-of-plane velocity component. The assembly of Peltier-cooled 12 bit CCD camera (*PCO, Sensicam*) and frame grabber with a frame speed of 8 Hz was used for acquisition of PIV images. Figure 3.4 shows geometric diagram of PIV measurements. A cross section of the flow is illuminated with a thin light sheet, and the tracer particles in the light sheet are projected onto a recording medium (CCD) in the image plane of a lens as shown in Figure 3.4. The intensity of the light sheet thickness ΔZ_o is assumed to changes only in the Z direction. The magnification of particle image depends upon the position of imaging lens. The CCD consisted of an array of 1280×1024 pixels. A

[2]The spatial resolution of a PIV system is the shortest distance between two points at which velocities can be obtained.

Nikon 50 mm manual lens with $f^{\#} = 1.4$ was attached to the CCD camera for covering the field of interest. Both the camera and laser were synchronized with a synchronizer controlled by a dual processor PC. The field of view employed in the present set of PIV measurements was 40 mm by 35 mm. Velocity vectors were calculated from particle traces by the adaptive cross-correlation method. The final interrogation size was 16×16 pixels starting from an initial size of 64×64. Thus, 5561 velocity vectors were obtained in the imaging area with a spatial resolution of 0.5 mm. Inconsistent velocity vectors were eliminated by local median filtering and subsequently replaced by interpolated data from adjacent vectors. The laser pulse width was 20 μs and the time delay between two successive pulses was varied from 40 to 200 μs depending on the fluid velocity (Keane and Adrian, 1990). The time-averaged velocity field was obtained by averaging a sequence of 200 velocity vector images, corresponding to a total time duration of 50 seconds. Laskin nozzles were used to produce seeding particles from corn oil. The mean diameter of oil particles was estimated to be 2μm.

Data generated from PIV carries superimposed noise. Noise is introduced during recording of PIV images (optical distortion, light sheet non-homogeneity, transfer function of the CCD, non-spherical particles, and speckle) and during data processing (peak fitting algorithm, image interpolation and peak deformation). The validation of the PIV technique was carried out by comparing velocities with pitot static tube and hotwire anemometry, as discussed in later sections.

3.2.1 Seeding arrangement for PIV

One of the most important steps in PIV measurements is seeding of the flow. In order to consider PIV as a non-intrusive technique, it is necessary that the addition of tracer particle does not alter the flow properties. Proper seeding is essential to capture complicated flow details, for example, the recirculation zone. Seeding should be homogeneous (spatially uniform) and sufficient (of high enough density). The injection of tracer particle has to be done without significantly disturbing the flow, but in a way and at a location that ensures homogeneous distribution of the tracers. Particles should be of small diameter so that they follow the original local air velocity without causing any disturbance. The particle density should ideally match that of the fluid to eliminate velocity lag. This issue is adequately taken care of by micron-sized particles for which surface forces are in excess of body forces.

For the present investigation, tracer particles (namely, droplets of corn oil) were

added to the main air flow by a number of copper tubes upstream of the honeycomb section. A large number of tiny holes, 0.1 mm diameter were drilled along the length of the copper tubes to make the seeding uniform over the entire test section. The seeding density was adjusted through an air pressure control valve. Laskin nozzles were used to produce oil droplets as tracers. For the range of frequencies in the wake, an expected slip velocity error of 0.3% to 0.5% relative to the instantaneous local velocity is expected in the present study (Adrian, 1991).

Laskin nozzles are widely used as atomizers of non-volatile liquids due to simplicity of design and the resulting uniform particle size distribution. The picture of the Laskin nozzle seed generator has been shown in Figure 3.5. A detailed schematic drawing of the Laskin nozzle seed generator is shown in Figure 3.6. The particles should be small in size, spherical in shape, of appropriate density and refractive index, and non-volatile. Above all, the liquid should be non-toxic and of low cost. The particles should be efficient scatterer of the illuminating laser light. This largely decides the illuminating laser type and the recording hardware i.e. camera. For example, if a given particle scatters weakly, then one would have to employ more powerful lasers or a more sensitive camera, both of which can drive up costs, as well as the associated safety issues. Corn oil was used for the present work, in view of its high surface tension required for producing small particles along with favorable light scattering properties.

An important source of error in velocity measurement is the particle weight. The following analysis ascertains that particle weight is not a major consideration in the present experiments in the sense that particles would follow the main flow without excessive slip. The approach is to find the settling velocity of the particles under a gravity field. Assuming that Stokes law of drag is applicable, the settling velocity u_∞ is given by

$$u_\infty = \frac{g d_p^2 (\rho_p - \rho_f)}{18\mu}$$

Here d_p and ρ_p are the particle diameter and density respectively, and μ and ρ_f are the fluid viscosity and density respectively. Particles are suitable as long as u_∞ is negligible compare to actual fluid velocity. For the present set experiments, u_∞ was estimated to be 0.014 m/s.

3.2.2 Particle dynamics

The particle dynamics as outlined by Adrian (1991) for successful PIV measurements is discussed in this section.

The PIV technique measures in principle the Lagrangian velocities of the particle, v. If the particle velocity is being used to infer Eulerian fluid velocity $u(x,t)$, one must consider the accuracy with which the particle follows the fluid motion. With subscript p denoting particle-level properties, the equation of motion of a single particle in a dilute suspension[3] is a balance between inertia and drag force is written as:

$$\rho_p \frac{\pi d_p^3}{6} \frac{dv}{dt} = C_D \frac{\rho \pi d_p^2}{4} |v-u|(v-u) \tag{3.1}$$

The above equation requires a correction for the added mass of the fluid, unsteady drag forces, pressure gradients in the fluid, and nonuniform fluid motion. In gaseous flows with small liquid particles, we may ignore all these terms except the static drag law with drag coefficient C_D. This term incorporates finite Reynolds number effects.

Particle response is often described in terms of the flow velocity and a characteristic frequency of oscillation. The first question is, how fast can the flow be, before the particle lag $|v-u|$ creates an unacceptably large error. An appropriate approach is to evaluate the particle slip velocity as a function of the applied acceleration. For the simplified drag law of the above equation, one has

$$|v-u| = \left[\frac{2}{3} \frac{\rho_p}{\rho} \frac{d_p}{C_D} |\dot{v}| \right]^{\frac{1}{2}} \tag{3.2}$$

This shows that the slip velocity for finite particle Reynolds number, where $C_D \sim$ constant, is only proportional to the square root of the acceleration. In the limit of small particle Reynolds number $|v-u|d_p/v \leq 1$, Stokes' law may be used to evaluate C_D, resulting in

$$|v-u| = \frac{\rho_p d_p^2 |\dot{v}|}{36 \rho v} \tag{3.3}$$

The time separation Δt is the single most important adjustable variable in a PIV system, as it determines the maximum and minimum velocities that can be measured. The duration of the light pulses δt, determines the degree to which an image is frozen during the pulse exposer. The accuracy of velocity measurements depends upon one's ability to determine the displacement of the particle, Δx over a certain time interval from measurements of the displacement of the image ΔX.

[3] an assumption of non-interacting particles

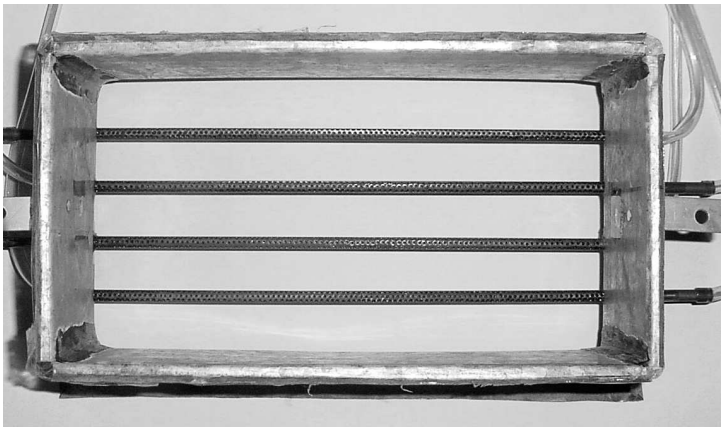

Figure 3.7: Distributed hole arrangement for uniform seeding distribution.

3.2.3 Generating a light sheet

For PIV measurement a high intensity light is required for efficient scattering of light from tracer particles. Light sheet is generated from a collimating laser beam using cylindrical lens and spherical lens. The effective intensity of a light sheet can be increased by sweeping a light beam to form sheet thereby concentrating the energy by a factor equal to the hight of the light sheet divided by the height of the beam. Figure 3.8 shows the schematic of a light sheet formation. A combination of cylindrical and spherical lens is used. A negative focal length lens is first use to avoid focal line. The cylindrical lens causes the laser beam to expand in one direction only, i.e. it "fans" the beam out. The position of the minimum thickness is determined by the focal length of the cylindrical lens. The spherical lens causes the expanding beam to focus along the perpendicular direction, at a distance of one focal length downstream to its beam waist.

3.2.4 Synchronizer

In order to make PIV measurements, different components of the PIV system need to be time coordinated, for example, the camera, the laser flash lamps and its Q-switches. The synchronizer controls the time sequence. A part of the functions is executed automatically, while others have to be defined by the user. The synchronizer thus manages all the timing events needed for doing PIV measurements[4].

The main task of the synchronizer is the control of the camera and the laser timing.

[4]The synchronizer of the present study was supplied as a part of the PIV system by *Oxford Lasers*.

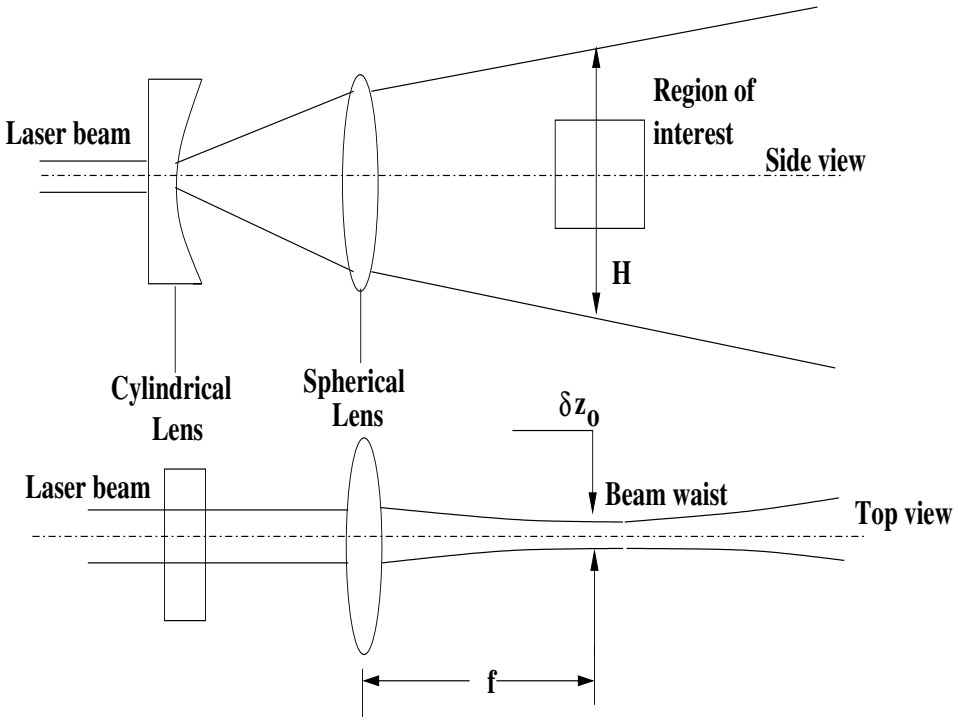

Figure 3.8: Light sheet formation using spherical and cylindrical lens for PIV.

The frame grabber needs 40 ns to lock onto the trigger signal. Afterwards, the control data can be transferred to the camera. The exposure time is controlled by the external trigger from the synchronizer in a user-defined range between 100 ns and 1 ms. Before the second exposure, the camera has a frame straddling time of 200 ns or 1 μs, which depends on the parameter settings of the cross correlation function. Before the next double exposure can be started, data of the first image pair is transferred to the frame grabber.

The laser must be synchronized to the double exposure mode of the camera. For emitting a laser pulse, a high energy must be generated in the laser cavity. The laser cavity has a Nd:YAG rod that is pumped with energy from a flash lamp. There is a nonlinear relation between the time the cavity is pumped and laser power emitted. During the pumping procedure, the mirror at the far end of the cavity is closed by a Q-Switch. The success of PIV measurements depends crucially on the time correlation between laser pulse generation and camera recording achieved by the synchronizer unit. Figure 3.9 shows the timing diagram for the pulsed laser with double shutter CCD camera.

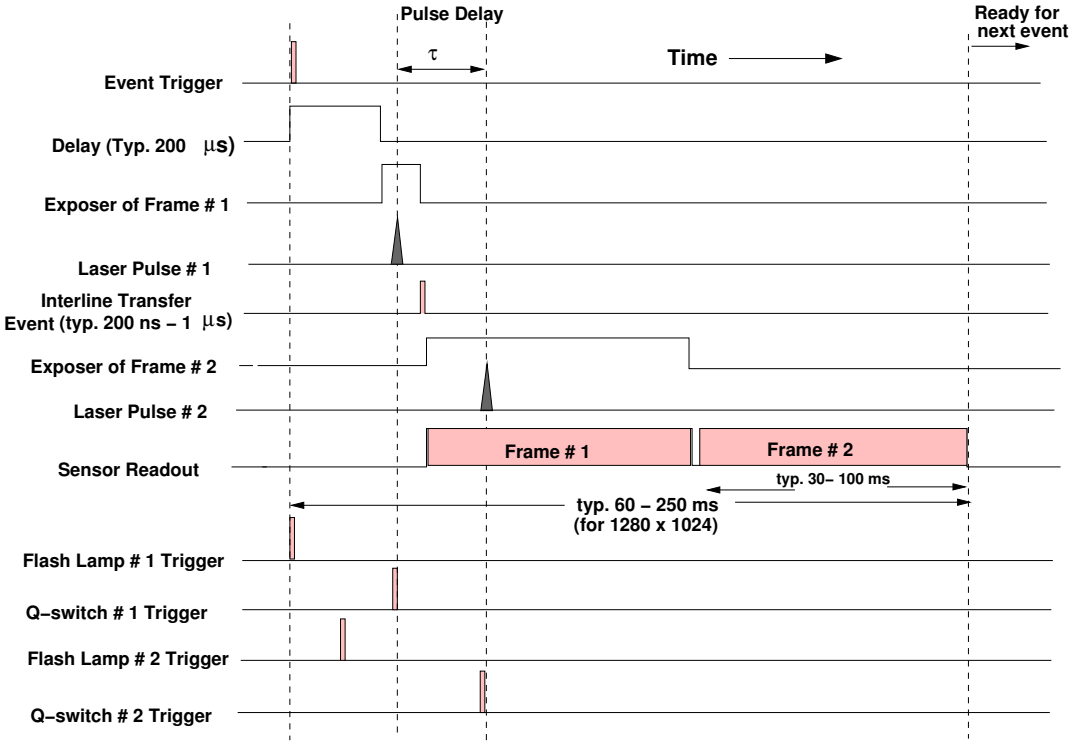

Figure 3.9: Timing diagram for CCD camera and double pulsed laser (PIV Manual, Oxford Lasers).

3.3 Hotwire anemometry

A two channel hotwire anemometer (*DANTEC*) was used for the present investigation. Hotwire anemometry (HWA) is based on the principle of compensation of the rate of heat loss $\dot{Q}$ of a small heated metallic wire exposed to flow. The probe responds primarily to the magnitude of the velocity vector. The anemometer output voltage then undergoes signal conditioning to filter out noise and improve the signal-to-noise ratio. The operating temperature of the hotwire is usually much higher than the room temperature, typically $150-250°$C in air flow measurements. In the present experiments, the probe operated at a temperature of around 150^oC; this minimized mixed convection and radiation errors[5], without appreciable loss of sensitivity. Higher temperatures enhance the sensitivity of wire but make the wire fragile. Additionally, to avoid oxidization it is essential that the wire temperature at any point along the wire element is kept well below 350^oC.

To illustrate these points, consider a typical hotwire probe (DANTEC 55P11) for which the electrical properties are $R_{20} = 3.5\Omega$ and $\alpha_{20} = 0.0036^oC^{-1}$. For an overheat

[5]that are significant at low velocities, as in the recirculation bubble

ratio of 1.5, the operational resistance of the wire will be $1.5 \times 3.5\Omega$. The corresponding mean wire temperature can be evaluated from the equation

$$R = R_{20} + \alpha_{20} R_{20} (T_{sensor} - T_{20})$$

as being equal to about 150^oC, which is well below the oxidation temperature. On the front panel of the anemometer, the parameter fixed is the operating resistance of the wire.

The output of the feedback circuit of the anemometer is a measure of the fluid velocity. After proper calibration of the probe, it is possible to measure fluid velocities with an accuracy of 0.05% or better, depending upon the measurement range and the quality of calibration. In view of the high frequency response of the hotwire anemometer[6], it can follow transients in the flow field without practically any time delay. The hot-wire has a limitation that it is insensitive to the flow direction. For an X-probe, the velocity measured by each wire is different from the component of velocity in the laboratory coordinates. The velocity sensed by each wire is known as the effective cooling velocity.

The minimum velocity that can be measured by the HWA is determined by the velocities associated with natural convection from the heated wire. If a probe is calibrated and used under the same orientation with respect to the gravity field, it may be used at low velocities. The limit is then reached when natural convection dominates forced convection. In dimensionless form, this limit is expressed in terms of Reynolds number Re and Grashoff number Gr as (Goldstein, 1997)

$$\mathrm{Re} < 2 \times \mathrm{Gr}^{\frac{1}{3}}$$

where Re=$U \times D/\nu$ and Gr=$gD^3\beta(T_w - T_o)/\nu^2$. The notation used is: U is the fluid velocity, D is the sensor diameter, ν is the kinematic viscosity of the fluid, β is the coefficient of thermal expansion (equal to $1/T$ for an ideal gas) and $T_w - T_o$ is the excess sensor temperature over the ambient. For the present experimental conditions, the minimum Reynolds number for which forced convection dominated natural convection was estimated as Re=23, which corresponds to an air velocity of 0.12 m/s.

The hotwire anemometer accompanied by a feedback circuit is referred to as the constant temperature anemometer (CTA), Figure 3.11. The CTA consists of a Wheatstone bridge and a servo amplifier. One arm of the Wheatstone bridge is the probe sensor. As the flow condition varies, the sensor tends to cool appropriately with a resulting change in resistance. The change in resistance leads to an error voltage $e_2 - e_1$.

[6] in excess of 1-5 kHz

These two voltages form the input to the operational amplifier. The selected amplifier has an output current, i, which is inversely proportional to the change in the resistance of the hot-wire sensor. Feeding this current back to the top of the bridge will restore the sensor's resistance to its original value. The feedback circuit plays an important role in improving the frequency response of the hotwire, typically from 10-20 Hz to several kHz.

The temporal flow field has been mapped in the present work using an X-probe for obtaining the u and v components of velocity. In two-dimensional measurements, calculation of velocity components involves solving a pair of non-linear, simultaneous equations. Thus, the accuracy of hotwire measurements is affected by the accuracy of the calibration procedure. In addition, the accuracy of the numerical solution that is used to solve the nonlinear simultaneous equations is relevant. Two approaches were applied for data reduction and are discussed in Chapter 4. Both approaches yielded nearly identical velocities, thus showing that numerical aspect of data reduction was satisfactory.

The X-probe supplied by DANTEC has been used in the present research, which mostly satisfies all the above- stated criteria. Additionally, some of recommended electronic tests[7], by the manufacturer[8] have also been carried out to optimize the response of the anemometer's output voltage.

3.3.1 Hotwire Probes

Two platinum-coated tungsten wires forming an X-probe in the vertical plane (normal to the cylinder axis) have been used in the present work. The probe was supplied by *DANTEC*. The wire properties are: $\alpha_{20} = 0.0036\Omega/\Omega^o$C, diameter=5$\mu$m, length=1.25 mm. The measurements of two components of velocity and velocity fluctuations were carried out by using X-probes, type-55P61, (Figure 3.12-b) and Type-55P11 (Figure 3.12-a), operating at constant temperature.

[7]The square wave test, or dynamic bridge balancing, serves two purposes: It can be used to optimize the bandwidth of the combined sensor/anemometer circuit or simply to check that the servo-loop operates stable and with sufficiently high bandwidth in the specific application. It is carried out by applying a square wave signal to the bridge top. The time it takes for the bridge to get into balance is related to the time constant, and hence the bandwidth, of the system. DANTEC CTA anemometer has the built-in square wave generators.

[8]DANTEC instruction manual: Type 56C17- CTA Bridge.

Figure 3.10: The picture of the Hotwire anemometer

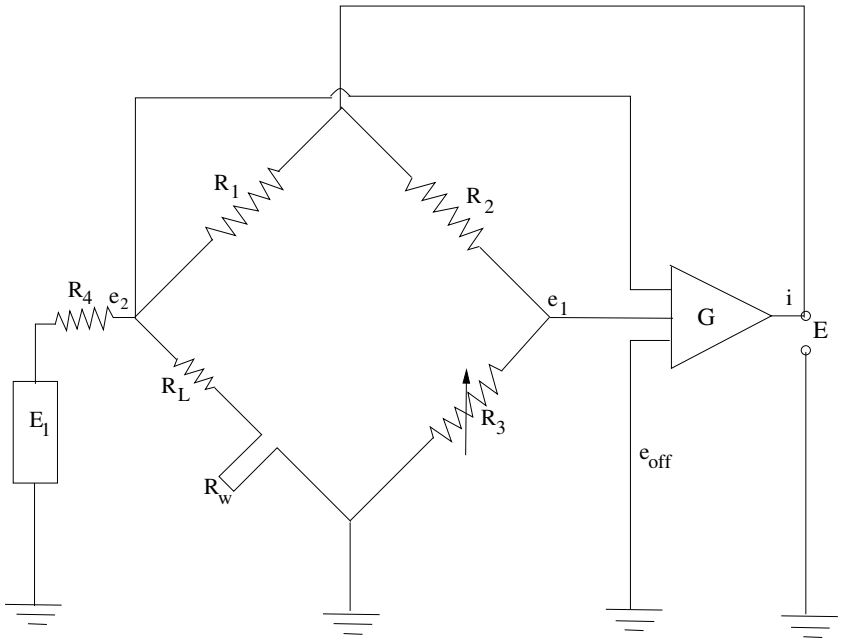

Figure 3.11: Circuit diagram of a Constant Temperature Anemometer (CTA).

3.3.2 CTA Bridge and Accessories

The hotwire probes were driven by the commercially available DANTEC 56C17 constant temperature Wheatstone bridge circuits. The 56C17 CTA bridge is supplied as a plug-in module for an existing 56C01 CTA system. The main unit 56C01 CTA delivers the

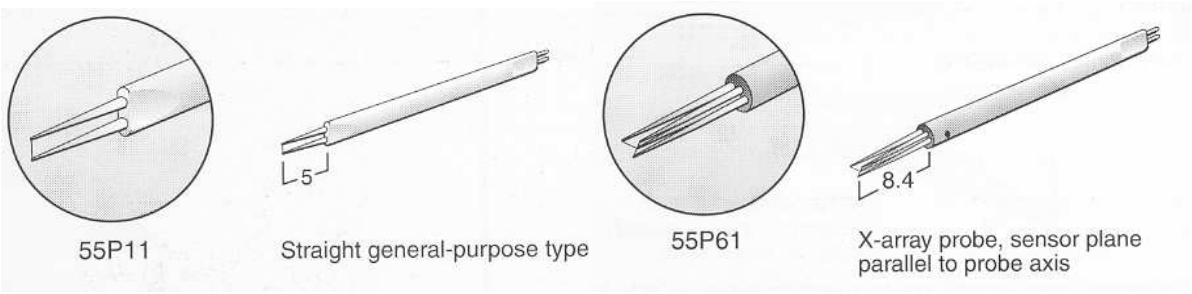

(a) (b)

Figure 3.12: Miniature Wire Probes – 5μm diameter, platinum-plated tungsten wire, welded at the ends of prongs to provide active sensor length of 1.25 mm.

servo-voltage as the output of the instrument. This voltage is a measure of fluid velocity. The 56C01 circuits contain servo amplifiers, filters, protective circuits, and a square-wave generator for dynamic balancing of the bridge.

The 56C01 CTA contains a function switch with three modes for operation, namely TEMP, STD.BY and FLOW. In TEMP position the resistance of the connected probe can be measured in terms of a current supplied to it. In STD.BY position no current flows through the bridge. In FLOW setting the CTA starts operating with the function of the servo amplifier. If the function switch is shifted quickly from position TEMP to FLOW, the square-wave generator is activated.

A setting named BRIDGE ADJ enables the adjustment of bridge balance for measurement of probe resistance and setting of the desired overheat resistance. BRIDGE ADJ has a switch pair for coarser adjustment of overheat resistance and a screw for fine adjustment. Resistance settings ranging from 0-30 Ω in steps of 0.001Ω are possible. This adjustment is crucial for adjusting the overheat resistance for the calibration procedure. CTA in TEMP mode produces a voltage proportional to resistance of wire[9]. From the wire resistance, the instantaneous temperature attained by the wire at a given location in the flow field can be determined.

The main-frame of the anemometer unit is fitted with the 56N20 signal conditioner unit, which is designed to amplify the AC signals up to a level suitable for PC-based data acquisition. The signal conditioner can selectively amplify the input signals with gain factors ranging from 1 to 900. The filter circuit comprises high-pass and low-pass filters as well as an amplifier. The filter settings were determined in the present work by examining the complete power spectrum of the velocity components. For the present

[9]Here it functions as a constant current anemometer, CCA, and measures the wire resistance.

investigations, voltage signals from the CTA were low-pass filtered at 3.0 kHz and high-pass filtered at 0.1 Hz. The mean-value unit 56N22 is a 5.5 digit display voltmeter, and the primary purpose of this module is to measure the DC component of the output signal from 56C01 CTA. This module has a 100 μV resolution, 1-1000 seconds integration time and switch selectable 14 inputs.

3.3.3 Data Acquisition System

The HWA output is a continuous analog voltage signal; it has been sampled as a time series consisting of discrete values by an analog-to-digital converter (A/D board). The accuracy of the analog output signal is determined by the quality of the anemometer hardware. The accuracy of the reduced time series depends on the choice of the A/D board, the selection of *sampling intervals*, *number of samples*, N, and the extent of digitization. The values for *sampling rate*, SR and N depend primarily on the specific experiment, the required data analysis (time-averaged or spectral analysis), the available computer memory and the acceptable level of uncertainty. The level of digitization is specified as m-bit, indicating a resolution of the ratio of the full-scale reading and 2^m. The full scale reading is in the range of 0-10 V. Smaller voltages can be measured by using a gain of upto 1000. The final accuracy is thus a product of instrument specifications and data acquisition set-up related to the actual flow.

Time-averaged analysis, such as the determination of the time-averaged velocity and of velocity fluctuations requires uncorrelated samples. It can be achieved when the time elapsed between individual samples is at least two times larger than the integral time scale of the velocity fluctuations. On the other hand, spectral analysis requires the sampling rate to be at least twice the highest frequency in the flow oscillations[10]. In the present experiments, a long signal, typically of 20 seconds duration with a sampling frequency of 1000 Hz was recorded from the hot-wire anemometer. A band pass filter (0.1 Hz- 1 kHz) and a gain setting (10) were additionally used. The A/D card was configured in the differential mode to avoid unwanted noise in the measured signal. The signal is amplified prior to digitization. The gain, ranges and resolution are selected on the basis of the characteristics (amplitude and spectral) of the input signal.

The instantaneous voltage signals have been recorded by using a DAQ card (*Keithley Instruments*, KPCI-3108) of 16 bit resolution. The advent of graphical programming concept introduces the possibility of creating a new type instrumentation, not in hard-

[10]This requirement emerges form the Nyquist criterion in digital signal processing.

ware but in software. This new approach is called *Virtual Instrumentation*, (VI). In the present investigation, *LabVIEW® Software* has been used for programming the Keithley A/D card. LabVIEW (*Laboratory Virtual Instrument Engineering Workbench*) delivers a powerful graphical development environment for signal acquisition, measurements, analysis, and data presentation. It gives the flexibility of a programming language without the complexity of traditional development tools. Both data acquisition as well as cylinder actuation have been conducted in the LabVIEW environment.

3.4 Electromagnetic Actuator

The arrangement of the cylinder in the test section and the apparatus used for achieving forced in-plane oscillations of the cylinder are shown in Figure 3.13. A dual channel power oscillator with two electromagnetic drive units was used to generate controlled movement of the cylinder. The actuator assembly was procured from *Spanktronics.* The electromagnetic actuator consists of the yoke, magnet and pole tip, and the moving coil assembly. It works by virtue of the interaction between the magnetic field and an oscillating current flowing in the coil of the moving assembly. Under such circumstances, a force is generated at right angles to the line of flux and the conductor carrying the current. This force is proportional to the product of instantaneous current and the magnetic flux density. The useful frequency range of the actuator is equal to 1-200 Hz. The maximum amplitude is 1.5 mm, corresponding to 50% of the cylinder size.

The cylinder was mounted horizontally and fixed on the two electromagnetic drive units on each side of the test cell. Proper care was taken to ensure that no leakage occurred at the junctions of the test cell and the cylinder. During experiments, the shedding frequency of a stationary cylinder was first measured using a hotwire. The cylinder was subsequently excited at various harmonics around the shedding frequency in the streamwise direction. The amplitude of excitation was set by the voltage input to the electromagnetic actuator. Both actuators operated from a single power source and thus ensuring identical phase. In an open loop arrangement, the activation signal was generated from a built-in signal generator in the power oscillator. With feedback, the activation signal was generated from the hotwire output with suitable amplification and phase inversion to the drive unit. Here, the feedback signal was low pass-filtered and sent to the digital-to-analog converter. The amplitude of the cylinder displacement was measured from magnified images of the cylinder oscillation using the CCD camera.

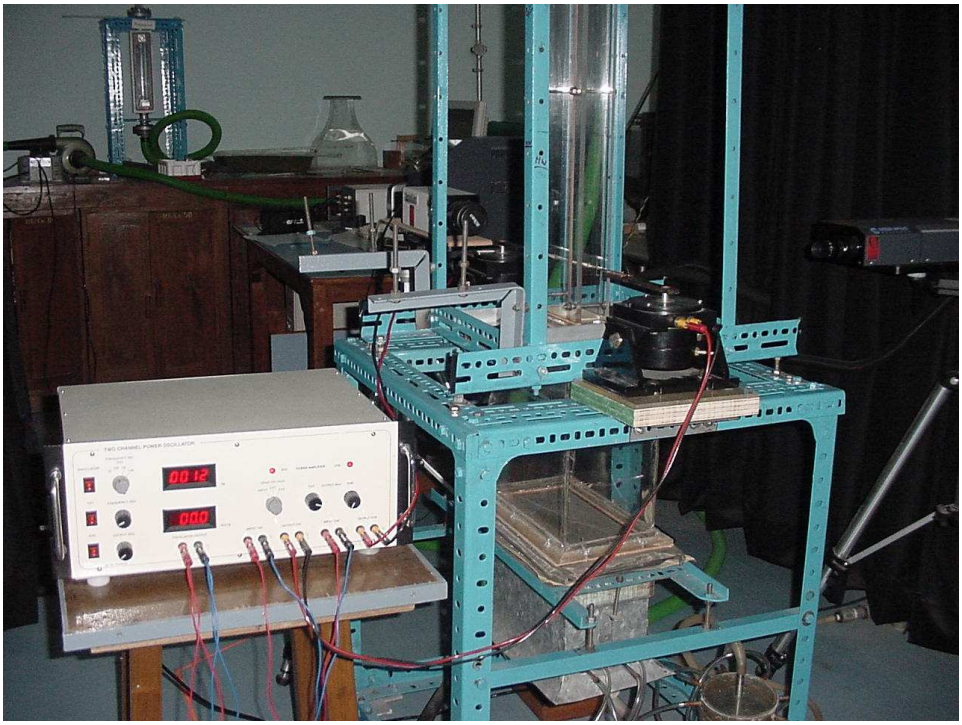

Figure 3.13: Experiments with actuator

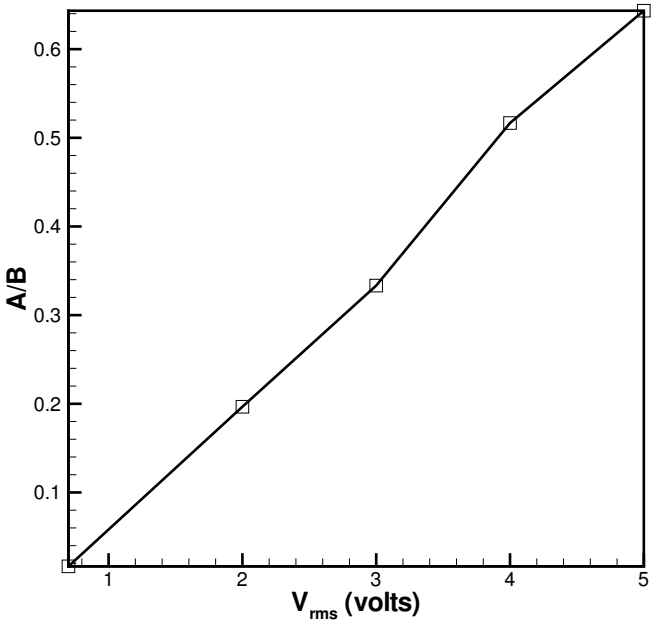

Figure 3.14: Variation of cylinder displacement with voltage applied on actuators.

3.5 Auxiliary instruments

Starting from the initial validation of the vertical test cell to the final measurements of the cylinder wake, various instruments, other than HWA and PIV have been used. A brief introduction to these instruments is presented below.

3.5.1 Digital Micromanometer

The pitot-static tube was used for velocity measurements in the undisturbed flow. It was connected to a high quality differential pressure micromanometer (model FC012, *Furness Controls*) with a pre-calibrated velocity output and a digital display. The micromanometer uses a capacitance-type differential pressure transducer. It measures differential pressures upto 1.99 mm H_2O with a resolution of 0.01 mm H_2O. It is equipped with a temperature correction chart to account for changes in the room temperature. The maximum measurable velocity with this manometer is equal to 5.6 m/s. The pitot-static tube and digital manometer combination have been used for calibration experiments of the hotwire anemometer.

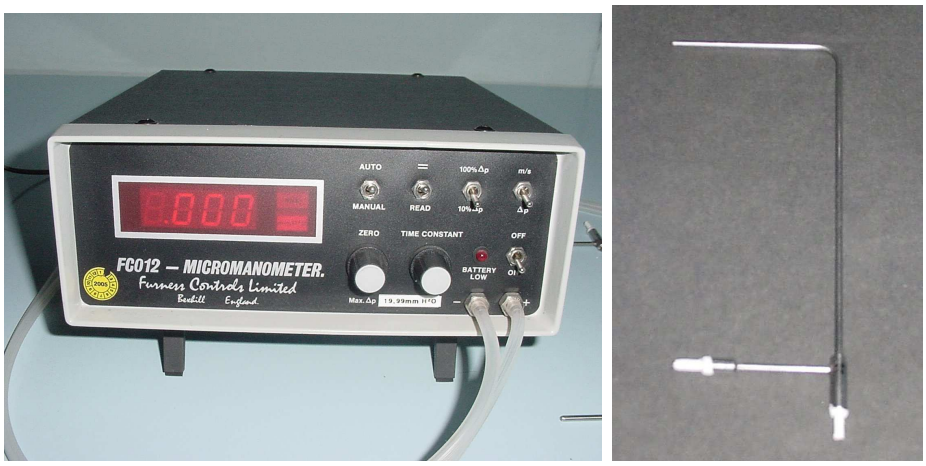

Figure 3.15: Picture of the micromanometer (left) and pitot static tube (right) used during the experiment

3.5.2 Digital Multimeter

The HP 3457A is a versatile digital multimeter. It can measure DC voltage, AC voltage, AC and DC currents and the resistance over a wide range of values. The math opera-

tion facility can manipulate or modify a set of measurements before display. The STAT operation can perform up to five running calculations on the present series of measurements and stores the results. It evaluates the standard deviation, time-mean, number of samples, upper reading and lower reading. These facilities can be used to measure mean temperature and the RMS value of the temperature fluctuations with the constant current mode of the hotwire anemometer.

3.5.3 Spectrum Analyzer

The digital spectrum analyzer used in the present work (*Advantest* R9211E) employs the Fast Fourier transform (FFT) algorithm for determining the signal statistics. Wide band as well as high sensitivity measurements can be performed in the frequency range of 10 mHz-100 kHz and input voltages of 1 μVrms-31.6 Vrms. The analyzer has four different modes of operation. The waveform and spectrum modes are important ones generally used in turbulence measurement. In waveform mode the spectrum analyzer does on-line measurement of the time signal, followed by calculations of the histogram (PDF), autocorrelation and cross-correlation functions. In the spectrum mode, it measures power spectrum and the complex spectrum. It has various options such as Math, Setup, Device and Copy. The Math menu does arithmetic operations between two arrays and integration and differentiation of an array. This facility can be used for the measurement of average of product of two-wire signals. All traces shown on the screen can be stored on a floppy and processed whenever required. These facilities have helped in standardizing the measuring procedures linked to the HWA[11].

3.5.4 Digital Oscilloscope

A two channel digital storage oscilloscope (*Gould* 1602) with a sampling speed of 20 Ms/sec and an operating frequency range of $0-20$ MHz has been used. The Gould 1602 can operate in storage as well as non-storage mode. In the former, it has a sampling speed of 2 MHz. The oscilloscope has been used for square wave testing of the hotwire anemometer.

[11]The use of LabVIEW during the later stages of research obviated the use of the spectrum analyzer.

Figure 3.16: Picture of the storage digital oscilloscope

3.6 Flow Visualization

Many of the most exciting discoveries in the field of fluid mechanics have been possible due to careful flow visualization. The flow visualization allows us to gain an overall view of flow patterns. It helps in identifying the vortex structures and other secondary flow features. The introduction of tracer particles and the study of their movement provides considerable information of the flow physics. In liquids, colored dyes and gas bubbles are common tracers, whereas for gas flows, smoke, helium-filled 'soap' bubbles or gas molecules made luminous by an ionizing electric spark have served as tracers.

For the present investigation, flow visualization was carried out in the test cell using light generated from the pulsed Nd:YAG laser. Visualization was carried out in the near-wake region of the cylinder. The flow was seeded with small diameter oil droplets that were produced by the commercial particle generator discussed in Section 3.2.1. There is an important difference between the nature of seeding for flow visualization compared to that of PIV measurements. In the latter, seeding is spatially homogeneous with a high particle density. The homogeneously seeded images appear featureless i.e. no flow structure is visible. Structures become visible only when the velocity field is evaluated. During flow visualization, seeding is done in an inhomogeneous manner. It clusters around the cylinder and the seeding density is reduced to highlight the flow structures. The CCD camera is once again synchronized with the firing of the laser, though image pairs are not required. The images of the CCD camera are each of 1280×1024 pixels. During experiments, images were acquired through a PC at a rate of 8 Hz. The light sheet and the camera were perpendicular to each other. The particle traces were further processed with an imaging software (*Paint-shop* available with MS-Windows) to improve

clarity.

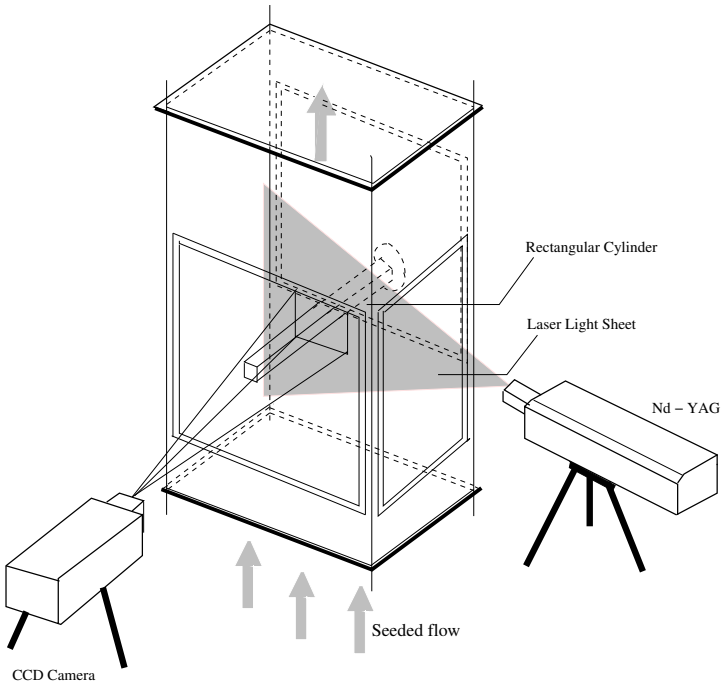

Figure 3.17: Schematic of the flow visualization arrangement.

3.7 Test Cell Flow Quality

The inlet flow turbulence level and the flow parallelism have been tested for flow quality of the test cell. Figure 3.18 shows representative vector plots at two different velocity settings from PIV measurements. The turbulence level in the incoming flow is equal to 0.06% (Figure 3.19). The turbulence intensity was measured from the hotwire signal. The test cell flow parallelism has been presented in Figure 3.20. Flow parallelism in the approach flow is better than 98% over 95% of the width of the test cell. Uniform and stable free stream velocities in the range 0.5-3 m/s were realized in the test cell to cover the Reynolds number range of 100-800. Figure 3.20 (a) also compares the velocity from pitot static tube with that from PIV. The excellent comparison between the two techniques indicates the successful implementation.

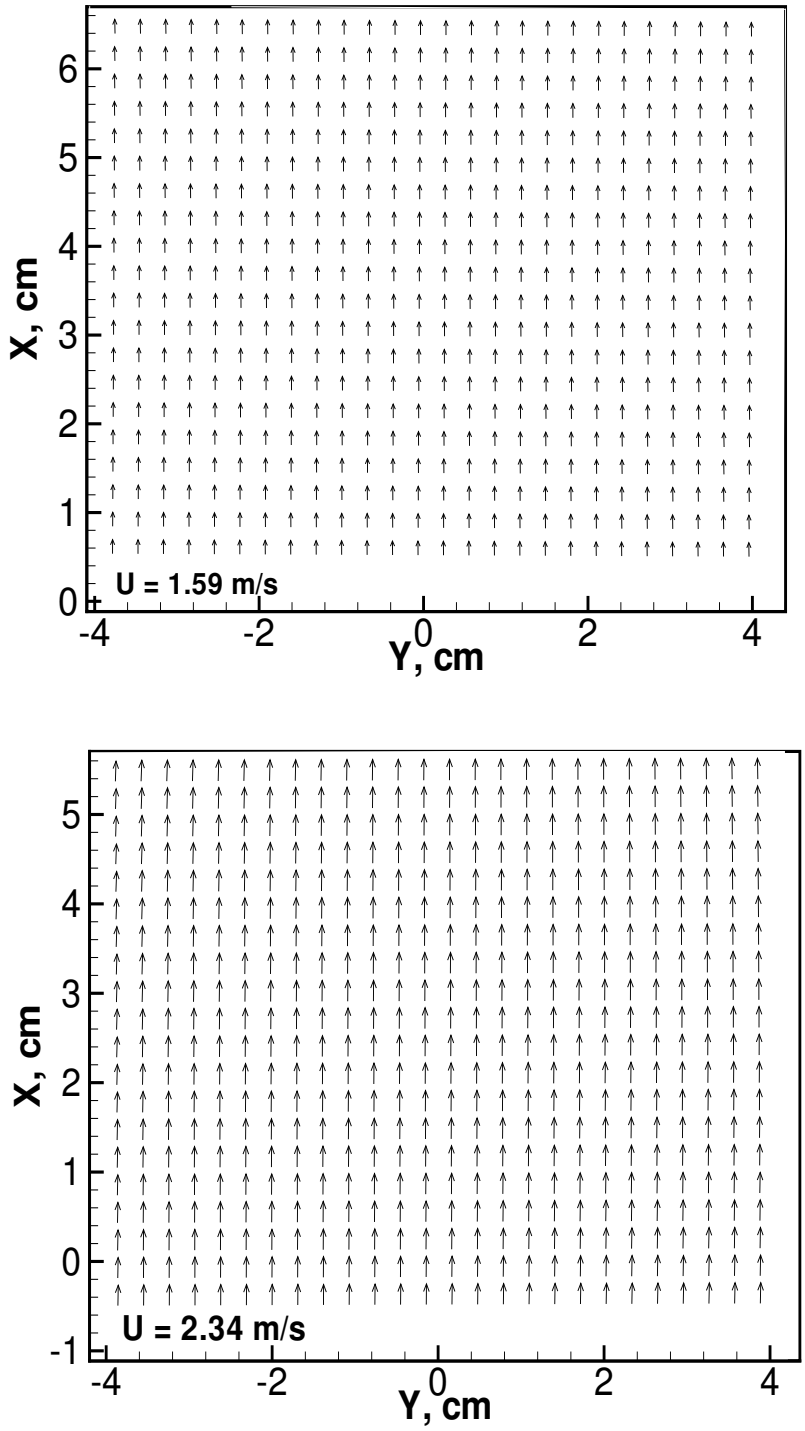

Figure 3.18: Time-averaged free stream velocity vectors from PIV at two blower settings.

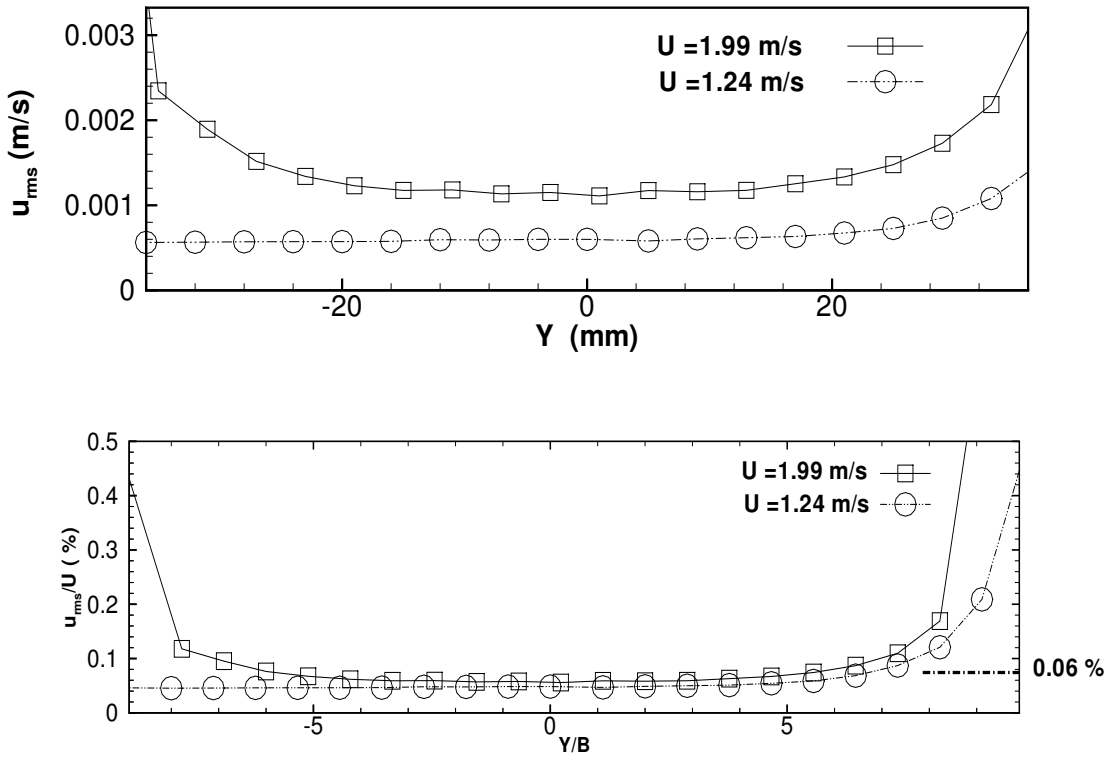

Figure 3.19: Turbulence level of the incoming flow measured by the hotwire anemometer. The average incoming velocity is denoted as U. The top and the bottom figures show dimensional and non-dimensional values respectively.

3.8 Influence of end-plates

The effect of end conditions on the aerodynamics behind bluff bodies is a known fact. The wake stability and the critical Reynolds number are also influenced by the aspect ratio of the cylinder. End plates reduce three-dimensional effects, i.e. they shield the cylinder from the interfering wall boundary layers. Different designs of end plates have been proposed in the literature. The effect of aspect ratio on the wake structure is also affected by the end plate design.

Measurements were done with and without endplates. Extensive iterations of the endplate geometry and their angle to the incoming flow were carried out to ensure parallel vortex shedding. The endplate parameters are based on work of Stansby (1974) and Norberg (1994). The base pressure can be reduced by suitably designing the endplates

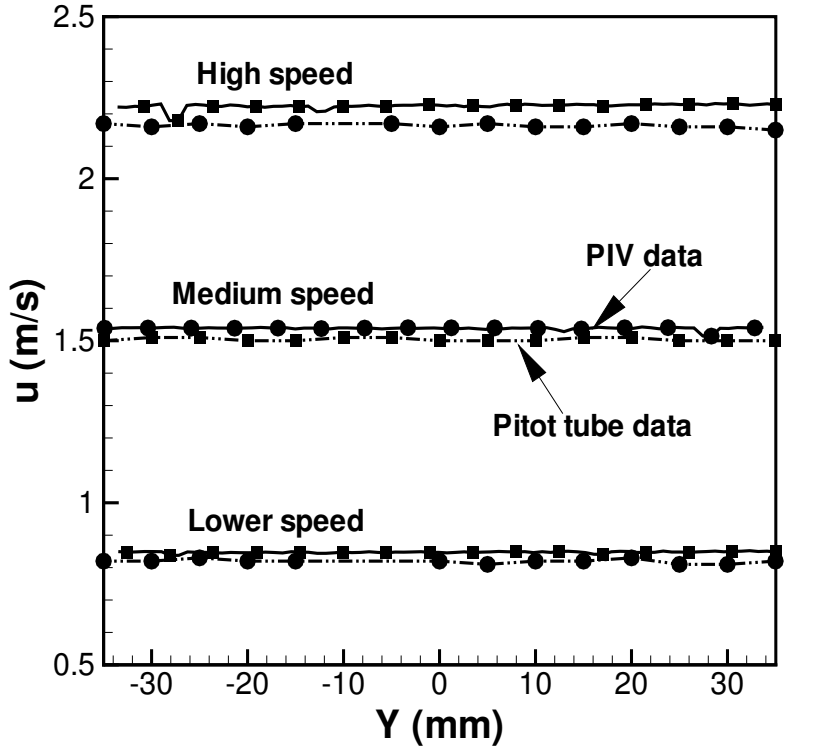

(a)

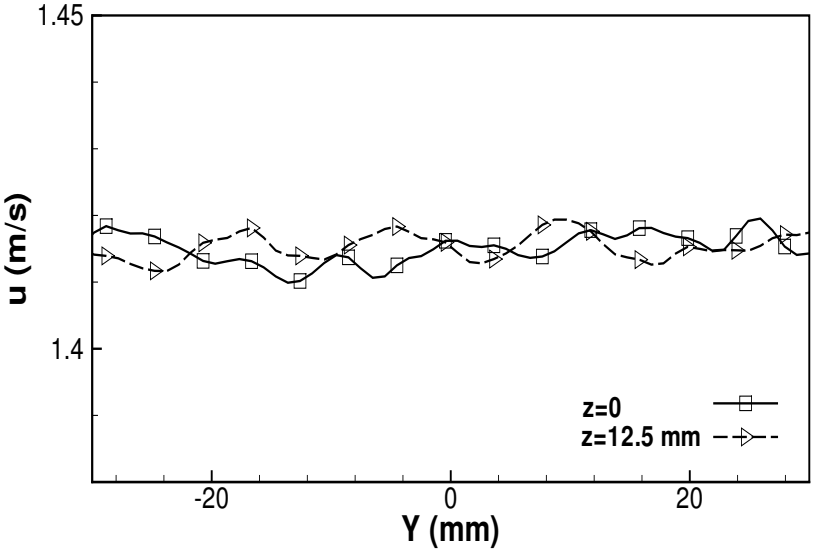

(b)

Figure 3.20: (a) Velocity profile of the incoming flow in the test cell from PIV and Pitot static tube measurements at three different tunnel speed settings (b) The incoming velocity profile at two different spanwise planes. The coordinate $z = 0$ falls on the vertical mid-plane of the test cell.

to keep the flow two dimensional (Stansby, 1974).

The distance of the cylinder axis from the outlet of the contraction is around ten times the cylinder edge to ensure adequate decay of free stream disturbances (Sohankar *et al.* (1998)). The velocity profiles behind a square cylinder with and without endplates are compared at the midplane and at an offset location ($z = 5$) for three downstream locations ($x = 2, 5$ and 10) (see Figures 3.21 and 3.22). Results from two Reynolds number (Re=220 and 370) have been shown. The difference in the velocity profiles at different spanwise location was found to be minimal for both configurations with and without end plates (except at x=10 and Re=370). At x=10 location, the effect of end plates is unclear. The low turbulence level in the test section along with thin boundary layers probably lead to a small wall effect. Hence no endplate has been used in the subsequent experiments. In the present study, the effect of cylinder oscillation on wake structure has been reported. The use of end plates would have increased the experimental complexity required for the end plate arrangements.

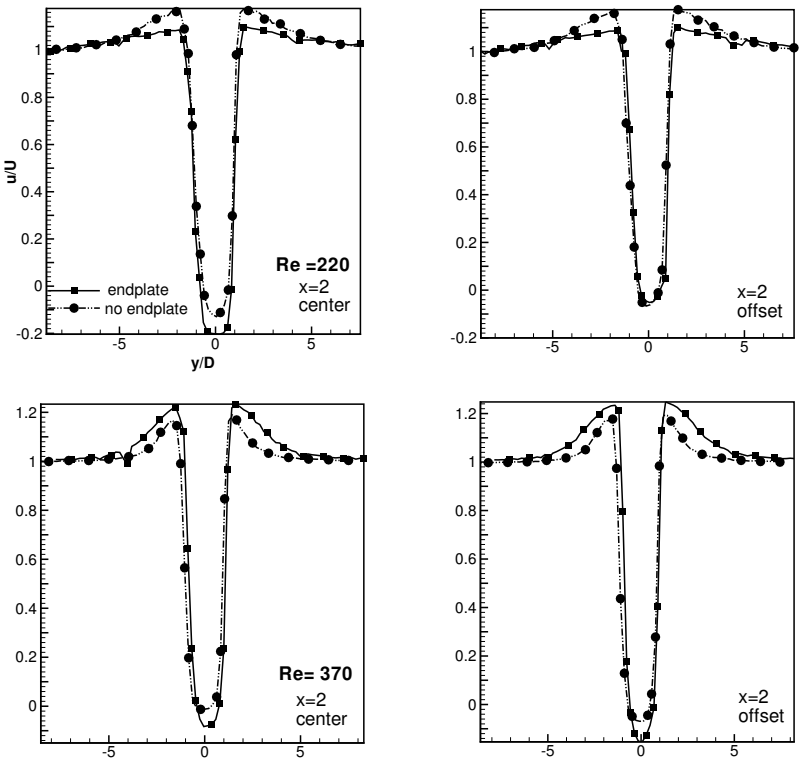

Figure 3.21: Effect of endplate on mean velocity profiles behind a square cylinder for two spanwise locations, z=0 (center) and z=5 (offset) at x=2. Reynolds number = 220 and 370.

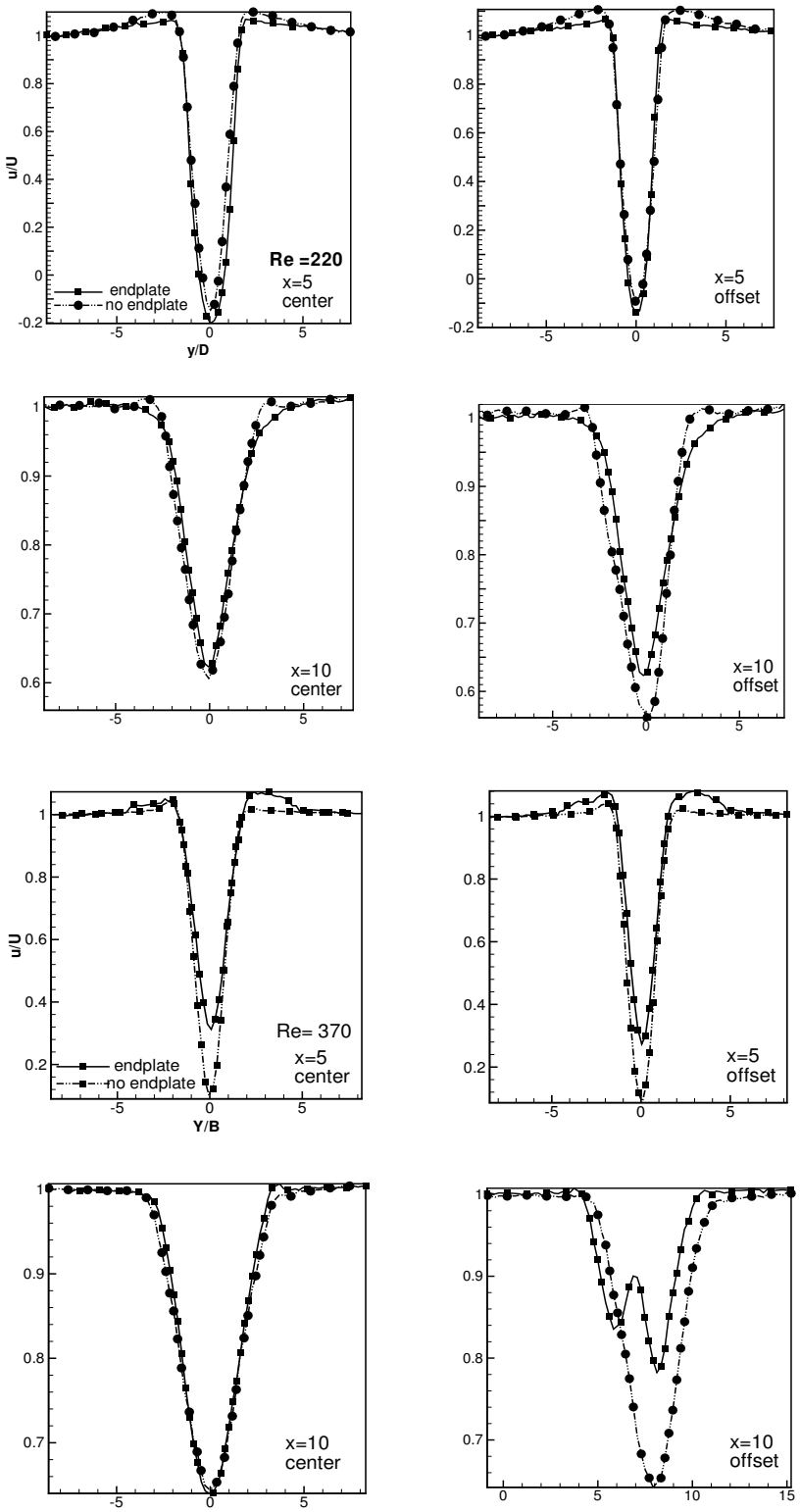

Figure 3.22: Effect of endplate on mean velocity profiles behind a square cylinder (Re=220 and 370). The result are shown at two downstream locations (x=5 and 10) and two spanwise locations (z=0 and z=5).

Chapter 4

Data Analysis

Introduction

In the present study, particle image velocimetry (PIV) and hotwire anemometry (HWA) have been used for velocity field measurements in the spatial and temporal domains respectively. These measurements have been used to calculate the mean and statistical quantities describing the flow, i.e. mean and rms velocities, power spectra, vorticity, drag coefficient, Strouhal number and turbulent kinetic energy. The details of calibration and data analysis procedures for these quantities are discussed below. The proper implementation of the measurement techniques is validated by comparing the recorded data against each other. The uncertainty in measurements is reported from a repeatability study. The measurements, experimental procedure and data analysis are validated from a comparison of Strouhal number and drag coefficient data with the published literature.

4.1 Principle of Operation of PIV

Particle image velocimetry is a non intrusive technique for measuring the spatial distribution of the velocity within a single plane inside the flow[1]. The measurement is indirect, via the displacement of moving particle groups within a certain time interval. For this purpose the flow is seeded homogeneously with appropriate tracer particles. The concentration of the particles must be well adjusted with regard to the finest flow structures. It is assumed that the particles are small enough to move with the local flow velocity. A plane within the flow is illuminated twice within a short time interval by a laser sheet.

[1]The discussion on PIV follows the earlier works of Westerweel (1997) and Adrian (1997)

The duration of the illumination light pulse must be short enough that the motion of the particle is *frozen* during the pulse exposure in order to avoid blurring of the image. The light from each pulse scattered by the tracer particles is recorded by a CCD sensor on separate frames. The time delay between the illumination pulses must be long enough to be able to determine the displacement between the images of the tracer particles with sufficient resolution. It should be short enough to avoid particles with an out-of-plane velocity component leaving the light sheet between subsequent illuminations. Analyzing one image pair, it is possible to identify the path a particle has traveled. Knowing the time delay between the two pulses, velocity can be calculated. The time interval between two pulses has to adjusted according to the mean flow velocity and the magnification of the camera lens. The particle displacement Δx must be small relative to the finest flow scale to be resolved.

After finding the displacement of each interrogation spot, the quantity is divided by Δt and the magnification factor M of the image system to calculate the first order approximation of the velocity field as follows:

$$\int_{t}^{t+\Delta t} u(t^{'})dt^{'} \quad \approx \quad \Delta x$$

Hence

$$\frac{\Delta x}{\Delta t} = \frac{\Delta X}{M\Delta t} \approx u$$

Correlation-based PIV has the advantage over particle tracking algorithms in which each particle path is followed. In contrast, in correlation based PIV, the average motion of small group of particles contained in the interrogation spot is calculated by spatial auto correlation or cross correlation. Auto correlation is performed when images for both laser pulses are recorded on the same sensor, while in cross correlation, each pulse is collected into separate frames. Cross correlation calculation becomes faster in the frequency domain since the FFT algorithm is now applicable. There is directional ambiguity in auto correlation technique. Hence, in case of reverse flow, this technique is not suitable. The drawback can be eliminated using the cross correlation technique. Cross correlation allows us to use a small interrogation area compared to auto correlation and leads to a reduction of the random error due to spatial velocity gradients. An important condition involves depth of field of recording optics and laser light sheet thickness. Generally, depth of the field should not be smaller than the thickness of the light sheet in order to avoid imaging out-of-focus particle.

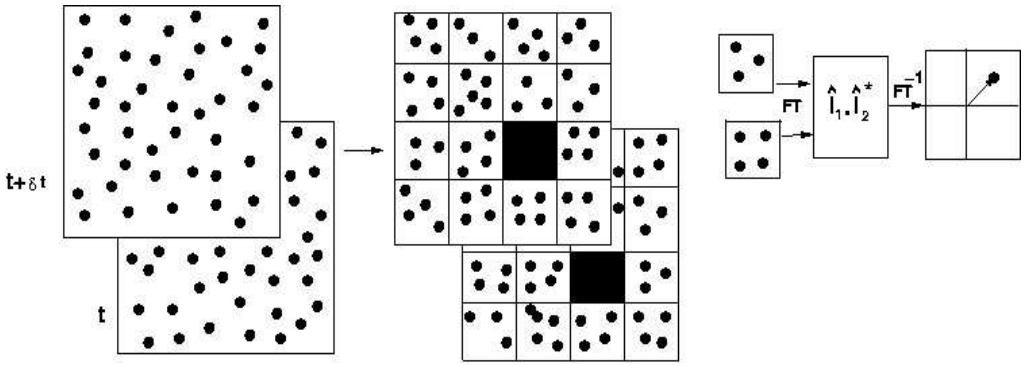

Figure 4.1: Cross correlation analysis of a PIV image pair.

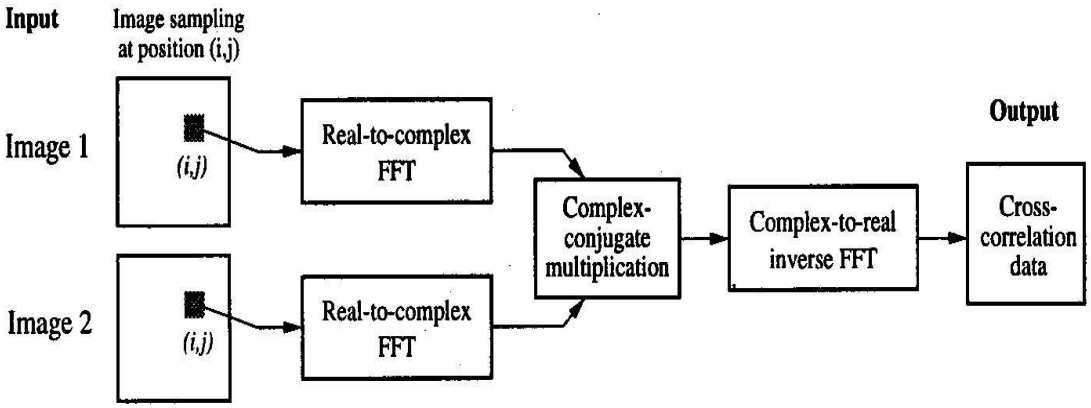

Figure 4.2: Computation of cross correlation using FFT.

4.1.1 Various aspects of PIV measurements

There are various aspects that should be taken into consideration while doing PIV measurements. Starting from image capturing to ultimately converting the image information into velocity vectors, each step requires proper validation. As already mentioned, the tracer particles should follow the flow faithfully without much velocity lag. Correspondingly, the tracer particles should be homogeneously distributed in the flow field. They should be small enough to follow the fluid movement and large enough to be visible. A set of six non-dimensional parameters that are most significant for optimization of PIV measurements were identified by Keane and Adrian [72]. These are the data validation criterion, the particle image density, the relative in-plane image displacement, the relative out-of-plane displacement, a velocity gradient parameter and the ratio of mean image diameter to the interrogation spot diameter. Two terms which are frequently used

in PIV measurements are source density

$$N_s = \frac{C\Delta z_o}{M_o^2}\frac{\pi}{4}d_\tau^2$$

and the image density

$$N_I = \frac{C\Delta z_o}{M_o^2}D_I^2$$

Here, C is the tracer particle concentration $[m^{-3}]$, Δz_o, light sheet thickness [m], M_o, image magnification, d_τ, particle image diameter [m] and D_i is the interrogation spot diameter [m]. The source density represents the type of image that is recorded. A source density larger than unity means that the image is a speckle pattern and when the source density is less than unity, the image consists of individual particle images. The image density represents the mean number of particle images in an interrogation region. It should larger than 10-15 for a good PIV measurement.

The optimal pulse separation between two images is influenced by a number of parameters. Two main types of error affect the choice of pulse separation (Δt) very much. These are random error and acceleration error. Random error arises from noise during recording of images and subsequent interrogation of the particle images. Acceleration error arises from approximation of Lagrangian motion of tracer particle to local Eulerian velocity based on small particle displacement. This two kinds of error contradict the selection of pulse separation. The random error contribution can be reduced by increasing Δt but acceleration error increases as Δt increases. At some intermediate value of Δt, the total error should be a minimum. The optimum separation can be derived by considering these two errors as

$$\Delta t_{opt} = \sqrt{\frac{2cd_\tau}{M|dv/dt|}}$$

In order to evaluate the correlation correctly with a single pass, the correlation function must be small with respect to the displacement correlation peak. This is accomplished when the following requirements are fulfilled:

1. There should be at least 7-10 particle image pairs in each interrogation spot.

2. The in-plane displacement should be limited to 1/4 of the size of the interrogation region.

3. The out-of-plane displacement should be limited to 1/4 of the thickness of the light sheet.

4. The displacement difference over the interrogation volume should be less than 3-5% of the size of the interrogation region.

4.1.2 Recording of the particle images

Besides particle dynamics, the registration, storage and read-out of the individual particle images are other key elements in PIV. This is because the accuracy of the technique is strongly depends upon the precision with which the image displacement can be related to particle locations and their respective particle displacements. The continuous intensity distribution of the particle image is transformed into a discrete signal of limited bandwidth. When the discretization of the image signal matches the minimum sampling rate, the frequency contents of the original signal, and thus the particle location as well, can be reconstructed without any losses . According to the well-known Nyquist criterion of signal processing, the bandwidth limited signal can be perfectly reconstructed from its discrete samples when the sampling rate of the signal is at least twice the signal bandwidth.

4.1.2.1 Evaluation of image pairs

Statistical evaluation technique is used to extract information of the displacement from the two single exposed grey level patterns acquired at t and $t^{'}$. Statistical evaluation technique is suitable since individual particle image pair detection is not possible for high resolution PIV measurement. It is less sensitive to noise and image discretization errors. In this technique, the whole image is sampled with an appropriate step size. For each sampling location, a two dimensional grey level sample $I(x, y)$ of certain shape and size is extracted from the source image. It is cross correlated with the corresponding sample $I^{'}(x, y)$ from the second image.

In general, the cross correlation function is given by

$$R(x, y) = \sum_{i=-k}^{k} \sum_{j=-l}^{l} I(i, j) I'(i + x, j + y)$$

Here I and I' are intensity values of the image pair. The cross correlation function produces a signal peak when the images align with each other, since the sum of the product of the pixel intensities will be larger than elsewhere.

In general calculation of the correlation function is done in the Fourier space. For FFT analysis the data should be periodic. There are other issues such as aliasing and bias errors that need to be taken into consideration. Each subregion is transformed into the Fourier space via a Fourier transformation. The sub-windows are the spatially shifted and their Fourier transforms determined until the correlation is found. The correlation values are weighted accordingly to reduce bias error.

The cross correlation of two functions is equivalent to a complex conjugate multiplication of their Fourier transforms. In actual applications, the formulas used are

$$R \leftrightarrow \hat{I}\hat{I}'$$

where $\hat{I}$ and $\hat{I}'$ are the Fourier transforms of the image intensities I and I' respectively.

Once the correlation is found, the Fourier transformations are converted back into the physical space. The displacement that yields a maximum in the correlation function over the interrogation area is regarded as the particle displacement. Actually it is not the particle displacement which is computed but the displacement of the interrogation area. The displacement vector is of first order, i.e. the average shift of the particles is geometrically linear within the interrogation window. The size of the interrogation should be sufficiently small such that the second order effect, i.e. displacement gradients can be neglected.

4.1.2.2 Peak detection and displacement estimation

One of the important steps in evaluation of PIV images is to measure the position of correlation peak accurately to sub-pixel accuracy. To increase the accuracy in determining the location of the displacement peak from ± 0.5 pixel to sub-pixel accuracy, an analytical function is fitted to the highest correlation peak by using the adjacent correlation values. Various methods of estimating the location of the correlation peak have been proposed. Some of these are peak centroid fit, Gaussian peak fit and the parabolic peak fit. Of the three, the Gaussian fit is most frequently to estimate the shape of the signal around its peak assuming under ideal imaging conditions. This function is

$$f(x) = C_o \exp[-\frac{(x_o - x)^2}{k}]$$

where x_o indicates the exact location of the maximum peak and C_o and k are the coefficients. Using this expression for the main and the adjacent correlation values and the fact that the first derivative of this expression at x_o must be zero, the position can

be estimated with sub-pixel accuracy. Generally, a 3-point Gaussian peak fit gives good results. When the particle image size is small, the displacement tends to bias towards integer values. The assumed peak shape does not match the actual shape of the peak and the three point Gaussian estimator cannot represent the true shape of the correlation function. This is called the *peak-locking* effect. In actual displacement data, the presence of the peak-locking effect can be detected from histogram plot.

4.1.2.3 Data validation

In particle image velocimetry the measurements contain a number of *spurious* vectors. These vectors deviate unphysically in magnitude and direction from the nearby vectors that are, in turn, physically meaningful. They originate from those interrogation spots that contains insufficient number of particle images, or whose signal to noise ratio is very low. In post processing process, the first step is to identify these bad vectors and subsequently discard them to form the valid data set. The detection of either a valid or spurious displacement depends on the number and spatial distribution of particle image pairs inside the interrogation spot. In practice, there should be at least four particle image pairs to obtain an unambiguous measurement of the displacement (Westerweel [176]). The number of particle images inside an interrogation spot is a stochastic variable with a Poisson probability distribution. Hence an average of 10 particle images per interrogation spot at an average in-plane displacement of $\frac{1}{4}D_I$ will give a probability of 95% of finding at least four particle image pairs. Here, D_I is the size of interrogation spot. The valid data yield can be improved by increasing the seeding density. But by increasing the seeding density we increase the influence of the seeding on the flow.

There are various way to detect spurious vector in a velocity field. Three mainly used tests are the global mean test, local mean test and local-median test. The global mean and the local mean are both linear estimators of valid vector. The local median test is a nonlinear estimator that is often used in outliers identification. The outliers in turn, are identified by the median of the sample data. Out of the above three, Westerweel [176] has shown that the local median test has the highest efficiency. In these techniques, the value at a grid point is compared with the neighboring grid points; if it exceeds a certain threshold, the value is discarded.

For the present analysis, multi-pass interrogation technique has been applied. In the first evaluation, the images were sub-divided into 64×64-pixel non-overlapping interrogation images. The corresponding sub-images in the translated image and the reference

image were analyzed by computation of the cross-correlation function. Since there was no overlap between adjacent interrogation images, each pair yielded 320 statistically independent displacement vectors. In the second evaluation, a 32×32 pixel interrogation window was used with an overlap of 50%. The corresponding resolution is 0.5 mm and 5120 vectors were recovered from one pair of images. All measured integer displacements that deviated more than one pixel from the expected displacement were considered as spurious vectors. They were subsequently discarded from the data set. Such a strict test for spurious data can only be done if one has exact *a priori* knowledge of the displacement field.

4.1.2.4 Dynamic velocity and spatial range

Dynamic spatial range is related to spatial resolution and dynamic velocity range is related to the fundamental velocity resolution and hence, the accuracy of a PIV. Dynamic velocity range (DVR) specifies the range of velocity over which measurements can be made. It is the ratio of the maximum velocity to the minimum resolvable velocity, or equivalently the RMS error in the velocity measurement, i.e.

$$\text{DVR} = \frac{U_{max}}{\sigma_u} = \frac{U_{max}}{\sigma_{\Delta x} M_o^{-1} \Delta t^{-1}}$$

where M_o is the image magnification and Δt is the maximum time interval used for the experiments. The RMS error of the displacement field on the pixel plane ($= \sigma_{\Delta x}$) generally lies between 1-10% and so

$$\sigma_{\Delta x} = 0.1(d_e^2 + d_r^2)^{\frac{1}{2}}$$

where d_r represent the resolution of the recording medium that is taken to be equivalent to the pixel size, and d_e is the diameter of the particle image prior to being recorded on the pixel plane. Assuming that the particle image is diffraction limited and its image intensity is Gaussian, the diameter of the diffracted image of the particle is expressed as:

$$d_e^2 = M_o^2 d_p^2 + [2.44(1 + M_o) f^{\#} \lambda]^2$$

where d_p is the seeding particle diameter, $f^{\#}$ is the F-number of the imaging lens and λ is the laser wavelength. For the present experiments, image magnification is M_o=0.04, the pulse interval Δt =70 μs, d_r represent the pixel size (=6.7 μm), $f^{\#}$=1.4, particle diameter d_p ≈2 μm yielding a dynamic velocity range of 30. The dynamic spatial range (DSR) is defined as the ratio of the maximum resolvable scale to the minimum resolvable

scale, i.e.

$$\text{DSR} = \frac{L_x/M_o}{U_{max}\Delta t}$$

where the CCD pixel array dimension L_x= 8.58 mm and DSR=1020.

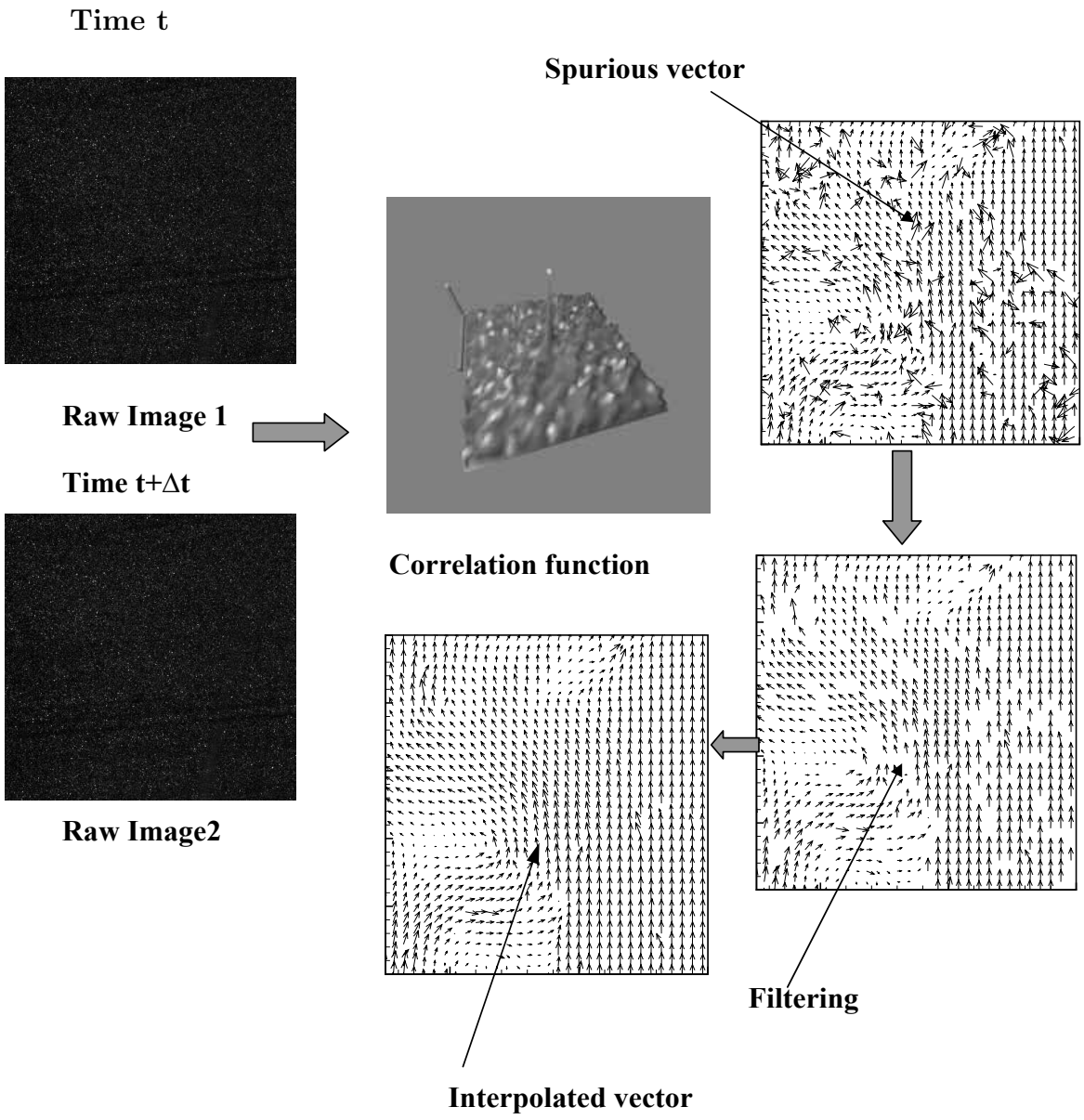

Figure 4.3: Processing of piv images

4.1.3 Calibration of PIV

To convert the velocity field from image coordinates to laboratory coordinates, length calibration is performed with a calibration sheet. Calibration sheet is a set of grid points on which the distance between two grid points is 10 mm. By putting the calibration sheet at the image plane, the image of the grid is captured and superimposed on the PIV image. Two types of calibration are followed depending upon the geometry of the flow field: linear and nonlinear calibration. In the case of plane geometry with a distortion free image, linear mapping is adequate. In this route, a minimum of four grid points is required. At the four grid points x and y coordinates of the image are specified and the corresponding pixel numbers identified from the image. By linear interpolation, all other x and y-coordinates are calculated for each pixel location. Once we get the real coordinates of each pixel of the image, the velocity vectors can be determined from the time interval between two images. Nonlinear calibration is recommended when image distortion is expected during recording by the camera.

4.2 Data Analysis from Velocity Vectors

In applications, the velocity information is often necessary but not sufficient and other quantities will be of interest as well. The velocity field obtained from PIV measurements can be used to estimate relevant quantities by means of differentiation and integration. The vorticity field is of special interest because, unlike the velocity field it is independent of the frame of reference. In particular, if it is resolved temporally, the vorticity field can be much more useful in the study of flow phenomena than the velocity field. This is particularly true in highly vortical flow such as turbulent shear layers, wake vortices and complex vortical flows. Integral quantities can also be obtained from the velocity data. The instantaneous velocity field obtained by PIV can be integrated, yielding either a single path integrated value or another field such as the stream function. Analogous to the vorticity field, the circulation obtained through path integration is also of special interest in the study of vortex dynamics, mainly because it is also independent of the reference frame. In the following section, data analysis for calculation of various derived quantities from PIV measurements are presented.

4.2.1 Velocity differentials

The differential terms are estimated from the velocity vectors obtained from PIV. Since PIV provides the velocity vector field sampled on a two dimensional evenly spaced grid specified as $(\Delta x, \Delta y)$, finite differencing can be employed to get the spatial derivatives. There are a number of finite difference schemes that can be used to obtain the derivatives. The truncation error associated with each operator is estimated by means of a Taylor series expansion. The actual uncertainty in differentiation is due to that in the uncertainty of the velocity estimate ϵ_U. It can be obtained using standard error propagation methods assuming individual data to be independent of the other. There are two schemes that reduce the error associated with differentiation: Richardson extrapolation and least squares approach. The former minimizes the truncation error while the least squares approach reduces the effect of random error, i.e. the measurement uncertainty, ϵ_U. These approaches are briefly discussed below[2].

Least squares estimate of the first derivative:

$$\left(\frac{df}{dx}\right)_i \approx \frac{2f_{i+2} + f_{i+1} - f_{i-1} - 2f_{i-2}}{10\Delta x}$$

Here, the accuracy is of the order of Δx^2 and the associated uncertainty is $\epsilon_U/\Delta x$.

The derivative using Richardson extrapolation is calculated as:

$$\left(\frac{df}{dx}\right)_i \approx \frac{f_{i-2} - 8f_{i-1} + 8f_{i+1} - f_{i+2}}{12\Delta x}$$

The accuracy of the above approximation is of order Δx^3 and the uncertainty associated with the expression is $0.95\epsilon_U/\Delta x$.

4.2.2 Vorticity and circulation

The vorticity in the x, y and z directions can be calculated from the partial derivatives of velocity using:

$$\omega_x = \partial w/\partial y - \partial v/\partial z$$

$$\omega_y = \partial u/\partial z - \partial w/\partial x$$

$$\omega_z = \partial v/\partial x - \partial u/\partial y$$

[2]The discussion on the analysis of PIV images follows Raffel *et al.*, 1998

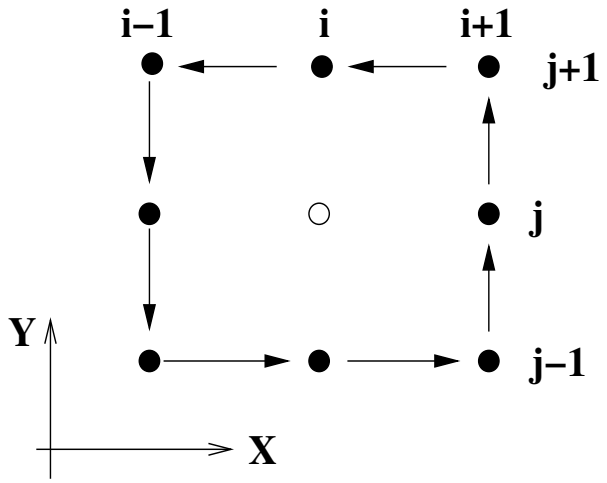

Figure 4.4: Contour for the calculation of circulation for the estimation of vorticity at a point (i, j).

The expression of mass continuity for an interrogation spot on the x-y plane can be written as

$$\nabla \cdot \mathbf{u} \approx \partial u/\partial x + \partial v/\partial y$$

Circulation can be computed from either velocity using

$$\Gamma = \oint \mathbf{u} \cdot dl$$

or vorticity as

$$\Gamma = \int \omega \cdot dA$$

In the present work, vorticity has been calculated by choosing a small rectangular contour around which the circulation is calculated from the velocity field using a numerical integration scheme, such as trapezoidal rule. The local circulation is then divided by the enclosed area to arrive at an average vorticity for the sub-domain. The following formula provides a vorticity estimate at a point (i, j) based on circulation using eight neighboring points (see Figure 4.4):

$$(\omega_z)_{i,j} \cong \frac{\Gamma_{i,j}}{4\Delta X \Delta Y}$$

with

$$\begin{aligned}\Gamma_{i,j} &= \frac{1}{2}\Delta x(U_{i-1,j-1} + 2U_{i,j-1} + U_{i+1,j-1}) \\ &+\frac{1}{2}\Delta y(V_{i+1,j-1} + 2V_{i+1,j} + V_{i+1,j+1}) \\ &-\frac{1}{2}\Delta x(U_{i+1,j+1} + 2U_{i,j+1} + U_{i-1,j+1}) \\ &-\frac{1}{2}\Delta x(V_{i-1,j+1} + 2V_{i-1,j} + V_{i-1,j-1})\end{aligned}$$

It has been observed from experiments that a circulation calculation *via* the velocity field yields better estimates of vorticity, and in particular, the peak vorticity that is otherwise under-predicted. At other locations, the vorticity field determined by the two approaches are practically identical. The accuracy of the vorticity measurement from PIV data depends on the spatial resolution of the velocity sampling and the accuracy of the velocity measurements. Therefore, the vorticity error can be associated with calculation scheme and the grid size used for velocity sampling. Another source of uncertainty is that propagated from the velocity measurements. PIV velocity measurements are the local averages of the actual velocity in the sense that it represents a low pass filtered version of the actual velocity field. Thus, vorticity from PIV data is only a local average of an already averaged velocity field and not a point measurement[3].

4.2.3 RMS velocity

Though the PIV image sequence is collected with a time spacing of 0.25 seconds[4], RMS velocity fluctuations in the near wake can still be obtained from them. The reasoning is that the near wake is dominated by large structures that in turn are associated with large time scales. A validation of PIV measurement of RMS velocity with hotwire data is reported later in this chapter.

The root mean square velocity (for a generic component u) at a location in the wake is calculated from the formula

$$u_{\text{RMS}} = \sqrt{\frac{1}{N-1}\sum(u')^2}$$

[3]In the case of the expression of mass continuity, the value should be zero for perfectly two-dimensional incompressible flow. Any instance of non-zero values can be attributed to either error in the PIV measurement or three dimensional effects.Vorticity and strain rate are expected to have finite non-zero values in a nonuniform flow field.

[4]an unacceptably large value

The summation extends over N samples, N being the number of acquired velocity fields in time. Further, u' is the unsteady part of the velocity field that is given as

$$u' = u(x,t) - U(x)$$

The time averaged velocity field U is determined by averaging the instantaneous velocity vectors using the formula

$$U(x) = \frac{1}{N}\sum_{i=1}^{N} u(x,t_i)$$

4.2.4 Drag coefficient

Two important parameters in the study of flow past bluff bodies are drag coefficient and Strouhal number. Drag coefficient is the dimensionless form of the force acting on the body in the direction of flow. Strouhal number is the non-dimensional vortex shedding frequency. It is also indicative of the time scale of the unsteady forces and determines the nature of flow induced vibrations of the body in both stream-wise and transverse directions.

In the present study, drag coefficient has been calculated by a momentum integration approach over a control volume. It is also called the *wake survey method*, and has been extensively discussed (Schlichting, 1979). Generally, the method is used to calculate drag coefficient from velocity profiles in the intermediate and far wakes, where there is no static pressure variation across the flow. In the present experiments of flow past a square cylinder in a closed channel, static pressure variation has been observed under some conditions even at twenty cylinder widths downstream. Therefore, it is necessary to consider the static pressure variation in the calculations. The drag coefficient is given by the formula (White, 1991)

$$C_d = \frac{\int_{-H}^{H} \rho u(y)(U_a - u(y)) + \Delta p)dy}{0.5\rho U_a^2 D}$$

Here $u(y)$ is the velocity profile in the wake where x and y are coordinates parallel and perpendicular to the main flow direction. Additionally, U_a is the approach velocity, D is the projected area of the cylinder normal to the flow direction (per unit length along the cylinder axis) and Δp is the static pressure drop between the free stream and the point under consideration. To maintain uniformity with the nomenclature in the published literature, the projected dimension has been taken to be equal to the edge of the cylinder for straight as well as inclined cylinders.

It is clear from the above expression that the drag coefficient cannot be determined exclusively from PIV images. Most experiments in which the pressure drop was measured using a static probe showed that the correction was to the extent of ±5%. Hence, results have also been presented without the pressure correction term. For such data, the drag coefficient can be interpreted simply as a momentum loss coefficient.

The symbol H in the formula for the drag coefficient is the width of the control volume over which the local velocity attains the free stream value. In external flow measurements, this location coincides with a boundary that has zero shear. Accordingly, the external force calculated from the momentum balance formula can be attributed entirely to drag on the cylinder. In channel flow, the asymptotic limit is not reached unambiguously; hence the value of H has been selected by first examining the velocity vectors. A second approach employed was to set H equal to the channel half-width and make corrections for the wall shear. Both of these approaches were found to give very similar drag coefficients. The extent of uncertainty in drag coefficient is reported in Section 4.5.

4.2.5 Streamlines

The flow pattern is visually brought out in terms of streamlines. For this purpose, the stream function is first calculated by integrating the velocity field as per the formula

$$\psi = \int_x u(x, y)\ dy$$

starting from an exterior point where v=0. Here, u and v indicate the time-averaged velocity components of the flow field. The streamlines are then plotted simply as contours of constant stream function in the flow domain.

4.2.6 Turbulent kinetic energy budget

The turbulent kinetic energy budget helps in examining how turbulence is spatially distributed after being produced in the flow field[5]. It also explores the development of the cascade process that directs the kinetic energy of velocity fluctuations from large scales towards the small scales, ultimately to be dissipated by molecular-level processes. Under unique circumstances, reverse cascading, namely energy transfer towards the large scale structures is also possible.

[5]The flow field in the wake of the cylinder is being characterized here as *turbulent* purely because of the appearance of time-dependent fluctuations.

The equation describing the transport of turbulent kinetic energy is (Wilcox, 1998)

$$\frac{\partial K_t}{\partial t} = -U_j \frac{\partial K_t}{\partial x_j} - \langle u_i^{'} u_j^{'} \rangle S_{ij} - \frac{\partial}{\partial x_j} \langle u_i^{'} u_i^{'} u_j^{'} \rangle - \nu \langle s_{ij} s_{ij} \rangle - \frac{\partial}{\partial x_j} \langle 2\nu u_i^{'} s_{ij} \rangle - \frac{\partial}{\partial x_j} \frac{1}{\rho} \langle u_j^{'} p^{'} \rangle \quad (4.1)$$

The symbols used are defined in Nomenclature; in any case they follow the meaning employed in the literature on turbulent flows. Lower case symbols (say, u) indicate velocity fluctuations, while the upper case symbol is for the time-averaged velocity (say, U). In the above equation, the turbulent kinetic energy (K_t) is a time-averaged quantity ($\langle \cdot \rangle$)

$$K_t = \frac{1}{2} \langle u^{'} u^{'} + v^{'} v^{'} + w^{'} w^{'} \rangle$$

The mean rate of strain(S_{ij}) and fluctuating rate of strain (s_{ij}) are

$$[S_{ij} = \frac{1}{2} \left(\frac{\partial U_i}{\partial x_j} + \frac{\partial U_j}{\partial x_i} \right), \quad s_{ij} = \frac{1}{2} \left(\frac{\partial u_i}{\partial x_j} + \frac{\partial u_j}{\partial x_i} \right)$$

The first term on the right hand side of the turbulent kinetic energy equation is advection. Under the assumption of a negligible w-velocity ($w = 0$) it reduces to:

$$\text{Advection} = U \frac{\partial K_t}{\partial x} + V \frac{\partial K_t}{\partial y}$$

The second term in Equation 4.1 is the production of turbulent kinetic energy. With the symmetry assumption at the mid-plane of the test cell ($\partial / \partial z$ =0) it becomes:

$$\text{Production} = \langle u^{'} u^{'} \rangle \frac{\partial U}{\partial x} + \langle v^{'} v^{'} \rangle \frac{\partial V}{\partial x} + \langle u^{'} v^{'} \rangle \frac{\partial U}{\partial y} + \langle u^{'} v^{'} \rangle \frac{\partial V}{\partial x}$$

The third term indicates diffusion; under the assumption ($\langle w^{'2} v^{'} \rangle = \langle v^{'3} \rangle$ and $\langle w^{'2} u^{'} \rangle = \langle v^{'2} u^{'} \rangle$) it can be expressed as:

$$\text{Diffusion} = \frac{\partial}{\partial y} \frac{1}{2} \langle u^{'2} v^{'} \rangle + \frac{\partial}{\partial y} \langle v^{'3} \rangle + \frac{\partial}{\partial x} \frac{1}{2} \langle u^{'3} \rangle + \frac{\partial}{\partial x} \langle u^{'} v^{'2} \rangle$$

The fourth term is viscous dissipation. If local isotropy in velocity fluctuations is assumed, we get

$$\text{Isotropic Dissipation} = 15\nu \langle \frac{\partial u^{'}}{\partial x} \rangle^2$$

Dissipation can also be calculated based on the assumption of locally axisymmetric turbulence and is equal to (Schenck and Jovanovic, 2002):

$$\text{Axisymmetric dissipation} = \nu \lfloor -\langle (\frac{\partial u^{'}}{\partial x})^2 \rangle + \langle 2(\frac{\partial u^{'}}{\partial y})^2 \rangle + \langle 2(\frac{\partial v^{'}}{\partial x})^2 \rangle + 8\langle (\frac{\partial v^{'}}{\partial y})^2 \rangle \rfloor$$

The 5^{th} and 6^{th} terms in the turbulent kinetic energy equation are termed as viscous diffusion and pressure diffusion respectively. The sum of these two terms has been obtained as the residual of the turbulent kinetic energy equation. It should be noted that the viscous diffusion can be expected to be insignificant at intermediate and high Reynolds number. Therefore the residual term is primarily due to the pressure transport.

The individual budget terms of the turbulent kinetic energy equation have been calculated from PIV measurements. It has been assumed that the total kinetic energy is 1.33 times that of that measured from two dimensions. Panigrahi *et al.*, (2005) have validated the above assumptions from an experiment on flow past a rib using 2-component and stereo-PIV.

The dissipation term of the kinetic energy budget equation has been calculated based on the assumption of both local isotropy and axisymmetry. The assumption of local isotropy requires the eight ratios of velocity fluctuations to be equal to unity. Schenck and Jovanovic (2002) reported the eight isotropic ratios to be in the range of 0.4 to 1.7 from hotwire measurements of the plane wake of a circular cylinder and axisymmetric wake of a sphere. The diffusion term in the turbulent kinetic energy equation is calculated using the assumptions: ($\langle w'^2 v' \rangle = \langle v'^3 \rangle$ and $\langle w'^2 u' \rangle = \langle v'^2 u' \rangle$). The above assumption has also been justified by Panigrahi *et al.* (2005) through experiments involving flow past a rib.

4.3 Hotwire Anemometry

High temporal resolution is possible with a hotwire anemometer, though the attendant disadvantages of intrusive effects and low spatial resolution are equally significant. The principle of operation of a hotwire anemometer is briefly described below.

The output of a hotwire anemometer depends on convective heat transfer from a very fine (micron-sized) heated wire to the flowing fluid. The thermal equilibrium of the wire placed in a fluid medium gives the following energy balance relationship:

$$H_{convec} + \dot{E} \;=\; i^2 R_w \tag{4.2}$$

Here $H_{convec} = hA(T_w - T_f)$ and $\dot{E}$ is the change in internal energy of the wire. Further, A is the surface area of hotwire per unit length in units of m, h is the convective heat transfer coefficient, W $^\circ$ C^{-1} m^{-2}, T_w is the temperature of the wire, °C, T_f is the

temperature of fluid, °C, i is the current flowing through wire, Amp, and R_w is the resistance of wire, Ω. One can write

$$\dot{E} = mC\frac{dT_w}{dt} \tag{4.3}$$

where m is the mass of wire per unit length, kg/m and C is the specific heat of the wire material, J $\text{kg}^{-1}\text{°C}^{-1}$. The differential equation governing time-dependent convective heat transfer is now expressed as

$$mC\frac{dT_w}{dt} + Ah\,(T_w - T_f) - i^2 R_w \;=\; 0 \tag{4.4}$$

The quantity of interest in the above formulation is the convective heat transfer coefficient h. The rate of change of internal energy is practically zero for the CTA (*constant temperature anemometer*) mode of the hotwire[6]. This approximation leads to the equation

$$H \;=\; 2\pi K_f l\,(T_w - T_f)\,\text{Nu} \tag{4.5}$$

where $\text{Nu} = \frac{hd}{K_f}$ is the Nusselt number, d is the sensor diameter, K_f is the thermal conductivity of fluid, and $2l$ is the length of the sensitive area of the hotwire probe.

The term which contains the effects of fluid velocity, temperature of the wire and the fluid temperature is Nusselt number. The general expression for Nusselt number in forced convective heat transfer for incompressible flow is given by

$$\text{Nu} \;=\; f\left(\text{Re}, \text{Pr}, a_1, \text{Gr}, \text{Ma}, \gamma, a_T, 2\frac{l}{d}, \frac{K_f}{K_w}\right) \tag{4.6}$$

where $\text{Re} = \frac{U_c d}{\nu}$ is the Reynolds number, U_c is the effective cooling velocity, ν is the kinematic viscosity of fluid, Pr is the fluid Prandtl number, C_p is the specific heat of the fluid at constant pressure, a_1 is the angle between the free stream direction and the normal to wire, Gr is Grashoff number, Ma is Mach number, $\gamma = \frac{C_p}{C_v}$, C_v is the specific heat of fluid at constant volume, and $a_T = \frac{(T_w - T_f)}{T_f}$ is the temperature loading or overheat ratio. Further, k_w and K_f are the thermal conductivities of the wire material and the fluid medium respectively. Fortunately, most applications permit a significant reduction in the number of parameters that must be included. The reasons are:

1. Forced convection parallel to the wire is small.

[6]The feedback electronics that accomplish this step are responsible for the excellent temporal and frequency response of the hotwire.

2. Prandtl number depends only on fluid properties.

3. Buoyancy effects can be neglected for $\mathrm{Gr}\times\mathrm{Pr} < \mathrm{Re}^2$. This expression shows that for air velocities greater than about 5.2 cm/s, buoyancy effects can be neglected.

4. For near atmospheric conditions of pressure and temperature and low velocities, Mach number is negligibly small.

5. Over a suitable range of temperatures (where HWA is commonly employed) C_p and C_v can be assumed to be constant.

The general equation governing the operation of hotwire can be now be simplified to

$$\mathrm{Nu} \;=\; f\left(\mathrm{Re}, a_T\right) \tag{4.7}$$

In isothermal flow measurements Equation 4.7 can be further simplified as

$$\mathrm{Nu} \;=\; f\left(\mathrm{Re}\right) \tag{4.8}$$

A relationship between Nusselt number and Reynolds number with a_T as a parameter that can be reliably used for converting the voltage output of the anemometer into velocity cannot be analytically derived. The analytical solution of flow past a circular cylinder for a wire-diameter based Reynolds number less than 40 shows that a power law relation is generally valid. The value of the exponent is 0.5 when the wire is taken to be infinitely long, flow is two dimensional and fluid properties are independent of temperature. However, the exponent depends on the geometric and physical properties of the wire, physical properties of fluid, and interference effects due to the prongs. A value of 0.45 is generally preferred; other empirical correlations derived using individual calibration of the wires is recommended in hotwire applications (Chew and Simpson, 1988).

4.3.1 Hotwire measurements

Velocity was measured using a two channel hot wire anemometer along with an $\times$-wire probe. The $\times$ was formed in the vertical plane, with the cylinder placed in the horizontal position. The probe was mounted on a traversing mechanism that facilitates all three orthogonal movements, to a positional accuracy in the most significant direction, namely the vertical at ± 0.1 mm. The commercially available *DANTEC* anemometer and probes were employed in the present work. The two wires of the probe were calibrated in

the wind tunnel itself. Small changes in room temperature ($\pm 1^o$C) were compensated through the use of a correction formula that assumes a temperature-independent heat transfer coefficient over this range. The probe was recalibrated for larger changes in room temperature. Both wires were operated at 150^oC, and their calibration curves were seen to be almost identical. The assumption of equal sensitivity coefficients of the two wires was occasionally employed during data reduction (Section 4.3.3). The calibration curves were smoothed using a fifth order polynomial. A pitot-static tube connected to a 19.99 mm of H_2O (*Furness Controls*) digital manometer was used for calibration. Both DC and RMS values of voltages were recorded using *true* voltmeters supplied by the manufacturer[7]. Integration time of typically 100 s was used to obtain all time-averaged quantities. For the range of velocities considered in the present work (namely, 1-5 m/s), incompressible flow conditions have been assumed to prevail for the sake of data analysis.

Before the start of measurements, the stability of the CTA bridge as well as the signal conditioner setup was checked. Static and dynamic balancing of the circuits had to be ensured. The static bridge balancing requires the use of a proper overheat setting while dynamic balancing is checked by square wave test.

Local time-averaged velocity and velocity fluctuations were measured using the $\times$-wire probe. The $\times$-wire probe was used for measuring two components of velocity along the x and y directions. The continuous output voltage from the anemometer was acquired independently for each wire *via* an analog to digital (A/D) converter. The filter settings were determined by examining the complete power spectrum of the velocity components. Voltage signals from the CTA were low-pass filtered at 1-3 kHz and high-pass filtered at 0.1 Hz using the 56N20 amplifier/filter unit. Further, the 56N20 signal conditioner was used for amplifying the input signals with gain factors of 10. The anemometer output voltage was collected by a PC (*HCL*) through a data acquisition card (*Keithley*) with LabVIEW software. In the low velocity regime, measurements with the pitot-static tube as well as the hotwire anemometer are prone to errors. These can arise from higher order physical phenomena as well as probe interference effects. The errors can be controlled by using a pitot-static tube of small diameter (3 mm in the present study); in addition the hotwire probe in the present work operated at a lower temperature (of around 150^oC). It was felt that the lower wire temperature minimized free convection and radiation errors, without excessive loss of sensitivity. The accuracy

[7]True meters refer to those that use a time series of voltages to perform the integration indicated by DC and RMS values.

of measurement was validated by examining the published Strouhal number-Reynolds number data for a circular cylinder at low Reynolds numbers. The power spectra of the velocity fluctuations were determined using the FFT algorithm. The sampling frequency used was 1000 Hz, the signal length for RMS measurements being 20 seconds.

4.3.2 Calibration Methodology

There are different approaches available for hotwire calibration. Two important steps involved in any approach are data generation and curve fitting. Calibration data are generated by measuring the output of the anemometer when the probe is subjected to a flow with a known velocity and low turbulence levels. In principle, specially designed apparatus are used to generate high quality flow with uniform velocity, temperature and very low turbulence level (say $< 0.1\%$). However, a test cell that has clean approach flow conditions can also be used to carry out an *in situ* calibration (Perry, 1982). In the present study, calibration has been performed in the test cell itself, very close to the inflow plane. A much wider range of expected velocity variation was covered during calibration. Air velocity was directly measured using a pitot-static tube with an external diameter of 3 mm, mounted along the centerline of the test section. Calibration data are generated by measuring the output of the anemometer when the probe is subjected to uniform known velocity.

Small changes in room temperature can occur over the day of the experiment. For changes up to $\pm$ 1^{o}C, the recorded data can be compensated through the use of a correction formula that assumes a constant heat transfer coefficient over this small temperature range (Bearman, 1971). The anemometer output voltage is corrected as

$$E_{corr} = \sqrt{\left(\frac{T_w - T_0}{T_w - T_a}\right)} E_a \tag{4.9}$$

Here E_a is the acquired voltage, T_w the sensor hot temperature, T_0 the ambient reference temperature at which calibration data is available, and T_a is the ambient temperature during the experiment. In the present work, the probe was re-calibrated for larger changes in room temperature.

4.3.3 Curve fitting

A number of functions for curve fitting the hotwire calibration data have been proposed in the literature. These functions are individually applied to the two wires of the $\times$ probe.

The most commonly used functions are (Bruun, 1995): polynomials, power laws (King's law [8]) and look-up tables. Low order polynomials, say second or third, do not show an oscillatory trend between calibration points. Jorgensen (2002) has shown that for a wide range of velocities (0.2-60 m-s^{-1}), power law fits are less accurate than polynomial fits and show a systematic error distribution. The fourth- and fifth-order polynomials are preferable and gives less error, almost of equal accuracy. The reported maximum errors for these polynomials are 0.74 and -0.53% respectively.

For velocity measurements in the lower range, say 0.5 to 4 m/s, a number of special calibration procedures is available. In present investigation, two different approaches were examined, but the difference between them was found to be negligible. These approaches are based on the linearizer function (recommended by *DANTEC*) and a high order polynomial. In linearizer approach the mathematical relationship used is

$$y = 10^{A+Bx+Ey} + Cx + D \tag{4.10}$$

Here A, B, C, D and E are curve fitting parameters. They are selected to give a fluid velocity equal to 10 m/sec for a wire output of 10 V. The quantity y is the output quantity equal to normalized velocity of fluid, defined as

$$y = 10 \times \frac{U}{U_{max}} \tag{4.11}$$

The velocity referred here is the effective fluid velocity (at normal incidence to the wire). Further, x is the normalized voltage defined as

$$x = 10 \times \left[\frac{E - E_0}{E_{max} - E_0}\right] \tag{4.12}$$

where E_0 is the output of wire measured at zero velocity of fluid and E_{max} measured at maximum velocity of fluid U_{max}. The function given above can closely match the calibration data, but its nonlinearity is a source of computational complexity.

The parameters A, B, C, D and E are obtained by means of an iterative least square error approach as follows. For any calibration point (x_i, y_i) Equation 4.10 will produce an error ϕ_i given by

$$\phi_i = y_i - \left[10^{A+Bx_i+Ey_i} + Cx_i + D\right]. \tag{4.13}$$

The least square approach requires the sum of errors at all calibration points to be

[8] Originally proposed by King (1914). King's evaluation suggested that the relationship $E = F(U)$ may be assumed to be of the form $E^2 = A + BU^n$, where $n = 0.5$.

minimum *i.e.*

$$\Phi = \sum_{i=1}^{n} \phi_i^2 = \sum_{i=1}^{n} \left\{ y_i - \left[10^{A+Bx_i+Ey_i} + Cx_i + D \right] \right\}^2 \tag{4.14}$$

$$\text{and} \qquad \frac{\partial \Phi}{\partial A} = \frac{\partial \Phi}{\partial B} = \frac{\partial \Phi}{\partial C} = \frac{\partial \Phi}{\partial D} = \frac{\partial \Phi}{\partial E} = 0. \tag{4.15}$$

Let I be any of the parameters A, B, C, D or E; then, the derivatives can be evaluated as

$$\frac{\partial \Phi}{\partial I} = 2 \sum_{i=1}^{n} \phi_i \frac{\partial \phi_i}{\partial I} = 0 \tag{4.16}$$

Each derivative has to be expanded algebraically and solved for the corresponding parameter. At this stage, other parameters would take on assumed values. When one cycle of calculations is completed, the procedure is repeated for the next iteration.

In the polynomial curve fitting approach the data points are fitted with fourth order polynomial functions. It has been found that the fourth- and fifth-order polynomials were of nearly equal accuracy (the maximum error being 0.27% for the velocity range 0.2-3.5 m/s of interest to the present work). With C_0 - C_4 as calibration parameters, the fourth order polynomial is of the form

$$U = C_0 + C_1 E + C_2 E^2 + C_3 E^3 + C_4 E^4 \tag{4.17}$$

Here, U is velocity and E is voltage. Typical calibration data and the 4^{th} order fit are shown in Figure 4.5. It is also shown that the calibration curves for both wires operating at practically equal overheat ratios are very close to each other.

4.3.4 Directional probe sensitivity

Directional calibration of multi-sensor probes (×- or tri -axial) provides their individual directional sensitivity coefficients. These are yaw factor, k_n and pitch-factor, P_h. They are required to decompose effective velocities derived from the calibration data into velocity components in laboratory coordinates. The effective cooling velocity acting on a hot wire can be expressed by means of the normal (U_n), tangential (U_t) and binormal components (U_{bn}) modified by the yaw and pitch factors, k_n and P_h (Jorgensen, 2002) as follows:

$$U_{eff}^2 = U_n^2 + k_n^2 U_t^2 + h^2 U_{bn}^2 \tag{4.18}$$

During directional calibration, the probe is turned through a number of inclination angles with respect to a known flow vector. In each position, U_n, U_t and U_{bn} are calculated from

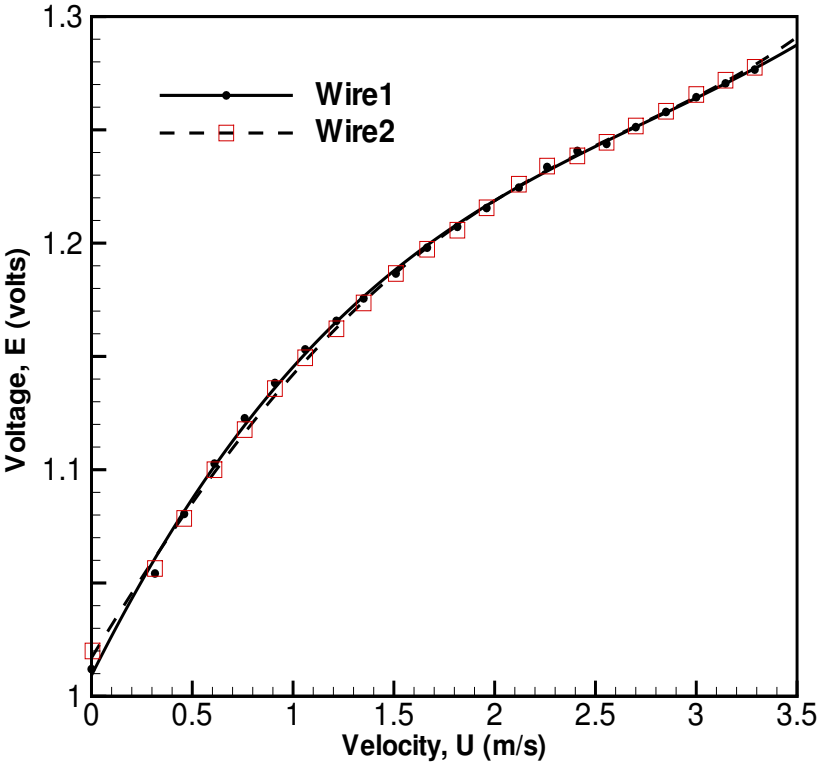

Figure 4.5: Calibration data for a ×-wire hotwire probe (symbols) compared with a fourth order curve fitting formula (lines).

the probe velocity transfer function. This provides a set of equations for determining k_n and P_h for each wire in each angular position. The ×-array probes uses the yaw coefficients, k_1 and k_2, in order to decompose the calibration velocities U_{cal1} and U_{cal2} into the U and V components. As the yaw coefficients, k_1 and k_2 depend only on the geometry, the directional calibration test is needed to be carried out only once in the life of the probe. In the present work, the freshly supplied probe (DANTEC probe 55P63) was used. The default values of k_1 and k_2 ($= 0.2$) was used during analysis.

4.3.5 Data Reduction

The time-mean component of the voltage signal has been obtained independently through a $4\frac{1}{2}$-digit voltmeter, *DANTEC* 56N22. In order to achieve the best utilization of the analog to digital converter resolution, the fluctuating component of the voltage signal has been amplified by a gain factor of 10, prior to acquisition in the PC. This approach[9]

[9]of measuring DC and fluctuations individually

has the advantage that integration time constants can be applied unrestrictedly on the time-mean and fluctuating component of the signal. A typical value of 100 s integration constant has been used to measure the time-mean voltage. The fluctuation part was acquired for 20 seconds duration with a gain setting of 10. The time-mean and the fluctuating voltage have been added during data processing to get the complete instantaneous signal. It has been subsequently used with the calibration equation to calculate the instantaneous velocity.

For the $\times$-probes that are oriented at $\alpha = 45^o$ to the incoming flow direction and yaw coefficients k_1^2 and k_2^2 for each wire, the velocities $U_1(t)$ and $U_2(t)$ in the *wire-coordinate system* are related to the calibration velocity of each wire as (Bruun, 1995):

$$k_1^2 U_1^2 + U_2^2 = \frac{1}{2}\left(1 + k_1^2\right) {U_{cal1}}^2 \tag{4.19}$$

$$U_1^2 + k_2^2 U_2^2 = \frac{1}{2}\left(1 + k_2^2\right) {U_{cal2}}^2 \tag{4.20}$$

The above equations can be rearranged as:

$$U_1 = \frac{1}{\sqrt{2}}\sqrt{\left(1 + k_2^2\right) {U_{cal2}}^2 - k_2^2 {U_{cal1}}^2} \tag{4.21}$$

$$U_2 = \frac{1}{\sqrt{2}}\sqrt{\left(1 + k_1^2\right) {U_{cal1}}^2 - k_1^2 {U_{cal2}}^2} \tag{4.22}$$

The velocity components, $U(t)$ and $V(t)$ in the laboratory coordinates x and y can be calculated from the velocity in the wire coordinate using an appropriate geometrical transformation, leading to:

$$U = \frac{1}{\sqrt{2}} U_1 + \frac{1}{\sqrt{2}} U_2 \tag{4.23}$$

$$V = \frac{1}{\sqrt{2}} U_1 - \frac{1}{\sqrt{2}} U_2 \tag{4.24}$$

The digitization of the hotwire signal results in N evenly distributed and statistically independent samples that, to a first approximation, can be taken as *statistically stationary*[10]. The mean value of the velocities U and V can be evaluated as the ensemble average of the velocity signals $u(t)$ and $v(t)$, i.e.

$$U = \frac{1}{N}\sum_{i=1}^{N} u \tag{4.25}$$

$$V = \frac{1}{N}\sum_{i=1}^{N} v \tag{4.26}$$

[10]If the signal is obtained for total time of T seconds at a sampling rate of SR per second, then $N = SR \times T$.

Subsequently, the velocity fluctuations, $u'(t)$ and $v'(t)$ are calculated by subtracting the mean component of velocity from the velocity signals $U(t)$ and $V(t)$. Hence

$$u'(t) = u(t) - U \tag{4.27}$$

$$v'(t) = v(t) - V \tag{4.28}$$

The root mean square components of velocities, $\overline{u'^2}$, $\overline{v'^2}$ and the Reynolds shear stress $\overline{u'v'}$ have been evaluated as:

$$u_{rms} = \left[\frac{1}{N}\sum_{i=1}^{N}(u')^2\right]^{1/2} \tag{4.29}$$

$$v_{rms} = \left[\frac{1}{N}\sum_{i=1}^{N}(v')^2\right]^{1/2} \tag{4.30}$$

$$\overline{u'v'} = \frac{1}{N}\sum_{i=1}^{N}u'v' \tag{4.31}$$

Here, the measurements from the two wires of the probe are taken to be *simultaneous.* This assumption neglects the small time lag introduced during data transfer in the A/D card.

4.4 Uncertainty

The seeding of flow with oil particles, calibration, laser light reflection, background illumination, image digitization, cross correlation calculation, velocity gradients and out-of-plane particle motion affect the accuracy of PIV measurements. Tracer particles need to follow the main air flow without any lag. For the particle size utilized and the range of frequencies in the wake, an expected slip velocity error of 0.3% to 0.5% relative to the instantaneous local velocity is expected. A second source of error in velocity measurement is due to the weight of the particle. In the present experiments, the effect of the weight of the seed particles was examined by conducting experiments at a fixed Reynolds number by varying the size of the cylinder and fixed inflow velocity. The streamline plot and the dimensionless size of the recirculation region were found to be identical in each case, and independent of the fluid velocity. The noise due to background light was minimized by using a band-pass filter (at the wavelength of the laser) before the camera sensor. The hotwire measurements are effected by the error due to calibration, free convection effect at small velocity, curve fitting error, electrical noise, digitization error and turbulence intensity in the incoming fluid stream. The pitot static tube, hotwire

anemometry and PIV measurements of mean velocity compared exceedingly well with each other indicating less than 2% error in velocity measurements. The drag coefficient calculation has been carried out at various stream-wise location and found to be within 5% of each other. From repeated measurements at the zero degree cylinder orientation (Figure 4.6, with Reynolds number kept constant to within ± 1%), the uncertainty in drag coefficient has been determined to be within ± 5%. The Strouhal number has been calculated at different x and y locations from both u and v-velocity measurements indicating the uncertainty on Strouhal number to be ± 2%. The influence of particle density on the measured flow field is shown in Figure 4.7; the influence is seen to be small.

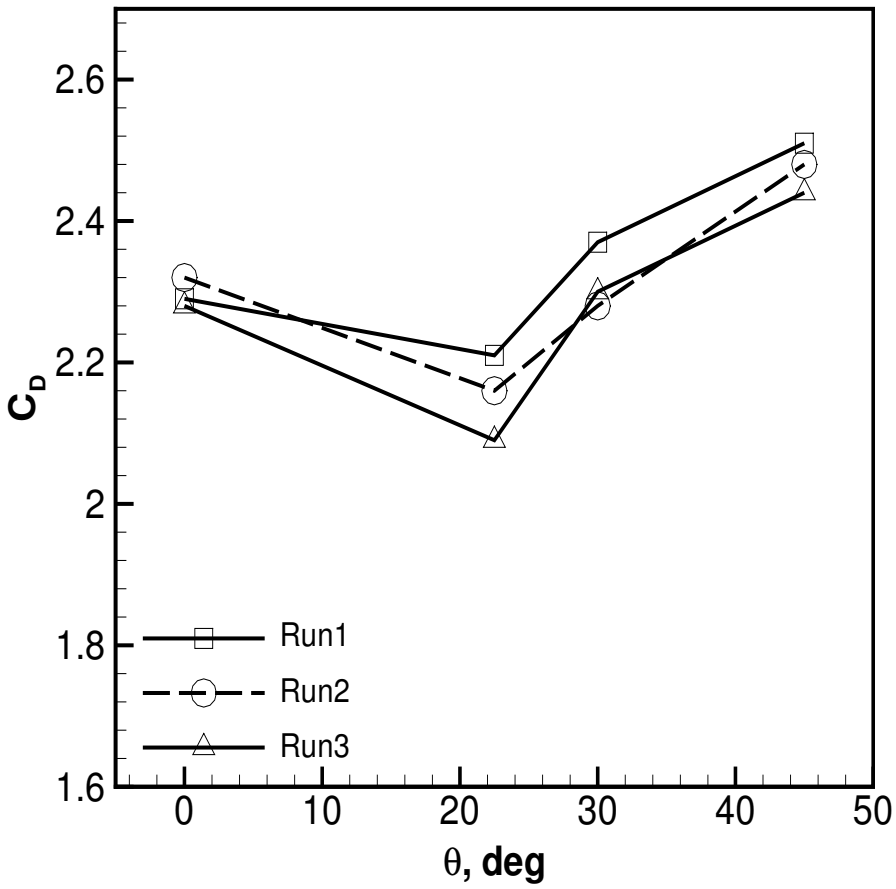

Figure 4.6: Variation of drag coefficient with cylinder orientation. Experiments were conducted on three different days under nominally similar conditions.

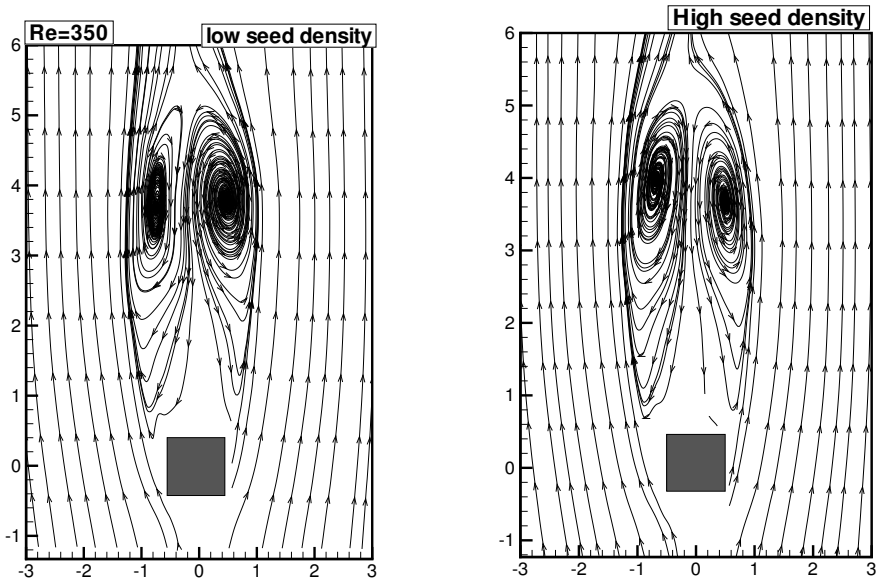

Figure 4.7: Effect of seeding density on the velocity field.

4.5 Validation Experiments

The validation of the experimental technique, data analysis procedure and computer implementation has been carried out in two ways: (i) Comparison between different measurement techniques, (ii) Comparison of the standard calculated quantities with that in the literature. The validation results of mean velocity, vorticity patterns, Strouhal number and drag coefficient are discussed in the following sections.

4.5.1 Comparison of hotwire and PIV data

Benchmark experiments were conducted at selected planes in the wake of the square cylinder under identical conditions. Both hotwire and PIV measurements were recorded. A cross-check in terms of the two components of time-averaged velocity is presented in Figures 4.8, 4.9, 4.10, 4.11, 4.12 and 4.13 at two different Reynolds number (Re=410 and 610). At x=5 the u-velocity profiles recorded by the two techniques show significant difference in the velocity deficit, Figure 4.8. Since the recirculation zone extends upto x=6, the time-averaged velocity is negative at all earlier x-locations. The hotwire probe cannot resolve the negative stream-wise velocity component, while PIV does not suffer from this drawback. Hence, adjacent to the cylinder, the PIV data can be assumed to be more accurate. As one moves downstream, the match between the two measure-

ments is better. At x=15 units, the stream-wise velocity profiles from hotwire and PIV measurements merge with each other (Figure 4.10).

Figure 4.11, 4.12 and 4.13 compare the transverse v-velocity for cylinder at different orientations and Re=410 and 610. The overall trends in the v-velocity are similar. At x=5 location, the maximum deviation of v-velocity between hotwire and PIV measurements is within the uncertainty of the velocity measurements (see Figure 4.11). This is in contrast to the high deviation in the u-velocity measurements in Figure 4.8. The hotwire measurement error in the recirculation zone is higher for the u-velocity than the v-velocity. The v-velocity trend at x=10 and 15 are similar between hotwire and PIV measurements. The higher percentage deviation of the v-velocity at these locations compared to the earlier x-location can be be attributed to the lower absolute magnitude of the v-velocity. Figure 4.14 shows the comparison of u_{rms} velocity at two x locations. At x=5 the PIV data shows a slightly higher peak RMS value compared to hotwire measurements. At x=10, both PIV and hotwire results coincide.

4.5.2 Drag coefficient

Table 4.1 presents a comparison of time-averaged drag coefficient of a square cylinder for zero angle of incidence; experiments as well as numerical simulation are compared. For three dimensional numerical simulation, the drag coefficient is a value averaged over the entire span of the cylinder. The experimental value is that of the cylinder mid-plane, obtained by a wake survey method. The drag coefficient from all studies are in the range of 1.95 to 2.32 and are comparable to each other.

Figure 4.15 shows the comparison of drag coefficient (C_D) with cylinder orientation from present experiments and two dimensional numerical simulation of Sohankar *et al.* (1998). The drag coefficient is based on the cylinder dimension rather than the projected area. The match is not good when we compare the mid-plane value with that of Sohankar (1998), possibly because of the dimensionality of the numerical simulation. The match improves when the 3-plane averaged value is compared with the cylinder average of three dimensional simulation. The minimum in the drag coefficient at 22.5^o is to be seen in both the mid-plane value as well as the average data. Sohankar *et al.* (1999) conducted a 3D numerical simulation of flow past a square cylinder at a low aspect ratio and found substantial variation in drag coefficient along the span-wise direction.

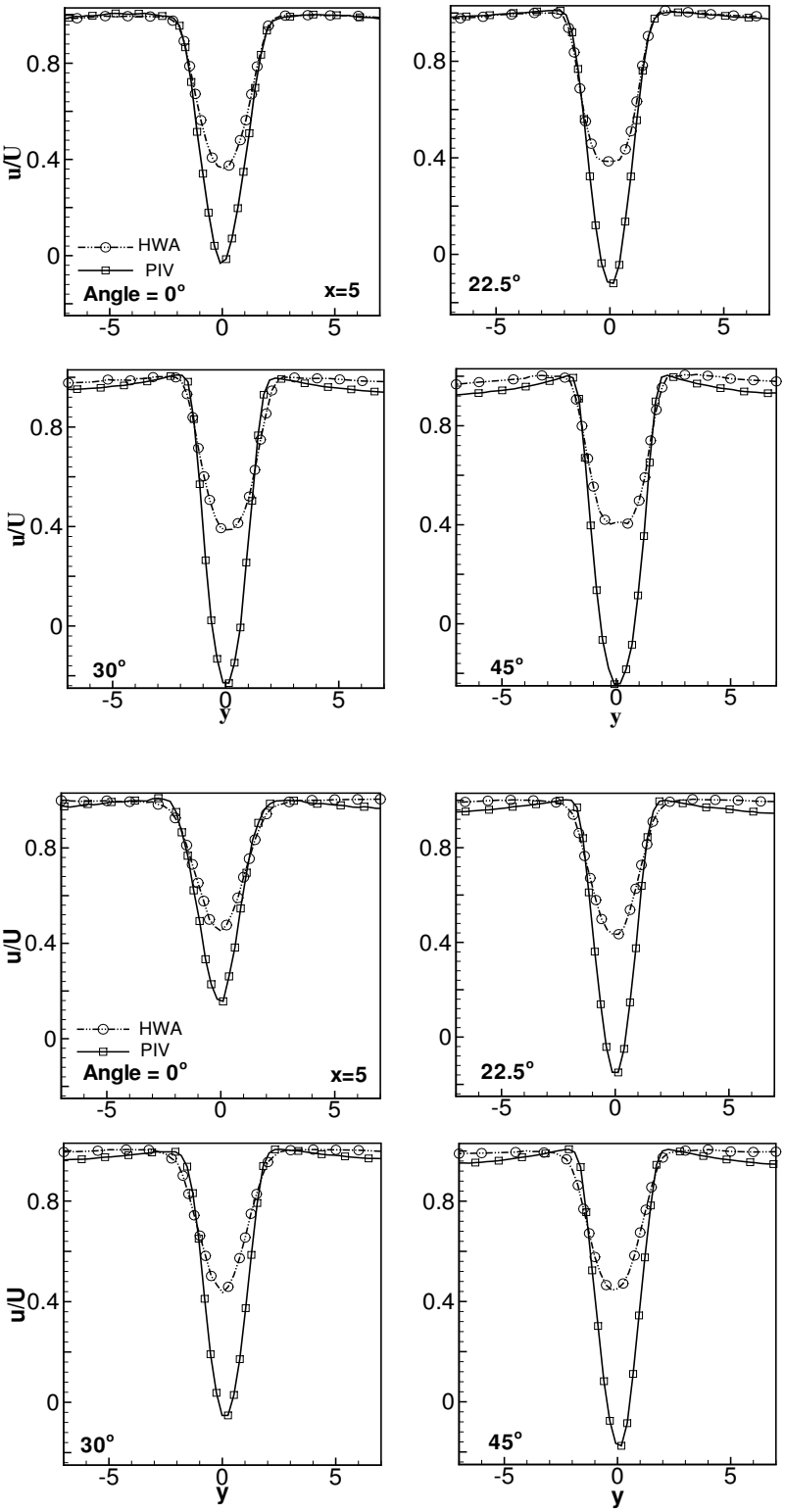

Figure 4.8: Comparison of time-averaged u-velocity profiles in the wake of a square cylinder. PIV and HWA measurements at four cylinder orientations (0, 22.5, 30 and 45^o) are presented at $x = 5$ location. Reynolds number=410(top) and 610(bottom).

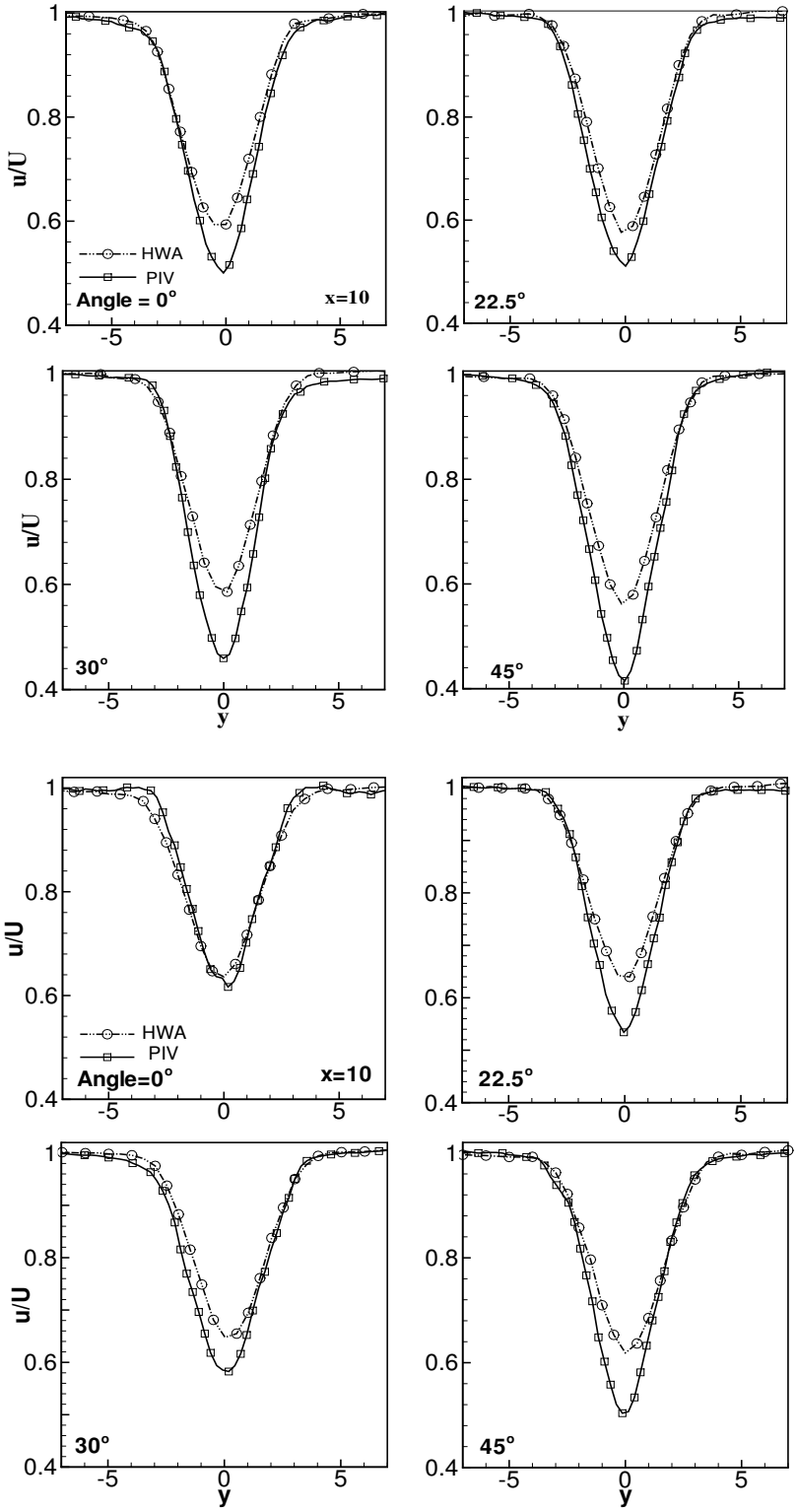

Figure 4.9: Comparison of time-averaged u-velocity profiles in the wake of a square cylinder. PIV and HWA measurements at four cylinder orientations (0, 22.5, 30 and 45^o) are presented at $x = 10$ location. Reynolds number=410(top) and 610(bottom).

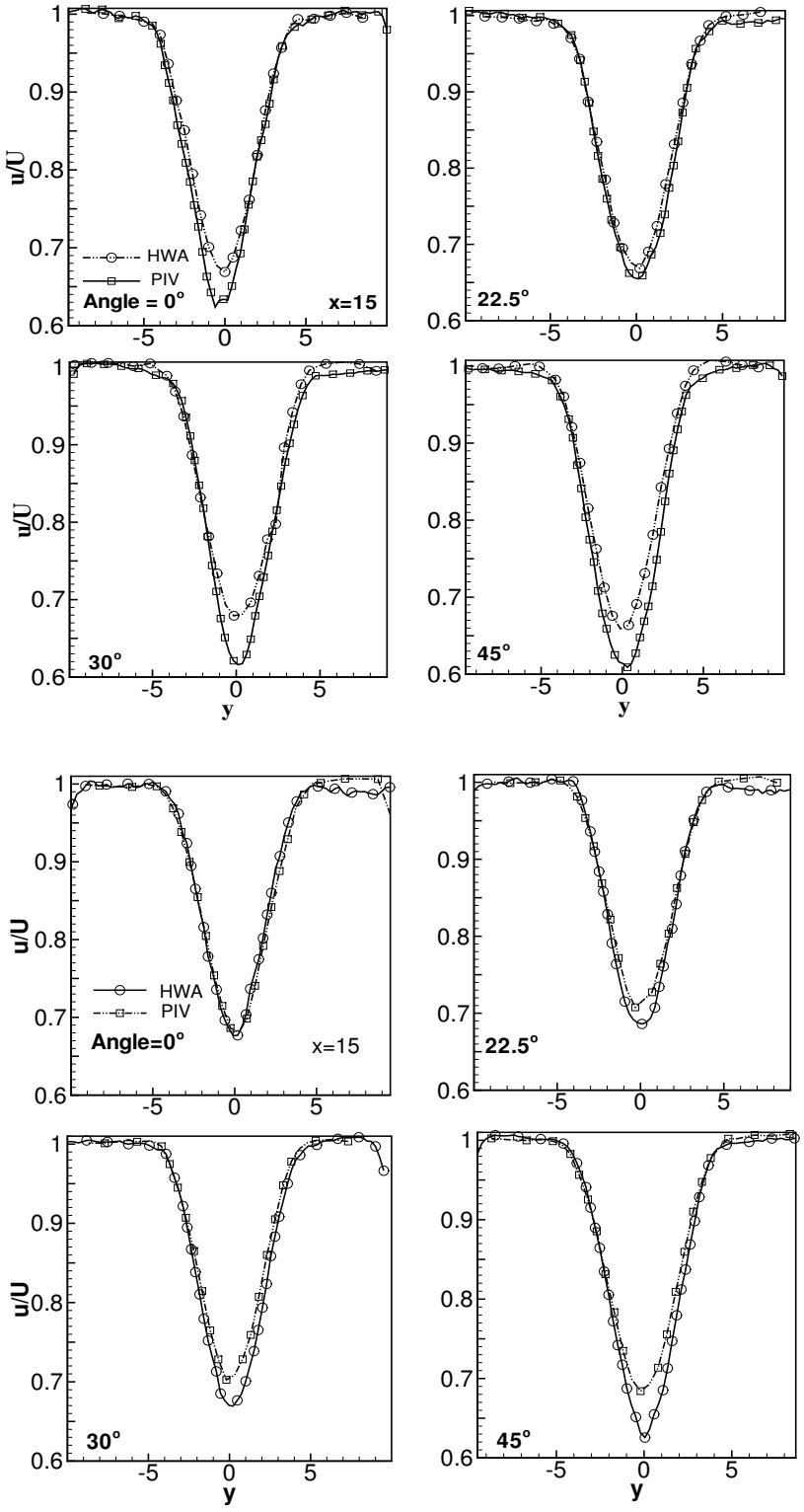

Figure 4.10: Comparison of time-averaged u-velocity profiles in the wake of a square cylinder. PIV and HWA measurements at four cylinder orientations (0, 22.5, 30 and 45^o) are presented at $x = 15$ location. Reynolds number=410(top) and 610(bottom).

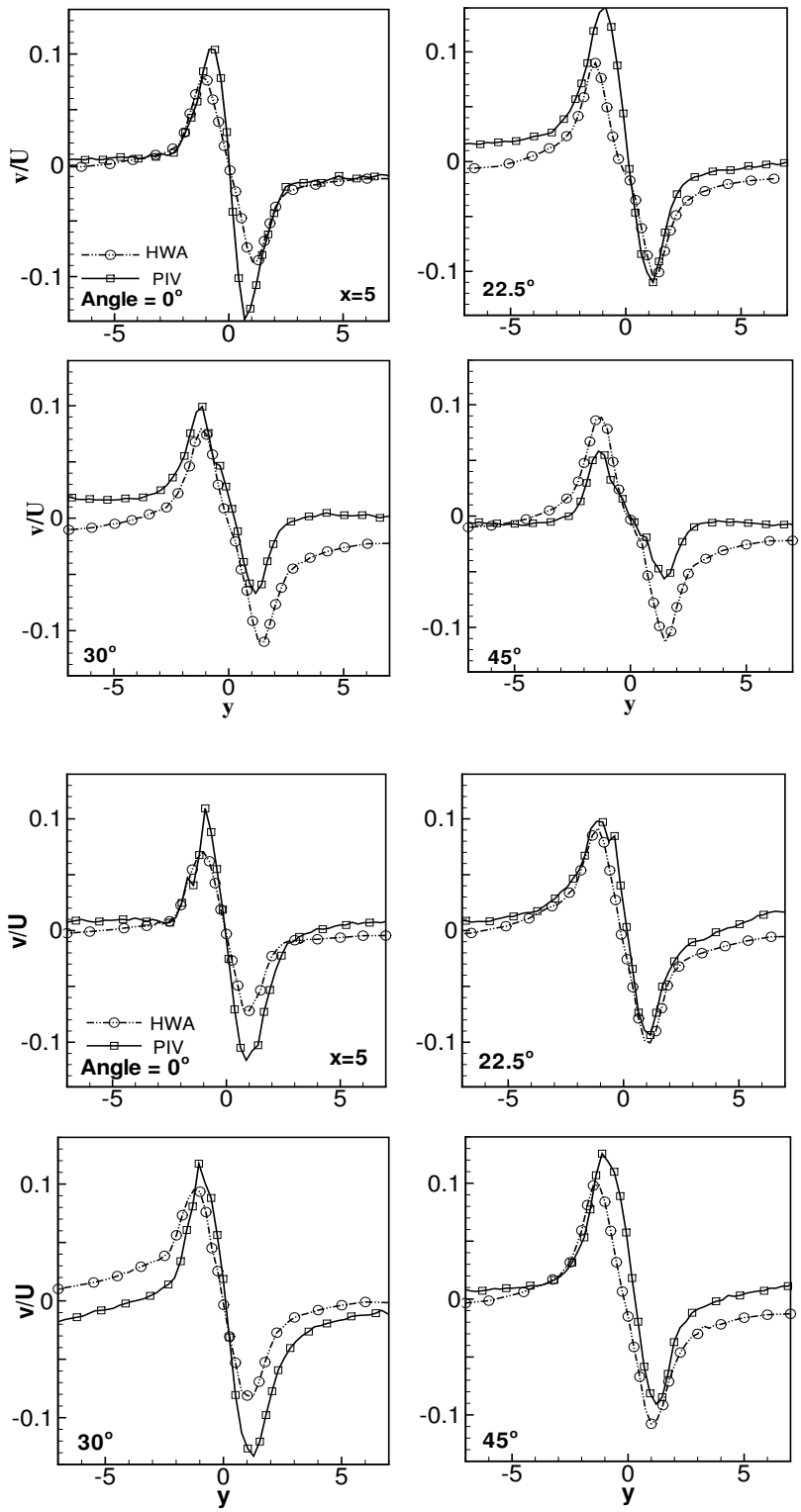

Figure 4.11: Comparison of time-averaged v-velocity profiles in the wake of a square cylinder. PIV and HWA measurements at four cylinder orientations (0, 22.5, 30 and 45^o) are presented at x=5 location. Reynolds number=410(top) and 610(bottom).

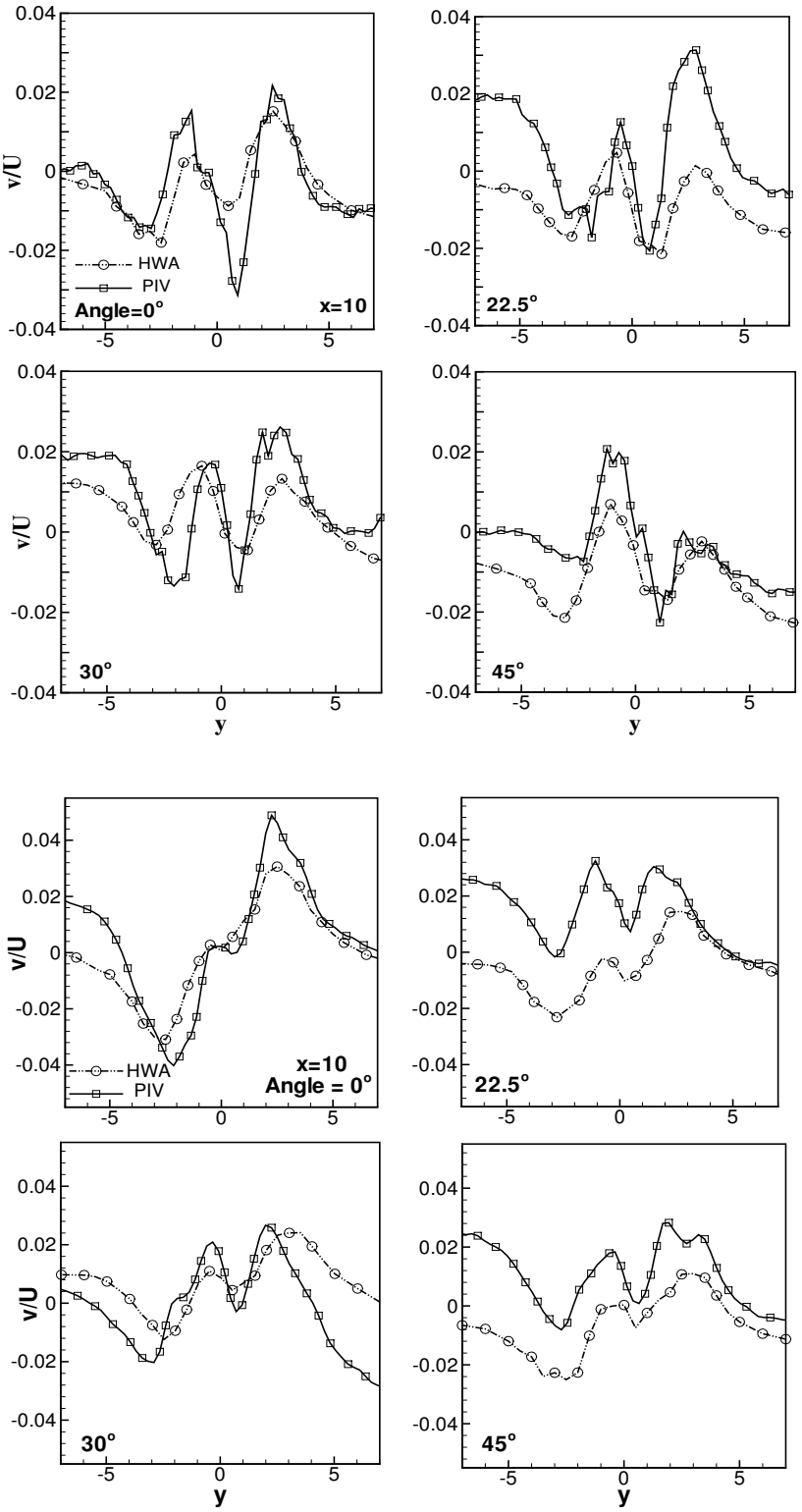

Figure 4.12: Comparison of time-averaged v-velocity profiles in the wake of a square cylinder. PIV and HWA measurements at four cylinder orientations (0, 22.5, 30 and 45^o) are presented at x= 10 location. Reynolds number=410(top) and 610(bottom).

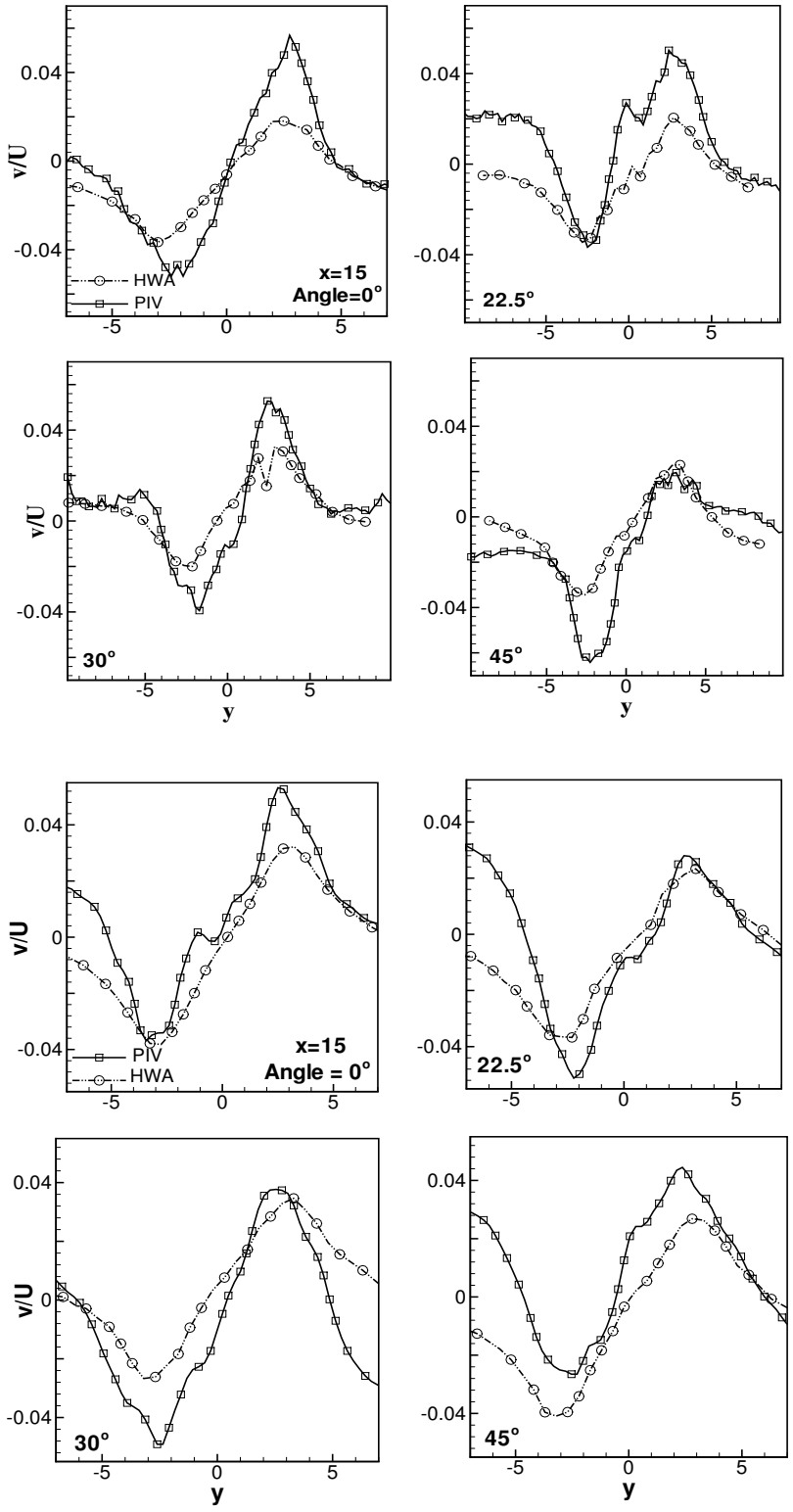

Figure 4.13: Comparison of time-averaged v-velocity profiles in the wake of a square cylinder. PIV and HWA measurements at four cylinder orientations (0, 22.5, 30 and 45^o) are presented at $x = 15$ location. Reynolds number=410(top) and 610 (bottom).

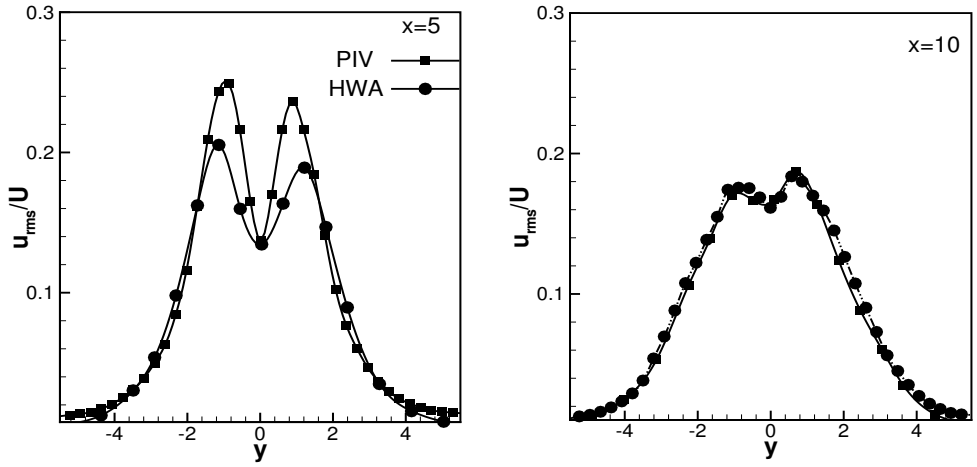

Figure 4.14: Comparison of u_{rms}-velocity profiles using PIV and HWA in the wake of a square cylinder at 0^o cylinder orientation at two x locations (x=5 and 10).

Table 4.1: Comparison of drag coefficient with the published literature for flow past a square cylinder.

Authors	Nature of study	Aspect ratio	Blockage	Re	$\overline{C}_D$
Davis *et al.* (1984)	Numerical (2D)	-	0.170	470	1.95
Sohankar *et al.* (1999)	Numerical (3D)	6	0.055	400	1.67
Saha *et al.* (2003)	Numerical (3D)	6-10	0.100	400	2.21
Present	Experimental	16	0.030	410	2.32
		28	0.060	420	2.03

4.5.3 Strouhal number

Table 4.2 compares the Strouhal number from the present work with that of other investigations at similar Reynolds numbers and zero degree orientation. A maximum deviation of ±7% between the present work and that of other investigations is indicated in Table 4.2. The difference between the present study and literature can be attributed to the difference in aspect ratio, blockage and inlet turbulence level. Figure 4.16 shows the comparison of the present experiments with the published literature in terms of Strouhal number for a circular cylinder (top) and square cylinder (bottom). Various Reynolds numbers have been considered. Each individual data set shows only a weak dependence of Strouhal number on Reynolds number. A certain level of scatter is visible. Data

recorded in the present experiments at aspect ratios 16, 28 and 60 are shown by shaded and unshaded diamonds and unshaded squares. Broadly, these three lines bound the Strouhal number values reported in the literature. Thus, one can conclude that aspect ratio can explain the minor discrepancy in Strouhal number data of a square cylinder. The experimental data of the present study in the Figure 4.16 show that Strouhal number increases with an increase in aspect ratio. The trend recorded for a circular cylinder by Norberg (1994) is supported by the present study.

Table 4.2: Comparison of Strouhal number with the published literature for flow past a square cylinder.

Authors	Nature of study	Aspect ratio	Blockage	Re	St	Re	St
Okajima (1982)	Experimental	120	0.016	300	0.143	500	0.130
Davis *et al.* (1984)	Numerical (2D)	300	0.080	250	0.164	600	0.150
Sohankar *et al.* (1999)	Numerical (3D)	10	0.056	300	0.153	520	0.130
Saha *et al.* (2003)	Numerical (3D)	6-10	0.100	295	0.135	575	0.140
Present	Experimental	16	0.030	310	0.122	550	0.129
		28	0.060	310	0.153	516	0.140
		60	0.030	295	0.155	500	0.145

4.5.4 Secondary vorticity pattern

Figure 4.17 shows the instantaneous stream-wise vorticity contours (ω_x) above a circular cylinder obtained in the present work using PIV. The axis of the vorticity component is along the flow direction. The PIV results of Brede *et al.*[9] are shown for comparison. The Reynolds number of the present work is 330, while that of the reference is 290. At these Reynolds numbers, secondary (streamwise) vortices are generated along with the spanwise (Kárman) vortices. The secondary vortices are arranged along a line parallel to the cylinder axis. The sense of rotation alternates along the spanwise direction. The secondary vortices correspond to mode B of Williamson (1997). The spanwise wavelength of the secondary vortices is around one cylinder diameter, the spacing between the vorticity peaks being, in general, a constant. These trends are realized in both sets of experiments. Overall, the favorable comparison of vorticity patterns with the published

literature confirms the correct implementation of the PIV technique in the present study.

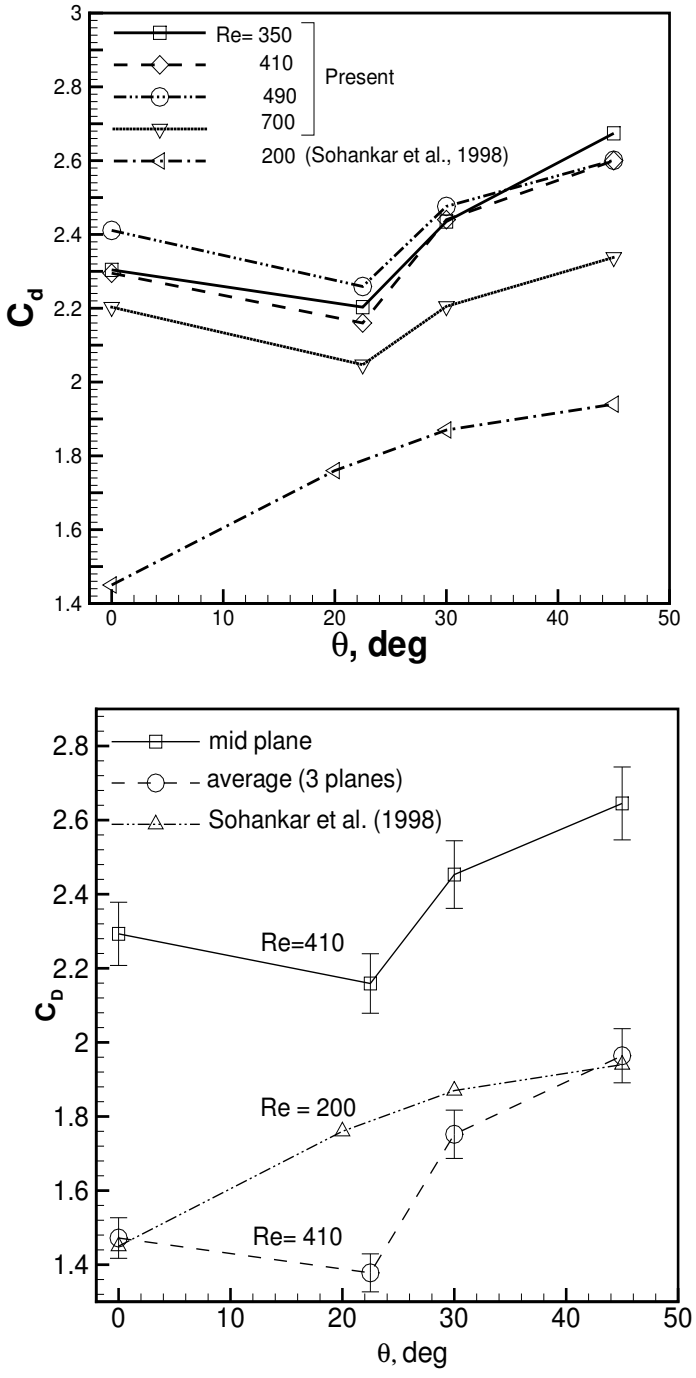

Figure 4.15: Variation of drag coefficient with incidence angle. The data of the present study in the top figure is for mid-plane of the cylinder. The numerical simulation of Sohankar *et al.* (1998) reports an average over the cylinder length. The drag coefficient data averaged over 3-planes has been shown in the bottom figure.

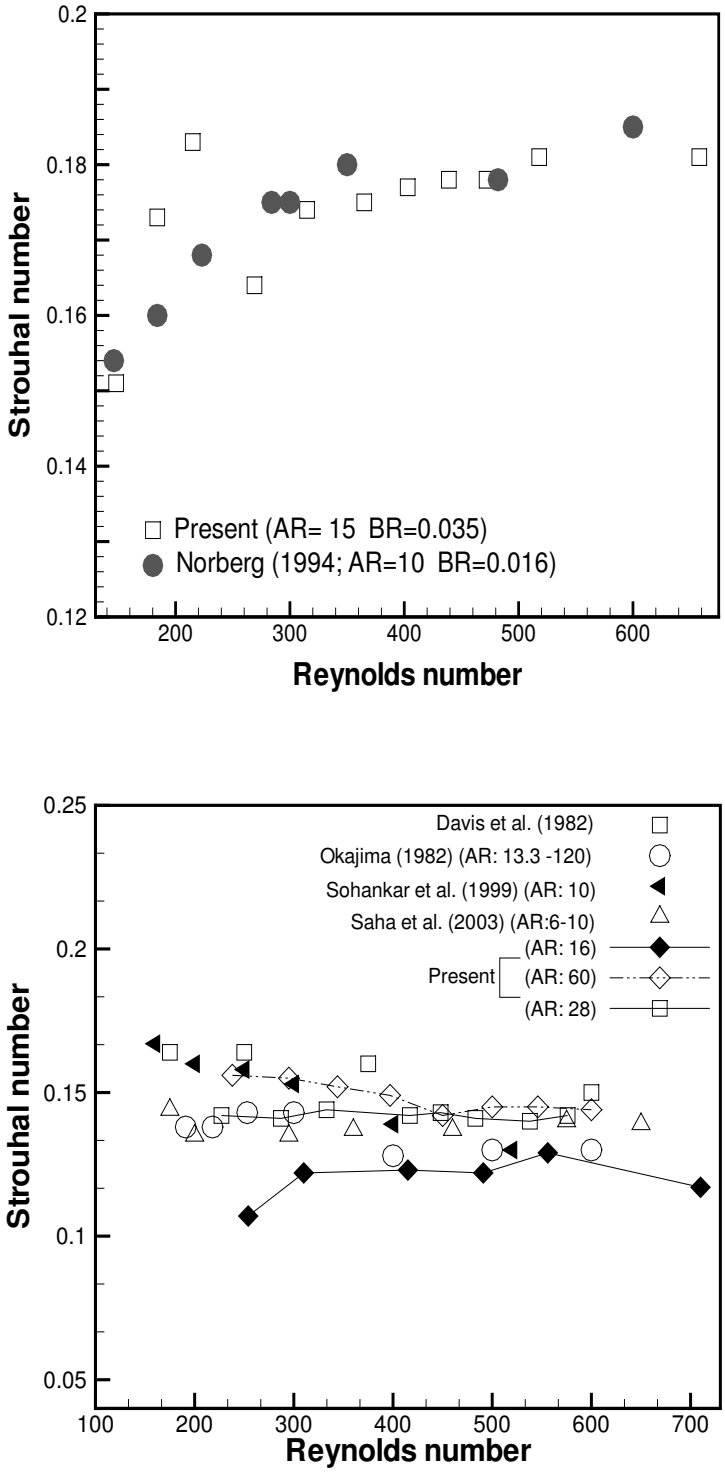

Figure 4.16: Comparison of Strouhal number as a function of Reynolds number for flow past circular (top) and square (bottom) cylinder at zero angle of incidence.

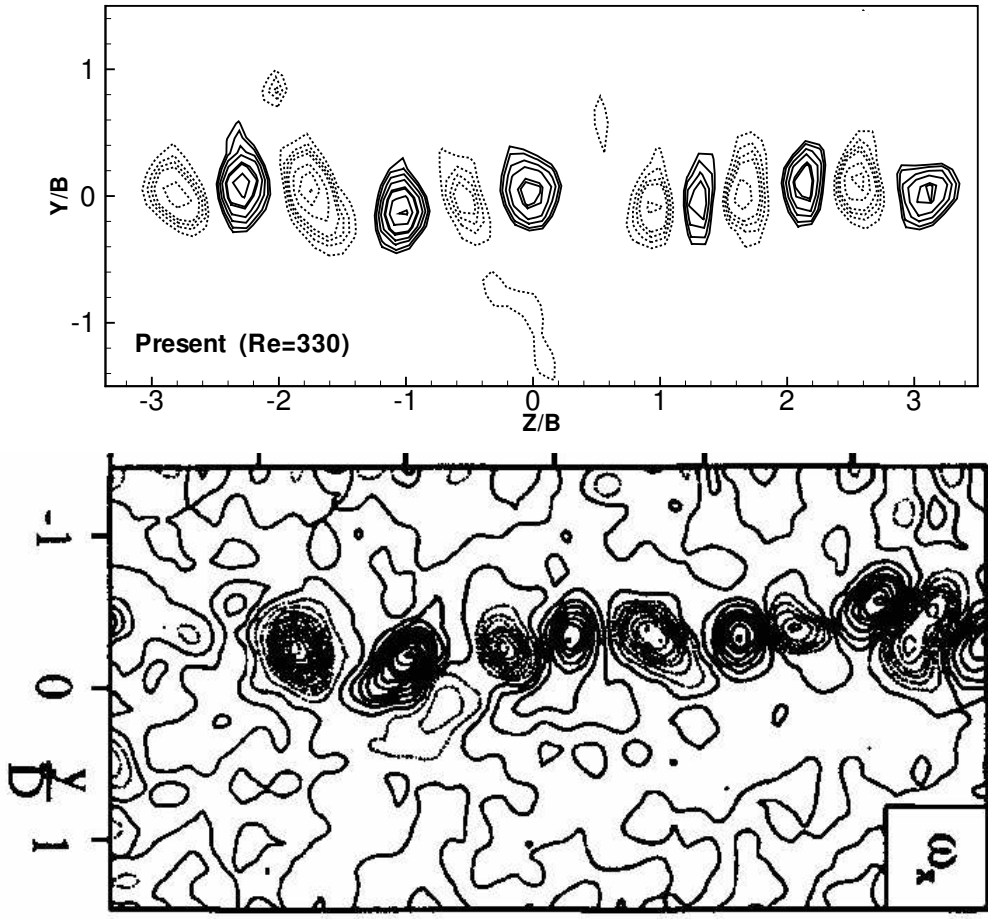

Figure 4.17: Comparison of instantaneous vorticity contours on the y-z plane above a circular cylinder. Top: present work, followed by the vorticity map of Brede *et al.* (1996)

.

Chapter 5

Flow Past a Stationary Square Cylinder

Introduction

This chapter presents results for flow past a stationary square cylinder placed at various orientations with respect to the incoming flow. The wake characteristics as a function of cylinder orientation have been investigated in detail as a technique for passive control of wake mixing and development. The sharp leading edge of a square cylinder move relative to each other due to the change in orientation leading to different asymmetry level of separation process. The aspect ratio of the cylinder has been varied to study the effect of end condition and three dimensionality. The Reynolds number affects the instability of the separated shear layer. Focus is on the intermediate range of Reynolds numbers and two aspect ratios. The ranges of parameters considered in the study are: incidence angle (referred interchangeably as *cylinder orientation*) in the range of 0-45^o, Reynolds number between 100-600, aspect ratio 16 and 28, blockage ratio 0.03 and 0.06. For comparison, limited data at an aspect ratio of 60 and blockage ratio of 0.04 are also presented. The high aspect ratio (≈ 60) experiments were performed in a separate wind tunnel of larger cross-section. The Strouhal number, drag coefficient, time-averaged velocity field, stream traces, vorticity, turbulence intensity, centerline velocity recovery, power spectra, kinetic energy budgets and flow visualization results have been presented. The vorticity field at different planes have been presented to show the primary and secondary vortical structures. Similarly, the flow visualization results at different measurement planes have been shown to explain the flow structures and three dimensionality. The drag coefficient and Strouhal number are based on B, the cylinder dimension, irrespective of the cylinder

orientation[1].

The chapter is primarily organized as per the following sections: (1) Effect of cylinder orientation, (2) Effect of aspect ratio, (3) Effect of Reynolds number. The detailed results have been discussed under the above broad classifications.

5.1 Effect of Cylinder Orientation

Cylinder wakes at low and high Reynolds numbers can be compared in the following manner. For a circular cylinder, the point of separation is Reynolds number dependent. Hence properties such as the wake size, drag coefficient and Strouhal number exhibit strong dependence on Reynolds number. For a square cylinder, the points of separation are fixed at the upstream corners, and the dependence on Reynolds number is less severe. There is a possibility of flow detaching from the upstream corner, closing in on the face of the cylinder and separating once again from the rear corners. This is more likely at high Reynolds number flows. It is also specific to square cylinders at zero angle of incidence. When the square cylinder is inclined to the mean flow, only one pair of corners contribute to flow separation. Hence, these orientations display only a weak dependence of the point of separation on the Reynolds number. The point of separation at the top and bottom corner of the cylinder are displaced from each other in the streamwise (x) direction depending on the cylinder orientation. The size of the turbulent structures and the broadening of the power spectra are dependent on the diffusion and dissipation mechanisms in the wake. These are clearly sensitive to Reynolds number, particularly when Re is towards the lower end of the scale.

The change in the angle of the cylinder affects the wake primarily due to the following two factors:

1. The projected dimension normal to the flow direction is altered.

2. The point of separation is altered. The second factor alters the position of the dividing streamline that defines the wake.

The dividing streamlines are symmetric for 0 and 45^o angles, but evolve unsymmetrically at all other angles. The loss of symmetry is felt in the time-averaged velocity distribution.

[1]Both drag coefficient and Strouhal number measured in the present experiments pertain to the central plane of the cylinder that divides the equally the cylinder length.

The projected dimension affects the minimum streamwise velocity in the near-wake. The lowest u-velocity is to be expected for an angle of 45^o, in comparison to all other angles. Mirror images of the 0-45^o flow fields are produced for cylinder angles between 45 to 90^o. For a square cylinder, the points of separation are fixed at the upstream corners. When the square cylinder is inclined to the mean flow, only one pair of corners contribute to flow separation.

Thus, global properties of the wake such as Strouhal number, drag coefficient and wake size as well as local properties such a center-line recovery of velocity and decay of velocity fluctuations are dependent on the cylinder orientation. The immediate effect of changing the cylinder orientation can be expected to be an increase in drag (and hence drag coefficient) due to an increase in the projected dimension with respect to the flow direction. Simultaneously, one can expect a reduction in the vortex shedding frequency (and hence Strouhal number) since the vortices are now of larger size. A cylinder with a square cross-section does not reveal these trends, as discussed in detail in the following sections.

5.1.1 Strouhal number

Figure 5.1 shows the Strouhal number variation with cylinder orientation for three different aspect ratios (AR = 16, 28 and 60) at Re=410. The change in Strouhal number with respect to the incidence angle is similar for the three aspect ratios, with a maximum Strouhal number seen at the 22.5^o orientation. Strouhal number increases from the 0^o incidence angle to 22.5^o, followed by a drop for subsequent rise in the incidence angle. From experiments, Chen and Liu [27] observed an increase in Strouhal number with respect to the incidence angle for a square cylinder till 17^o (at which St was 0.187) followed by a marginal drop to an asymptotic value of about 0.175. The Reynolds number range considered was 2000-21,000. The incidence angle that produces a maximum in Strouhal number was attributed to the onset of flow re-attachment to the side face of the cylinder. The differences in the Strouhal numbers between the present study and that of Chen and Liu [27] should be attributed to the difference in Reynolds number.

The Strouhal number variation with incidence angle is on one hand related to an increase in the projected dimension of the cylinder with respect to the incoming flow. More fundamentally, the vortex shedding frequency is influenced by the width between the two shear layers on each side of the cylinder and the incoming free stream velocity. The increase in the incidence angle leads to an increase in the distance between the two

shear layers. Therefore, an increase in the incidence angle results in reduced interaction between the two shear layers and a drop in the Strouhal number. This explanation is applicable for angles beyond 22.5^o. It is also possible that the separating shear layer on one side has a different vortex roll up distance compared to the neighboring vortex in the opposite shear layer, leading to a strong interaction between the two and therefore an increase in the Strouhal number. Thus, a maximum seen at 22.5^o incidence angle is due to the competing effects of an increased projected dimension and a shorter vortex roll-up distance.

The effect of orientation on vortex shedding frequency has been explained in the following manner by Gerrard [45]. The distance of the separation point to the position of vortex center changes with cylinder orientation. The shear layer is thicker at the position of vortex formation. A growing vortex continues to be fed by circulation from the shear layer until it becomes strong enough to draw the other shear layer across the wake. The approach of sufficiently strong vorticity of opposite signs cuts off further supply of circulation to the vortex, which then ceases to increase in strength. Changing the cylinder orientation changes the strength of the shear layer and it takes a longer time for a sufficient concentration of vorticity to be carried across the wake to initiate shedding. At higher orientation angle, the vortices on each side are sufficiently apart for the change in the individual vortex strength to be of importance.

The above explanations do not include the influence of three dimensionality of the near-wake on the spanwise vortices and hence the Strouhal number.

5.1.2 Drag coefficient

Figure 5.2 shows the effect of cylinder orientation on drag coefficient for two aspect ratios. The figure shows that drag is a minimum at 22.5^o when compared to other angles. The same result is seen for the high Reynolds number data as well (Obasaju [122], Dutta *et al.* [33]). The magnitude of drag coefficient is higher at the lower aspect ratio (AR = 16) when compared to the higher (AR = 28). This trend is opposite to that of the Strouhal number, where the Strouhal number for the higher aspect ratio is higher. A higher Strouhal number is an indication of the positive interaction between the opposed shear layers that feed the fluid to the growing vortex and cause early shedding. This increased interaction between the opposite shear layer also leads to weakening of the wake by increased mixing and therefore a reduction in the drag coefficient.

The influence of aspect ratio on Strouhal number and drag coefficient can be ex-

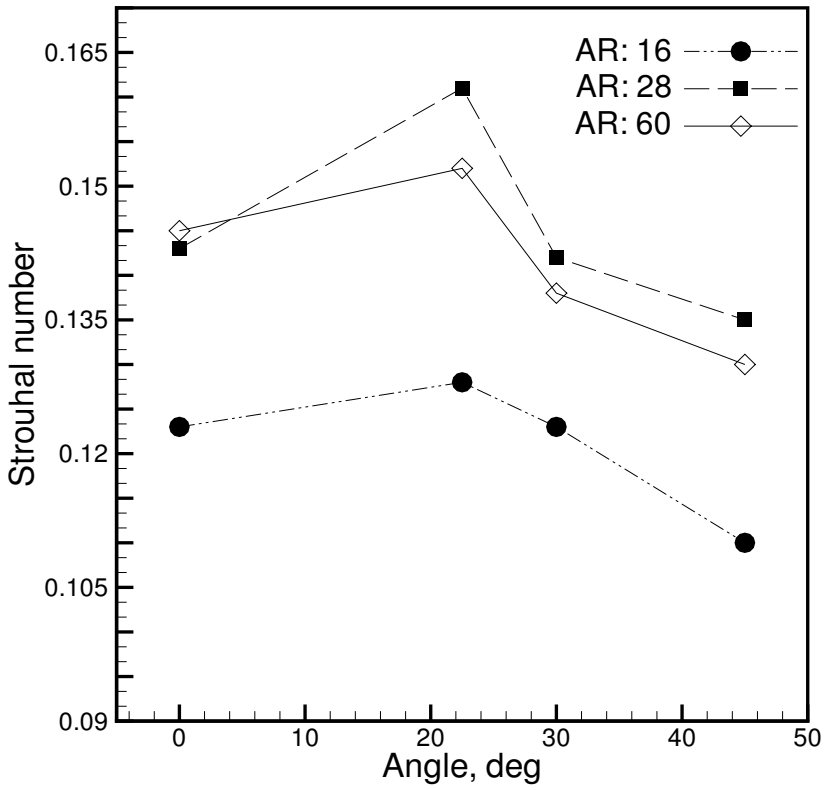

Figure 5.1: Variation of Strouhal number with cylinder orientation for three aspect ratios (AR= 16, 28 and 60) at Re=410.

plained in terms of the strength of the secondary flow along the length of the cylinder. The secondary flow can be seen as a mechanism by which the overall pressure difference across the cylinder (and hence C_D) is reduced. Figure 5.2 shows that in the limit of two dimensionality, a minimum in drag coefficient would be realized. Alternatively, the strength of the secondary flow would be a maximum. Since interaction of shear layers is predominantly a two dimensional phenomenon, secondary flow does not alter Strouhal number and an asymptotic limit is reached for increasing aspect ratios. The present data at low Reynolds numbers has been compared with the two dimensional simulation of Sohankar *et al.* (1998).

The difference between present work and the numerical work by Sohankar *et al.*(1998) can be attributed to the following factors:

1. The experimental results are based on mid-plane measurements, while the numerical simulation is an average over all axial positions of the cylinder;

2. Experimental data include confinement effects due the channel walls, while the numerical simulation is purely two dimensional.

3. The approach flow in numerical simulation does not have superimposed fluctuations, while in experiments, free stream turbulence of the incoming flow is necessarily non-zero[2].

Factors 1 and 2 indirectly confirm that the flow is three dimensional to a point where the average properties of the flow field are influenced.

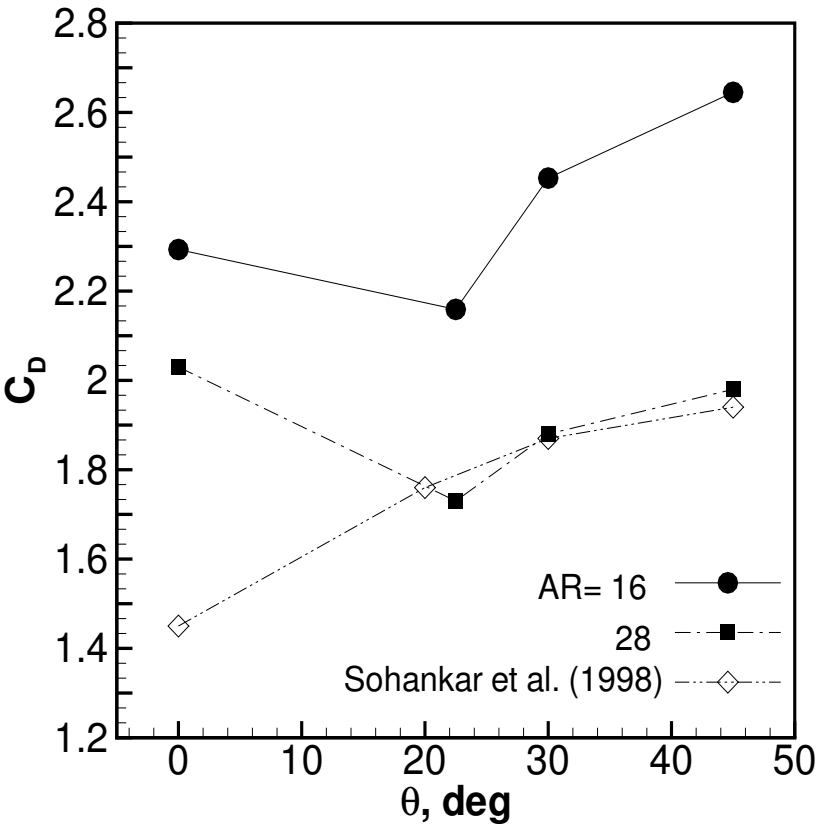

Figure 5.2: Variation of time-averaged drag coefficient with cylinder orientation for two aspect ratios (AR=16 and 28) at Re=410.

5.1.3 Time-averaged velocity field

The wake behind the square cylinder is unsteady for the range of Reynolds numbers studied. Hence, it is not possible to compare instantaneous velocity vectors for various

[2]being of the order of 0.27% of the inflow velocity

cylinder orientations. A collection of 200 PIV image pairs[3] were averaged to generate a time-averaged picture of the velocity field. The differences between averages with 100 images and 200 images were seen to be indistinguishable.

Figure 5.3 shows time-averaged velocity vectors for four cylinder orientations (0, 22.5, 30 and 45^o). A Reynolds number of 410 has been considered. The x- and y-coordinates have been normalized by the cylinder edge. The shaded contours are of resultant velocity. The vectors very close to the cylinder are not completely resolved owing to the interference effects. The wake region is however, clearly visible. Between 0 and 45^o, there is an increase in the wake size, but the increase is not monotonic with angle. The wake size corresponding to 22.5^o is the smallest. The size of the stagnant (dark zone) region is minimum for 22.5^o cylinder orientation angle. It explains the minimum in drag coefficient (Figure 5.2) at this angle .

Figures 5.4 and 5.5 present the time-averaged velocity profiles of the x- and y-components of velocity from PIV images for four incidence angles (0, 22.5, 30 and 45^o) for Re=410 and 610 respectively. Velocity has been non-dimensionalized with that of the incoming stream and x, y scales are non-dimensionalized with the cylinder edge. Comparison is presented for four downstream locations (x = 2, 4, 6, and 8). These streamwise locations have been selected to include important regions of interest; namely the pre-recirculation bubble (x=2), the core recirculation bubble (x=4,6) and post recirculation region (x=8). Fluid particles are entrained from each side of the wake. Hence, both positive and negative transverse velocities are seen above and below the mid-plane of the cylinder. Figure 5.4 and 5.5 show that the transverse velocity is a stronger function of cylinder orientation when compared to the streamwise component. A definite change in velocity magnitude and symmetricity is found with change in cylinder orientations. With an increase in the downstream distance, the x-component of the centerline velocity recovers towards the free-stream value, while the y-component velocity approaches zero. The transverse velocity changes direction with downstream direction over the distance considered. This trend has also been observed in numerical simulation (Saha *et al.* [147]). The change in direction is not monotonic and shows a strong dependence on cylinder orientation. The v-velocity profile is asymmetric for 22.5 and 30^o orientations. Therefore, the local instability modes and their amplification rates are altered for these orientations of the square cylinder leading to the appearance of additional harmonics in the flow fluctuations (section 5.1.9). The asymmetric separation process for 22.5 and 30^o incidence angles are clear from the v-velocity profile when compared to the u-velocity. At

[3]300 image pairs for turbulence statistics

the end of the recirculation bubble, the transverse velocity magnitude reduces, leading to a slow but definite recovery of the streamwise velocity. The wake becomes broader due to the entrainment of the fluid into the wake. In the near wake, the wake size increases rapidly because of displacement by the two oppositely oriented eddies. In the far downstream, the wake size reaches a limiting value since the eddies are weakened by viscous dissipation and diffusion.

5.1.4 Time-averaged streamtraces

Figure 5.6 compares the time-averaged stream traces in the wake of the cylinder at Reynolds numbers of 410 for four cylinder orientations. The stream traces are plotted at the mid-plane ($z = 0$) of the cylinder. Two bubbles with opposed direction of circulation form behind the cylinder. The overall size of the recirculation bubble shows strong dependence on cylinder orientations.

The shape of recirculation bubbles in Figure 5.6 demonstrates that flow is asymmetric when the orientation of the cylinder is 22.5 or 30^o. The streamwise length of the recirculation bubble is a maximum for 0^o and a minimum occurs at 22.5^o. These results correlate with the time-averaged drag since a large wake and high drag occur jointly in bluff body wakes. The separating streamlines on each side of the recirculation bubble are oriented at an angle with respect to the mean flow, indicating greater interaction between the two. The core location and transverse extent of the recirculation bubbles are dependent on cylinder orientations. Figure 5.7 shows the time-averaged streamlines for Reynolds number of 610. Greater asymmetry is observed in Figure 5.7 for symmetric geometries ($\theta = 0^o$ and 45^o) compared to that in Figure 5.6. The streamlines in Figure 5.7 have probably not converged even after recording 200 image pairs. This may be attributed to the greater unsteadiness at higher Reynolds number.

5.1.5 Time-averaged vorticity

Figures 5.8 and 5.9 show time-averaged spanwise vorticity contours (ω_z) for four cylinder inclinations and Reynolds numbers of Re=410 and 610 respectively[4]. Vortices with positive values of vorticity are shown with solid lines and negative-valued vortices are shown with dotted lines. A contour of constant vorticity is loosely identified in the following discussion as a *vortex*. Positive vortices have a counter-clockwise sense while negative vortices are oriented clockwise. Vorticity has been calculated by differentiating

[4]It should be recalled that the axis of spanwise vorticity is parallel to the cylinder axis.

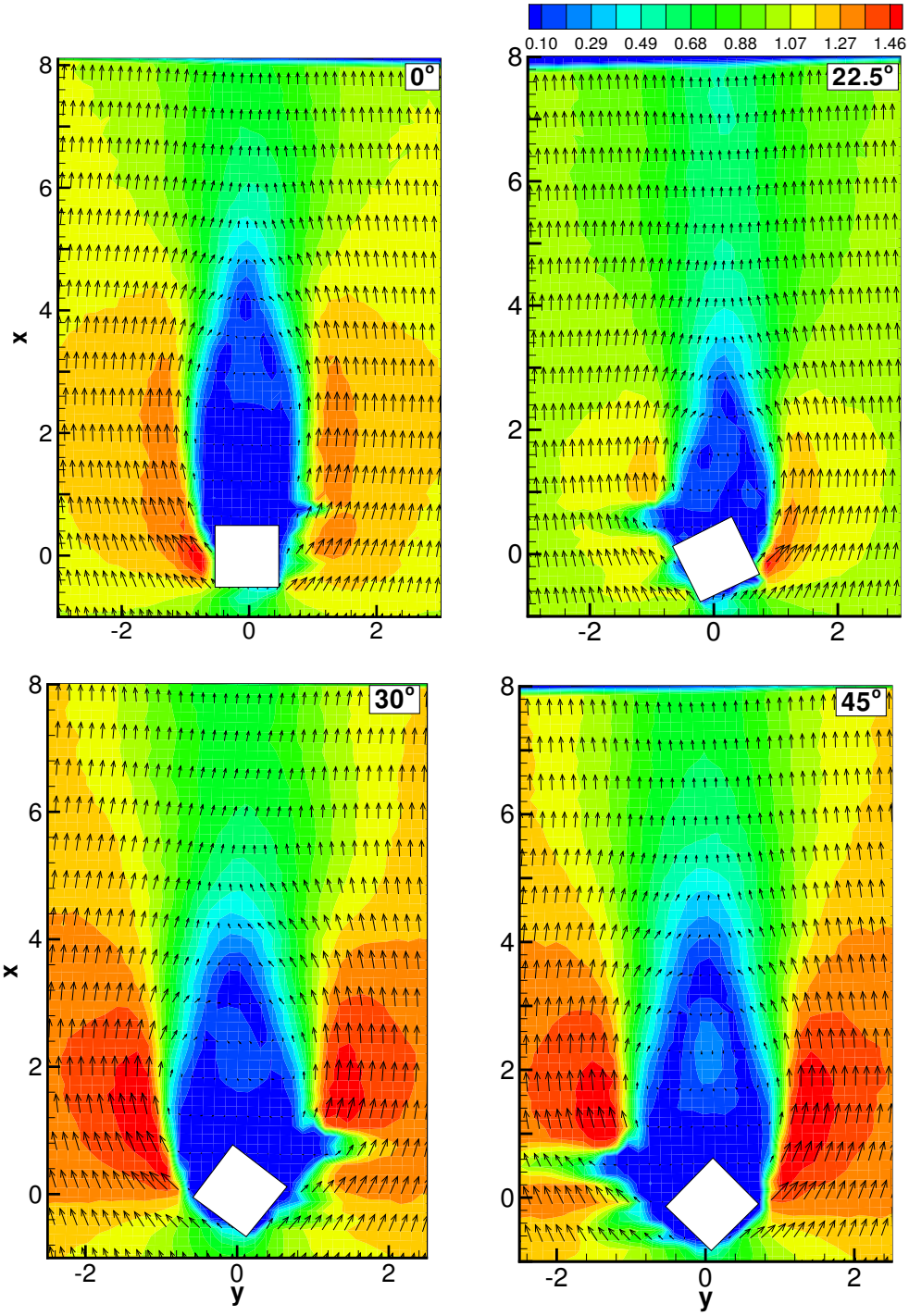

Figure 5.3: Time-averaged velocity vectors in the wake of a square cylinder at a Reynolds number of 410 for aspect ratio 28 and different cylinder orientations (θ=0, 22.5, 30 and 45). The flooded contours represent the absolute velocity magnitude.

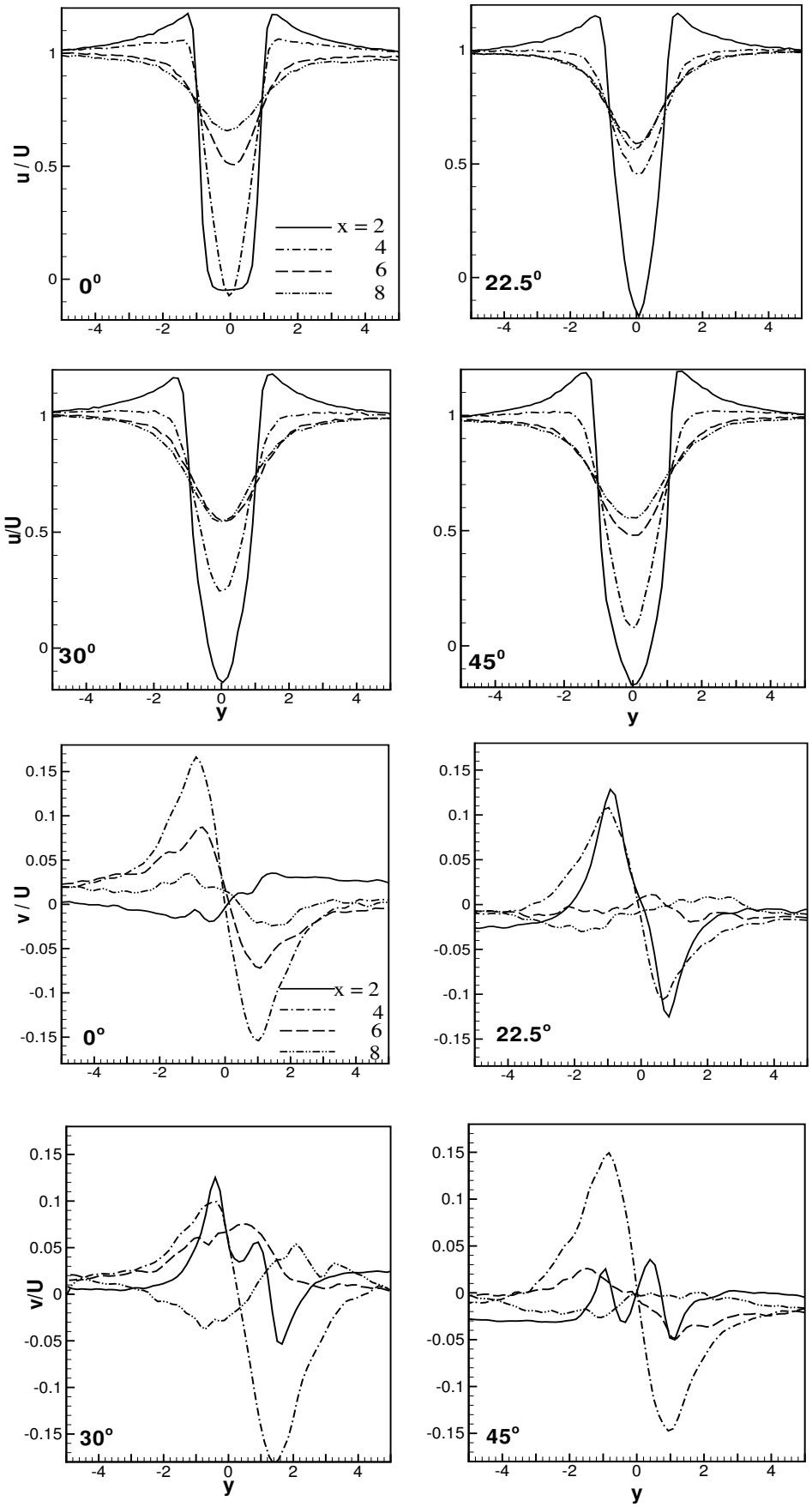

Figure 5.4: Time-averaged u and v velocity profiles at four downstream locations (x= 2, 4, 6 and 8) for aspect ratio 28 and four cylinder orientations (0, 22.5, 30 and 45^o) at Re=410.

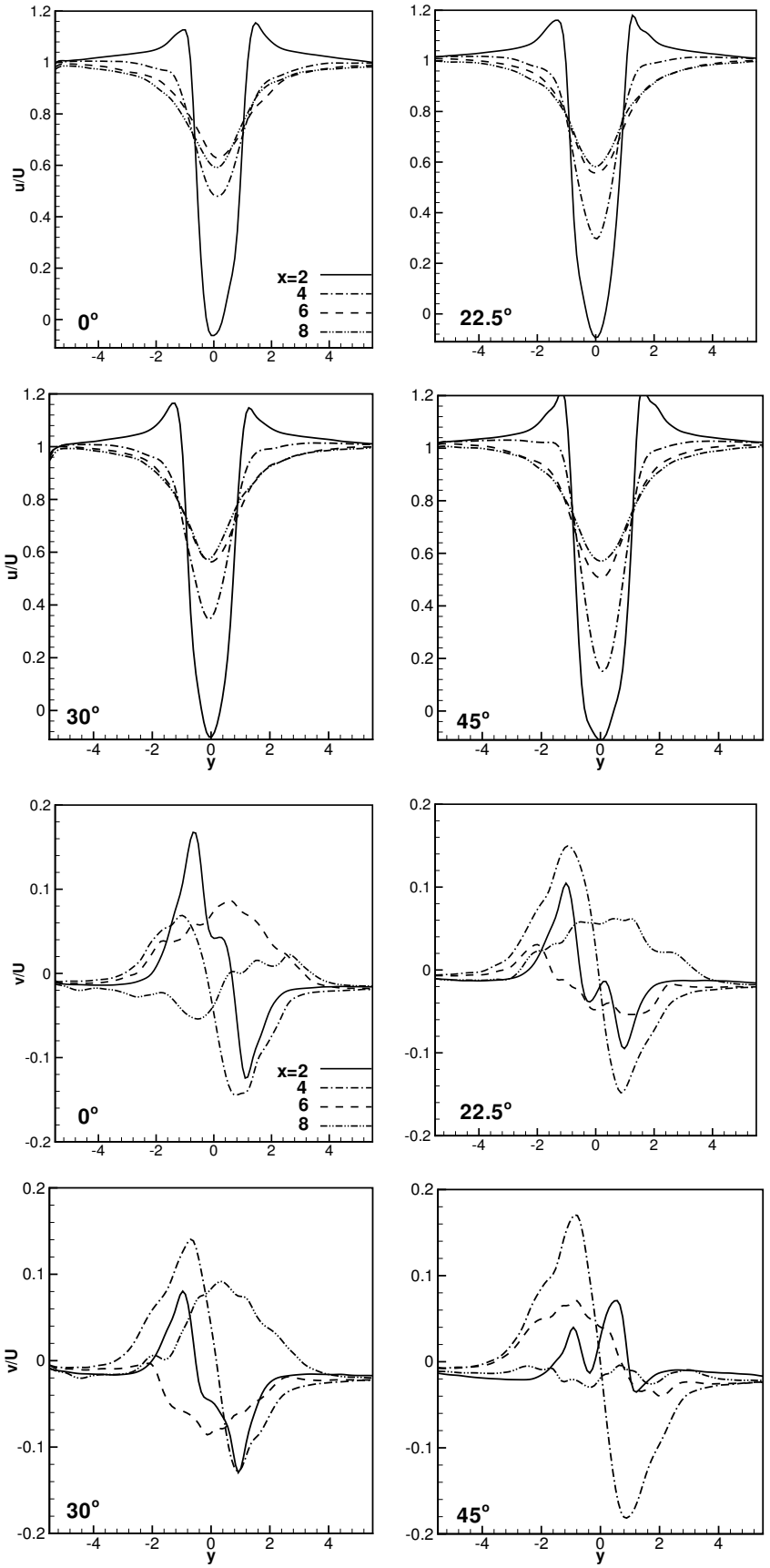

Figure 5.5: Time-averaged u and v- component of velocity profiles at four downstream locations (x=2, 4, 6 and 8) and four cylinder orientations at AR=28, Re=610.

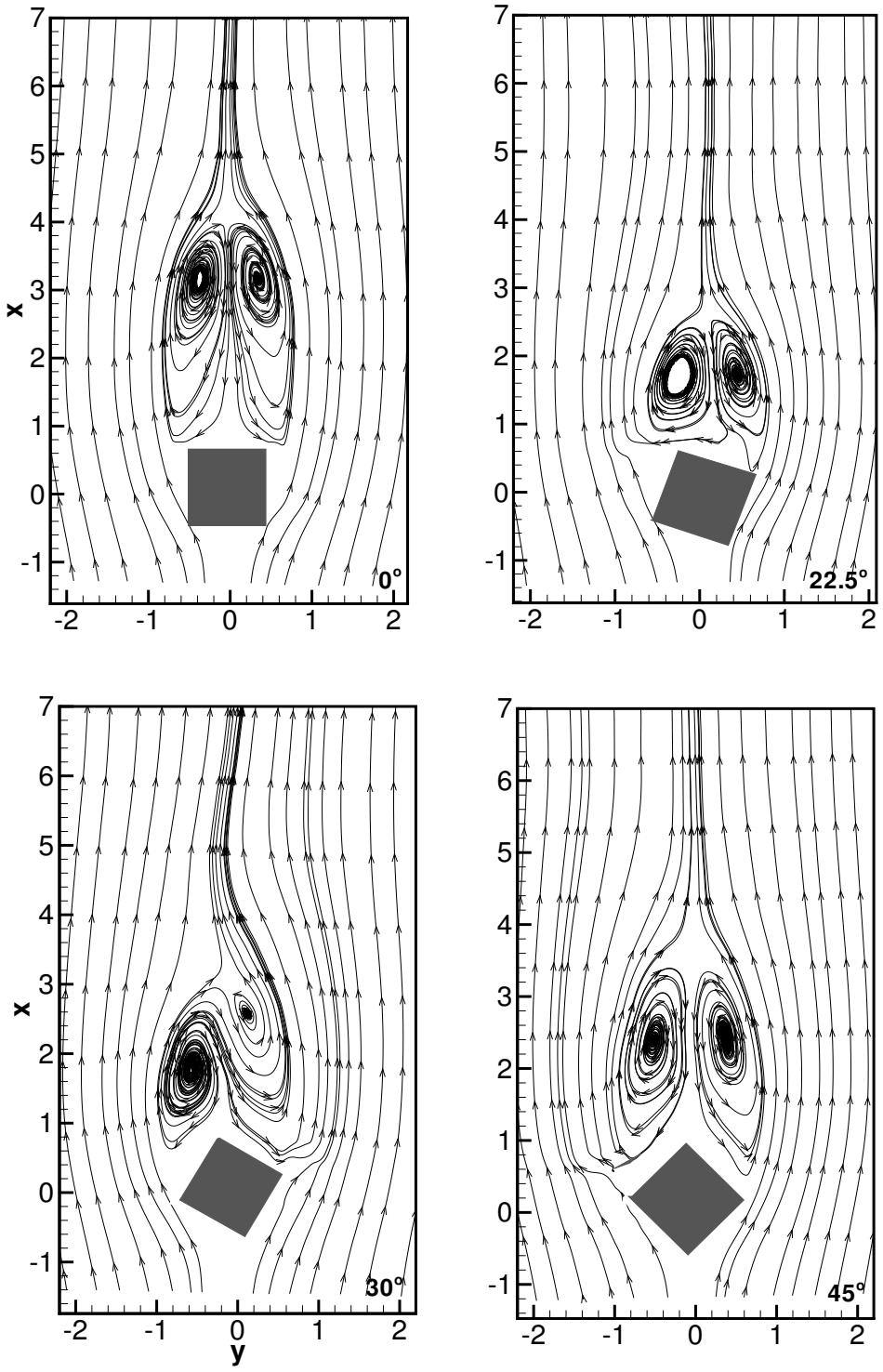

Figure 5.6: Time-averaged stream traces in the wake of a square cylinder at Re=410 and different cylinder orientations (θ=0, 22.5 30 and 45^o), AR=28.

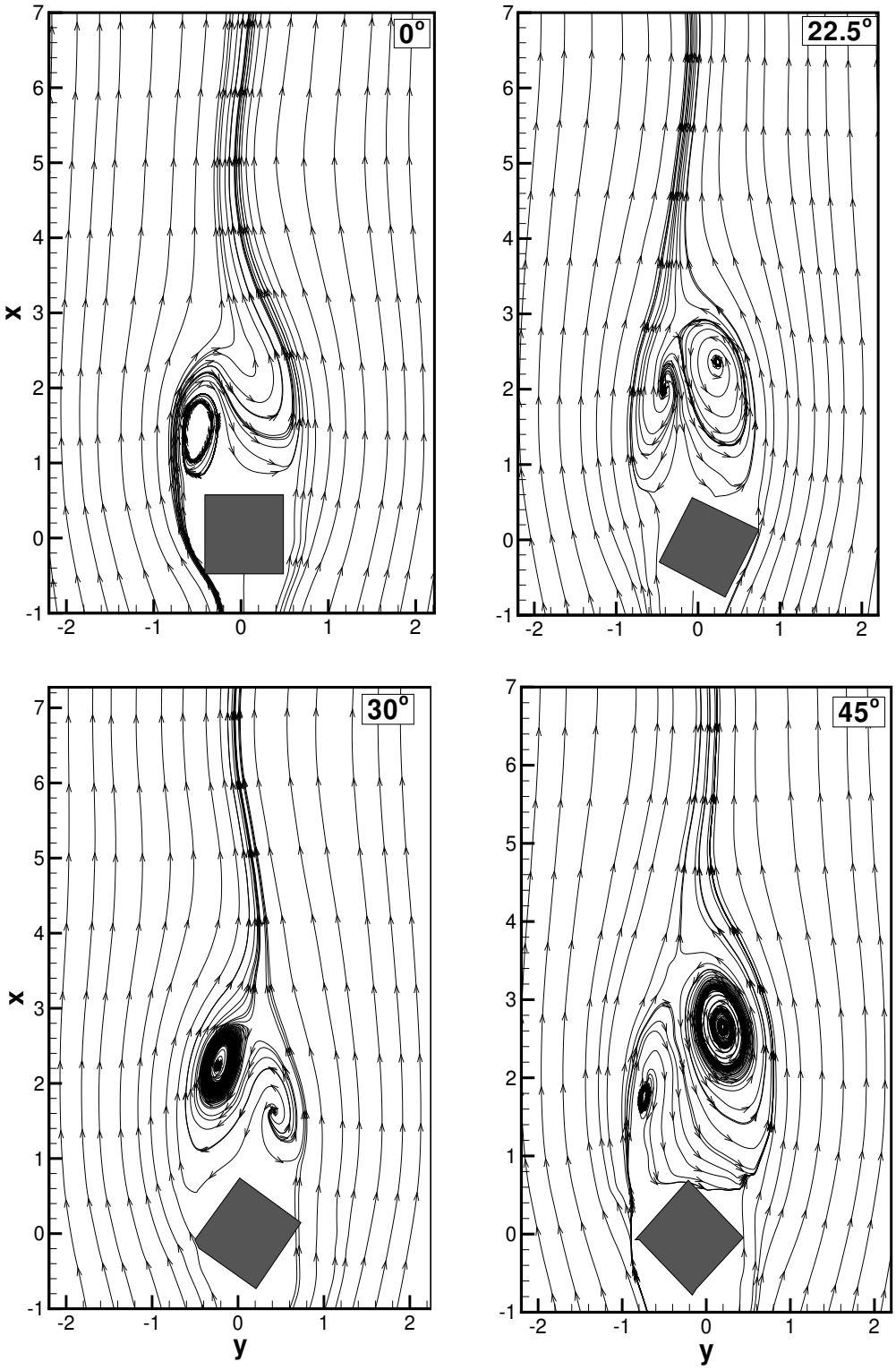

Figure 5.7: Time-averaged stream traces in the wake of a square cylinder at Re=610 and different cylinder orientations (θ= 0, 22.5, 30 and 45^o), AR=28.

the time-averaged velocity signal in spatial domain. Vorticity values as well as the coordinates have been non dimensionalized with the incoming average velocity and cylinder diameter. Strong vortices are seen to be clustered around the upstream cylinder corners along the shear layers originate. Vorticity contours appear to be distorted very near the cylinder edges due to the multiple reflections of the cylinder in the original PIV images. Broadly speaking, oppositely oriented vortices of nearly equal strength are generated from the cylinder corners. The spreading of vortices is symmetric and shows weak dependence on cylinder orientation. The spreading of vortices in the streamwise direction, however, shows a strong dependence on cylinder orientation, being a maximum at 45^o and a minimum at 22.5^o. The spread of vorticity in the flow direction is a measure of the distance over which the shear layers roll up.

The strength of the spanwise vorticity component is related to the reduction in pressure at the base of the cylinder. The transport of vortices generated at the corners of the cylinder is controlled by two opposing factors. One is the lower average pressure within the wake. This is opposed by the growing wake size transverse to the main flow, and thus a shift of the vortex center outwards. The latter comprises viscous diffusion along with transport by the time-dependent transverse velocity. The second factor is more significant at low Reynolds numbers, since viscous diffusion aids to momentum transfer in the transverse direction, along with transport by the time-dependent transverse velocity field.

5.1.6 Instantaneous vorticity

At intermediate Reynolds numbers of the present study, flow is characterized by staggered array of vortices. In addition to spanwise vortices (ω_z), secondary vortices are also generated in the wake. Two types of secondary vortices are present in the three-dimensional flow field, namely streamwise (ω_x) and transverse vortices (ω_y). Figure 5.10 shows a time sequence of instantaneous spanwise vortices at the mid-plane of the cylinder. The figure reveals the alternating staggered nature of the vortex street, thus signifying dominant periodicity in the flow. The wavelength of these vortices (in the flow direction) is about 3 times cylinder size though not strictly a constant. Specifically, the near wake wavelength is smaller as compared to the farwake. The distance over which the shear layer rolls up is a strong function of cylinder orientation and minimum is seen at θ=30^o.

The instantaneous transverse (ω_y) vorticity contours are presented in Figure 5.11. The vortices are plotted in the vertical mid-plane(y=0). The spanwise wavelength (λ_z)

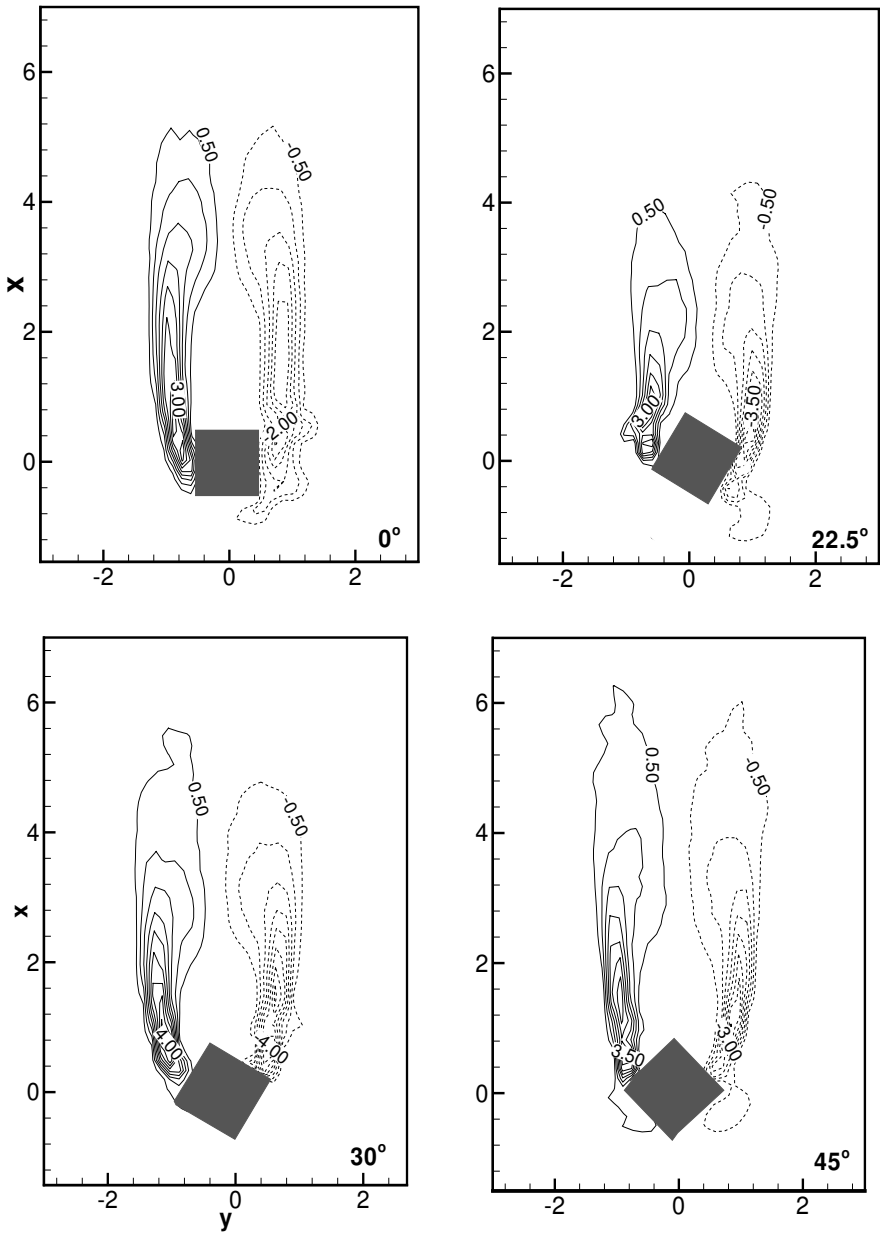

Figure 5.8: Time-averaged spanwise vorticity (ω_z) for four cylinder orientations (θ= 0, 22.5, 30 and 45^o), AR 28 and Re=410. Dashed lines show negative vorticity while solid lines represent positive vorticity, $\Delta\omega_z = 0.5$.

of these vortices is about unity. The vorticity contours give a clear indication of the appearance of irregular finer-scales. Similar patterns of instantaneous vorticity were observed by Saha *et al.* [153] and Sohankar *et al.* [140]. Figure 5.12 shows instantaneous secondary vorticity contours (ω_x) at a Reynolds number of 410. Vorticity contours are plotted on the y-z plane at $x = 4$ from the cylinder axis. Vorticities of opposite

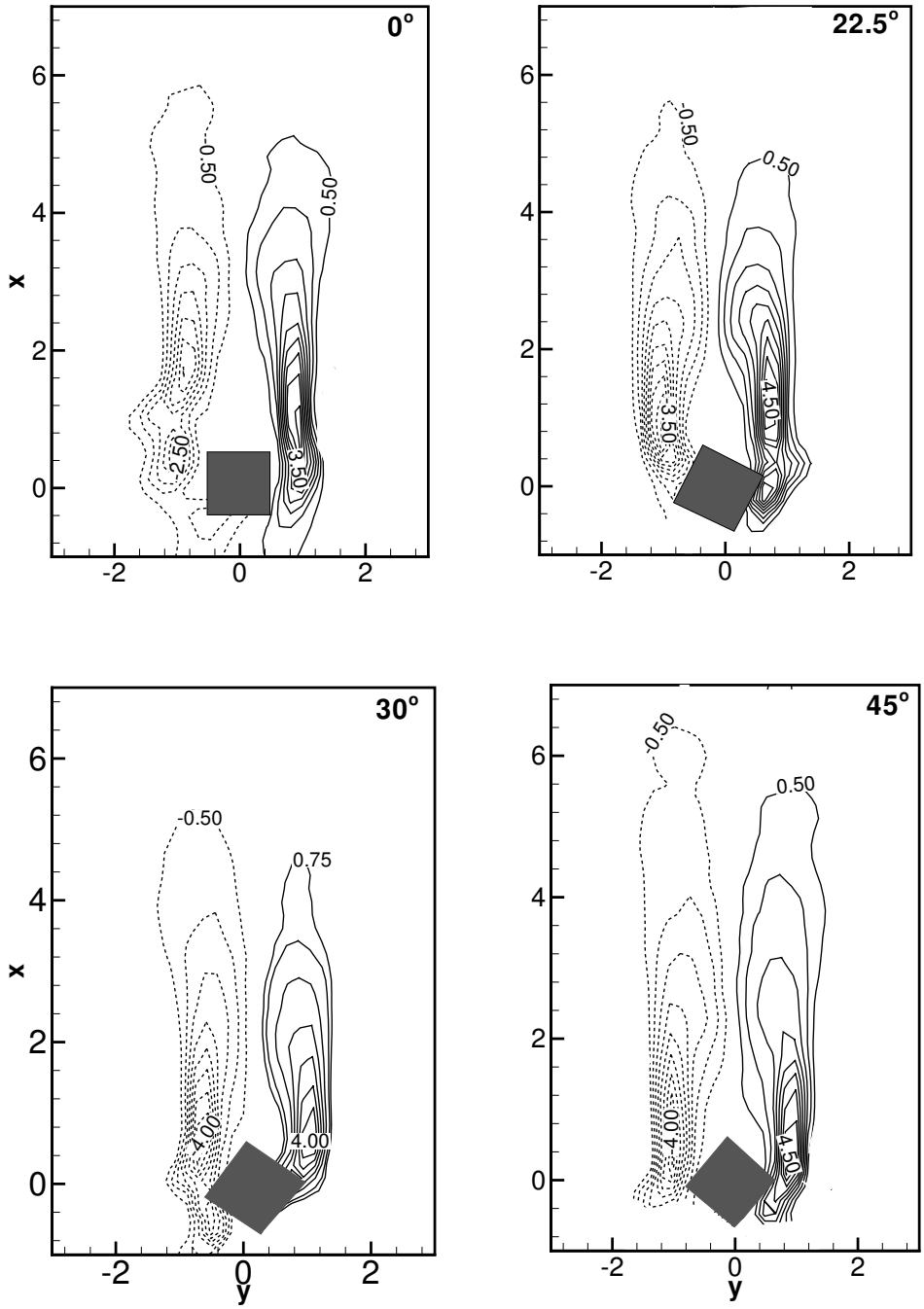

Figure 5.9: Time-averaged spanwise vorticity (ω_z) for four cylinder orientations (θ=0, 22.5, 30 and 45^o), AR= 28 and Re=610. Dashed lines show negative vorticity while solid lines represent positive vorticity, $\Delta\omega_z = 0.5$.

orientation are spread along the cylinder axis for all angles. The appearance of secondary vorticity component indicates improved mixing of the fluid in the wake; it is equivalent

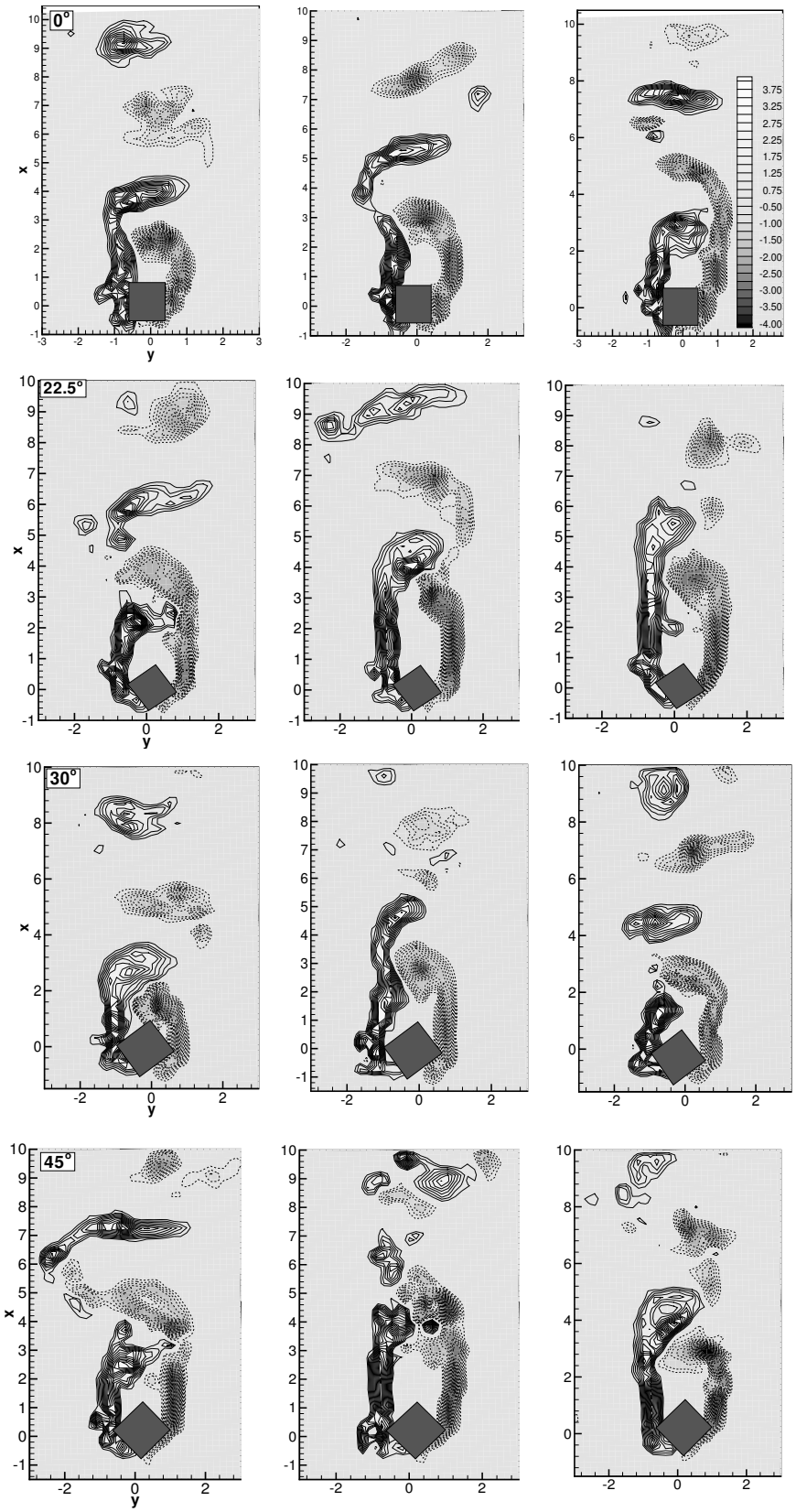

Figure 5.10: Instantaneous contours of spanwise vorticity (ω_z) for four cylinder orientations (θ=0, 22.5, 30 and 45^o), AR= 28 and Re=410. Dashed lines show negative vorticity while solid lines represent positive vorticity, $\omega_{z(max)}$=4.0, $\omega_{z(min)}$=-4.0 and $\Delta\omega_z = 0.25$.

to raising the base pressure of the cylinder. Here, the z-component of velocity leads to pressure equalization in the direction parallel to the cylinder axis. Hence, an increase in the strength of the secondary vorticity can be linked to the possibility to the drag reduction. A marginal increase in strength of secondary vortices is realized at orientations other than zero. z-component of velocity leads to pressure equalization in the direction parallel to the cylinder axis. Hence, as stated earlier, an increase in the strength of the secondary vorticity can be linked to the possibility of drag reduction. A marginal increase in strength of secondary vortices is realized at orientations other than zero.

5.1.7 Time-averaged velocity fluctuations

Figures 5.13 and 5.14 compare the total turbulence intensity fields ($= \sqrt{u'^2 + v'^2}/U$)at different cylinder orientations for two Reynolds number Re=410 and 610 respectively[5]. Velocity fluctuations play a major role in determining the fluctuating lift and drag forces, the association being extendable to rms-values. As expected, the shear layers, being regions of high velocity gradients, can be seen to be regions of high velocity fluctuations. The streamwise growth of the shear layer shows up in the figure with broadening of the high turbulent zones in the transverse direction. The turbulence intensity increases both in the streamwise and transverse direction from the edge of the cylinder and midplane of the cylinder axis respectively with a drop, after reaching a maximum value. The maximum turbulence intensity zone is closer to the cylinder for 22.5^o orientation angle at Re=410 (Figures 5.13). The higher turbulence intensity can be correlated to greater mixing and therefore reduction in drag at this orientation angle (Figure 5.2).

Figure 5.15 shows the streamwise variation of the turbulence intensity at the cylinder midplane ($y = 0$). The objective of this plot is to demonstrate differences in the formation length of the vortices. Turbulence intensity increases in the streamwise direction, reaching a maximum value followed by slow decay. For orientations of 0 and 45^o the turbulence intensity peaks at a different streamwise location when compared to 22.5 and 30^o. This is because at 22.5 and 30^o, the flow field is asymmetric when compared to the 0 and 45^o angles. For the asymmetric flow field, the turbulence intensity grows faster when compared to the symmetric wake. Figure 5.16 shows the development of turbulence intensity along the cylinder centerline for Re=610. The turbulence intensity reaches its maximum at a shorter distance , and decreases faster as well, when compared to Re=410. The effect of cylinder orientation is only minor at this Reynolds number.

[5]The velocity fluctuations referred to in this section have been obtained from the PIV images.

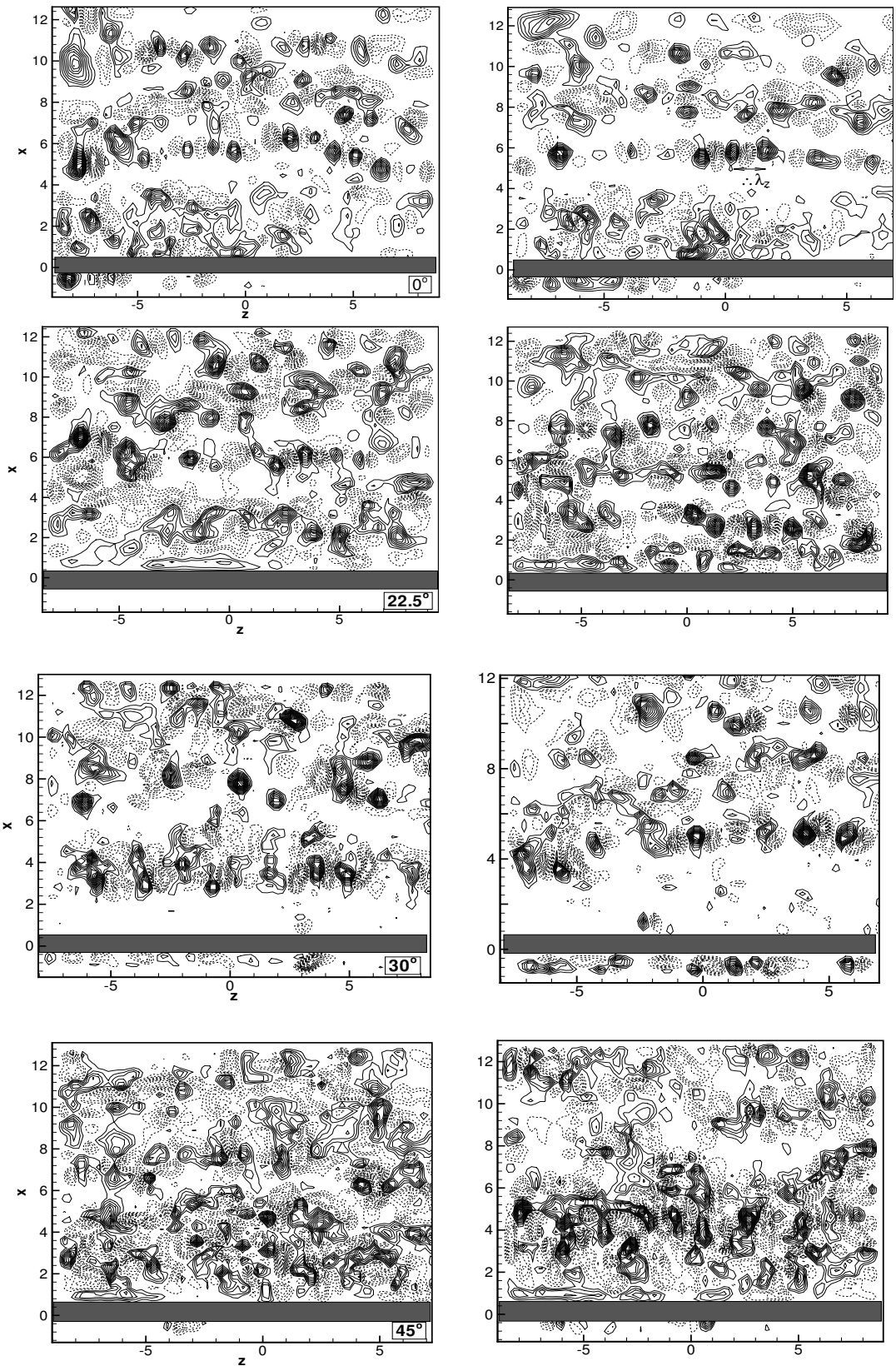

Figure 5.11: Instantaneous contours of secondary vorticity (ω_y) for four cylinder orientations (θ=0, 22.5, 30 and 45^o), AR=28 and Re=410. Dashed lines show negative vorticity while solid lines represent positive vorticity, $\omega_{y(max)}$=3.5, $\omega_{y(min)}$=-3.5 and $\Delta\omega_y = 0.5$.

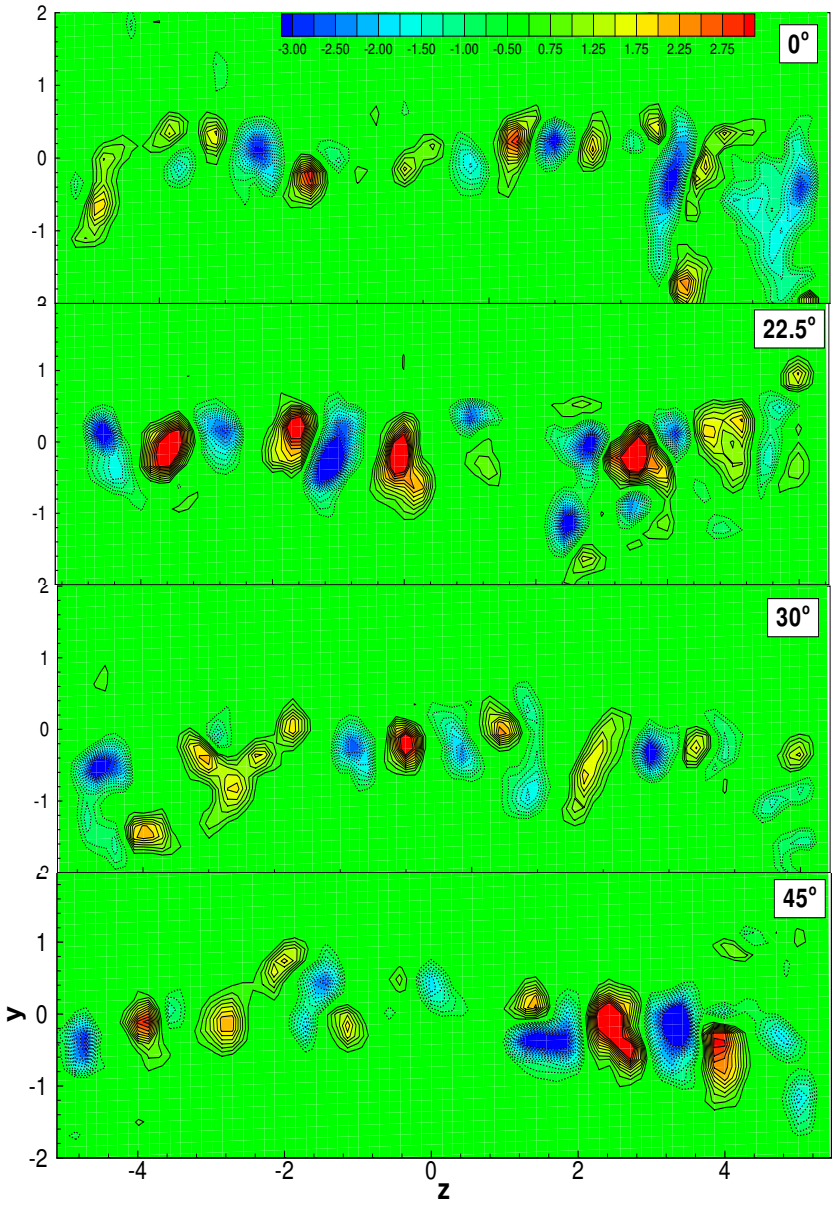

Figure 5.12: Instantaneous contours of secondary vorticity (ω_x) for four cylinder orientations and aspect ratio of 28 at Re=410. Dashed lines show negative vorticity while solid lines represent positive vorticity. $\Delta\omega_x = 0.25$.

Figures 5.17 and 5.18 show time-averaged profiles of u_{rms} and v_{rms} in the transverse direction at three streamwise locations (x=2, 4 and 6) at Reynolds number of 410. Four cylinder orientations have been considered. Profiles of u_{rms} show two peaks about the center-plane for all orientations and all the three locations. However, the peak magnitude vary with cylinder orientation. The v_{rms} profile shows a strong dependence on cylinder

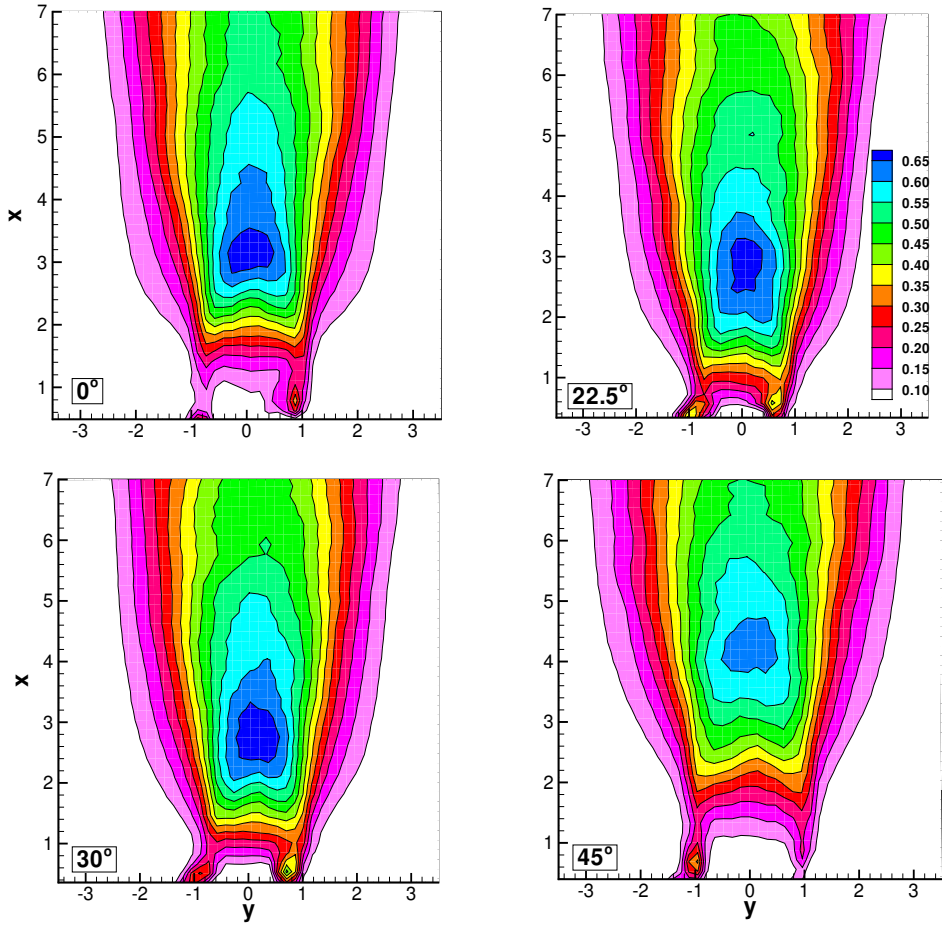

Figure 5.13: Contour plot of turbulence intensity $((u_{rms}^2 + v_{rms}^2)^{0.5}/U)$ in the wake of a square cylinder at a Reynolds number of 410 for aspect ratio 28 and four cylinder orientations.

orientation (Figure 5.18). The minimum in v_{rms} is seen at 0^o at x=2. The v_{rms} profile does not show dual peak as that of u_{rms}. The u_{rms} peak at both sides of the shear layer. The y-location of maximum v_{rms} velocity is different from that of u_{rms} velocity.

5.1.8 Recovery of centerline velocity

Centerline recovery of the streamwise and decay of the transverse velocity components for various angles are compared in Figure 5.19. The transverse velocity has been plotted along the flow direction at a particular offset location from cylinder centerline (y=1)[6]. The u-velocity is zero on the cylinder surface and is negative (in the time-averaged sense)

[6]This is because the transverse velocity is close to zero on the centerline.

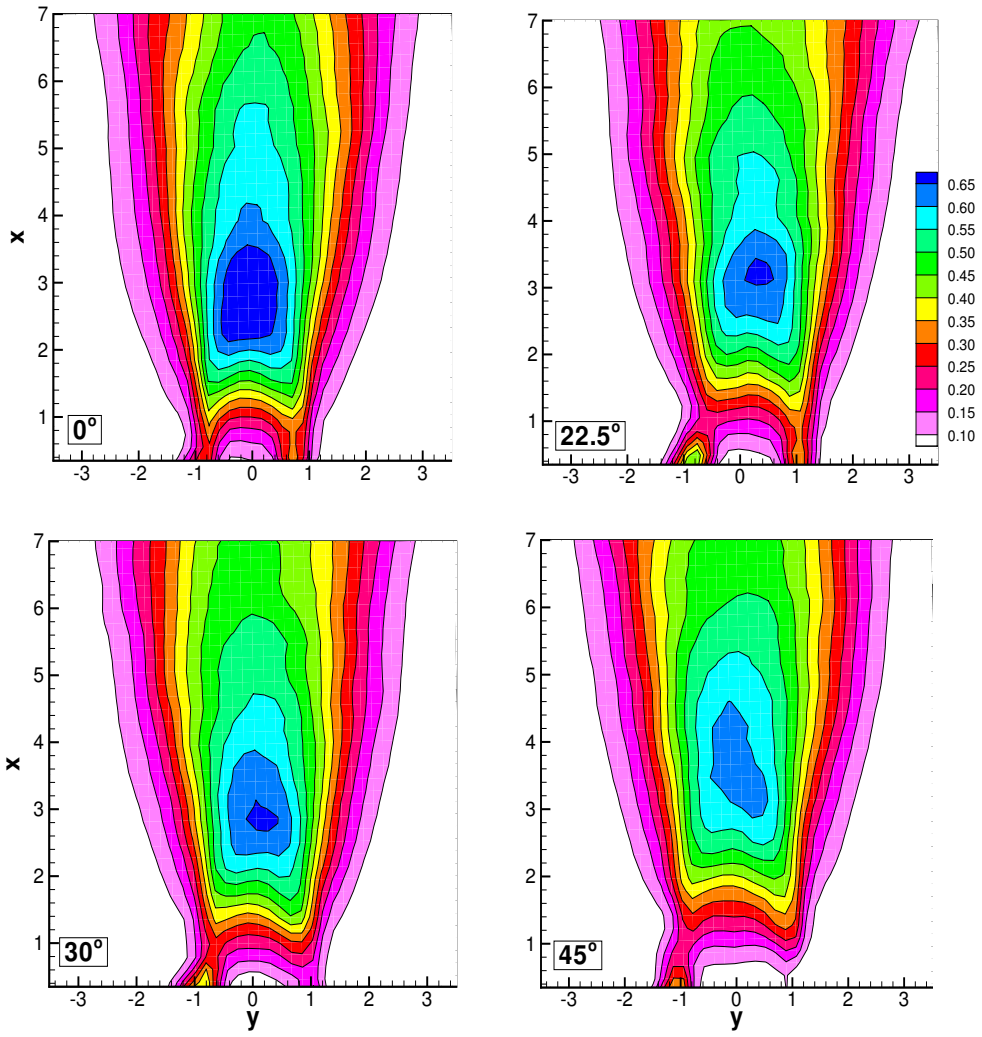

Figure 5.14: Contour plot of turbulence intensity $((u_{rms}^2 + v_{rms}^2)^{0.5}/U)$ in the wake of a square cylinder at a Reynolds number of 610 for aspect ratio 28 and four cylinder orientations.

up to certain downstream distance. Later, it increases with the x-coordinate and reaches an asymptotic value. The centerline velocity reaches an asymptotic value in the range of 0.6-0.65. The asymptotic limit of u-velocity is reached at a distance of around $x = 7$. The average centerline velocity is lower inside the recirculation zone, where the v-velocity is high. The minimum in centerline velocity value occurs around the core of the recirculation bubble. The streamwise location of v-velocity takes place at the end of the recirculation bubble.

For centerline recovery of the velocity field, two factors play major role. One is the wake size and the second is base pressure on the rear surface of the cylinder. With

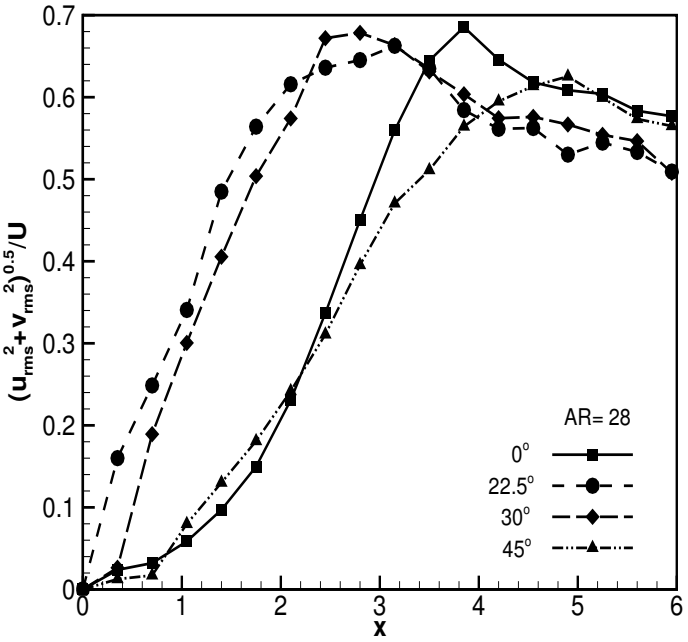

Figure 5.15: Turbulence intensity development along the cylinder centerline in the streamwise direction for different orientation angles of the cylinder at Re=410 (AR=28).

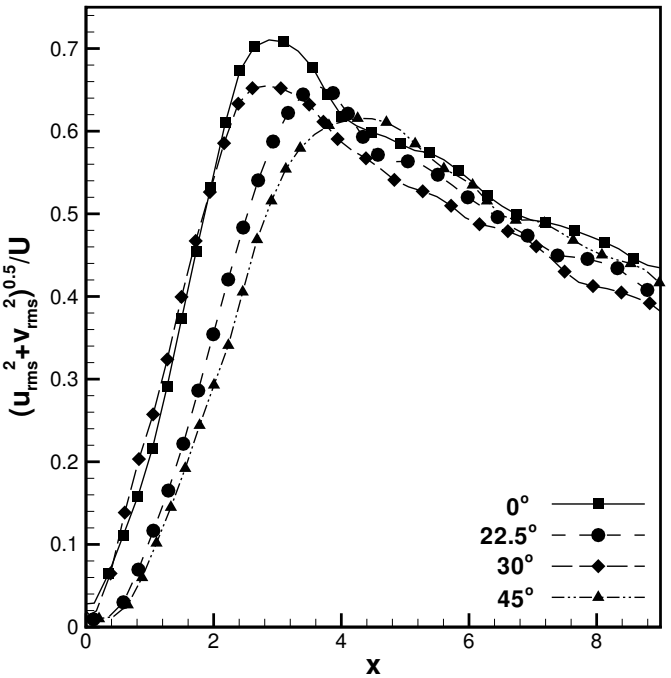

Figure 5.16: Turbulence intensity development along the cylinder centerline in the streamwise direction for different orientation angles of the cylinder at Re=610 (AR=28).

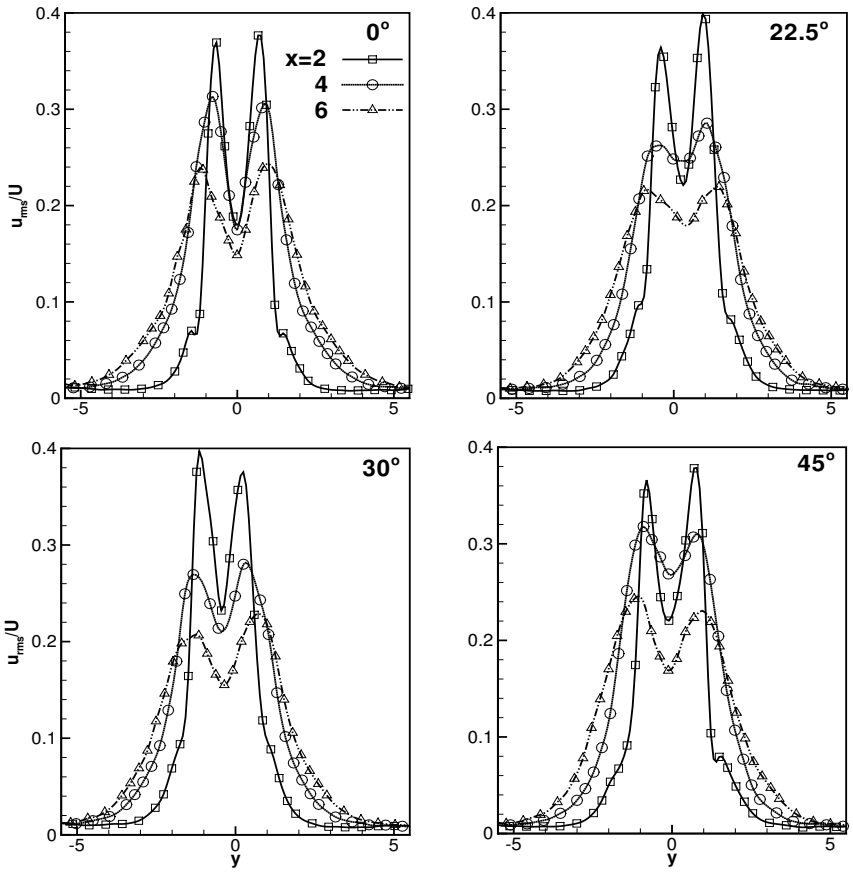

Figure 5.17: Time-averaged streamwise velocity fluctuation for three downstream locations (x=2, 4 and 6) and four cylinder orientations (θ=0, 22.5, 30 and 45^o), Re=410 (AR=28).

downstream distance, the wake becomes broader due to the entrainment of the fluid while the average pressure difference between the wake and the outer flow diminishes. Hence, the pressure difference between the core of the wake and the external flow determines the initial recovery. Downstream recovery in velocity depends on flow re-adjustment in the form of the fluid drawn into the wake from the external flow. The first factor is a strong function of cylinder orientation and aspect ratio. Hence the base region of the cylinder carries these characteristics; at longer distances downstream, these factors are less significant.

5.1.9 Power spectra

Spectra have been determined from a 2-wire hot-wire probe placed in the wake at a slightly off-set location. This y-location captures shear layer instabilities in the near-

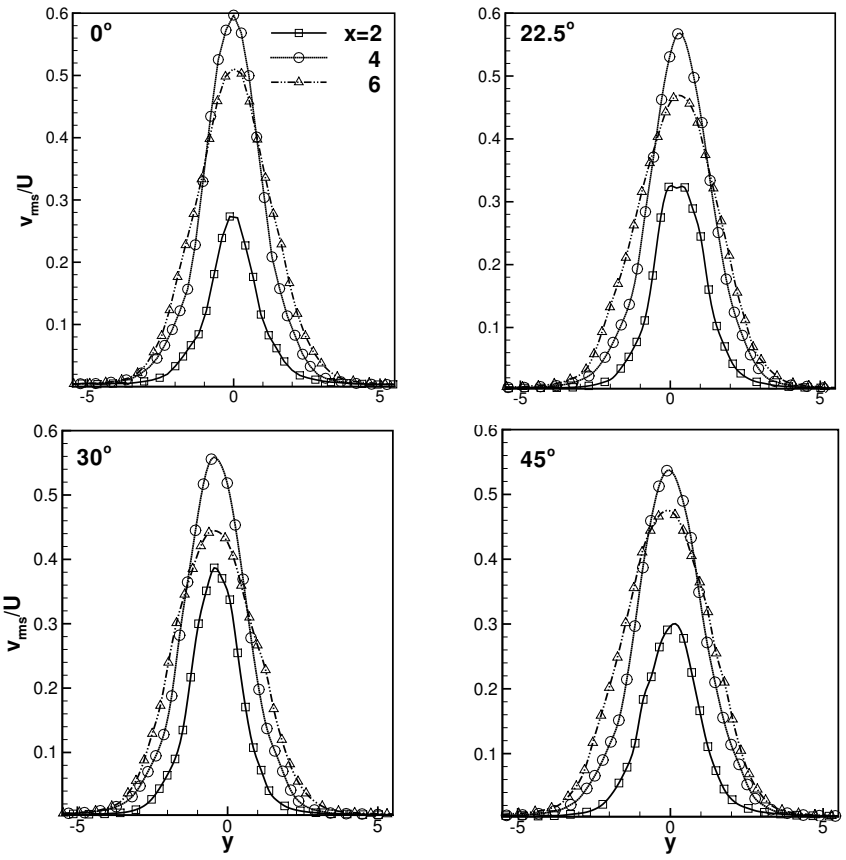

Figure 5.18: Time-averaged transverse velocity fluctuation for three downstream locations (x=2, 4 and 6) and four cylinder orientations (θ=0, 22.5, 30 and 45^o), Re=410 (AR=28).

wake. The far wake is less sensitive to the offset position of the probe. Between the streamwise and transverse components of velocity, the spectra from u component is seen to be noisy, though selected peaks are clearly visible. In the present analysis, spectra have been calculated using transverse component of velocity at selected points on the wake of the cylinder. The Fast Fourier Transform (FFT) algorithm has been used to calculate the power spectra of the time series of the velocity. The number of data points for the present study is 2^{12} with a time step of 0.001 sec. This corresponds to a minimum frequency 0.244 Hz and maximum frequency of 1000 Hz with a frequency resolution of 0.244 Hz. All calculations are carried out for at least 20 cycles of the dominant frequency components. The measured power spectra have been non-dimensionalized by the total area under the curve; thus the area under the curve is unity. Figure 5.20 shows the power spectra of v-velocity in the near field (x=5) and the far field (x= 10 and 15). A clear spectral peak is observed for all cylinder orientations and the peak locations do correspond to the vortex

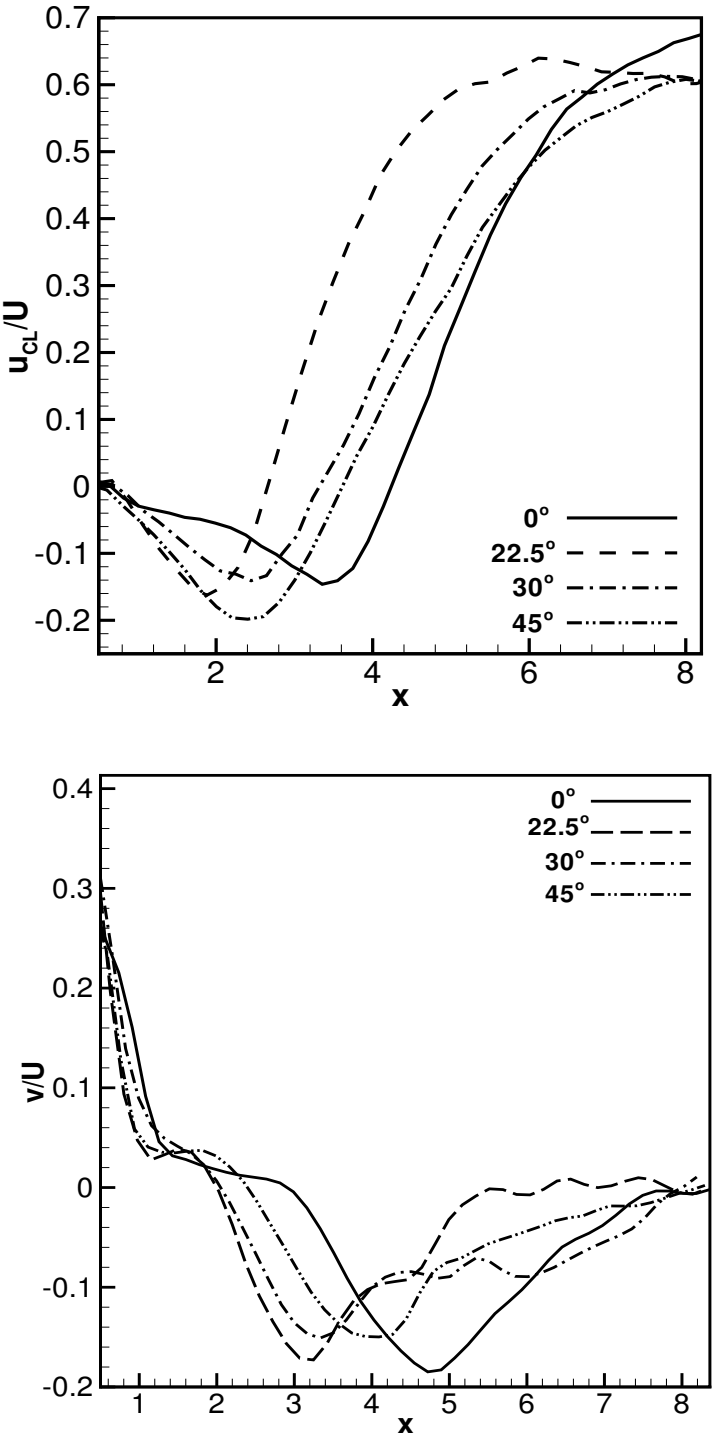

Figure 5.19: Centerline recovery of the streamwise (top) and transverse velocity (bottom) component for four cylinder orientations (0, 22.5, 30 and 45^o), aspect ratio=28 and Re=410.

shedding frequency. In the near field region, additional peaks at higher frequencies are seen though they disappear farther downstream (x=15). Additional peaks have also been observed by Dutta *et al.* [33] at comparatively higher Reynolds numbers (> 1000). Literature on low Reynolds number wakes shows the possibility of three dimensional temporal structure even in nominally two dimensional geometries (Williamson [179]). Thus it is likely that the energy cascade mechanism in the velocity fluctuations selectively energizes a few harmonics and the flow regime does not become turbulent in the classical sense. The appearance of these harmonics can be attributed to the nonlinear interaction among the shed Kárman vortices due to flow asymmetry. In the far-field region (x=15) the power spectra contain the fundamental; at higher frequencies, a negative slope of -5/3 was to be seen, corresponding to the inertial sub-range of fully developed turbulent flows.

5.1.10 Kinetic energy budget

There are similarities in laminar and turbulent wakes in the near field, since both are dominated by large scale structures, though the latter has fine-grained eddies as well. For these reasons, the kinetic energy of velocity fluctuations can be thought of as equivalent to that of turbulence. Against this background, the contributions of each terms of the turbulent kinetic energy equation have been examined. Here, a simplification being pursued is that the flow field is *stationary* in the near as well as far fields, in both laminar and turbulent contexts[7]. The kinetic energy budget quantities i.e. production, diffusion and dissipation along the streamwise direction at the cylinder centerline and an offset location (y=0.5) have been presented in Figure 5.21. These three quantities of the kinetic energy budget are strong function of cylinder orientation. All these three budget quantities are stronger in the near field region compared to the far field region. Among the three quantities, diffusion is most sensitive to cylinder orientation. The level of asymmetry in the maximum magnitude of diffusion is dependent on the cylinder orientation angle. The sign of diffusion reverses between the near field and far field region. The diffusion contribution is maximum for 22.5^o among all cylinder orientations. The higher value of diffusion for 22.5^o cylinder orientation is likely to be responsible for greater mixing at the immediate downstream of the cylinder and hence reduced drag at 22.5^o cylinder orientation angle. As the wake evolves with distance, it approaches equilibrium in the sense that production and dissipation terms become close to each

[7]Transitions and unsteady three dimensionality indicate departure from stationary behavior, but these factors are ignored for the present discussion.

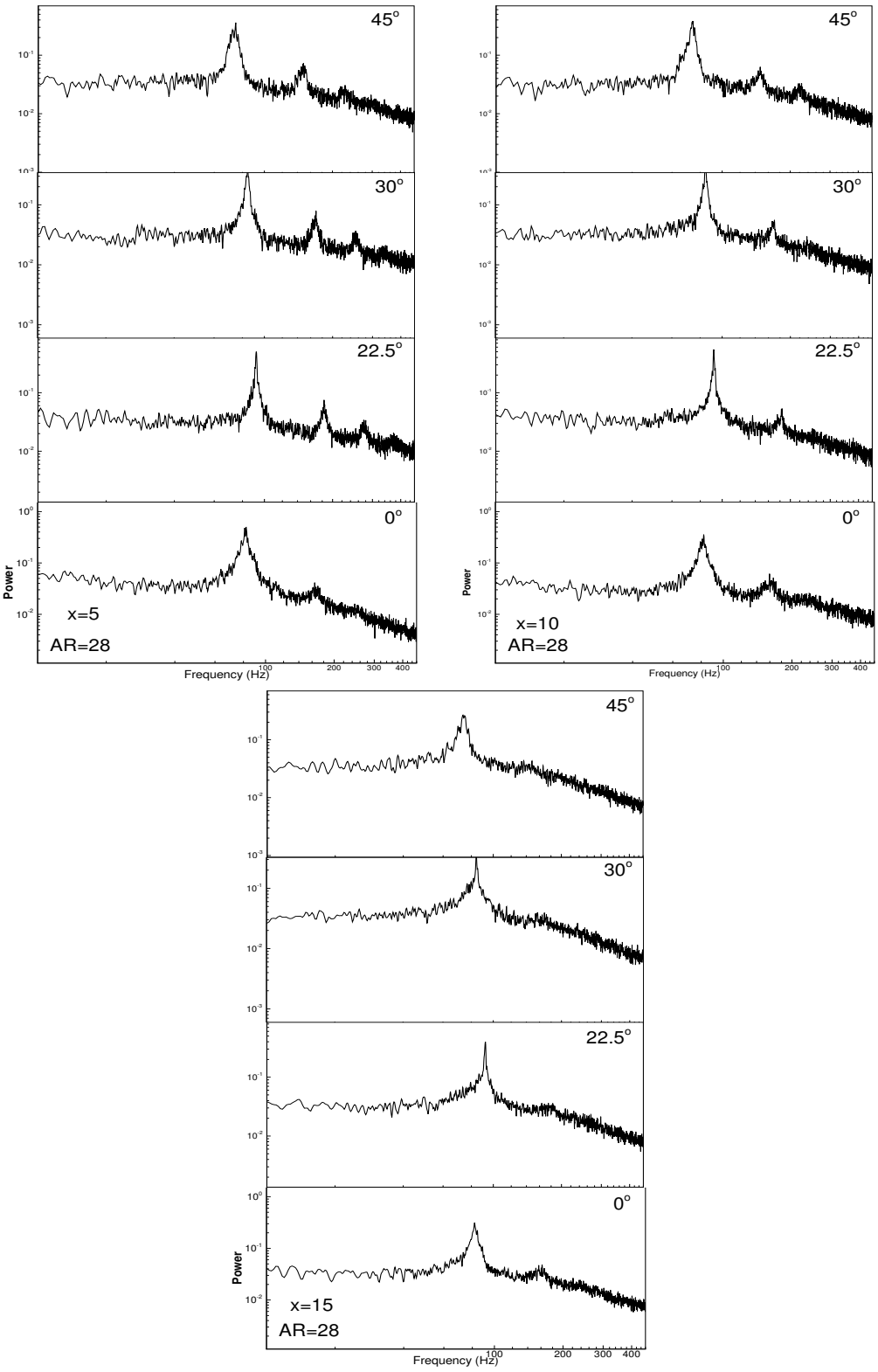

Figure 5.20: Power spectra of the v-component of velocity at Re=410 for four cylinder orientations (θ=0, 22.5, 30 and 45^o) at x=5, 10 and 15 and y=1.2.

other.

The turbulent budget quantities at an offset location (y=0.5) has been shown in Figure 5.21(b). The turbulent production profile shows dual peak i.e. a smaller peak in the near field region and a larger peak at a later streamwise location. The first peak is possibly due to the larger shear at the downstream cylinder corner and the second peak is because of the vortex shedding. The x-location of the turbulent production peak moves towards the cylinder with increase in cylinder orientation angle. In general the turbulent production has wider distribution for cylinder oriented to the mean flow compared to the zero orientation.

Figure 5.22 shows the contour plot of the production of turbulent kinetic energy of fluctuating velocities. The contour line shows that production of kinetic energy is most significant along the shear layer. It is in this location that energy from the time-mean flow is passed on to the fluctuating components by the mechanism of shear. The turbulent production contours shows greatest asymmetry i.e. the relative size in the transverse direction (y) of the opposite shear layer are different at 22.5^o cylinder orientation. This indicates greater interaction between the opposite shear layer i.e. better mixing in the wake. Figure 5.23 shows the contours of viscous dissipation of the kinetic energy of velocity fluctuations. Dissipation in the near wake is a very small in comparison to production. Dissipation leads to loss of turbulent kinetic energy and coincides with sites of large diffusion. The nature of dissipation contours is clearly a function of orientation angle. The asymmetry in the turbulent dissipation contours increases with cylinder orientation. Figure 5.24 shows the contours of the diffusion contribution. The shear layers on each side of the centerline are regions with a significant presence of diffusion. The turbulent diffusion contours move towards the cylinder due to cylinder orientation.

5.1.11 Flow visualization

Particle traces for different cylinder orientations (0, 22.5, 30 and 45^o) are shown in Figure 5.25. The interest here is in examining the possibility of shear layer re-attachment over the cylinder surface and the distance over which the separated shear layer rolls up. To examine these effects, the camera was held at a small inclination ($\simeq 3^o$) with respect to the cylinder axis. The images shown are instantaneous records. For angles of 0 and 45^o, flow separation is from the upstream corners of the cylinder. The separated shear layers diverge in the streamwise direction and the possibility of shear layer re-attachment is absent. At other angles (22.5 and 30^o), flow separation is asymmetric, with the shear

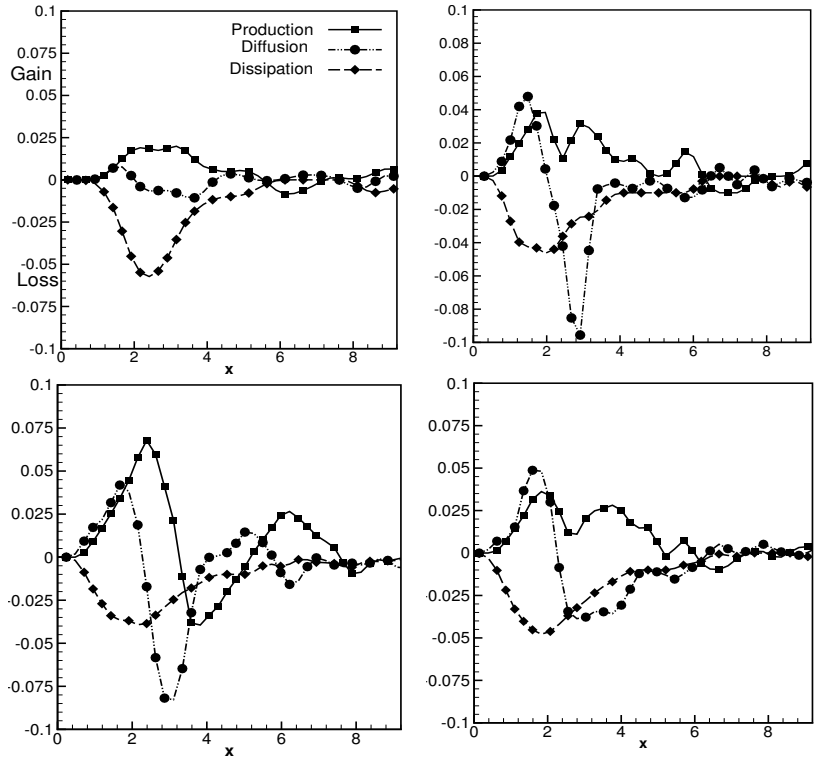

(a)

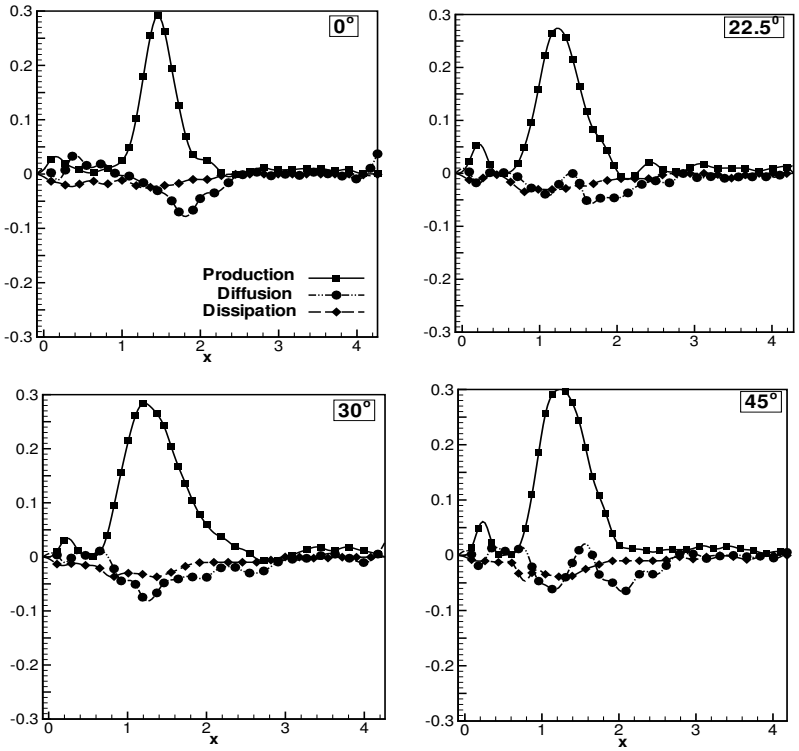

(b)

Figure 5.21: Streamwise variation of different terms of turbulent kinetic energy budgets (normalized by B/U^3) at y=0 and 0.5 for four cylinder orientations (θ=0, 22.5, 30 and 45^o), Re=410. (a) centerline and (b) offset location (y=0.5)

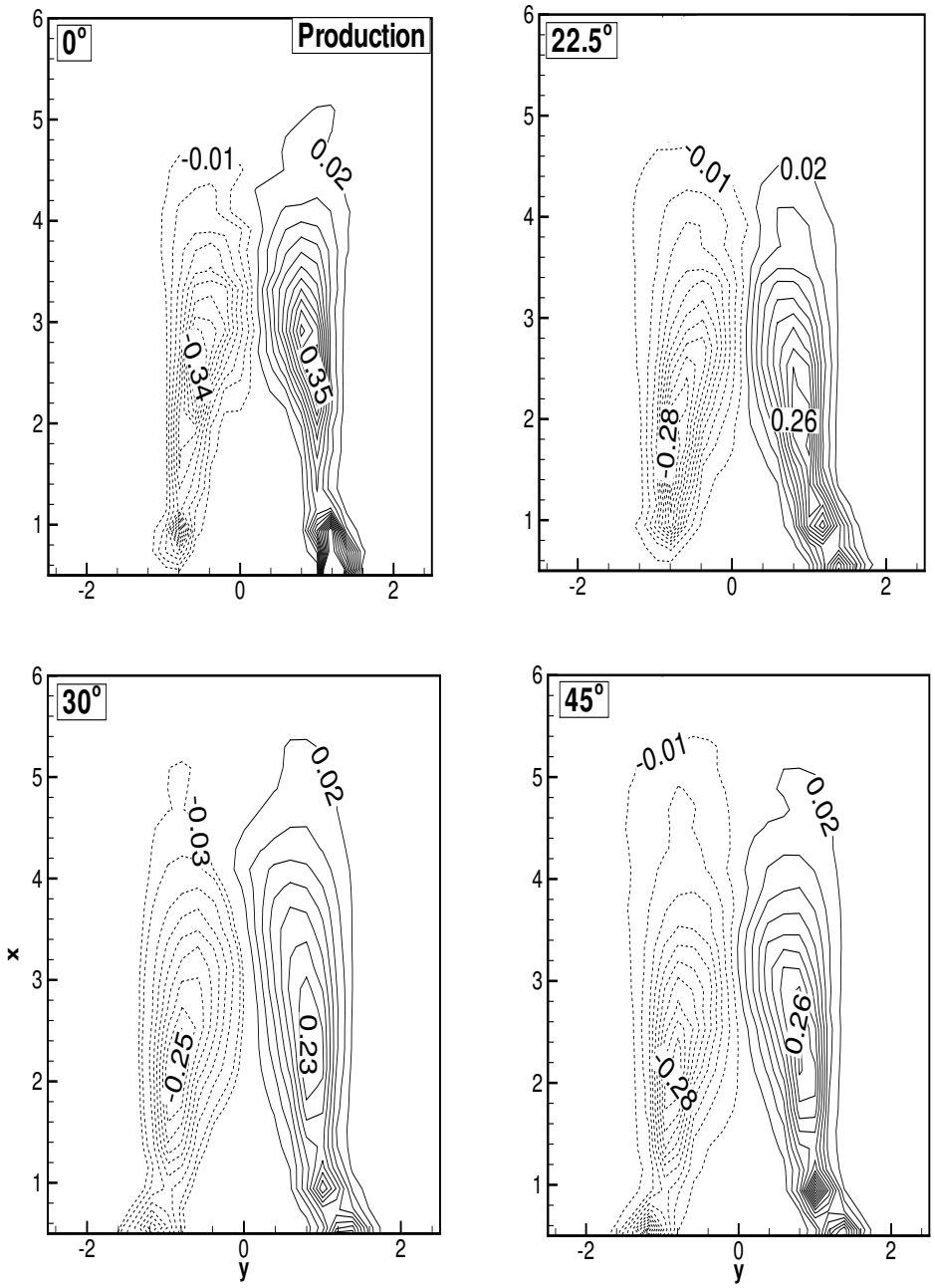

Figure 5.22: Contours of production of turbulent kinetic energy (normalized by B/U^3) for four cylinder orientations (θ= 0, 22.5, 30 and 45^o), Re=410, AR=28. Solid lines (min, max, incr)≡ 0.02, 0.4, 0.03; Broken lines (min, max, incr)≡ -0.4, -0.01, 0.02

.

layer from one side diverging away from the cylinder mid-plane. At the other side, the shear layer leaving a corner remains close to the cylinder surface that acts as an after-body. There are two asymmetric recirculation zones behind the two downstream edges

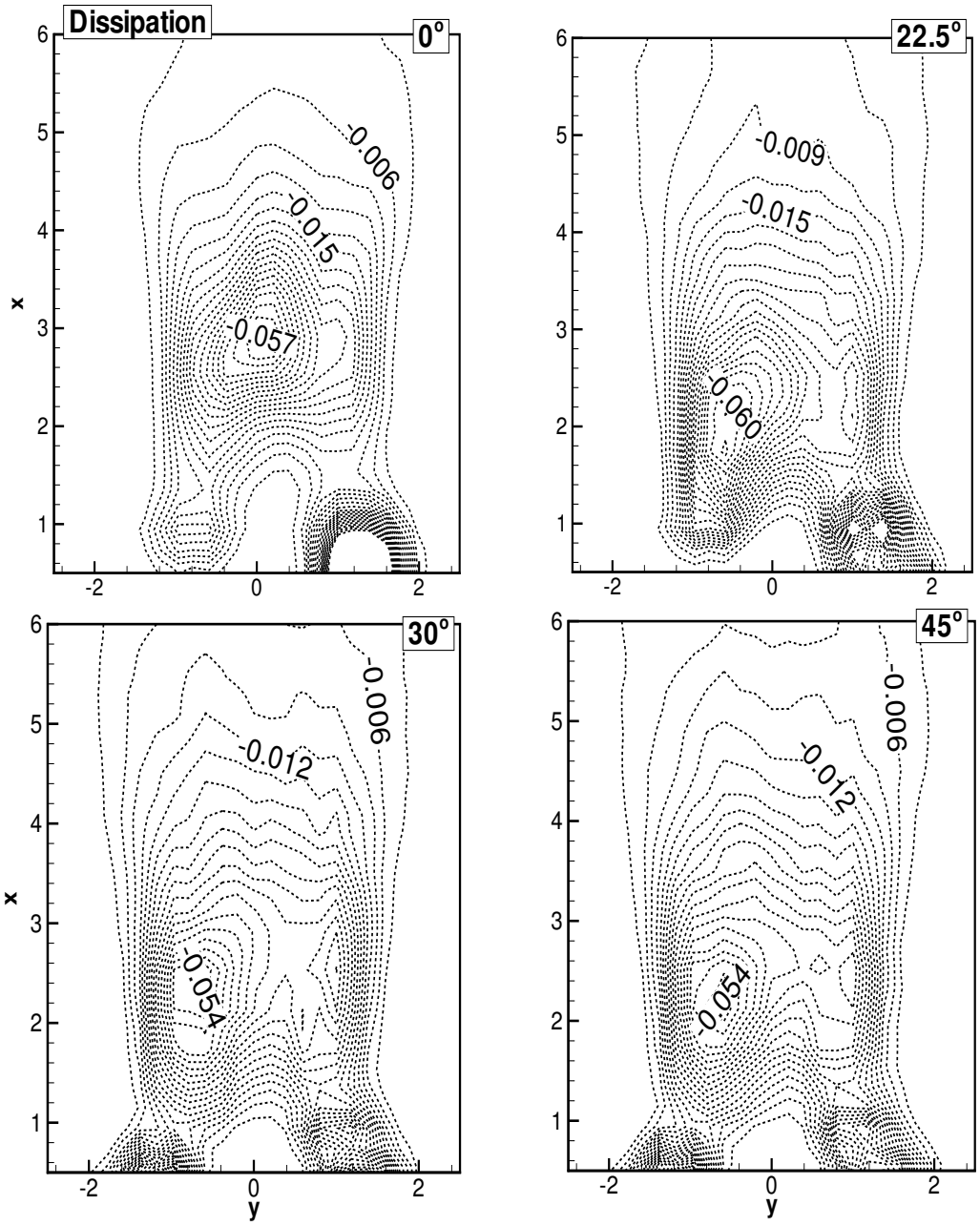

Figure 5.23: Contours of dissipation of turbulent kinetic energy (normalized by B/U^3) for four cylinder orientations (θ= 0, 22.5, 30 and 45^o), Re=410, AR=28. Max, min, incr $\equiv$ -0.06, -0.003, 0.003

.

of the cylinder. The shear layers do not allow an abrupt change in the slope of the path lines. It is hence to be concluded that experiments do not show re-attachment followed by separation at the second corner.

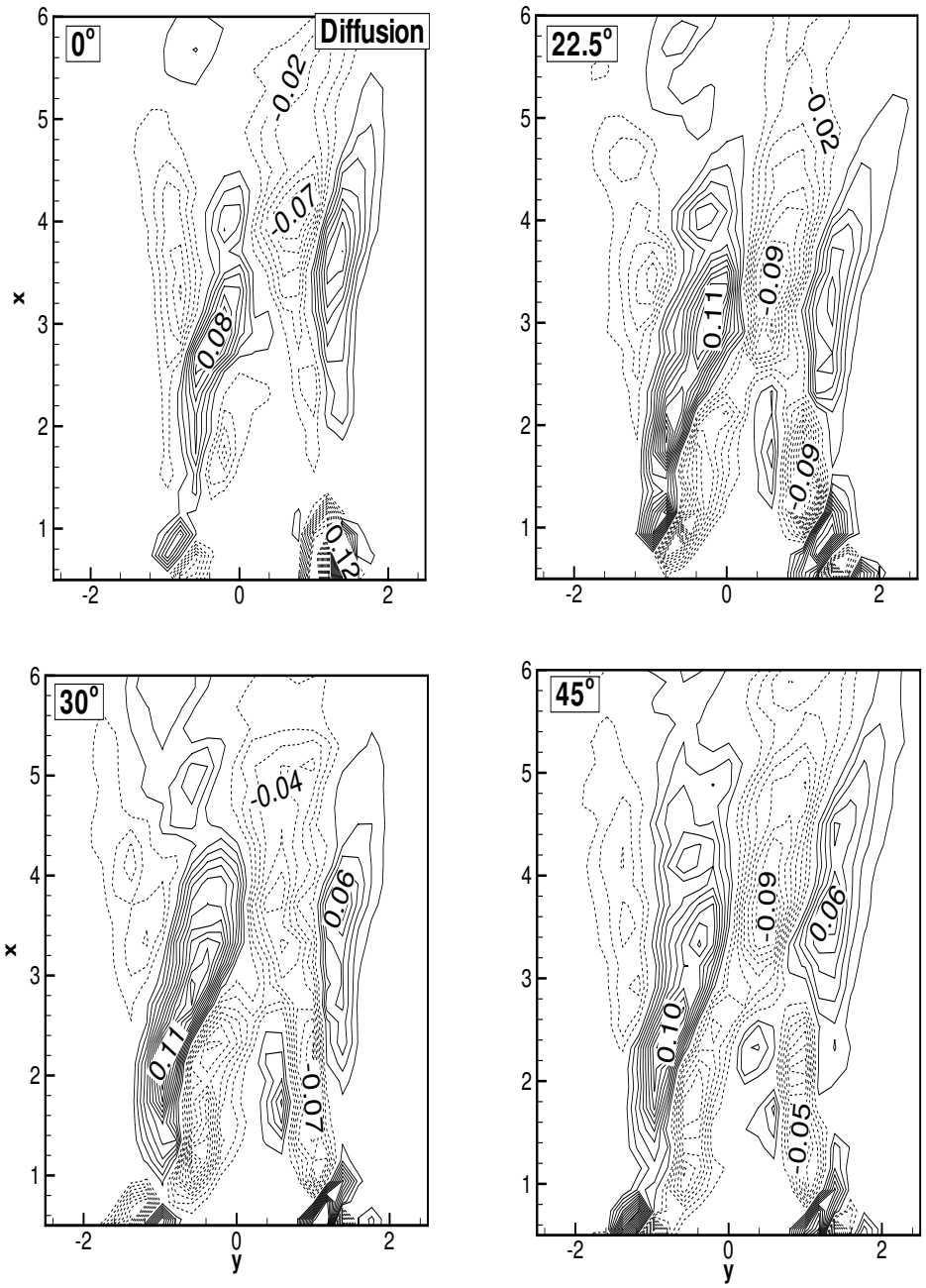

Figure 5.24: Contours of diffusion of turbulent kinetic energy for four cylinder orientations (θ= 0, 22.5, 30 and 45^o), Re=410, AR=28. Solid lines (min, max, incr)≡ 0.01, 0.12, 0.01; Broken lines (min, max, incr)≡ -0.12, -0.01, 0.01

.

The distance over which the shear layers roll up is a measure of the time taken for instability to set in, and hence inversely to Strouhal number. For 0 and 45^o, the shear layers on each side of the cylinder roll up over similar distances, and a well-defined

Strouhal number is obtained. At other orientations, the shear layers on each side are markedly different, and two vortex shedding frequencies are realized. It is also possible that the vortex shedding frequency corresponding to the vortex that rolls up over a shorter distance drives the unsteadiness in the wake. In this context, a single Strouhal number is once again realized. At other angles, the Strouhal number is determined by the vortex that rolls up over a shorter distance (though modulated by the second longer shear layer). This point has been clarified from the power spectra discussed in Section 5.1.9.

The flow visualization images of Figure 5.25 also explain the reduction in drag coefficient at certain angles. The drag coefficient is expected to increase continuously with angle due to increased blockage of flow. Simultaneously, the relatively longer shear layer formed at angles other than 0 and 45^o results in asymmetry of the wake, larger transverse velocities, better mixing and hence a higher base pressure. The distance between the vortices contained in the opposed shear layers (Figure 5.25) confirm this expectation. Thus, at an intermediate angle (22.5^o in the present study), a minimum in drag coefficient is realized. Figure 5.26 shows the flow visualization pictures behind the square cylinder in the x-z plane at different cylinder orientations for an aspect ratio of 28. The objective is to show the spanwise variation and hence the three dimensionality of flow behind the square cylinder. Mushroom type vortical pairs are seen in the visualization images. These structures are similar to those of Mode B seen behind a circular cylinder (Williamson [173]). However, these structures are comparatively irregular in the spanwise plane for the present study possibly due to a higher Reynolds number. The three dimensional vortex structures appear at streamwise x-locations that depend on the cylinder orientation. Three dimensionality shows up very close to the cylinder for an orientation equal to 22.5^o. The early appearance of three dimensionality may also be correlated to the minimum drag at this orientation. There is no spanwise variation in the onset of three dimensional flow structures for any of the cylinder orientations. This indicates parallel vortex shedding behind the square cylinder. The x-location at which three dimensionality first appears is related to the evolution of streamwise turbulent intensity. As discussed in the previous section, turbulence intensity peaks earlier at a cylinder angle of 22.5^o, correlating with three dimensionality and flow unsteadiness.

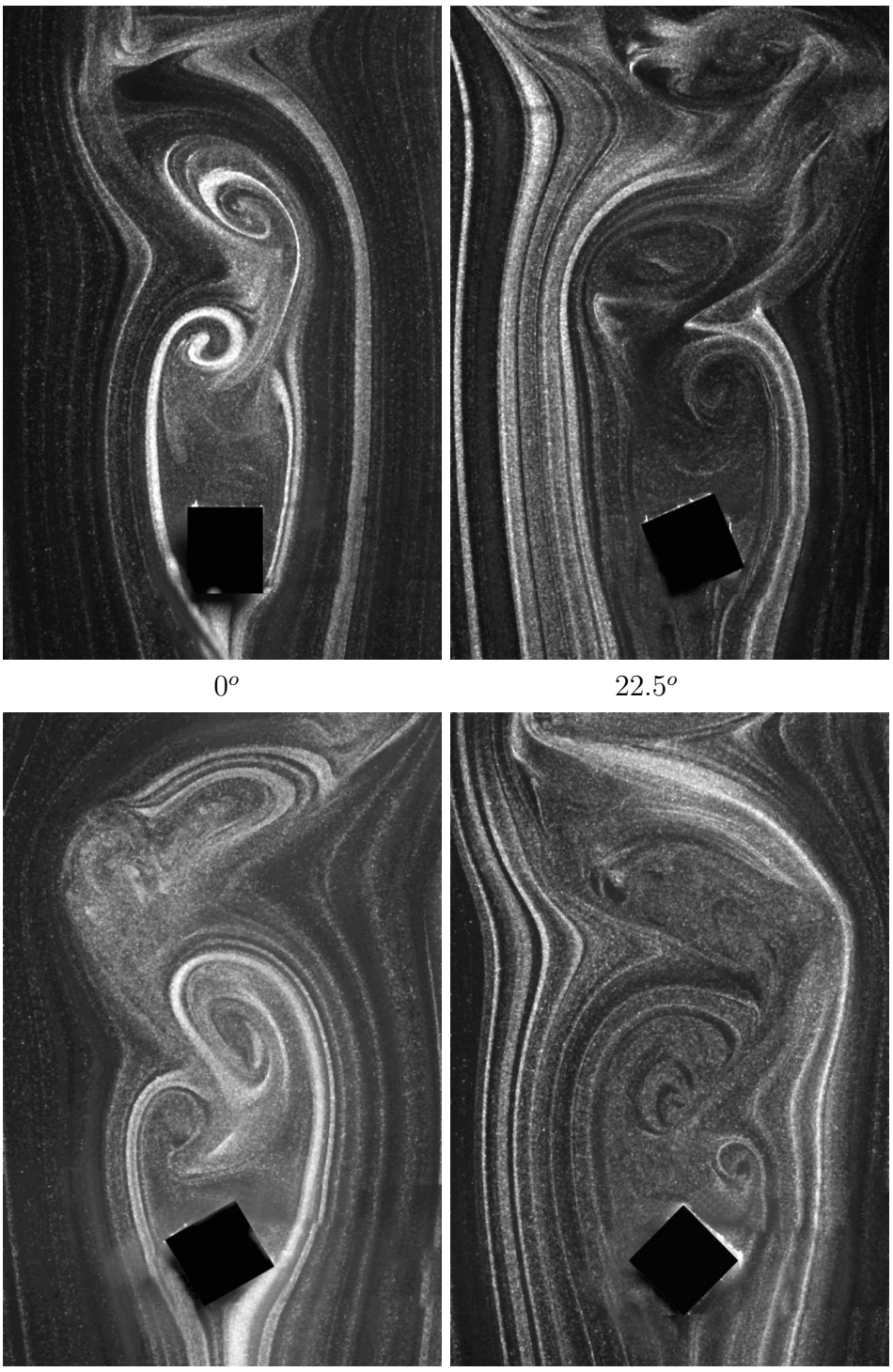

Figure 5.25: Near wake instantaneous particle traces behind the square cylinder for different orientations at Re=410, AR=28.

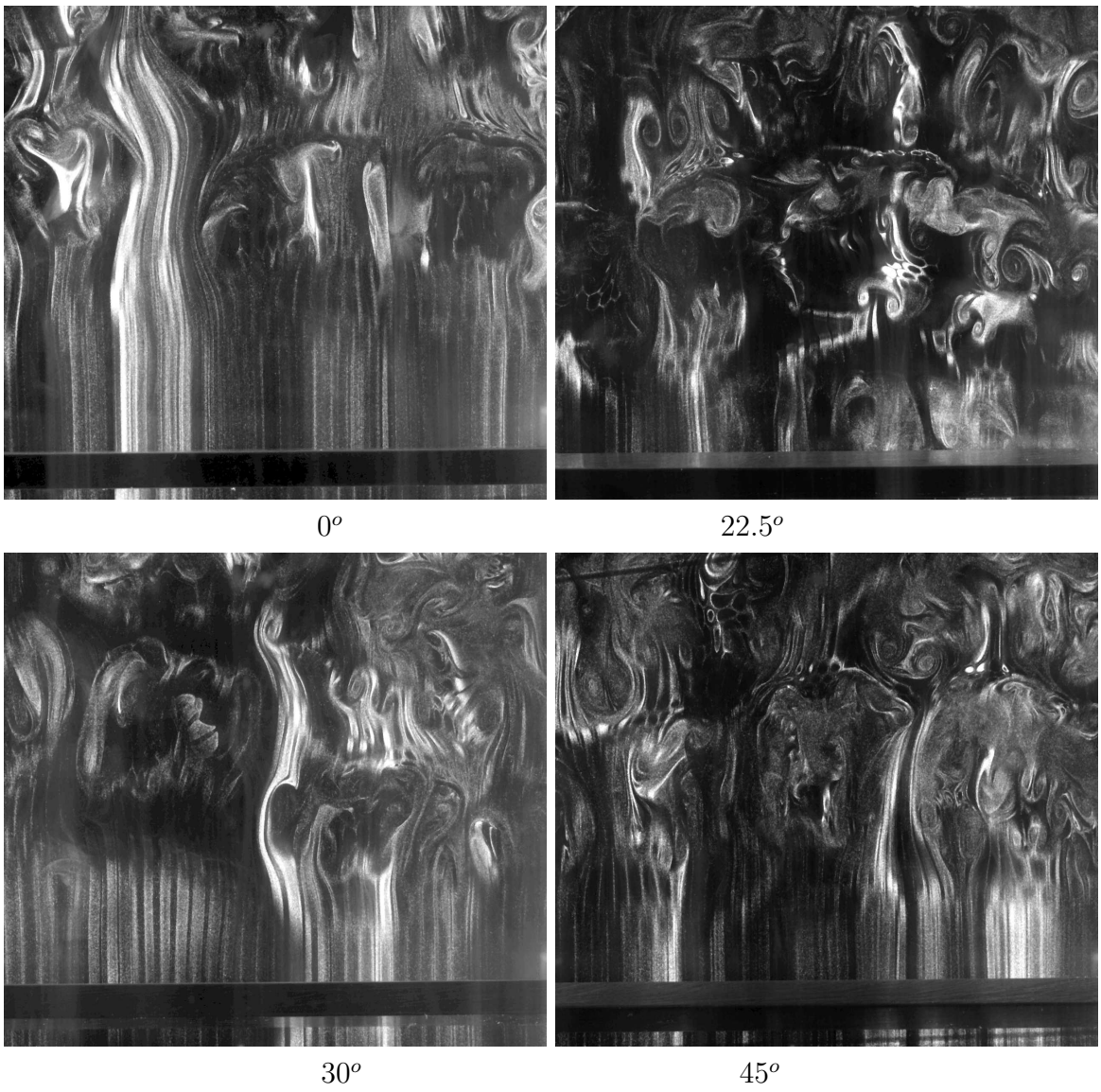

Figure 5.26: Spanwise near-field particle traces in the $x-z$ plane at y= 0.5 behind the square cylinder at different cylinder orientations at Re=410: AR=28.

5.1.12 Closure

A detailed study of the effect of cylinder orientation on flow parameters and flow structures is reported in the present section. Two Reynolds number (Re=410 and 610) and four cylinder orientations (θ=0, 22.5, 30 and 45^o) for an aspect ratio of 28 are considered. All flow characteristic parameters are seen to be affected by the cylinder orientation. A minimum in drag coefficient occurs at 22.5^o cylinder orientation. At this orientation the Strouhal number is a maximum. For orientations other than 0 and 45^o, the wake is

asymmetric. The v-velocity profile clearly brings out the wake asymmetry. The roll up of the shorter shear layer governs wake unsteadiness and hence Strouhal number. The loss of symmetry of the wake increases the transverse velocity, increases the base pressure and lowers the drag. This factor is counter-balanced by an increase in blockage itself, but the minimum in the drag coefficient at an orientation of 22.5^o reveals that the former has overall stronger influence at small cylinder angles. Stronger three dimensionality of the flow field at this angle additionally contributes to higher base pressure and lower drag.

5.2 Effect of Aspect Ratio

The present section considers the effect of aspect ratio on flow parameters and flow structures. Two aspect ratios, namely AR=16 and 28 have been considered. For a circular cylinder, the wave number of instability increases from about 4 diameters at onset to a level of about 6.7 diameters at higher Reynolds numbers (Re>300). The aspect ratio effects the influence of wall vortices on the development of the wake structures and three dimensionality. It is also important to know the influence of cylinder orientation as a function of aspect ratio. The detailed flow characteristics as a function of aspect ratio have been presented in the following sections.

5.2.1 Drag coefficient and Strouhal number

Figure 5.27 compares the present drag coefficient results with numerical simulation of Sohankar *et al.* [141]. The 3-plane average is lower than the mid-plane value, indicating that drag decreases along the length of the cylinder on each side of the mid-plane. The effect of aspect ratio on drag coefficient for different cylinder orientations is shown in Figure 5.2. A minimum in drag coefficient is observed at 22.5^o for both aspect ratios. The magnitude of drag coefficient is higher at the lower aspect ratio (AR = 16) compared to the higher (AR = 28). This trend is opposite to that of the Strouhal number (Figure 5.1), where the Strouhal number at the higher aspect ratio is also higher. A higher Strouhal number is an indication of the positive interaction between the opposed shear layers that feed the fluid to the growing vortex and cause early shedding. This increased interaction between the opposite shear layer also leads to weakening of the wake by increased mixing and therefore a reduction in the drag coefficient. The influence of aspect ratio on Strouhal number and drag coefficient can be partly explained in terms of the

strength of the secondary flow along the length of the cylinder. The secondary flow can be seen as a mechanism by which the overall pressure difference across the cylinder (and hence C_D) is reduced. Figure 5.2 shows that, for increasing aspect ratio, there would be a continuous reduction in the drag coefficient. Alternatively, the strength of the secondary flow would be a maximum. The corresponding trends in Strouhal number is expected to be different. Since interaction of shear layers is predominantly a two dimensional phenomenon, secondary flow does not alter Strouhal number and an asymptotic limit is reached for increasing aspect ratios. The Strouhal number increases with increasing aspect ratio (from 16 to 28) for all angles (Figure 5.1). The Strouhal number increases again from 0.124 to 0.145 for an increase in aspect ratio from 16 to 28 at 0^o orientation. There is, however, only a small difference in Strouhal number between AR = 28 to 60. Norberg [112] observed a jump in the Strouhal number from about 0.14 to 0.16 for a circular cylinder at an aspect ratio equal to 30. Lee and Budwig [86] observed a similar behavior of Strouhal number with respect to aspect ratio for a circular cylinder with a maximum in Strouhal number attained at about AR = 35. For subsequent increase in aspect ratio, no change in the Strouhal number value was observed. Among these studies, the differences in the Strouhal number realized and the critical aspect ratio[8] can be attributed to the differences in Reynolds number and the geometry of the bluff body. Overall, it can be concluded that the qualitative effect of aspect ratio on Strouhal number is similar for circular and square cylinders.

5.2.2 Time-averaged streamtraces

Figure 5.28 compares the time-averaged stream traces drawn in the wake of the square cylinder at a Reynolds number of 410. Two aspect ratios (16 and 28) have been considered. The size of the recirculation bubble in the streamwise as well as the transverse direction is greater for the low aspect ratio cylinder compared to the high. This result is seen at all cylinder orientations. The larger recirculation bubble at the lower aspect ratio indicates greater formation length of the vortex compared to the high aspect ratio cylinder. Similarly, the wake width is comparatively smaller for the high aspect ratio cylinder compared to that of the lower aspect ratio. The smaller recirculation bubble size and wake width for the high aspect ratio cylinder relates to the corresponding lower drag coefficient value in Figure 5.2. Figure 5.29 shows streamline patterns for a Reynolds number of 610. Among the four angles, the recirculation length is a minimum at 22.5^o at AR=16. The higher aspect ratio (AR=28) stream traces have been shown earlier in

[8] at which an asymptotic value of St is reached

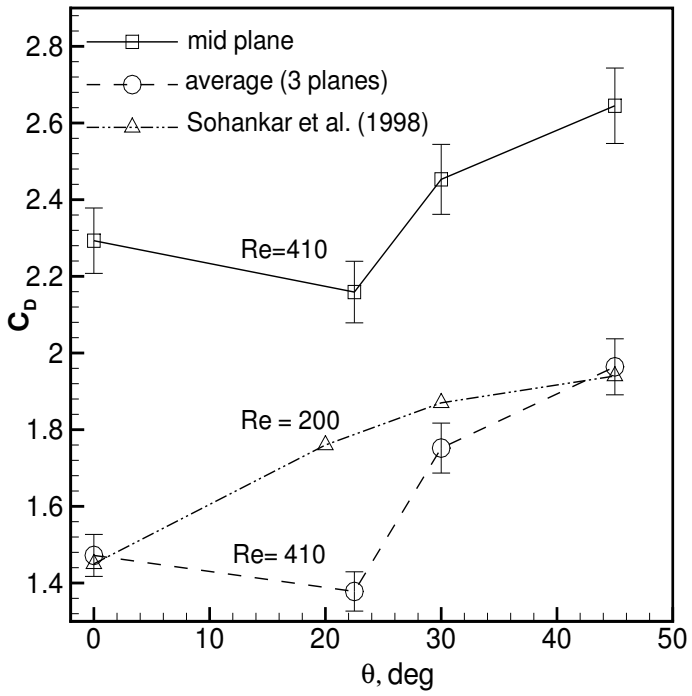

Figure 5.27: Variation of drag coefficient with incidence angle. The data of the present study is for the average of three planes along the cylinder length. The numerical simulation of Sohankar *et al.* (1998) reports an average over the cylinder length. (AR=16)

Figure 5.7. Two recirculation bubbles of opposite sense are seen for all angles. As in the experiment with Re=410, the streamlines show asymmetry for angles of 22.5 and 30^o. The extend of asymmetry is diminished at the higher Reynolds number. Contrast to Figure 5.7, definite recirculation patterns are observed in Figure 5.29. This indicate that the strength of unsteadiness is lower at lower aspect ratio and therefore converged recirculation bubble patterns is evident in Figure 5.29. The overall size of the recirculation bubble is higher at AR=16 for higher Reynolds number (Re=610). Similar trend is observed at lower Reynolds number i.e. Re=410.

The recirculation bubbles of Figure 5.28 demonstrate that flow is asymmetric when the orientation of the cylinder is 22.5 or 30^o. The separating streamlines on each side of the recirculation bubble are oriented at an angle with respect to the mean flow, indicating greater interaction between the two. The core location and transverse extent of the recirculation bubbles are different for these cylinder orientations. The effect is clearly evident for the higher aspect ratio when compared to the lower. A joint examination of Figure 5.2 and Figure 5.28 shows the following:

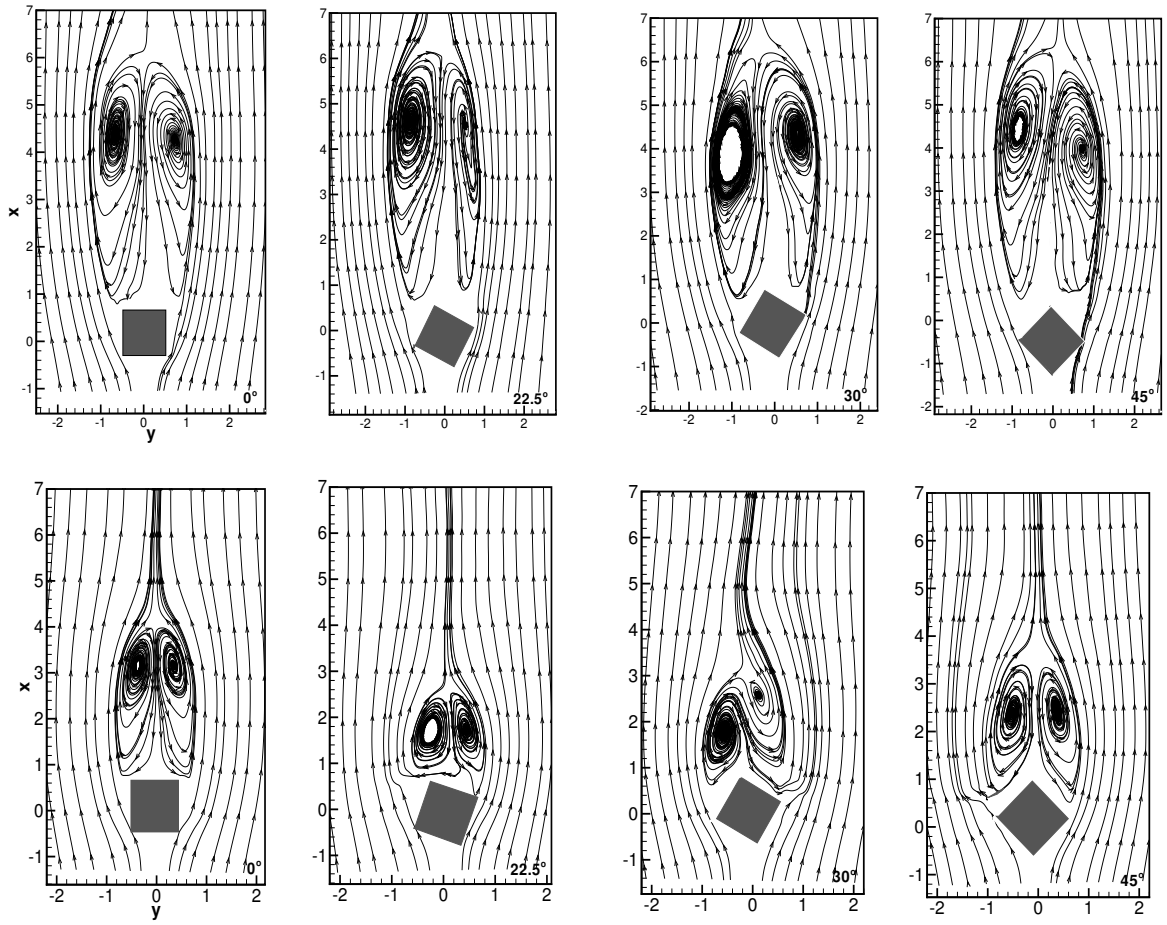

Figure 5.28: Time-averaged streamline contours in the wake of a square cylinder at Re=410; Influence of cylinder orientation. First row, AR=16 and second row, AR=28.

1. At a lower aspect ratio, the size of the recirculation bubble is higher and the drag coefficient[9] is also higher.

2. At a higher aspect ratio, the size of the recirculation bubble is lower and the drag coefficient is also lower.

5.2.3 Time-averaged velocity

Profiles of time-averaged u and v-velocity are compared in Figure 5.30 for four incidence angles (0, 22.5, 30 and 45^o) and two aspect ratios (AR = 16 and 28). The comparison is presented for four downstream locations (x = 2, 4, 6, and 8). Figure 5.30 shows

[9]the present discussion being restricted to the mid-plane

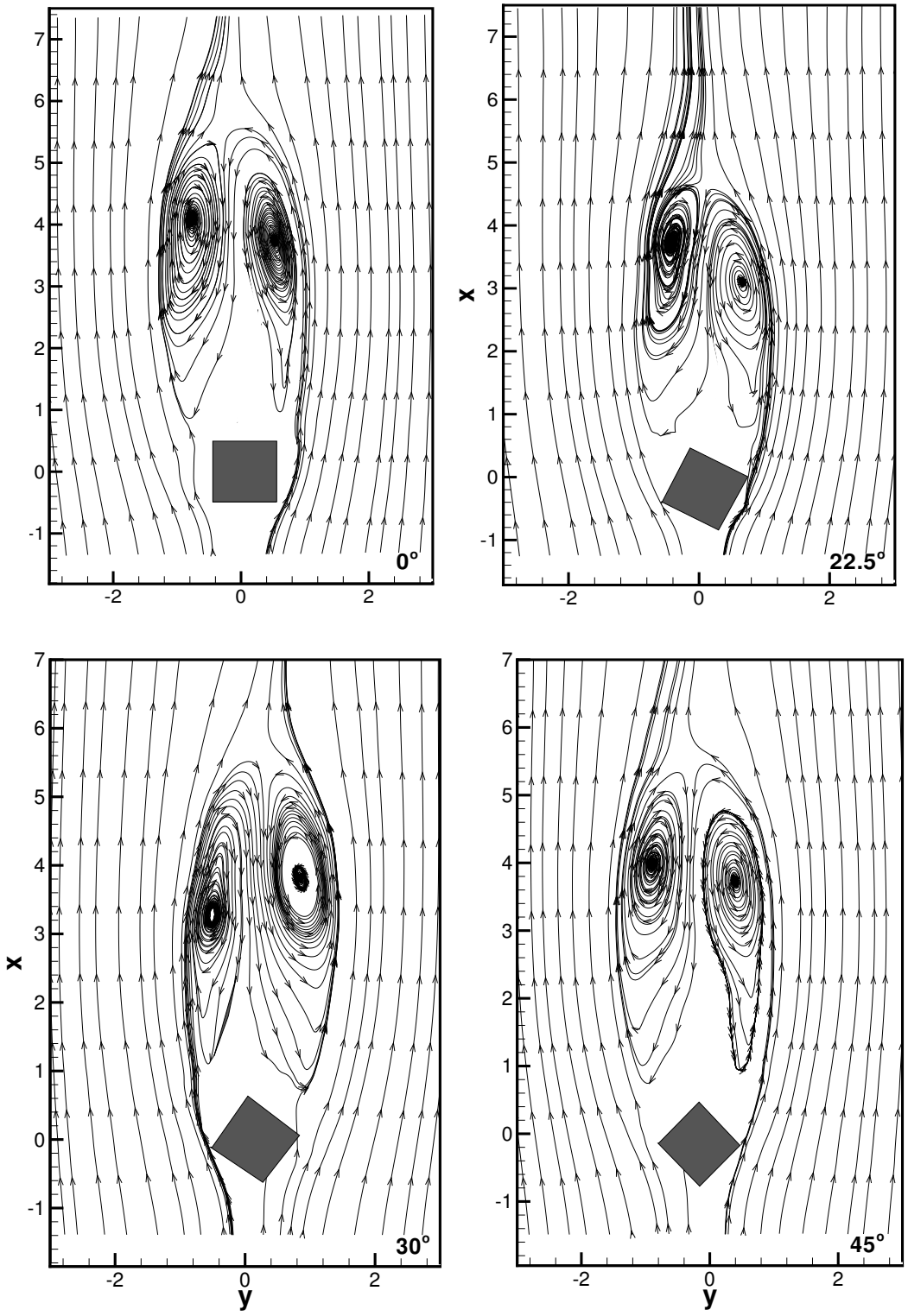

Figure 5.29: Time-averaged streamline contours in the wake of a square cylinder at Re=610. AR=16

that the u- and v-velocity profiles have a strong dependence on aspect ratio. For the streamwise velocity, recovery is much faster for the higher aspect ratio cylinder when compared to the lower. When the aspect ratio is high, the initial recovery of streamwise velocity is faster when compared to the low aspect ratio. This is related to the size of the recirculation bubble in the streamwise direction and its position on the x-z mid-plane. The u-velocity profile at 22.5^o orientation shows minimal velocity deficit compared to other cylinder angles for aspect ratio AR=16. For AR=28, there is not much change in u-velocity at downstream location x=8 but the wake width is smaller at 22.5^o which is responsible for minimum in drag coefficient at this angle. This trend is in conformity with the lowest drag coefficient seen at this orientation (Figure 5.2). The streamwise velocity profile for the low aspect ratio cylinder continues to develop till the location of x=8. In contrast, the streamwise velocity profile at the high aspect ratio attain a self-similar profile at x=8 for the 22.5 and 30^o orientations.

Both positive and negative transverse velocities are seen above and below the mid-plane of the cylinder. Thus, fluid particles are entrained from each side into the wake. Compared to the streamwise velocity, the transverse v-velocity shows greater variation with respect to the incidence angle and aspect ratio. At x =2, the v-velocity profile shows similar variation for all incidence angles at AR = 16. This is because, x = 2 is a location well within the recirculation bubble for this aspect ratio and cylinder orientations. In contrast, the v-velocity profile shows significant variation as a function of incidence angle for the high aspect cylinder (AR = 28). This is because x=2 is a location upstream of the recirculation bubble at 0^o and downstream of the recirculation bubble at 22.5^o (Figure 5.30). Therefore, on an average, the direction of v-velocity at 22.5^o is opposite to that of 0^o. Similarly, the v-velocity at x=6 shows an opposite trend when compared to x=2 for AR = 16. Immediately upstream of the core of the recirculation bubble, the v-velocity profile shows dual peaks at the x = 4 location for all incidence angles and AR = 16. Similar dual peaks are observed at x=2 and $\theta = 45^o$ for the high aspect ratio cylinder (AR = 28). This is due to the rapid change in streamwise velocity near the core location. The v-velocity profile is asymmetric for 22.5 and 30^o orientations. Therefore, the local instability modes and their amplification rates are altered for these orientations of the square cylinder leading to the appearance of additional harmonics in the flow fluctuations. These are shown in the previous section 5.1.9 in the form of power spectra. These modes are not as clearly evident at a low aspect ratio (AR=16) due to an early influence of three dimensionality (Figure 5.51). The asymmetric separation process for 22.5 and 30^o incidence angles are clear from the v-velocity profile when compared to the u-velocity. At the end of the recirculation bubble, the transverse

velocity magnitudes reduce, leading to a slow but definite recovery of the streamwise velocity. Figure 5.31 shows time-averaged velocity vectors for four cylinder orientations at AR=16. A Reynolds number of 410 has been considered. Comparing with velocity vectors for the higher aspect ratio (AR=28) in Figure 5.3, a distinct change in wake size and recirculation bubble is observed[10] The wake region is clearly visible. Between 0 and 45^o, there is an increase in wake size, but the increase is not monotonic with angle. The larger wake size for lower aspect ratio is evident in Figure 5.31 from the relative magnitude of the velocity. The influence of aspect ratio is also seen to be different on the cylinder orientation i.e. significant effect is observed for 0^o orientation angle compared to other orientation angle due to change is aspect ratio.

5.2.4 Time-averaged vorticity

Figures 5.32 and 5.33 show contours of time averaged spanwise vorticity (ω_z) for an aspect ratio of 16 at Re=410 and 610 respectively. When compared to vorticity contours at the larger aspect ratio (Figure 5.8 and 5.9) the spreading in streamwise and transverse direction is seen to be higher at the lower aspect ratio. The transverse spread of the vortices generated at the corners of the cylinder determines the wake size and is controlled by two opposing factors. First is the lower average pressure within the wake. This is balanced by momentum transport normal to the main flow direction. The latter comprises viscous diffusion along with transport by the time-dependent transverse velocity. These factors lead to a smaller recirculation bubble for the higher aspect ratio cylinder. In a two dimensional context, the peak in the spanwise vorticity component correlates with the minimum in pressure in the near wake, and hence the drag coefficient. Based on Figure 5.2, higher spanwise vorticity is then to be expected for the lower aspect ratio cylinder. Figure 5.8 and Figure 5.32, however, show that vorticity magnitudes are quite similar at both aspect ratios. A possible explanation is the stronger three dimensionality of the flow field at the smaller aspect ratio, that in turns equalizes pressure in the spanwise direction and lowers peak spanwise vorticity values.

5.2.5 Power spectra

Figure 5.34 compares power spectra between aspect ratios of 16 and 28 at a downstream location of x=5. The shedding frequency is lower for AR=16 when compared to 28. It

[10] As discussed earlier, velocity vectors very close to the cylinder are not completely resolved owing to interference effects.

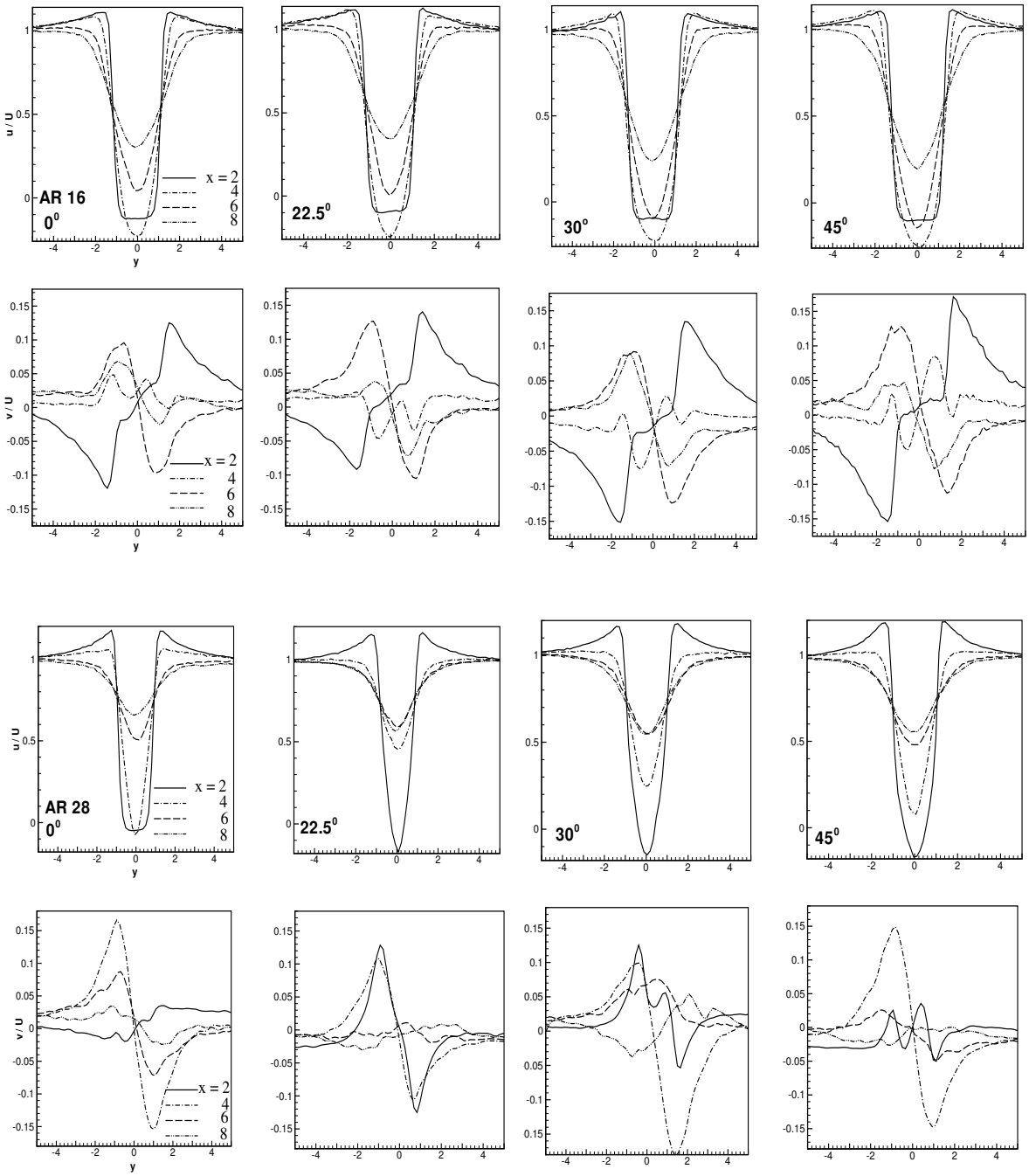

Figure 5.30: Time-averaged normalized u and v velocity profiles at four downstream locations (x= 2, 4, 6 and 8) for two aspect ratios (16 (top) and 28 (bottom)) and four cylinder orientations (0, 22.5, 30 and 45^o) at Re=410.

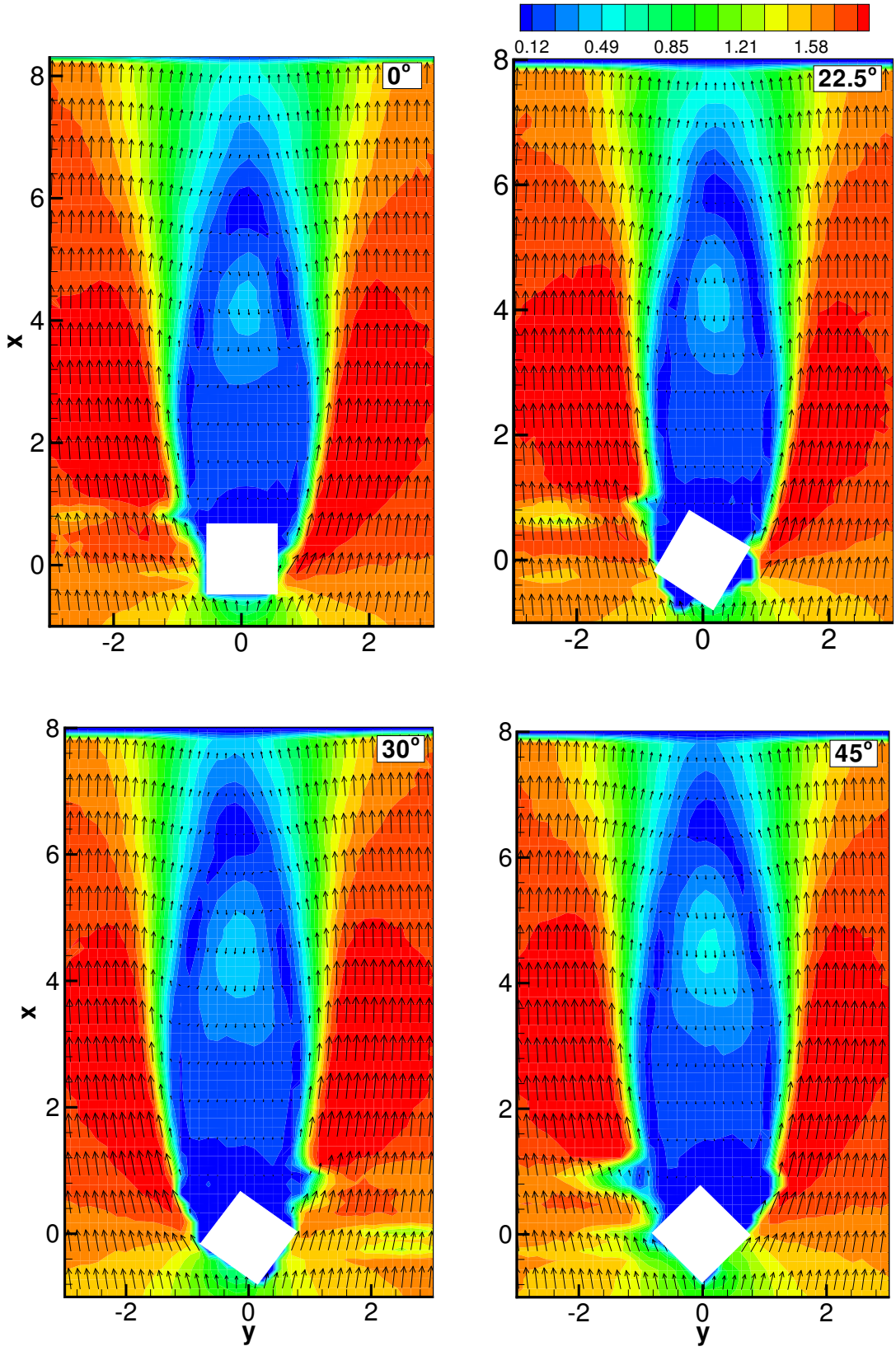

Figure 5.31: Time-averaged velocity vectors in the wake of a square cylinder at a Reynolds number of 410 and different cylinder orientations (θ= 0, 22.5, 30 and 45^o) for aspect ratio 16. The flooded contours represent the absolute velocity magnitude.

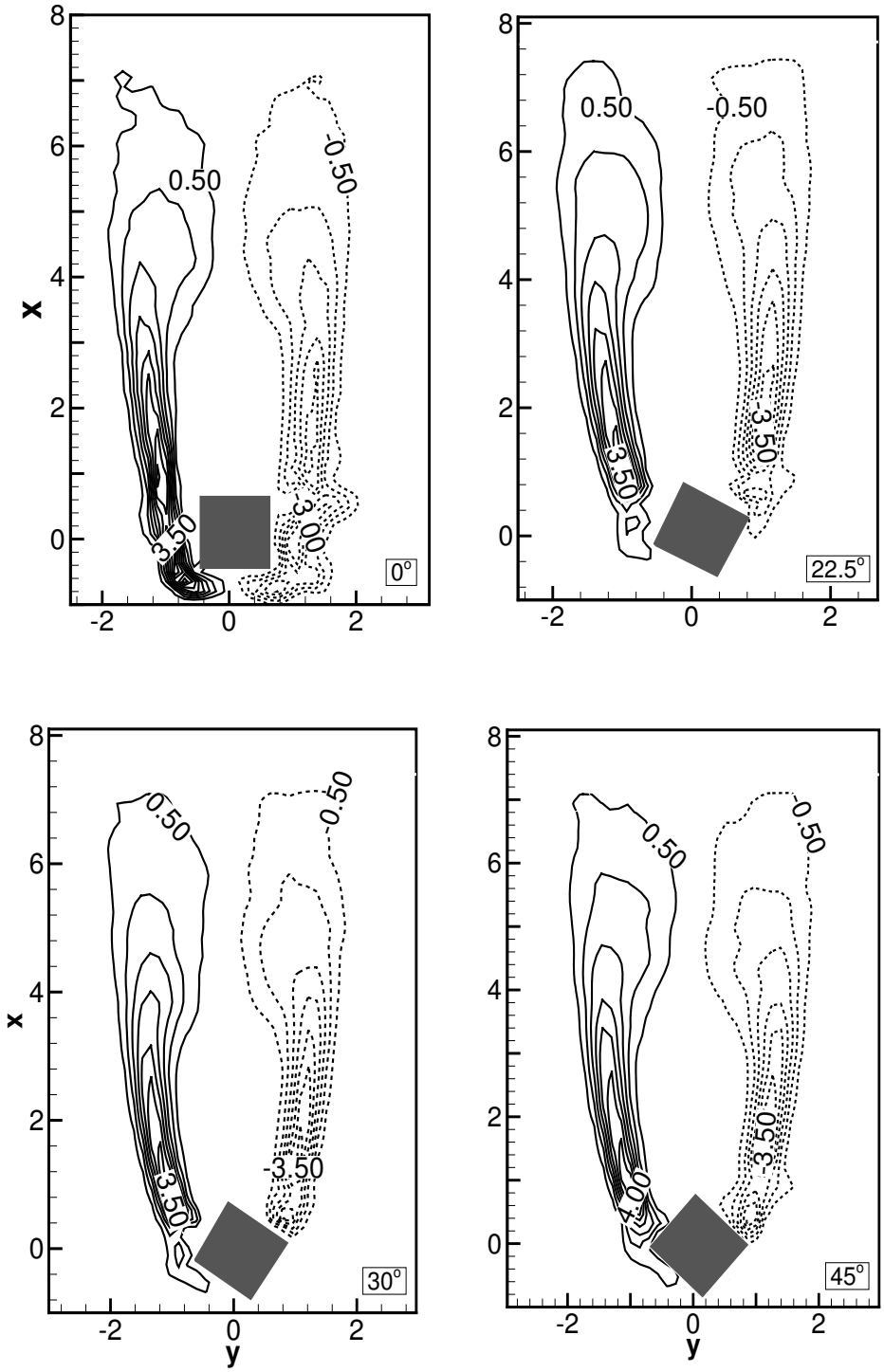

Figure 5.32: Time-averaged spanwise vorticity (ω_z) for four cylinder orientations at aspect ratio of 16, Re=410. Dashed lines show negative vorticity while solid lines represent positive vorticity, $\Delta\omega_z = 0.5$.

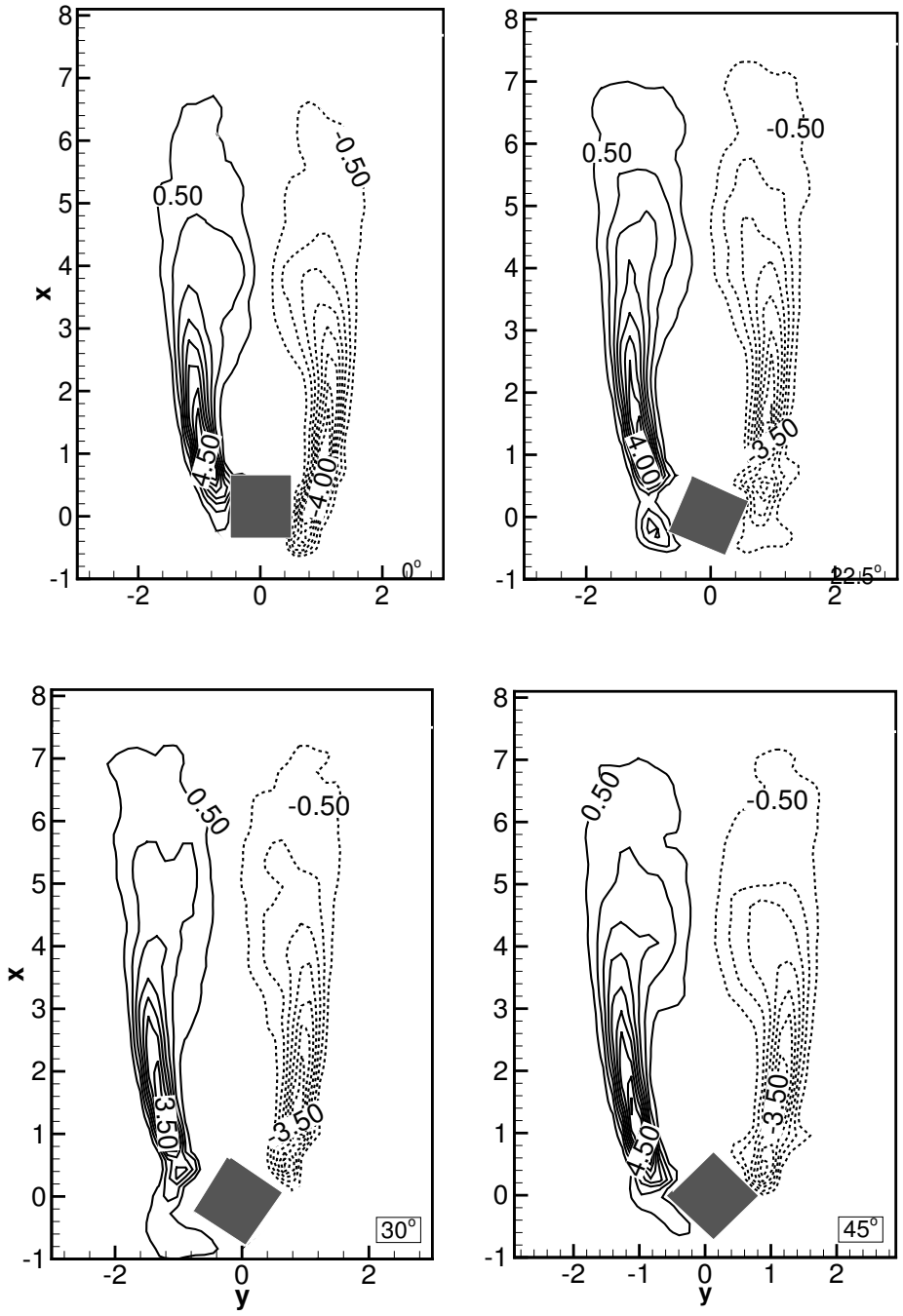

Figure 5.33: Time-averaged spanwise vorticity (ω_z) for four cylinder orientations at aspect ratio of 16, Re=610. Dashed lines show negative vorticity while solid lines represent positive vorticity, $\Delta\omega_z = 0.5$.

is according to the Strouhal number trend seen in Figure 5.1. The peak at the vortex shedding frequency is sharper for the high aspect ratio cylinder. The diminished strength at the low aspect ratio is due to a greater quasi-periodicity and jitter in the shedding pattern. The slope of the spectra in the inertial subrange is smaller for the high aspect ratio cylinder compared to the low[11] indicating an alternative route of energy transfer to dissipation.

In the near field region, a second peak is seen for AR=28 at all incidence angles equal to 22.5 and 30^o. The appearance of these harmonics can be attributed to the non-linear interaction between the K*á*rman vortices due to flow asymmetry at these angles. The structures of vortices, seen in the flow visualization pictures are different for low and high aspect ratio cylinders and support the additional harmonics of the power spectra. The separation distances between two consecutive shed vortices are different for the two aspect ratios. This result translates into differing frequency contents in the high aspect ratio experiment. The power spectra for higher aspect ratio is less noisy when compared to that of the lower aspect ratio in both near and far field regions. The spectra in the inertial subrange have a higher slope (closer to -5/3) for the lower aspect ratio. This is due to an early approach to three dimensionality of the flow field, and hence equilibrium. The complete set of spectra for the low aspect ratio cylinder is now presented. Figure 5.35, 5.36, 5.37, 5.38, 5.39, 5.40, 5.41 and 5.42 show the power spectra from both u and v-velocity for four cylinder orientations. Spectra based on u and v- velocities are shown, while two Reynolds numbers are considered. For all angles, power spectra based on v velocity show dominant peaks at all downstream locations. The peaks in the u-spectra diminish with downstream distance. All spectra follow nearly the $\frac{5}{3}$ law in inertial sub-range, a result commonly observed for fully developed turbulent flow. The negative $\frac{5}{3}$ line is shown in the graphs for comparison.

5.2.6 Velocity fluctuations

Figure 5.43 shows the total turbulence intensity field at different cylinder orientations and an aspect ratio of 16. The streamwise growth of the shear layer shows up in the figure with broadening of the high turbulence zones in the transverse direction. The turbulence intensity is higher for the larger aspect ratio cylinder (Figure 5.13) when compared to the low. A greater wall effect along with early onset of three dimensionality for the low aspect ratio cylinder is responsible for damping the turbulent fluctuations. In

[11] both being smaller than negative 5/3

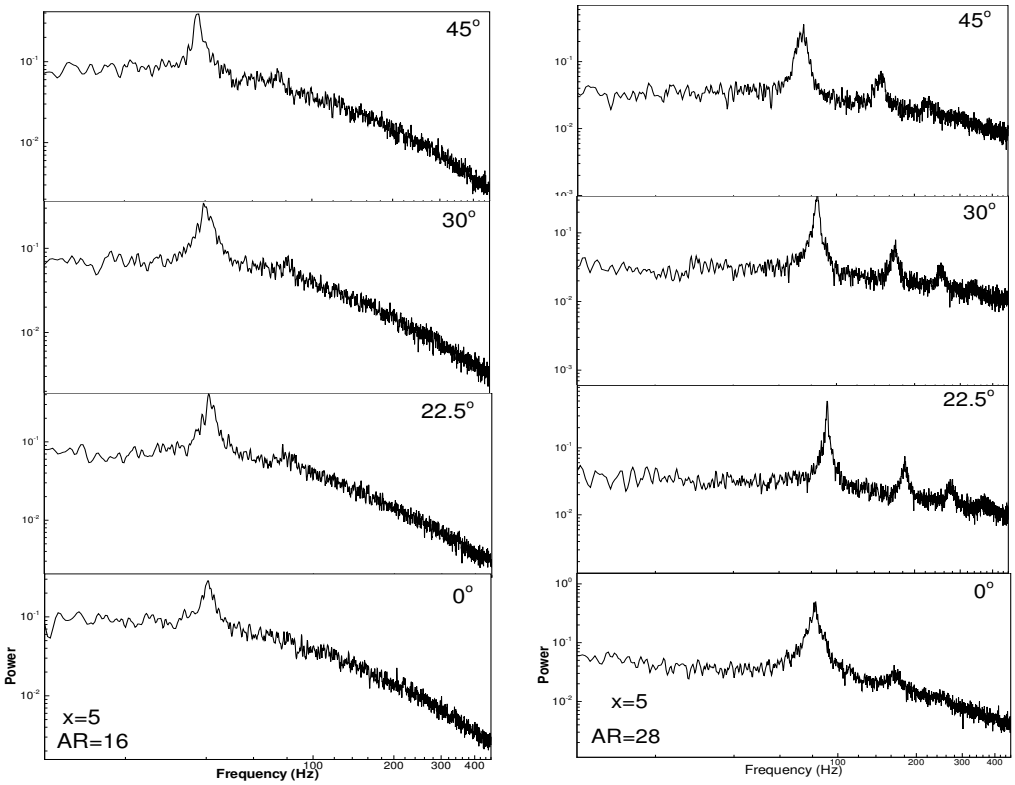

Figure 5.34: Power spectra comparison of v-velocity for two aspect ratios, AR=16 (left) and AR=28 (right) at x=5, y=1.2 and Re=410.

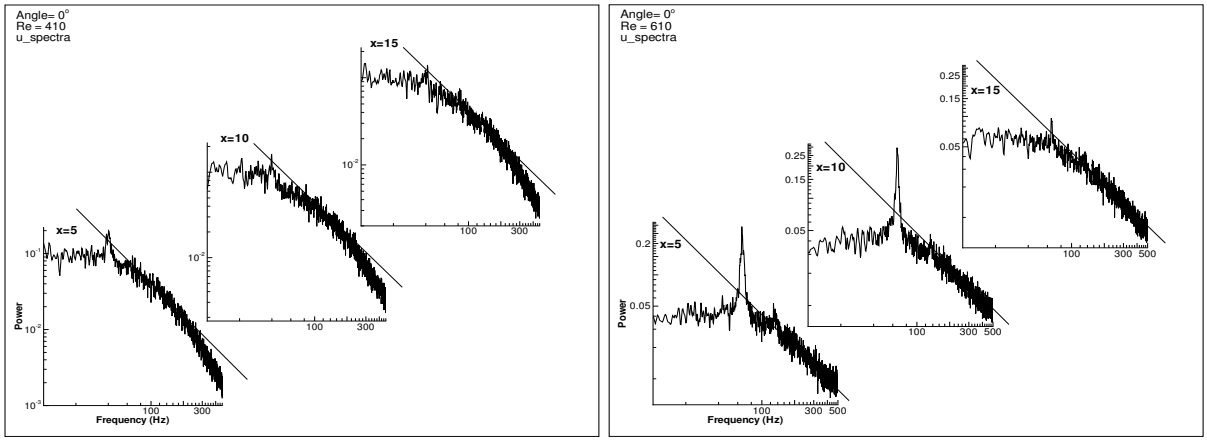

Figure 5.35: Power spectra based on u-component of velocity at x=5, 10 and 15 and y=1.2 for two Reynolds number (Re=410 and 610), AR=16 and Angle= 0^o.

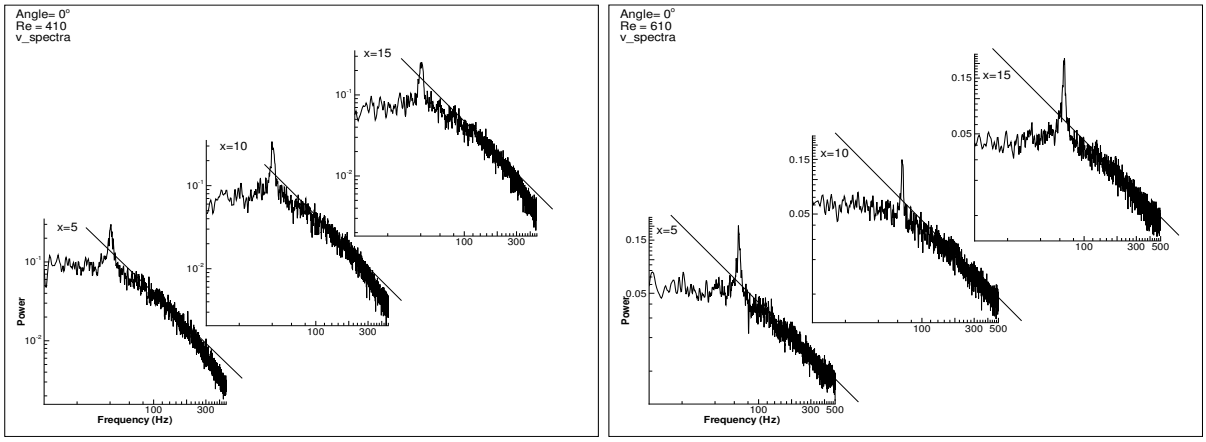

Figure 5.36: Power spectra based on v-component of velocity at x=5, 10 and 15 and y=1.2 for two Reynolds number (Re=410 and 610), AR=16 and Angle= 0^o.

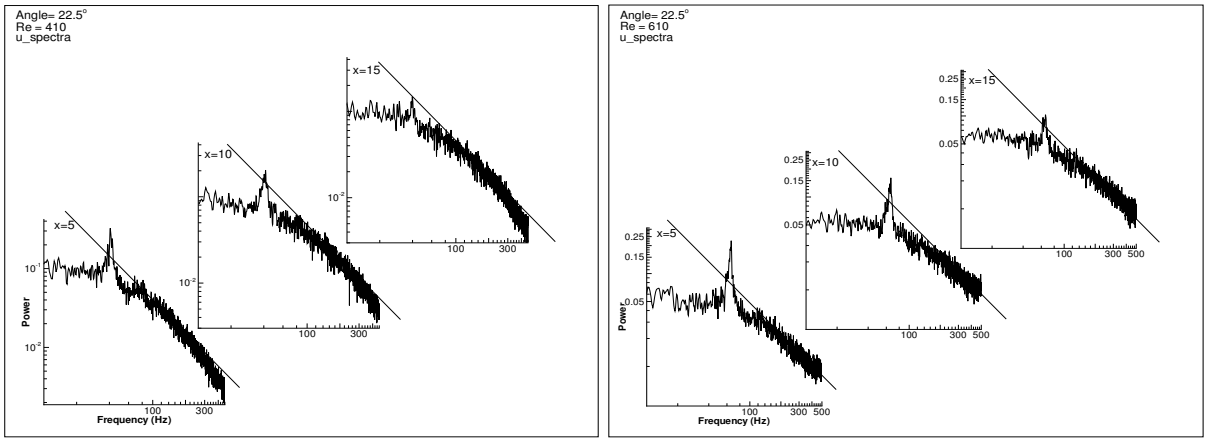

Figure 5.37: Power spectra based on u-component of velocity at x=5, 10 and 15 and y=1.2 for two Reynolds number (Re=410 and 610), AR=16 and Angle= 22.5^o.

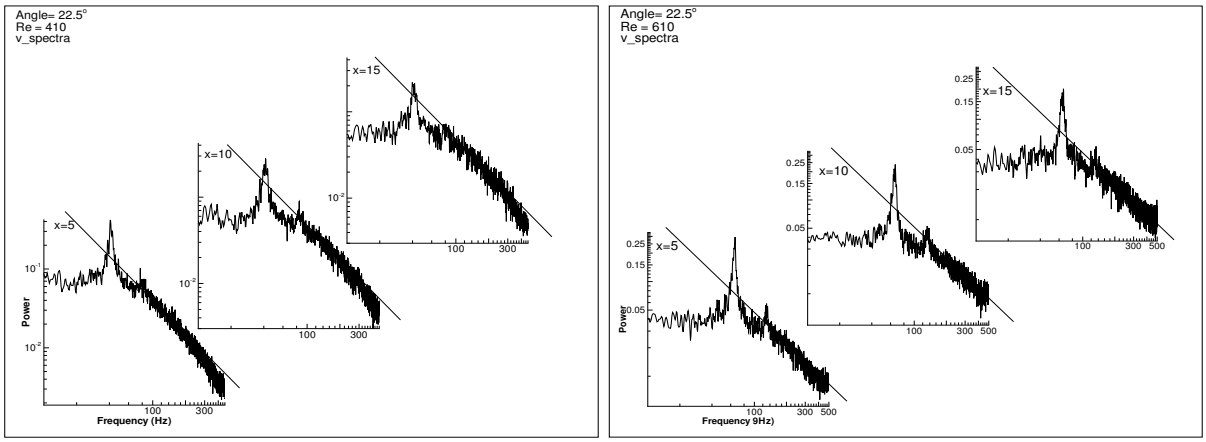

Figure 5.38: Power spectra based on v-component of velocity at x=5, 10 and 15 and y=1.2 for two Reynolds number (Re=410 and 610), AR=16 and Angle= 22.5^o.

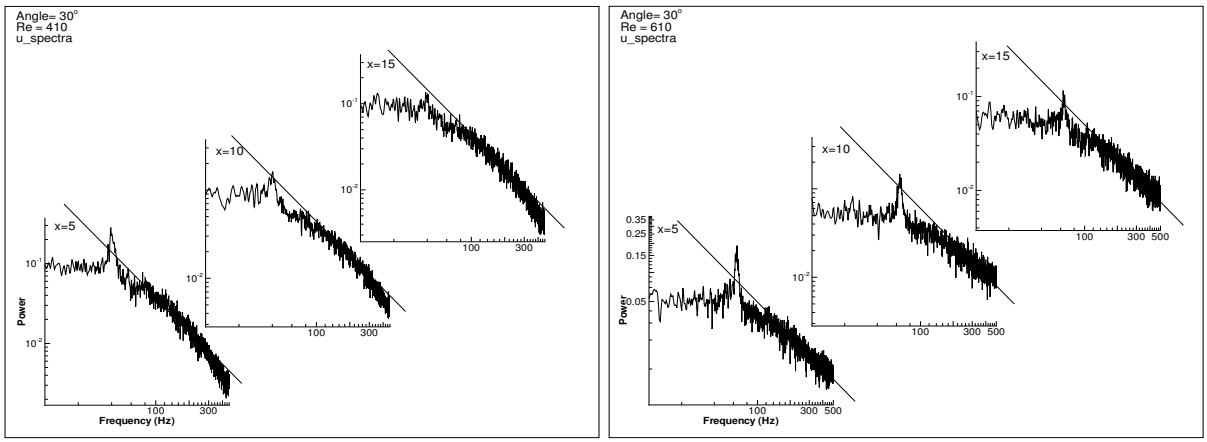

Figure 5.39: Power spectra based on u-component of velocity at x=5, 10 and 15 and y=1.2 for two Reynolds number (Re=410 and 610), AR=16 and Angle= 30^o.

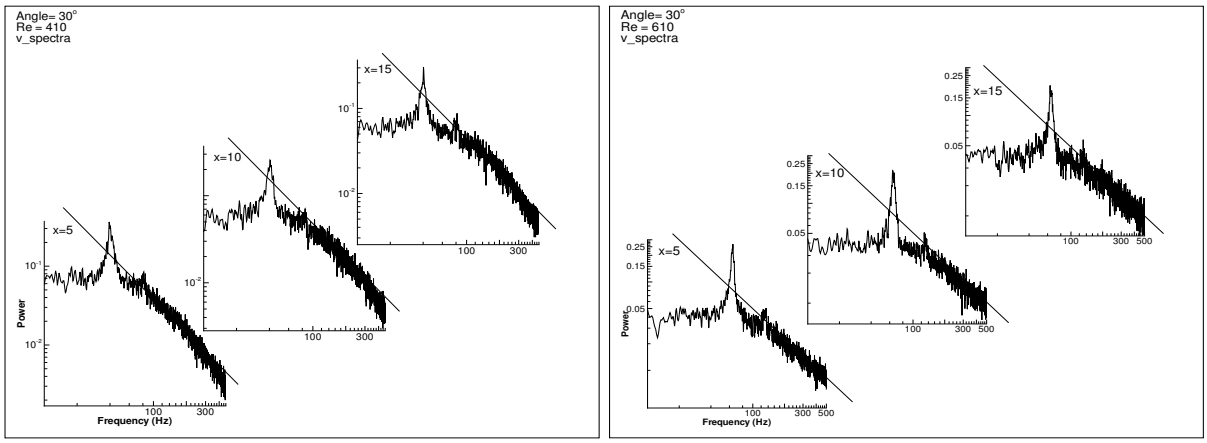

Figure 5.40: Power spectra based on v-component of velocity at x=5, 10 and 15 and y=1.2 for two Reynolds number (Re=410 and 610), AR=16 and Angle= 30^o.

addition, the turbulence production is higher for the large aspect ratio cylinder. This is because the smaller recirculation bubble leads to a higher velocity gradient in the shear layer. The consequence of these base flow patterns is of interest. Figure 5.43 shows that turbulence intensity increases both in the streamwise and transverse direction from the edge of the cylinder and midplane of the cylinder axis respectively with a subsequent drop after reaching a maximum value. The maximum turbulence intensity zone is located at a farther streamwise location for the low aspect ratio when compared to the high. This is in accordance with larger size of the recirculation bubble for the low aspect ratio cylinder (Figure 5.43).

Figure 5.44 compares the streamwise variation of the resultant velocity fluctuations at the central midplane ($y = 0$) for aspect ratios of 16 and 28 and various cylinder

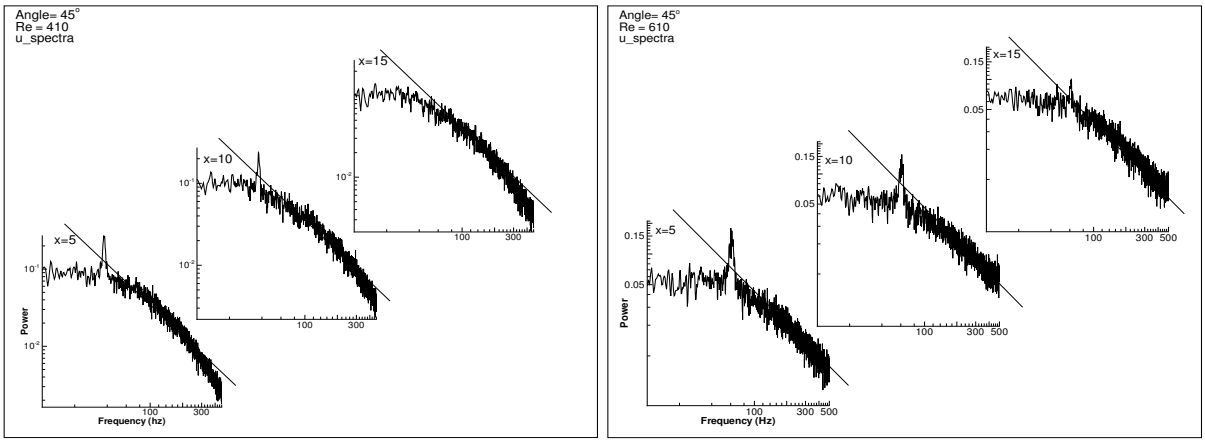

Figure 5.41: Power spectra based on u-component of velocity at x=5, 10 and 15 and y=1.2 for two Reynolds number (Re=410 and 610), AR=16 and Angle= 45^o.

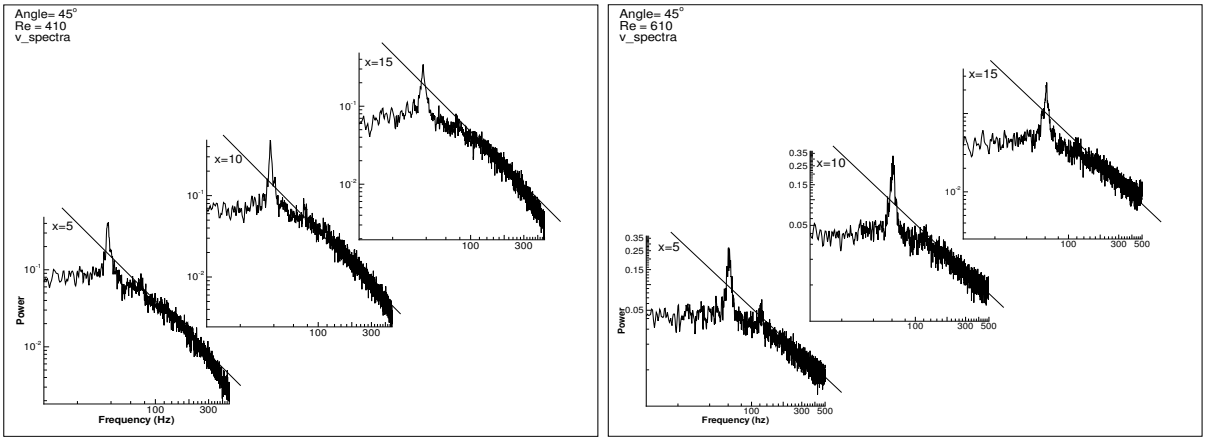

Figure 5.42: Power spectra based on v-component of velocity at x=5, 10 and 15 and y=1.2 for two Reynolds number (Re=410 and 610), AR=16 and Angle= 45^o.

orientations. The objective of this plot is to demonstrate differences in the formation length of the vortices. For both aspect ratios (AR=16 and 28), the turbulence intensity increases in the streamwise direction, reaches a maximum value and is followed by slow decay. The maximum turbulence intensity appears at a farther streamwise location for the lower aspect ratio cylinder when compared to the higher. No significant difference in the turbulence intensity between different incidence angles is observed in the near field region ($x < 2$) of the low aspect ratio cylinder. This is possibly due to an early appearance of three dimensionality in the base flow. However, the maximum turbulent intensity continues to be observed slightly earlier for the asymmetric cases of 22.5 and 30^o when compared to the symmetric (0 and 45 ^{o}). Figure 5.45 shows the decay in RMS values of u and v-velocities for two aspect ratios and four cylinder angles. The decay in the RMS value of the u-component is faster for AR=28 when compared to AR=16. The

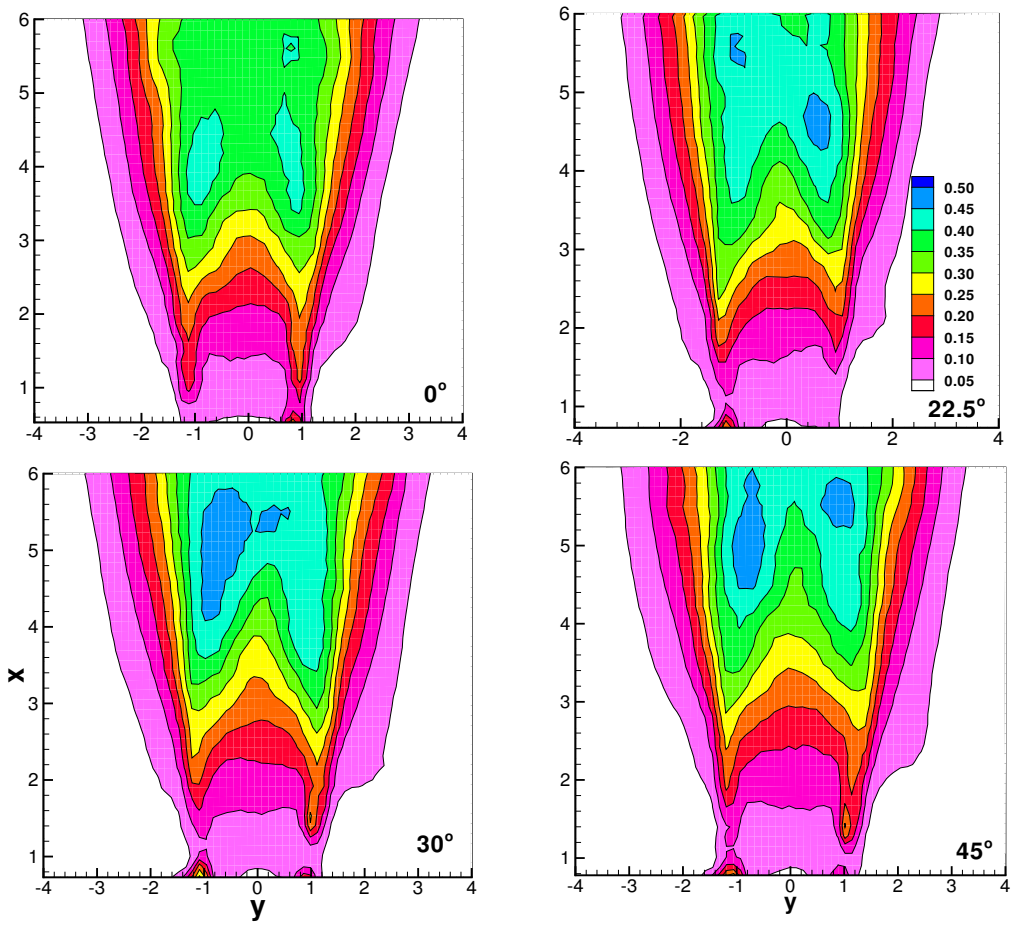

Figure 5.43: Contour plot of turbulence intensity $((u_{rms}^2 + v_{rms}^2)^{0.5}/U)$ in the wake of a square cylinder at a Reynolds number of 410 for aspect ratio 16 and four cylinder orientations.

magnitude of the RMS value of the v component is higher for AR=28 when compared to AR=16. Figure 5.46 shows the u_{rms} profiles for two Reynolds numbers at three downstream locations (x=5, 10 and 15). The profiles show some asymmetry for θ=22.5^o and 30^o in the near field region. Figure 5.47 shows the v_{rms} variation along downstream locations for Re=410 and 610. The v_{rms} profile shows the extent to which v_{rms} in the transverse direction is higher when compared to u_{rms}. Figure 5.48 shows the time-averaged turbulent shear stress distribution for two Reynolds number, namely 410 and 610. In both cases, the double-peaked curve shows that turbulence production is related to the shear layers emerging from the corners of the cylinder. A monotonic reduction of turbulence levels in the streamwise direction is characteristic of high Reynolds number wakes, as well.

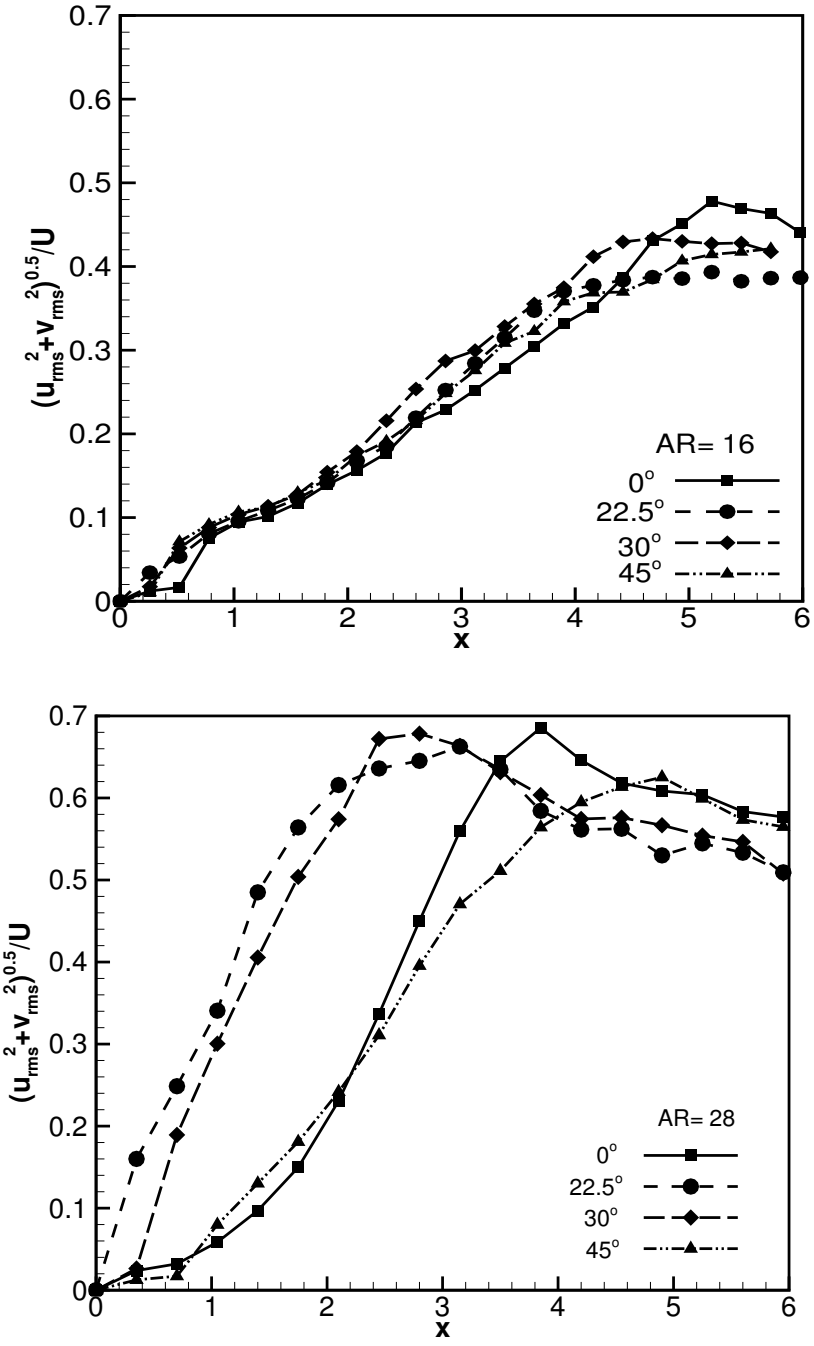

Figure 5.44: Turbulence intensity development in the streamwise direction along the cylinder centerline for different orientation angle (θ=0, 22.5, 30 and 45^o) of the cylinder; AR=16 (top) and AR=28 (bottom).

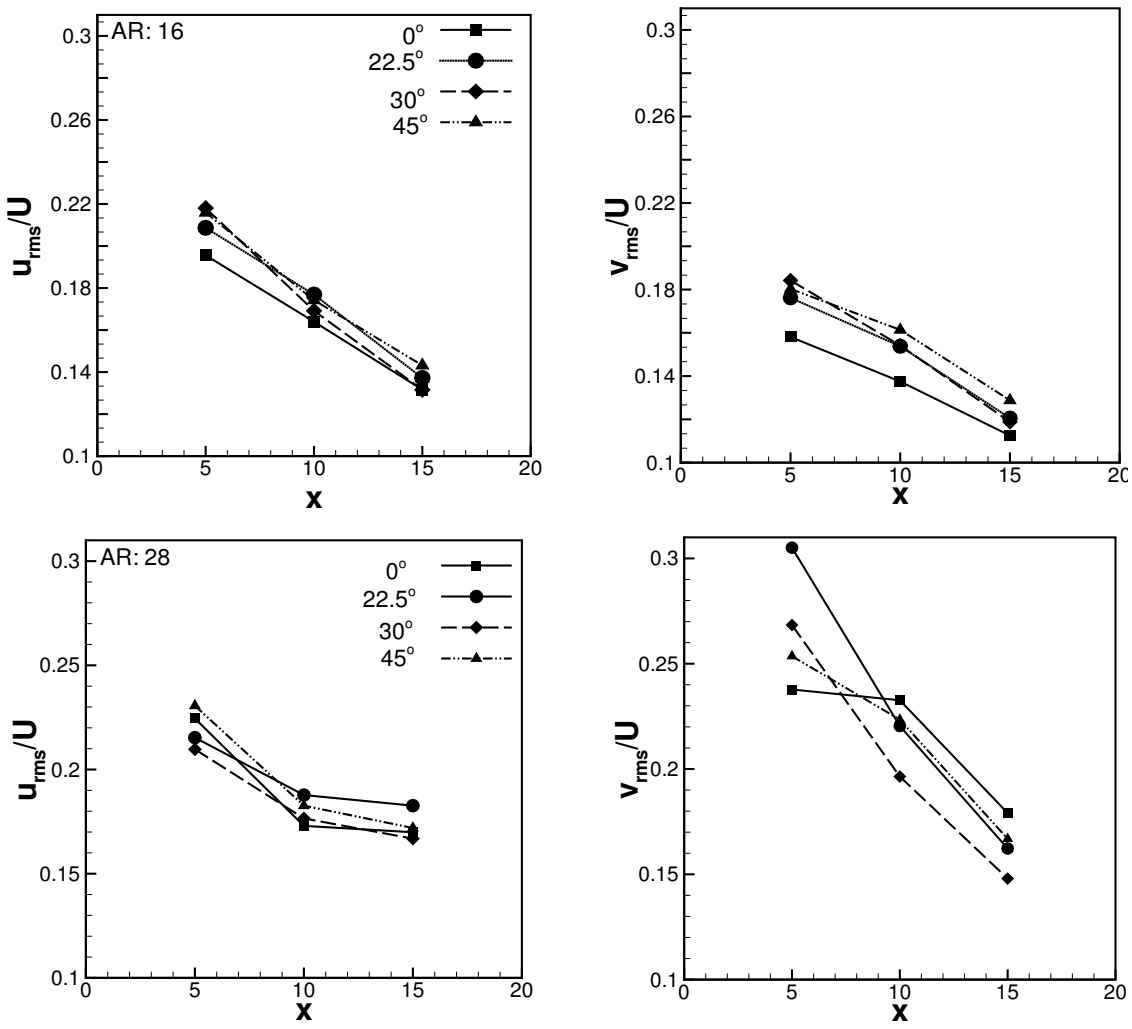

Figure 5.45: The decay of u and v rms velocities in the center-plane along the streamwise direction at AR=16 (top) and 28 (bottom), Re=410 from the hotwire measurements.

5.2.7 Recirculation length

The length of the recirculation region of the time-averaged flow field is presented in Table 5.1 for two Reynolds numbers (Re=410 and 610). Two aspect ratio and four cylinder orientations are considered. The recirculation length is defined here as the distance of the separating shear layer from the base of the cylinder to the re-attachment point along the wake centerline. It practically coincides with the location where the (time-averaged) centerline velocity changes its sign. At Re=410 the minimum recirculation length is found to occur at an angle of 22.5^o. It correlates with the minimum drag coefficient realized for this angle. The recirculation length for AR=28 is smaller when compared to AR=16,

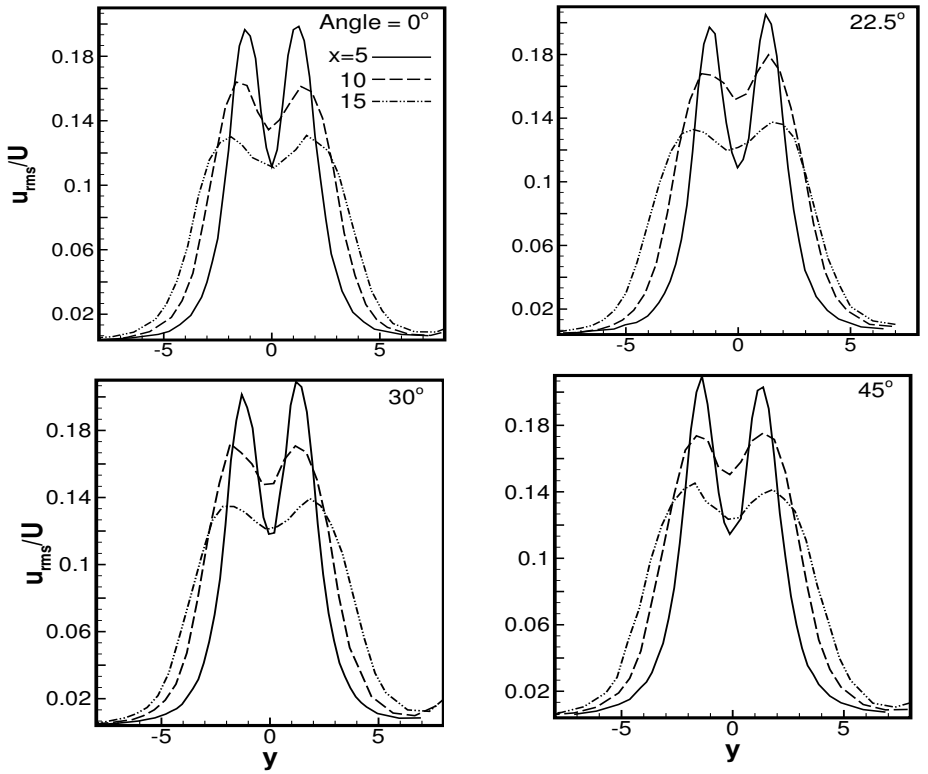

(a)

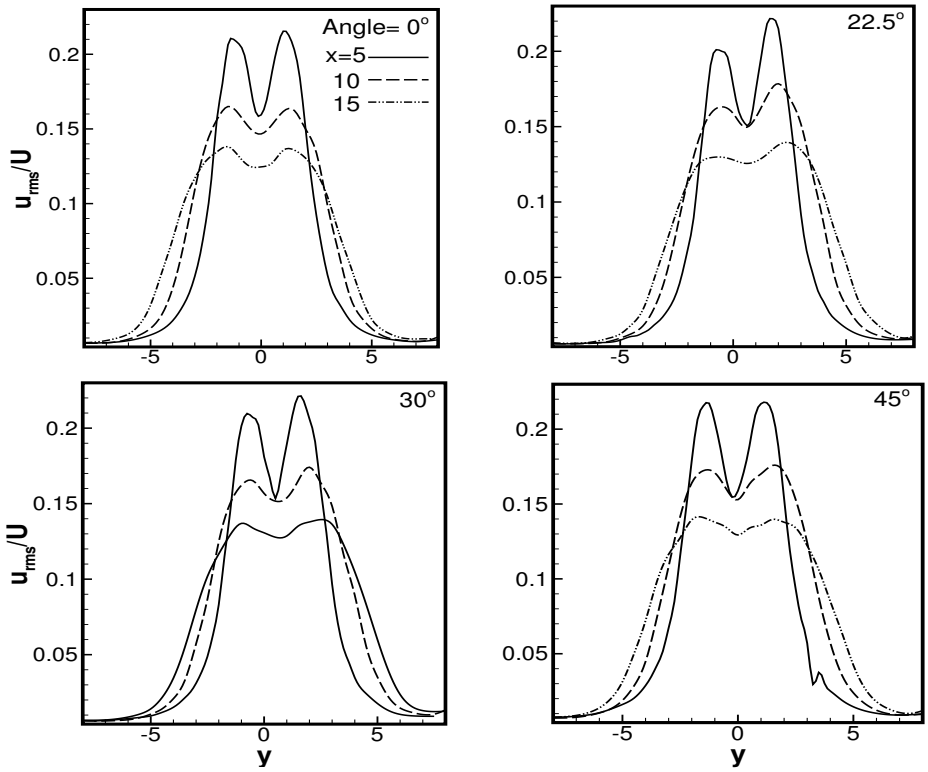

(b)

Figure 5.46: Time-averaged streamwise velocity fluctuations for three downstream locations (x=5, 10 and 15) and four cylinder orientations (θ=0, 22.5, 30 and 45^o), (a) Re=410 and (b) Re=610. AR=16.

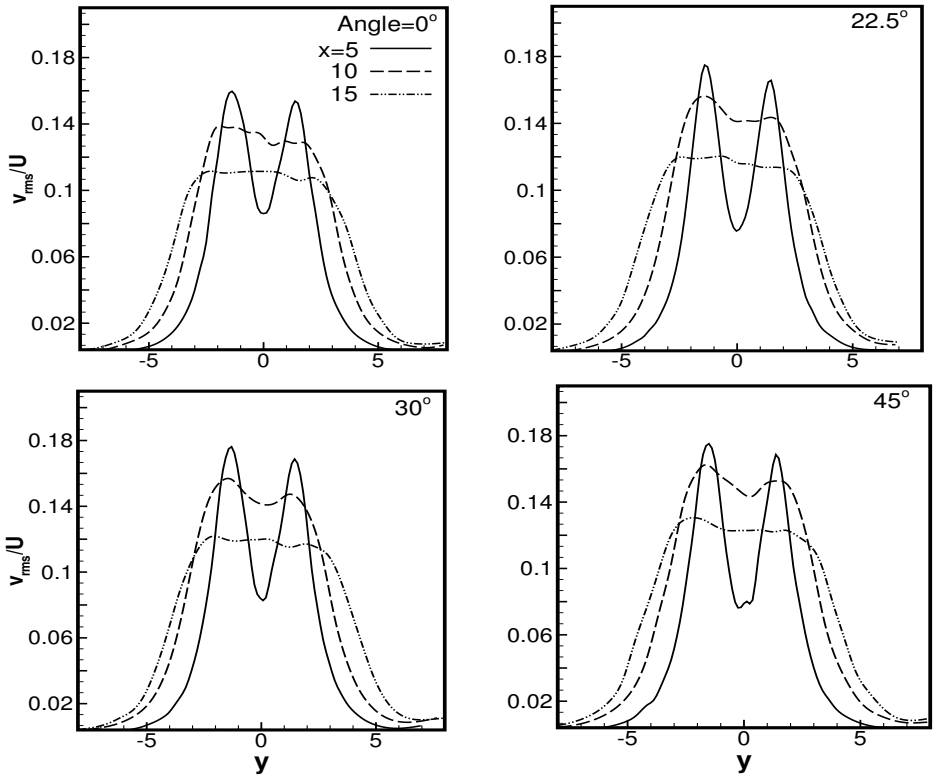

(a)

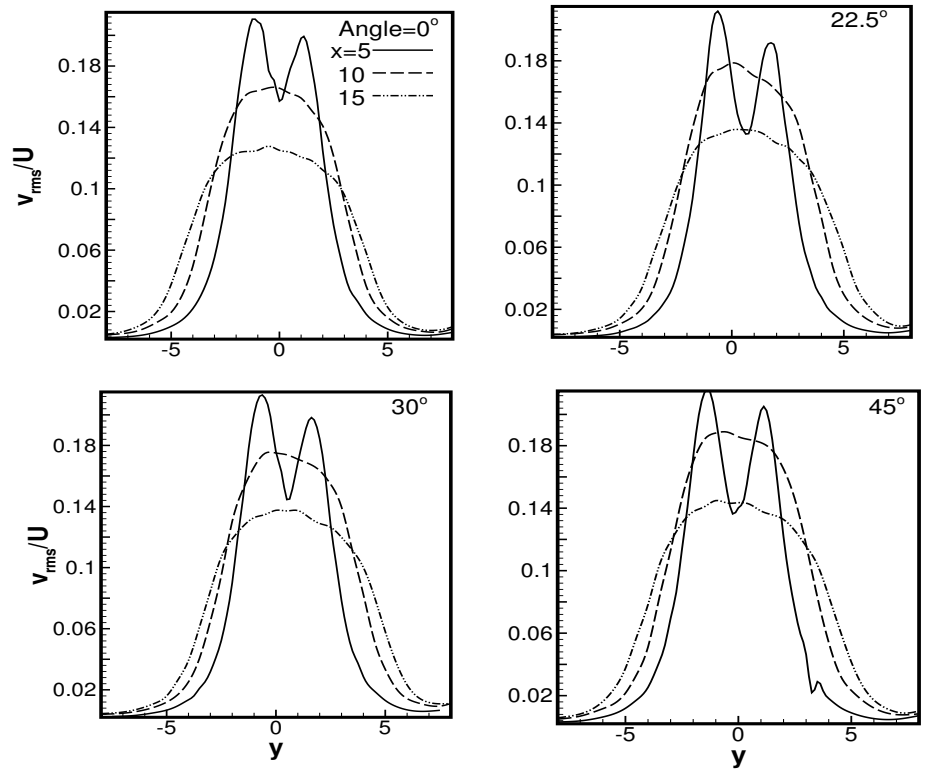

(b)

Figure 5.47: Time-averaged transverse velocity fluctuations for three downstream locations (x=5, 10 and 15) and four cylinder orientations (θ=0, 22.5, 30 and 45^o), (a) Re=410 and (b) Re=610. AR=16.

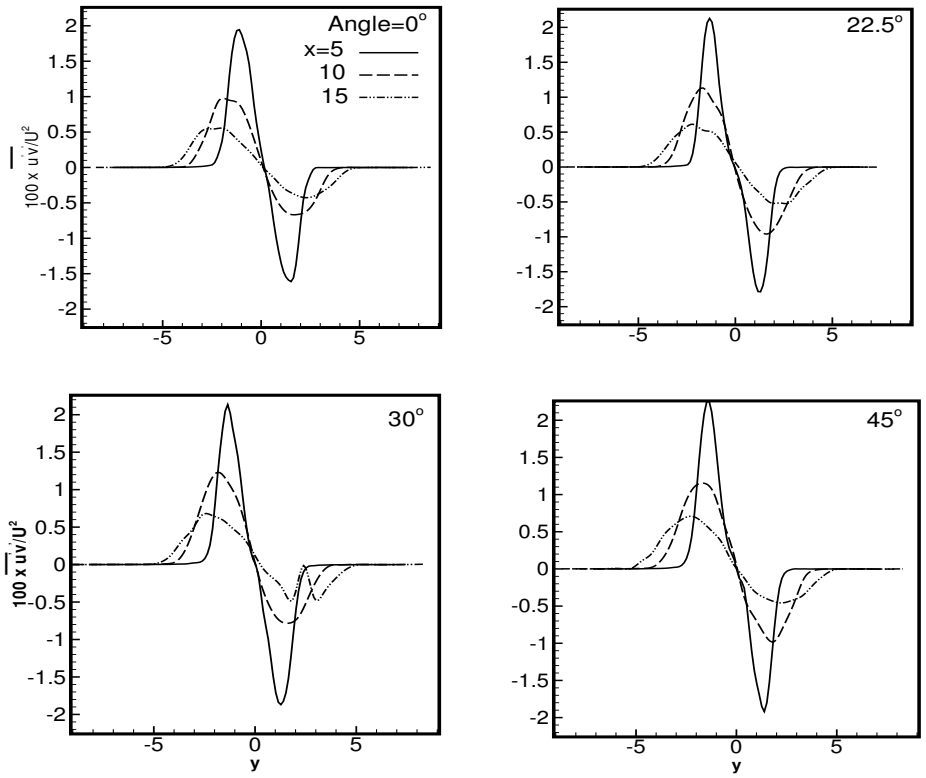

(a)

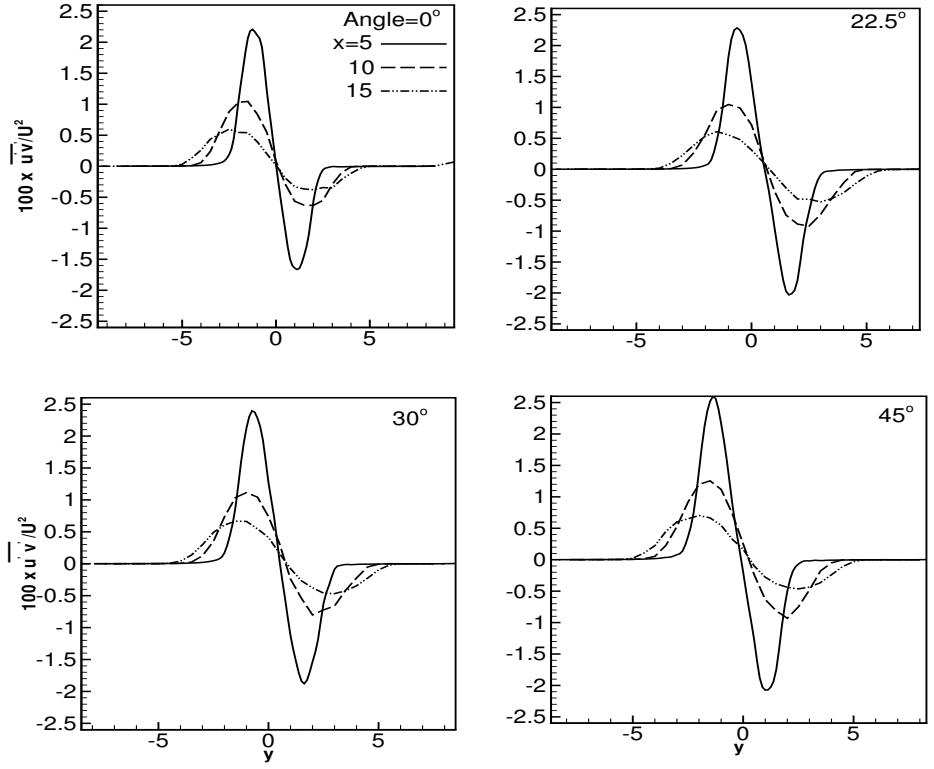

(b)

Figure 5.48: Time-averaged turbulent shear stress for three downstream locations (x=5, 10 and 15) and four cylinder orientations (θ=0, 22.5, 30 and 45^o), (a) Re=410 and (b)Re=610. AR=16.

at all cylinder angles and Reynolds numbers. The corresponding drag coefficients were similarly related, being smaller for the higher aspect ratio cylinder. As previously discussed, this result is attributed to stronger three dimensionality[12] in the high aspect ratio experiments. At Re=610, similar effect of aspect ratio as that at re=410.

Table 5.1: Recirculation length for two aspect ratios (AR=16 and 28) at different cylinder orientations for Re=410 and 610.

	Re=410		Re=610	
Angle	16	28	16	28
0	4.99	3.90	5.30	2.47
22.5	4.94	2.46	4.47	2.48
30	5.05	2.87	4.95	2.82
45	5.14	3.31	5.04	2.99

5.2.8 Centerline recovery

Figure 5.49 shows the recovery of centerline velocity along the downstream direction at AR=16. Various cylinder orientations and two Reynolds number (Re=410 and 610) have been considered. Compared to AR=28 (Figure 5.19) the recovery at AR=16 is slower, for both streamwise and transverse velocities. The streamwise velocity along the centerline reaches an asymptotic value in the range of 0.6-0.65. The asymptotic value of u-velocity is reached at around x=15 and x=7 respectively for the low and high aspect ratios. This is in accordance with the larger recirculation bubble for the low aspect ratio. The maximum negative value attained by the streamwise velocity is higher for AR=16 compared to AR=28. Similarly, the magnitude of the largest transverse velocity is higher for the low aspect ratio cylinder. The average centerline velocity is lower inside the recirculation zone, where the v-velocity is high. The minimum in centerline velocity value occurs around the core of the recirculation bubble. The streamwise location where the v-velocity attains a minimum occurs at the end of the recirculation bubble.

5.2.9 Flow visualization

Figure 5.50 shows the particle traces in the near-wake of the cylinder. The aspect ratio is 16 and four different cylinder orientations are considered. As seen in the high aspect ratio

[12]at the intermediate Reynolds number studied

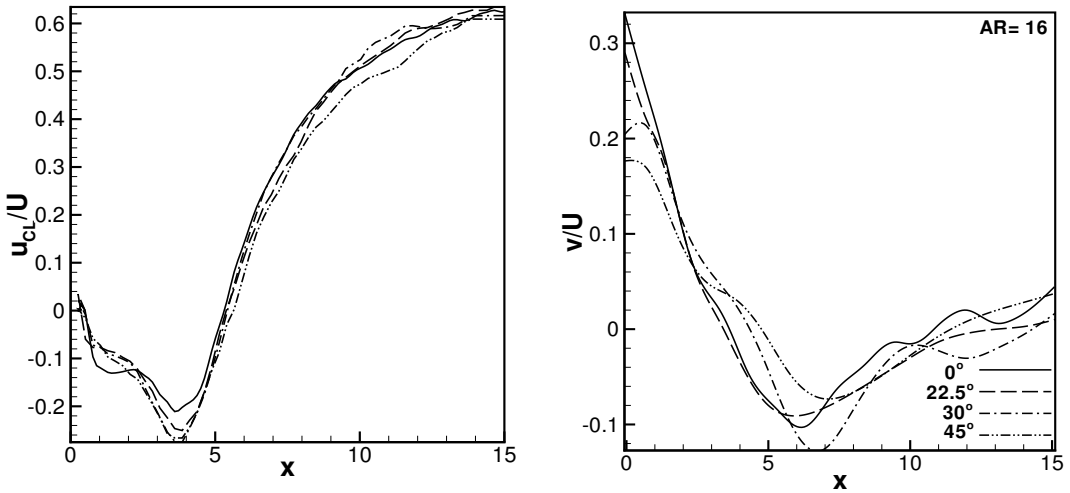

(a)

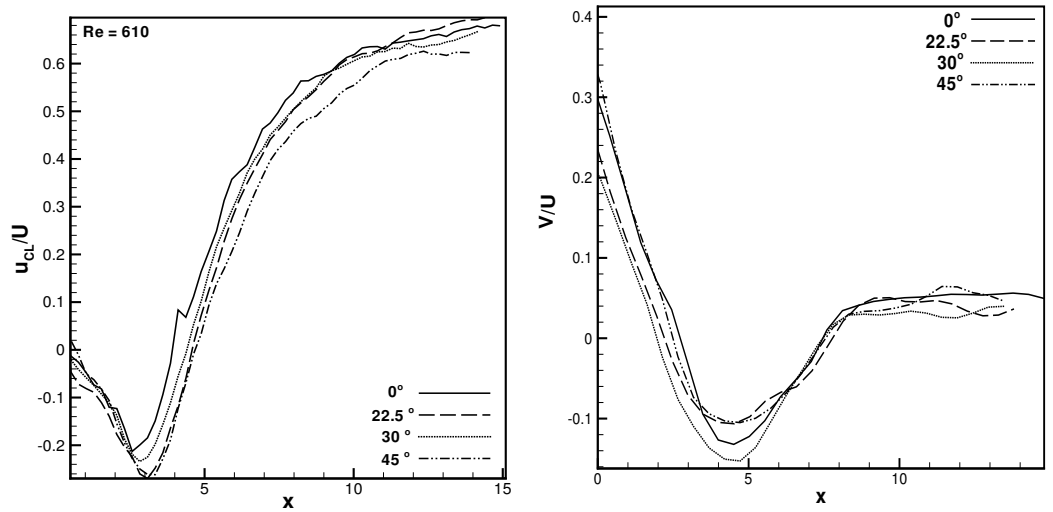

(b)

Figure 5.49: Centerline recovery of u and v- velocity at AR=16, (a) Re=410 and (b)Re= 610.

images of Figure 5.25, the shear layer separates at the leading corners of the cylinder, followed by divergence in the streamwise direction. The possibility of shear layer re-attachment is thus absent for both aspect ratios. In addition, the PIV-visualization images are quite similar to the smoke visualization photographs of Dutta *et al.* [33]. These were recorded close to the cylinder at high Reynolds numbers. The effect of aspect ratio on Strouhal number and drag coefficient (Figures 5.1, 5.2) is also explained from the flow visualization pictures of Figure 5.50. The separation between the vortices contained

in the opposed shear layers is lower for a higher aspect ratio (AR=28) compared to lower aspect ratio (AR=16). Thus the interaction between the alternating vortices is lower for the lower aspect ratio cylinder, leading to a reduction in Strouhal number and increase in drag coefficient. Figure 5.51 shows flow visualization pictures behind the square cylinder in the x-z plane at different cylinder orientations for an aspect ratio of 16. The objective here is to show the spanwise variation in the flow field and hence the three dimensionality of flow above the square cylinder. They are to be compared with the high aspect ratio images given in Figure 5.26. Three dimensionality appears closer to the surface of the cylinder at AR=16 when compared to AR=28. For a large aspect ratio (AR=28), the three dimensional vortex structures appear at streamwise x-locations that depend on the cylinder orientation. Three dimensionality shows up very close to the cylinder only for an orientation of 22.5^o. The early appearance of three dimensionality may also be correlated to the minimum drag at this orientation. The x-location at which three dimensionality appears is also related to the evolution of streamwise turbulent intensity. As discussed in Section 5.2.6, turbulence intensity peaks earlier at a cylinder angle of 22.5^o. There is no spanwise variation in the onset of 3-D flow structures for any of the cylinder orientations. This indicates parallel vortex shedding behind the square cylinder. For the low aspect ratio cylinder, (AR=16), three dimensionality appears closer to the cylinder; in addition this location is insensitive to the cylinder orientation.

5.2.10 Closure

The effect of aspect ratio on wake patterns has been discussed. The aspect ratio has been set equal to 16 and 28 for detailed study. Results have been obtained for two Reynolds number (Re=410 and 610) and four cylinder orientations (θ=0, 22.5, 30 and 45^o). The following conclusions have emerged from the study. Drag coefficient and Strouhal number are seen to be strong function of aspect ratio for the range of Reynolds number studied. Strouhal number increases with increase in aspect ratio and drag coefficient decreases with an increase in aspect ratio. For both aspect ratios, a minimum in drag coefficient is found at 22.5^o. For this orientation, Strouhal number is a maximum. The centerline recovery of streamwise velocity is faster for the high aspect ratio (AR=28) when compared to low aspect ratio (AR=16). The size of the recirculation bubble is lower at the higher aspect ratio (AR=28) and explain the above observation. The visualization pictures show that the separation distance between the alternating K*árman* vortices are function of both aspect ratio and cylinder orientation. The multiple modes in the power spectra indicate the modification of vortex shedding process and appearance of secondary vortical structure. From secondary flow visualization images it is seen

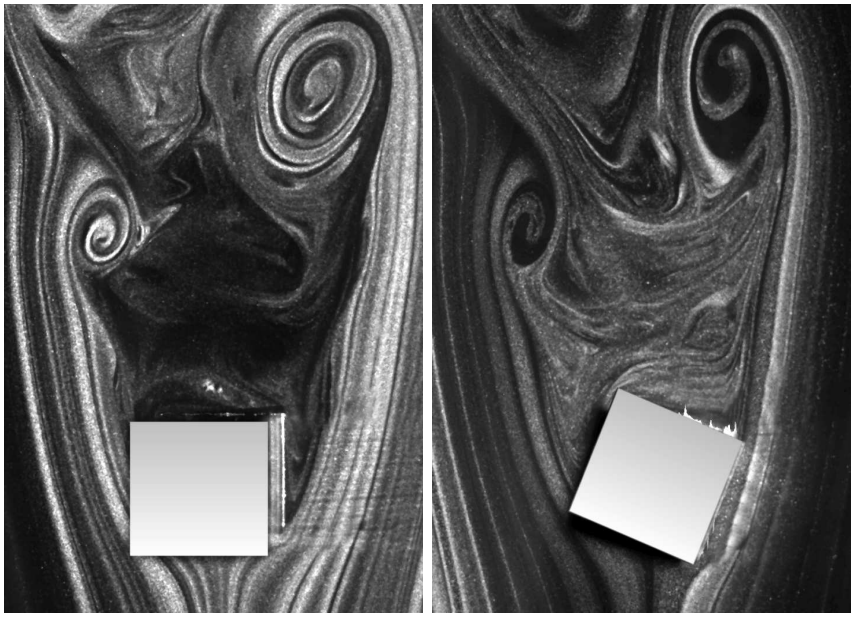

0^o 22.5^o

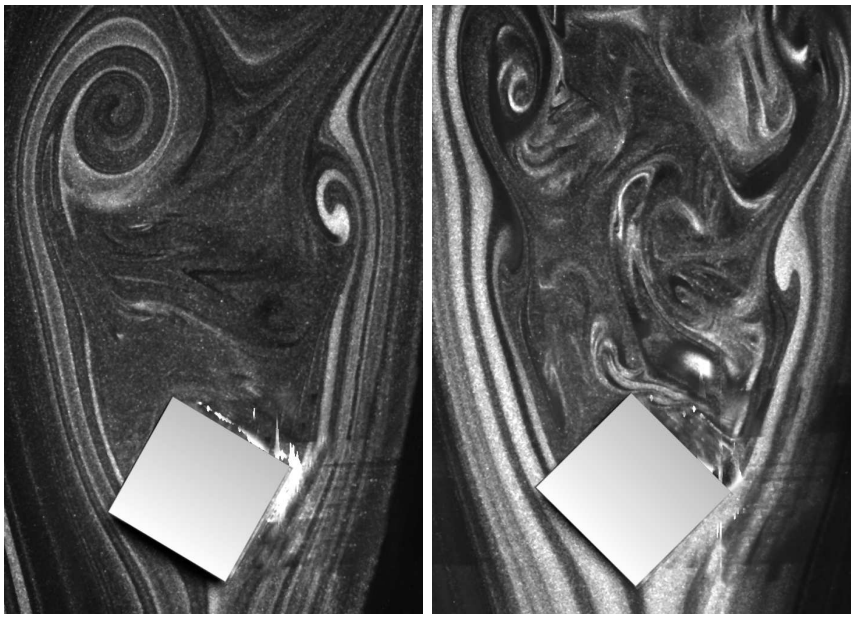

30^o 45^o

Figure 5.50: Near wake particle traces of the instantaneous flow field at different cylinder orientations, AR=16, Re=410.

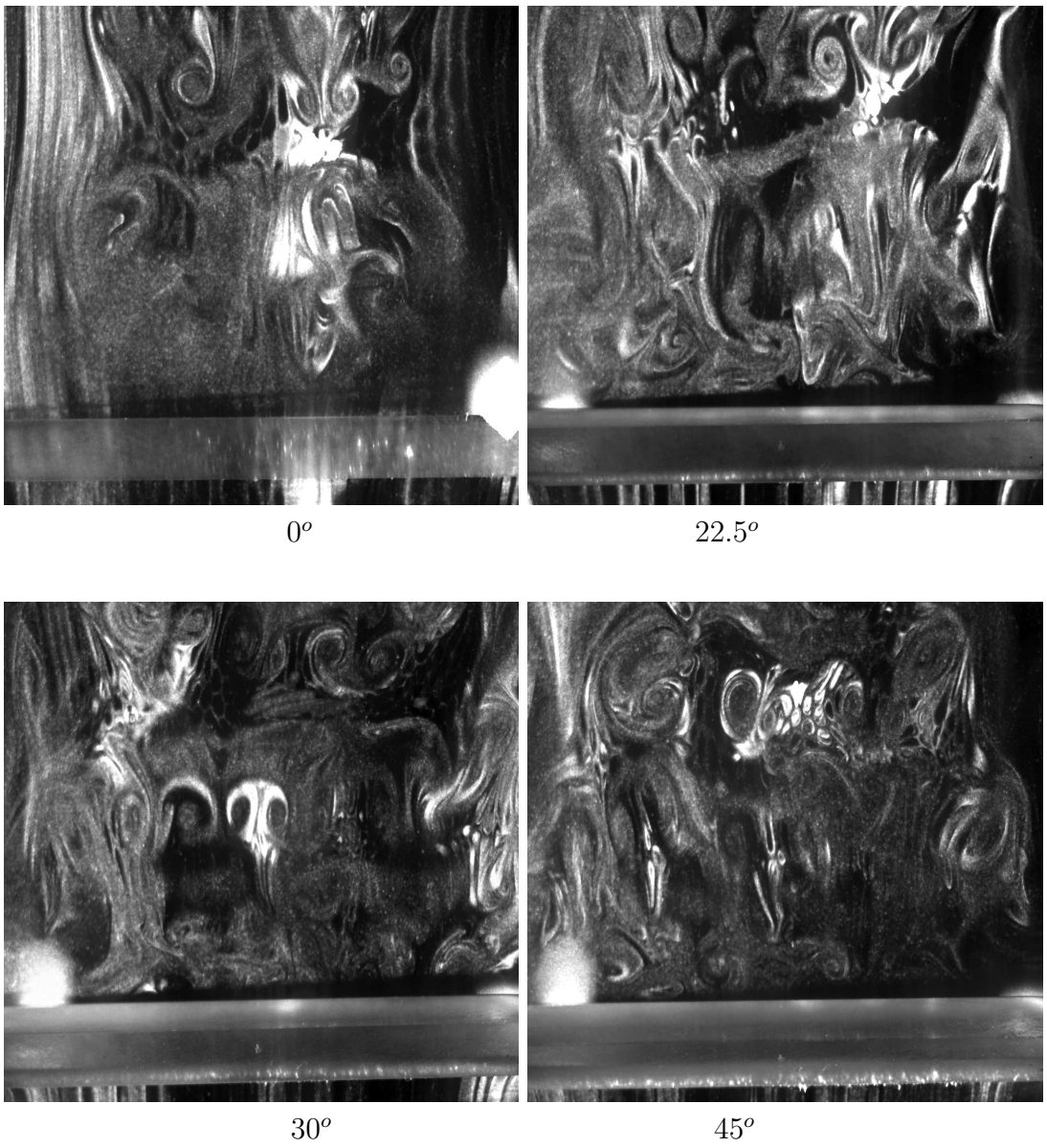

0^o 22.5^o

30^o 45^o

Figure 5.51: Near field particle traces in the spanwise $x-z$-plane at y=0.5 at different cylinder orientations, Re=410 and AR=16.

that the flow three dimensionality is stronger for AR=16 compared to that AR=28.

5.3 Effect of Reynolds Number

In present section, the effect of Reynolds number on the flow structure is discussed. The intermediate range of Reynolds number (Re=100-600) is considered. The aspect

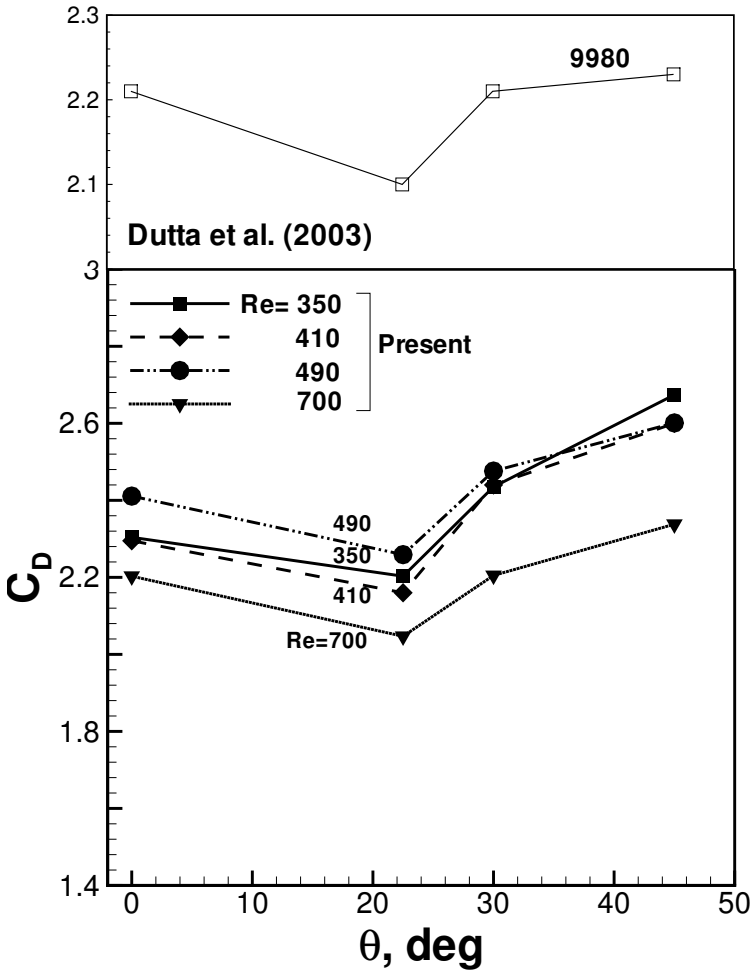

Figure 5.52: Drag coefficient as a function of cylinder orientation and Reynolds number for AR=16.

ratio has been set to 16, 28 and 60. Below Re=100, flow resembles that as a circular cylinder. The increase in Reynolds number leads to modification of flow instabilities and there interactions. When the square cylinder is inclined with respect to the mean flow, only one pair of corners contribute to flow separation. Hence, the cylinder orientations display a weak dependence on the separation process due to increase in Reynolds number. However, the size of the turbulent structures and the broadening of the power spectra are dependent on the diffusion and dissipation mechanism in the wake. These are clearly sensitive to Reynolds number, particularly when Re is towards the lower end of the scale.

5.3.1 Drag coefficient and Strouhal number

In the previous section 5.1.2 it is seen that drag coefficient is sensitive to cylinder orientation. But it is less sensitive to Reynolds number due to separation points being fixed to the upstream corners of the cylinder. However it depends on inlet flow condition, blockage, and aspect ratio. Figure 5.52 shows the effect of Reynolds number on the drag coefficient. The effect of Reynolds number on drag coefficient at these Reynolds numbers is less significant. The trend of drag coefficient is similar from this study with that of the literature (Dutta *et al.* [33]) at higher Reynolds number. Figure 5.53 compares the Strouhal number variation with Reynolds number at different cylinder orientation with that of Dutta *et al.* [33]. Two aspect ratio (AR=16 and 60) at different Reynolds number have been studied. The Strouhal number is less sensitive to Reynolds number at these range.

5.3.2 Time-averaged velocity profiles

Figure 5.54 shows the time-averaged streamwise and transverse components velocity profiles for three Reynolds number (Re=165, 495 and 595) at three downstream positions (x= 2, 4 and 6). The streamwise velocity is negative (particularly near the centerline) at x=2 for these Reynolds numbers. The recovery of velocity towards a positive asymptotic value is directly related to the wake-width, that in turn depends on the entrainment at the edge of the wake. Figure 5.54 broadly shows no difference in the wake-width for changing Reynolds number. The recovery rates at different Reynolds numbers are thus identical. At an axial location x=4, the wake width varies with Reynolds number. The wake width initially decreases with increase in Reynolds number at Re=495 possibly due to entrainment from the outer flow. With further increase in Reynolds number to 595, the wake width increases as the entrainment decreases. With further increase in axial location (x=6) the wake width further increases. The time-averaged transverse component of velocity is a measure of fluid entrainment. The entrained fluid mass from either side of the wake can cross the centerline of the wake. Thus, positive and negative transverse velocities on each side of the centerline are possible. The entrainment mechanism into the wake is due to oppositely oriented spanwise vortices generated by the separating shear layer. The resulting motion takes the fluid inwards, closer to the wake centerline. A maximum in transverse velocity is seen to occur at x=4 for all three Reynolds numbers.

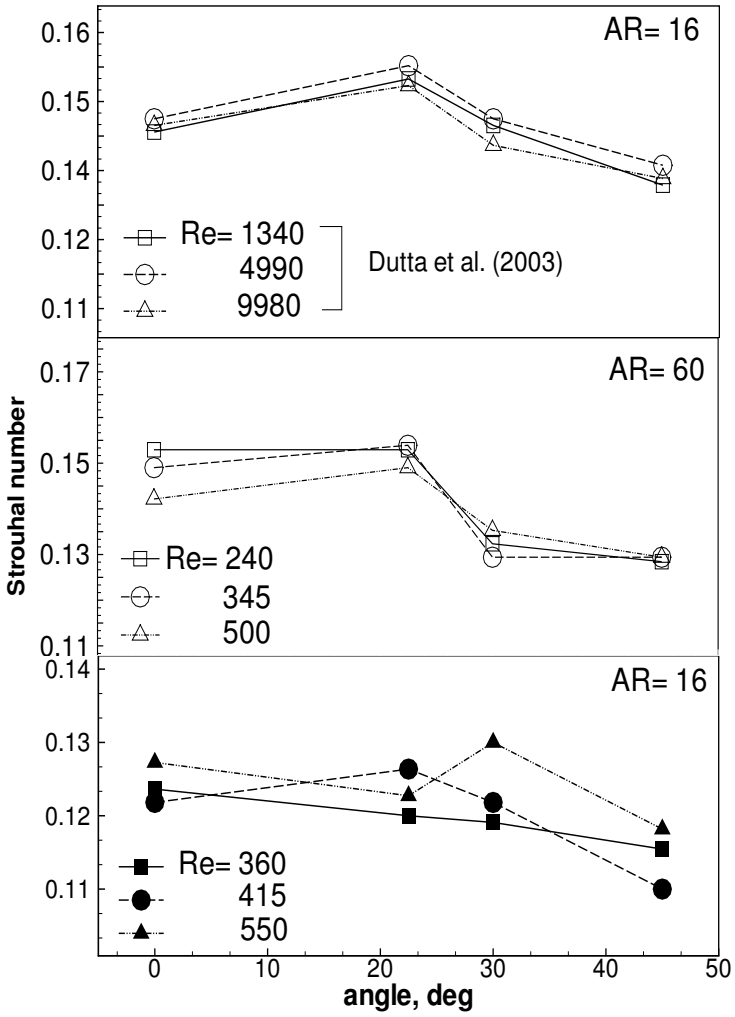

Figure 5.53: Strouhal number as a function of cylinder orientation, Reynolds number and aspect ratio.

5.3.3 Stream traces

Figure 5.55 shows the time-averaged stream traces in the wake for three Reynolds numbers. The stream traces are plotted at the midplane of the cylinder. Two symmetric bubbles of opposite sense are formed. A distinct change in recirculation bubble length is to be found for increasing Reynolds number. The length of recirculation is about 3 units for Re= 165 and 595 and about 4 units for Re=495. The base pressure is dependent on recirculation length and hence the drag coefficient. Higher the base pressure lower the drag coefficient. The streamlines converge towards the cylinder centerline indicating that fluid from the outer flow enters into the wake and thus compensates for mass deficit

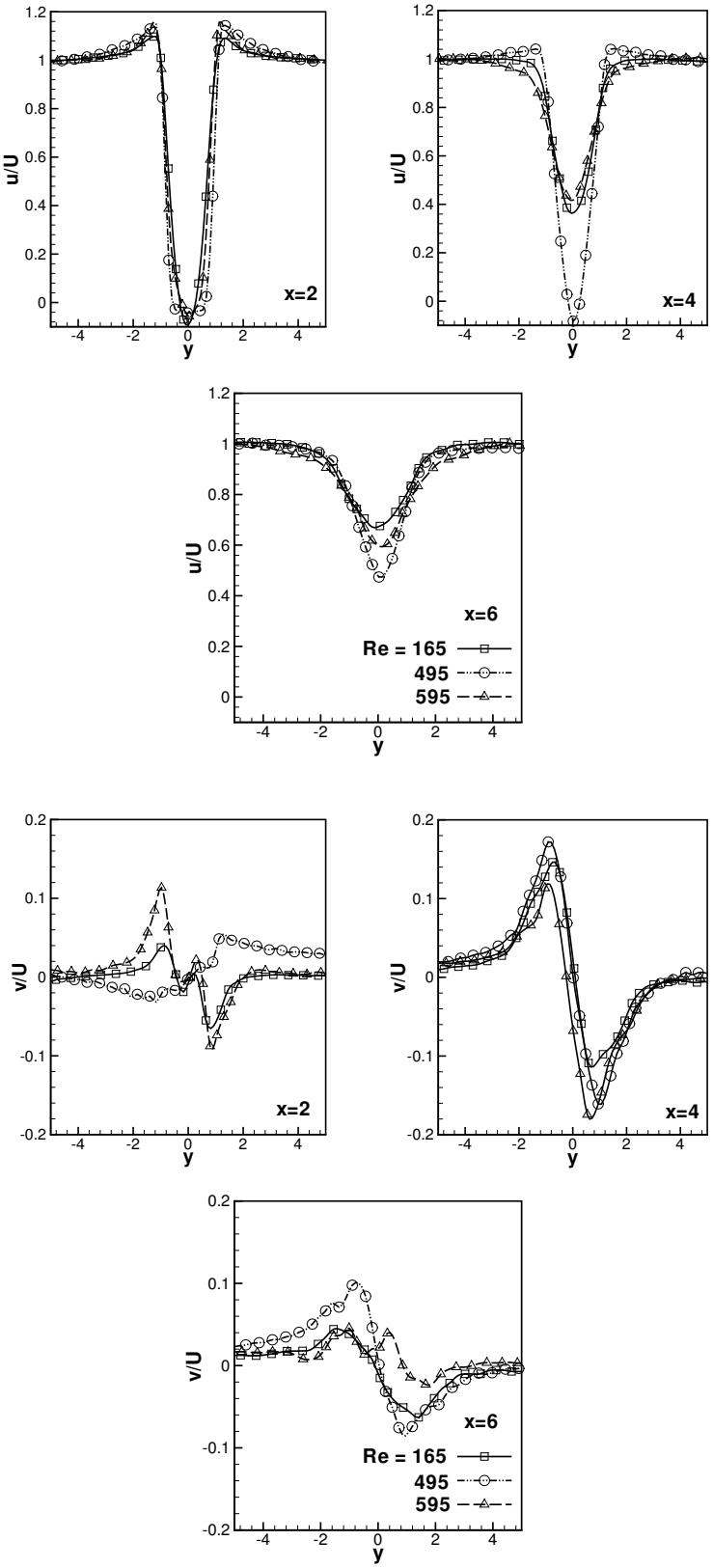

Figure 5.54: Time-averaged u and v- component of velocity profiles at three downstream locations (x=2, 4 and 6) at three Reynolds numbers (Re=165, 494 and 595). Aspect ratio (AR)=28, θ=0^o

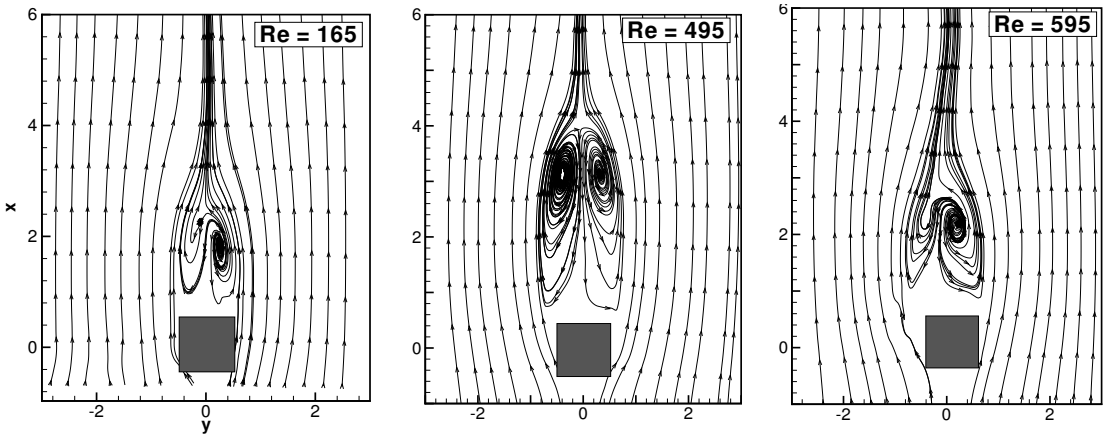

Figure 5.55: Average streamlines as a function of Reynolds number. AR=28 and θ=0^o.

in the wake.

5.3.4 Time-averaged vorticity contours

The spanwise time-averaged vorticity contours for three Reynolds number (Re=165, 495 and 595) are shown in Figure 5.56. These contours reveal the formation of separated shear layers from each side of the cylinder. The separated shear layer extends to a larger distance for Re=495 compared to the other two Reynolds numbers. The elongation is partly due to an increase in momentum diffusion for three dimensional flow. The interaction between primary and secondary vortices also plays a role in vortex formation length.

5.3.5 Velocity fluctuations

Figure 5.57 shows profiles of streamwise velocity fluctuations for three Reynolds number (Re= 165, 495 and 595) and three locations (x=2, 4 and 6). The u_{rms} values show dual peak indicating the higher turbulent production in the opposite shear layer. The fluctuations is higher for higher Reynolds number. This is understandable because the strain rates of primary vortices is enhanced at higher values of Re. The width of the zone of velocity fluctuations increases with downstream distance. The strength of fluctuations also decreases as one moves to downstream locations. The differences in the maximum fluctuation level at different streamwise locations with change in Reynolds number in-

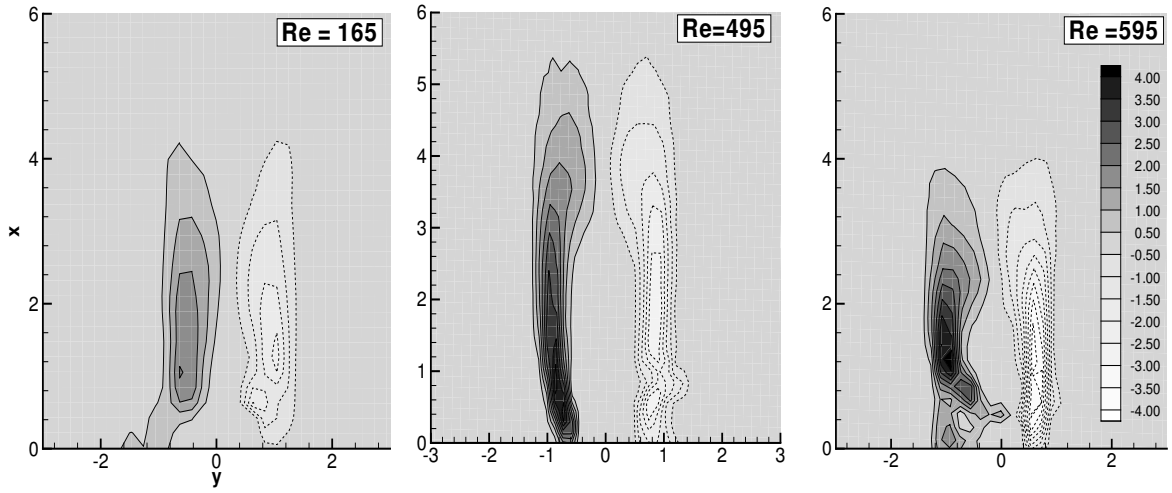

Figure 5.56: Time-averaged spanwise (ω_z) vorticity contours as a function of Reynolds number. AR=28 and θ=0^o.

dicate the influence of Reynolds number on turbulent kinetic energy budget quantities.

The higher level of fluctuations at the higher Reynolds number can be explained as follows: The primary vortices of opposite sign come closer to each other near the wake centerline and interact more intensely compared to the situation when they are apart. The interaction of these coherent structures is governed by tearing and pairing of vortices. They produce newer structures at other scales. As a result of the complex interactions the amplitude of velocity fluctuations increases. At this Reynolds numbers two rows of vortices of opposite sign are shed from both sides of the cylinder. These vortices travel parallel to the wake centerline. Consequently, twin peaks in the transverse velocity fluctuations compare to the two shear layers are to be seen at all the three Reynolds numbers studied. Figure 5.58 shows the v_{rms} velocity profiles at three Reynolds number and three streamwise locations. Similar to the u_{rms} velocity profile, the v_{rms} velocity is higher at higher Reynolds number. However, contrary to the u_{rms} velocity no dual peak is observed for the v_{rms} velocity profile. The v_{rms} maximum magnitude increases in the streamwise direction i.e. from x=2 to x=4 and subsequently reduces. This observation is in accordance with the velocity variation in Figure 5.54. The fluctuation of v-velocity attains peak at different x-location compare to that of u-velocity.

Figure 5.59 shows the spatial distribution of streamwise (top) and transverse (bottom) velocity fluctuations for three Reynolds numbers. For all the three Reynolds num-

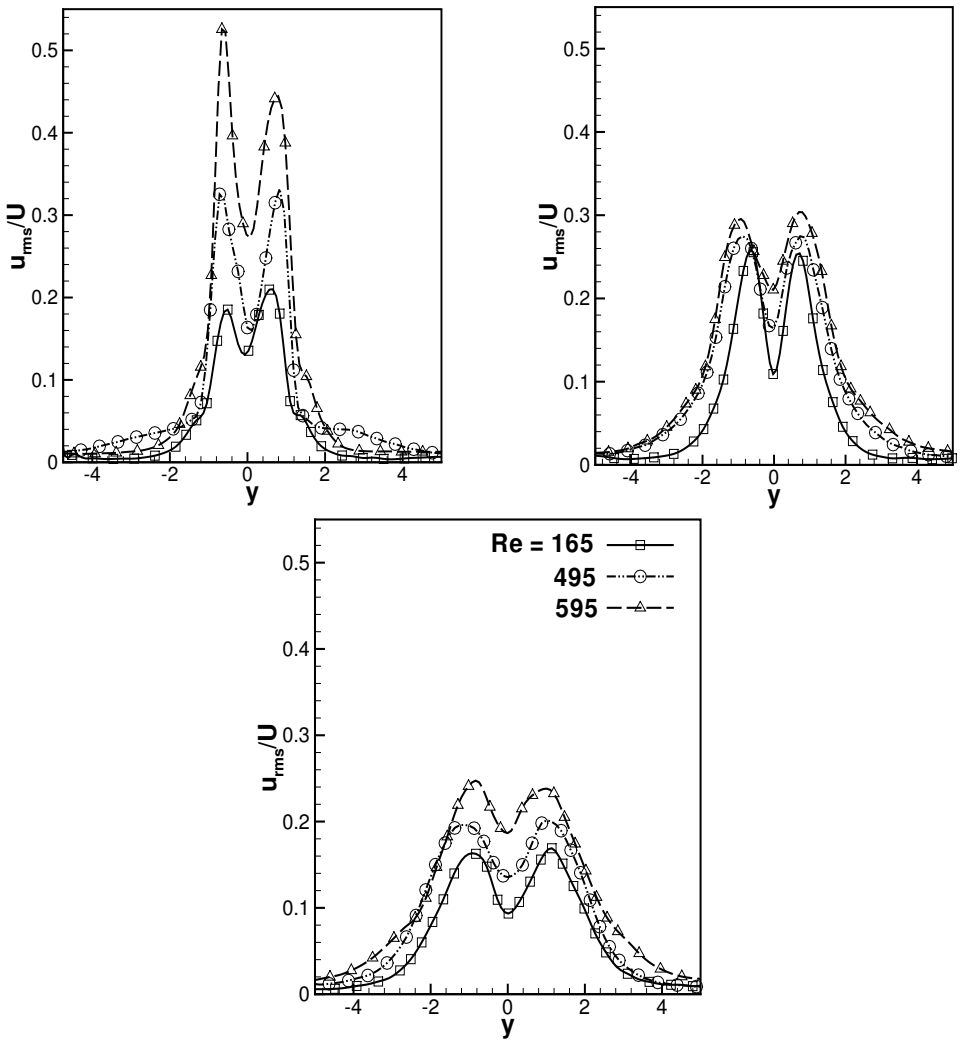

Figure 5.57: Variation of streamwise velocity fluctuations (u_{rms}) for three Reynolds number at different locations: x= 2, 4 and 6. AR=28 and θ= 0^o.

bers, a symmetric double peak of u_{rms} is seen about the wake centerline. The fluctuating field gets stronger with an increase in Reynolds number; these are to be seen in the magnitudes of the plotted contours. At a higher Reynolds number, a greater number of contours concentrate around the peak value. This behavior is seen in both streamwise as well as transverse component of velocity. The contour shapes match quite well with the two and three dimensional numerical simulation of Saha [147]. The fluctuating component of forces depend on the fluctuating velocity components since they affect the base pressure distribution on the cylinder surface. The downstream spreading of the fluctuating field affects the pressure variation on the suction side of the cylinder.

Figure 5.60 shows the variation of the fluctuating velocity u_{rms} (normalized) along

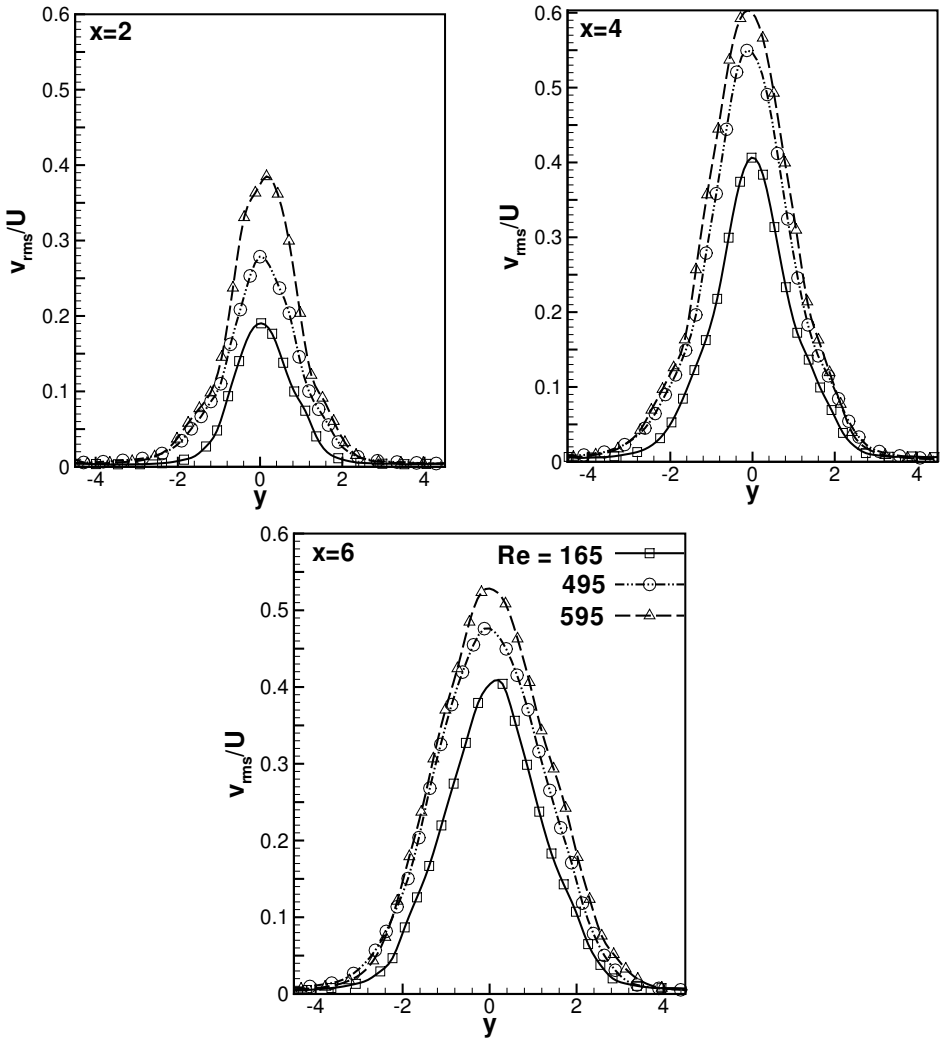

Figure 5.58: Variation of transverse velocity fluctuations (v_{rms}) for three Reynolds number at different locations: x= 2, 4 and 6. AR=28 and θ=0^o.

the wake centerline (y=0) for three different Reynolds number. The vortex formation length, defined as the distance at which u_{rms} is the highest shows a strong dependence on Reynolds number. The vortex formation length ($l_v f$) are 2.0, 2.8 and 2.4 for these Reynolds numbers (Re=165, 495 and 595). The corresponding peaks in u_{rms}/U are 0.17, 0.22 and 0.32 respectively. The peak values clearly increase with Reynolds number.

5.3.6 Centerline recovery

Figure 5.61 shows the evolution of the time-averaged streamwise component of velocity as a function of Reynolds number. The cylinder orientation corresponds to one of zero

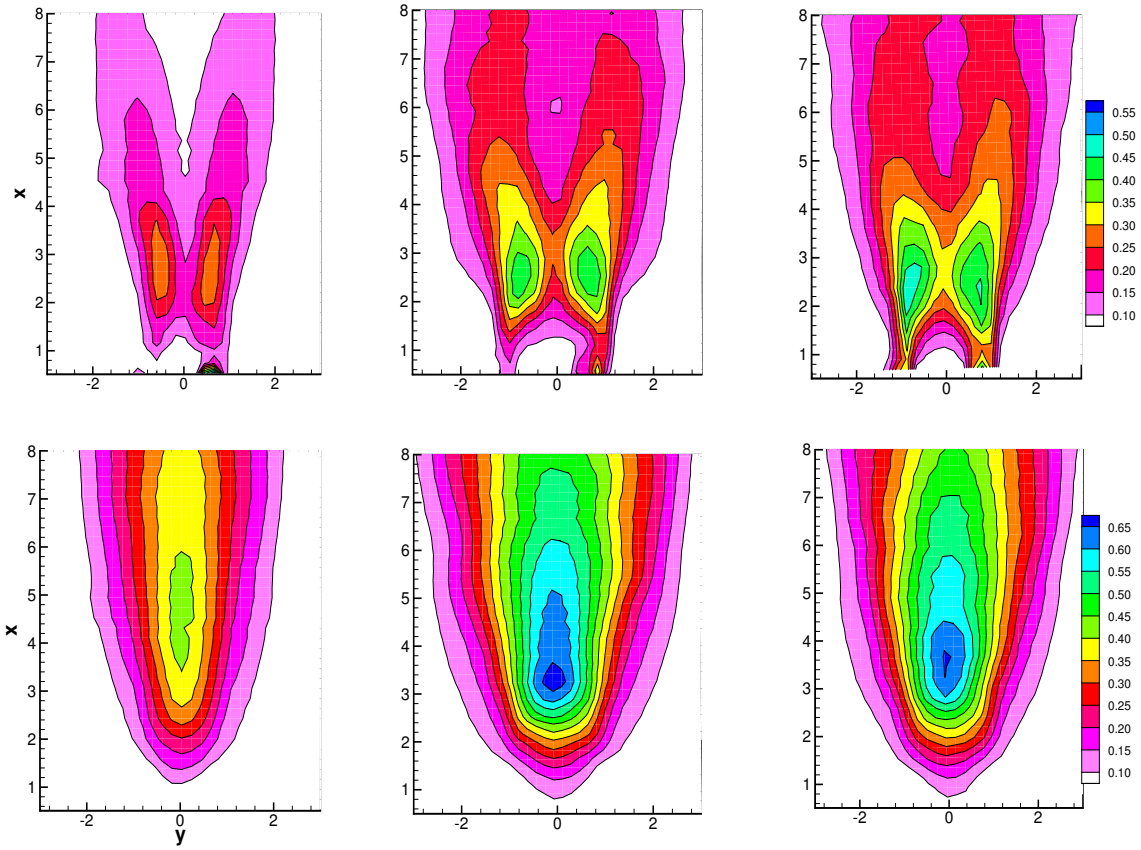

Figure 5.59: Comparison of u_{rms} (top) and v_{rms} (bottom) velocity contours for three different Reynolds number. AR=28 and θ=0^o.

angle. The recovery rates for each Reynolds number are practically identical except at Re= 97 and 300. For Re=97 the recovery rate is slower and it reaches an asymptotic value over a larger distance. At Re=300 the recovery rate is rapid and reaches an asymptotic value at x=4. For other Reynolds number the streamwise velocity reaches its asymptotic value at around x= 6. The asymptotic center-line velocity falls in the range of 0.62-0.68. The recirculation length is seen to vary with Reynolds number and is a maximum at Re=90. The initial recovery depends on the extent of pressure difference between the core of the wake and the external flow. Thus, rapid recovery can be correlated to the higher drag[13].

[13]though this effect is only marginal in the drag coefficient data of Section 5.3.1.

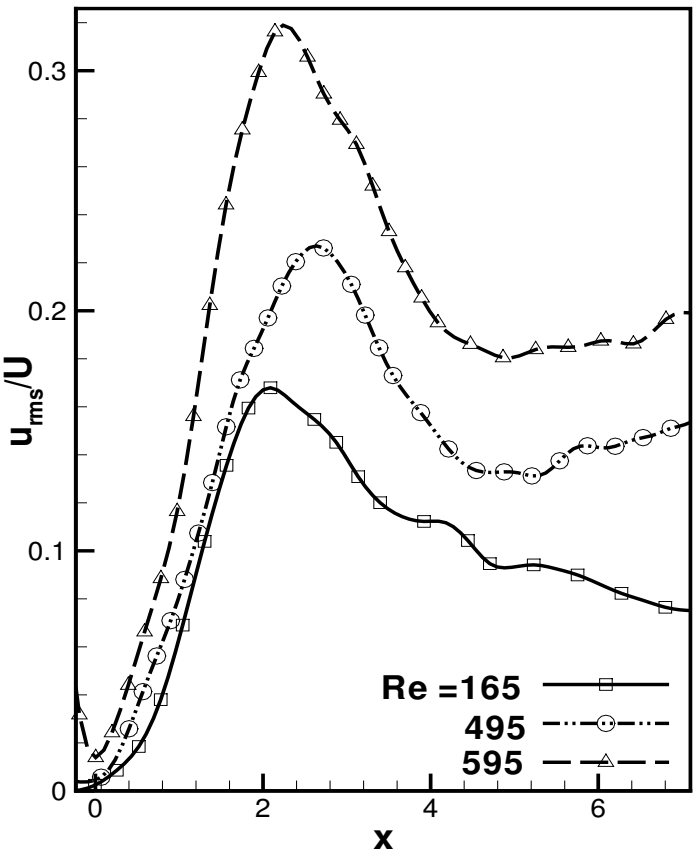

Figure 5.60: Variation of centerline u_{rms} velocity of flow past a square cylinder at 0^o cylinder orientation for three different Reynolds number (Re=165, 495 and 595). AR=28

5.3.7 Instantaneous vorticity field

Figure 5.62 shows selected instantaneous vorticity contours at three Reynolds numbers and three time instants. Positive vorticity corresponds to clockwise rotation and is indicated by solid lines whereas the negative spanwise vorticity corresponds to counter-clockwise rotation and is indicated by dashed lines. As expected the vortices are shed in an alternating sequence. The peak value of the vorticity decreases with downstream distance, a trend that can be attributed to vorticity diffusion. The distance between two alternate shedding vortex decreases with increase in Reynolds number. The two alternate vortices comes close to the cylinder centerline with increase in Reynolds number. The pattern becomes more symmetric about the cylinder centerline. With an increase in Reynolds number, small scale vortices embedded in large scale structure start to appear in the wake. The small scale structures decay faster owing to the viscosity of the fluid.

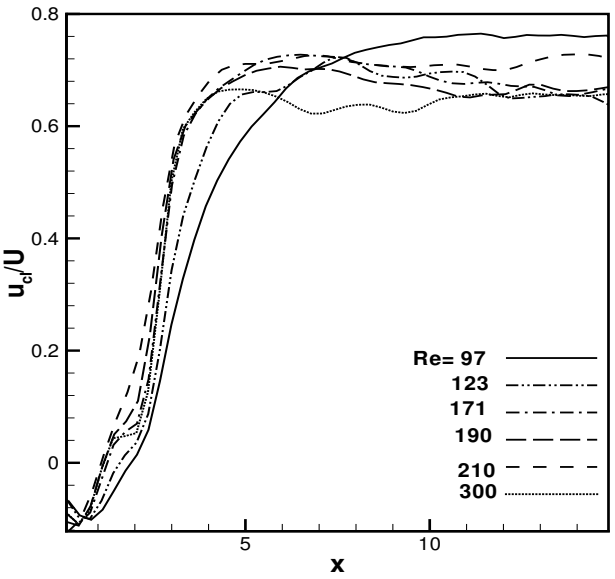

Figure 5.61: Centerline recovery of flow past a square cylinder at 0^o cylinder orientation at different Reynolds number. AR=28.

5.3.8 Power spectra

Power spectra were calculated from signals of 20 seconds length that were collected at a sampling rate of 1000 Hz. The corresponding minimum and maximum frequencies that resolved were 0.05 Hz and 500 Hz respectively. The voltage signal was first converted to a velocity signal using calibration data and the transverse component used for the calculations of the spectra. In the present study, it was observed that the transverse velocity signal (as opposed to the streamwise velocity component) was less noisy in terms of sporadic high frequency harmonics. Hotwire signals were mainly collected in the nearwake (x=5), at an offset of 1.2B from the cylinder centerline. The FFT algorithm was used to calculate the power spectra of the time series.

Figure 5.63 shows the power spectra for different Reynolds numbers at a location of $x = 5$ and $y = 1$. Two aspect ratios have been considered. The spectra is based on the v-component of velocity. A dominant peak is seen in all the spectra indicating clear vortex shedding for all Reynolds number. However the spectra has a broadband behavior with an increase in Reynolds number for both aspect ratios. The nature of broadband spectra is, however, different for these two aspect ratios. For AR=16 the number of harmonics is greater, while it is a narrow band for AR=28, centered around the dominant peak of vortex shedding. The broadband nature indicates that flow is

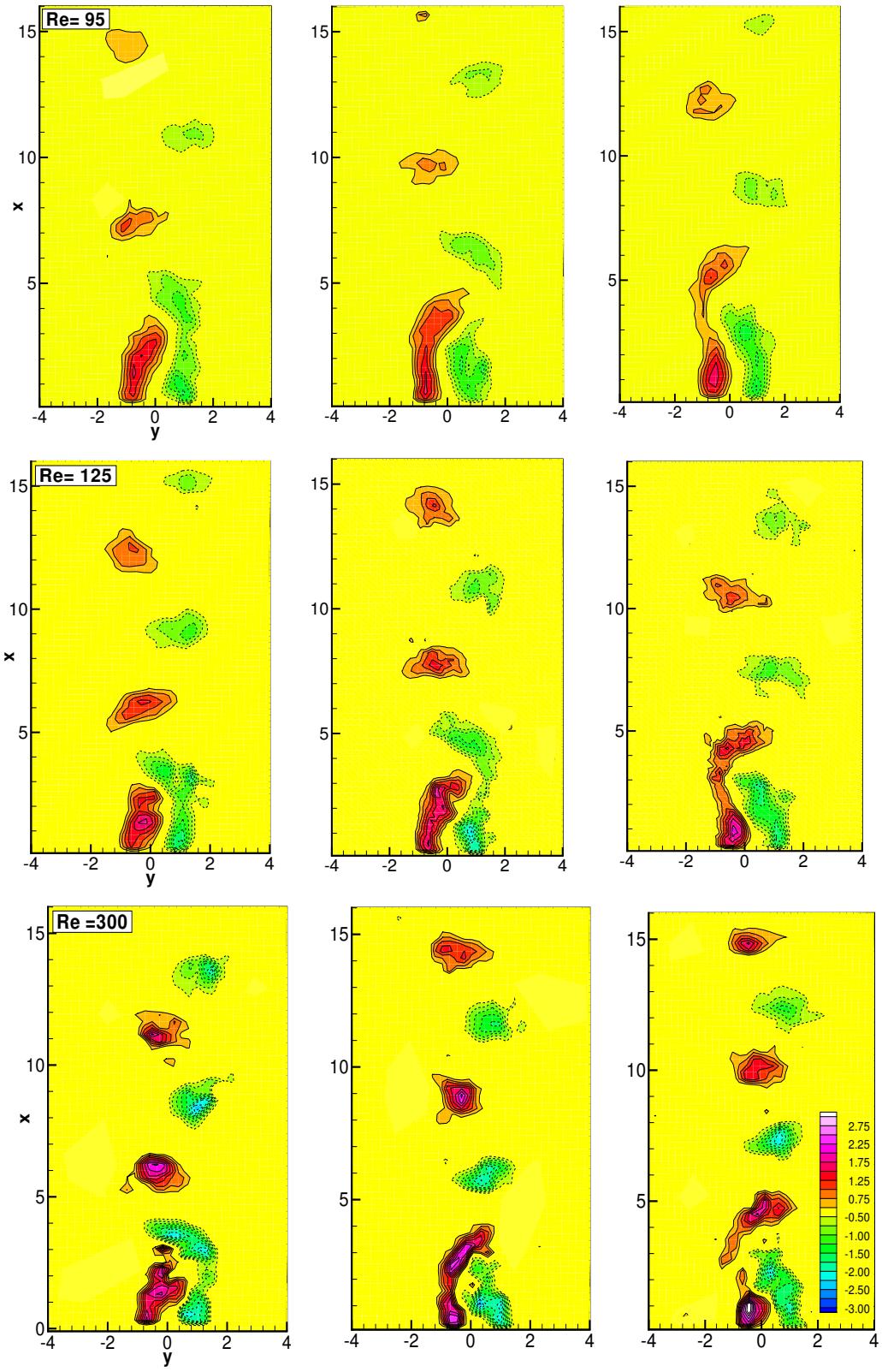

Figure 5.62: Instantaneous spanwise vorticity (ω_z) contours for three Reynolds numbers. AR=28 and θ=0^o.

quasi-periodic at a higher Reynolds number.

For a lower Reynolds number, vortices are alternately shed. The vortices on each side of the line of symmetry are of equal strength and are responsible for an enhanced signal. At a higher Reynolds number, flow unsteadiness results in varying strengths of vortices on each side, leading to aperiodic vortex shedding and hence a broadened spectrum. At higher Reynolds numbers, vortex dislocation and diffusion phenomena play an important role in broadening the spectra.This effect is more pronounced at the lower aspect ratio due to greater three dimensionality.

5.3.9 Autocorrelation function

The autocorrelation function $A(T)$ is a useful tool to measure of the predictability of fluid flows. Here, T indicates time lag. The autocorrelation function is a measure of the maximum time for which the fluid is correlated with itself. For organized fluid motion, the correlation function is finite for a longer time duration. For a periodic signal, $A(T)$ is a periodic function, whereas, for a white noise signal $A(T)$ is identically zero (except for zero time lag). For chaotic signals, the autocorrelation function tends to zero after some time $T > T_c$, where T_c is a measure of the time during which the motion can be predicted using appropriate initial conditions. The autocorrelation function is defined as

$$A(T) = \frac{\overline{v(t)v(t+T)}}{\overline{v(t)^2}} \tag{5.1}$$

Here overbar denotes the ensemble average of the product of the instantaneous signals $v(t)$ and its time shifted form $v(t+T)$. This average can be calculated as

$$\overline{v(t)v(t+T)} = \lim_{T\to\infty} \frac{1}{T_p} \int_0^{T_p} v(t)v(t+T)dt$$

In practice it is evaluated by successively using Fourier transforms (Castro, 1990). Typical transverse velocity signals, their power spectra and the respective autocorrelation functions are shown in Figure 5.64. At Reynolds number of 135, the wake is periodic with one dominant frequency. The auto correlation function also truly periodic. The magnitude of autocorrelation function decreases with increase in Reynolds number as seen from the Figure 5.64.

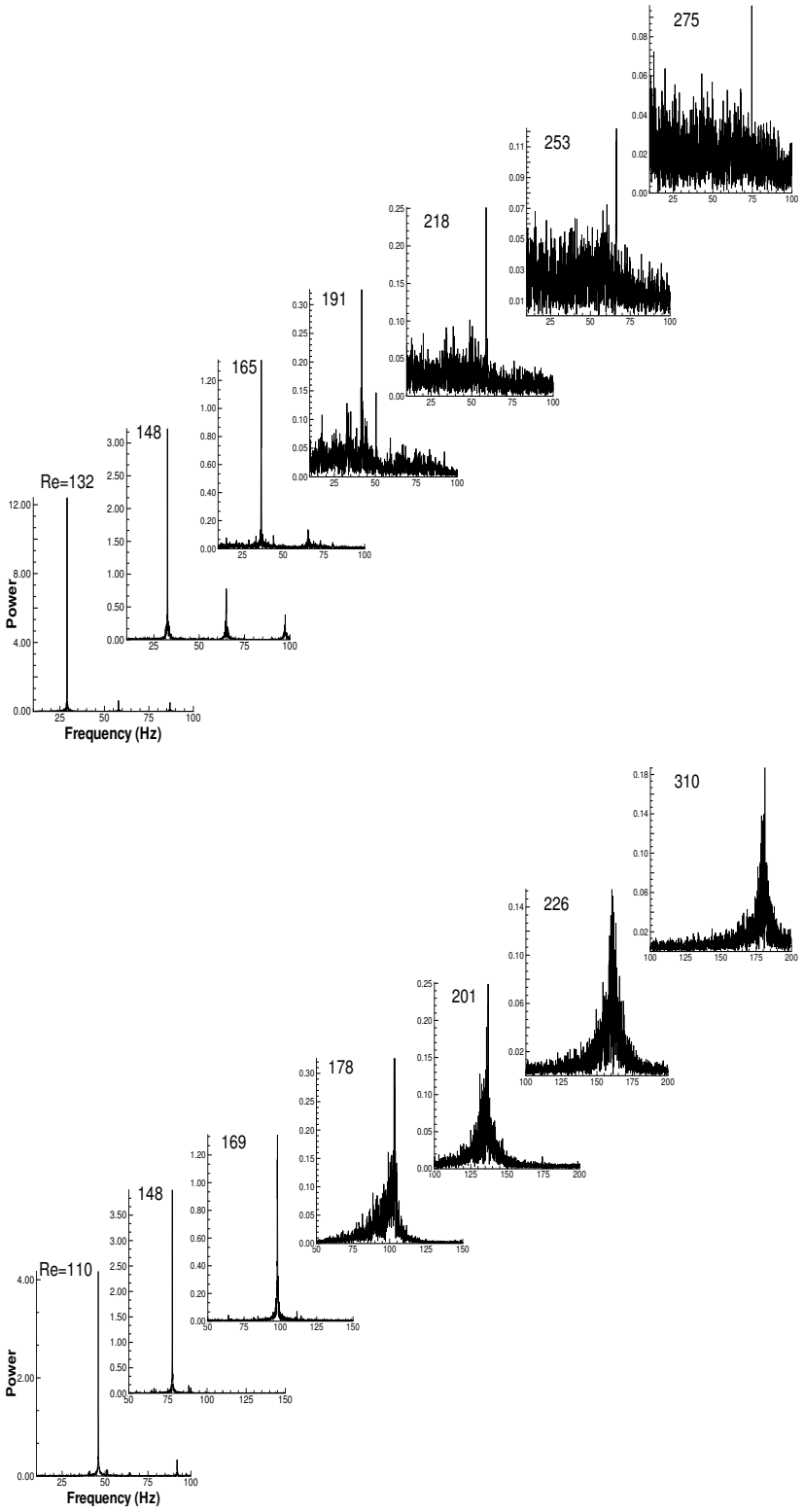

Figure 5.63: Effect of Reynolds number on velocity spectra at x=5 and y=1.2 for two aspect ratios. AR=16 (Top) and 28 (Bottom).

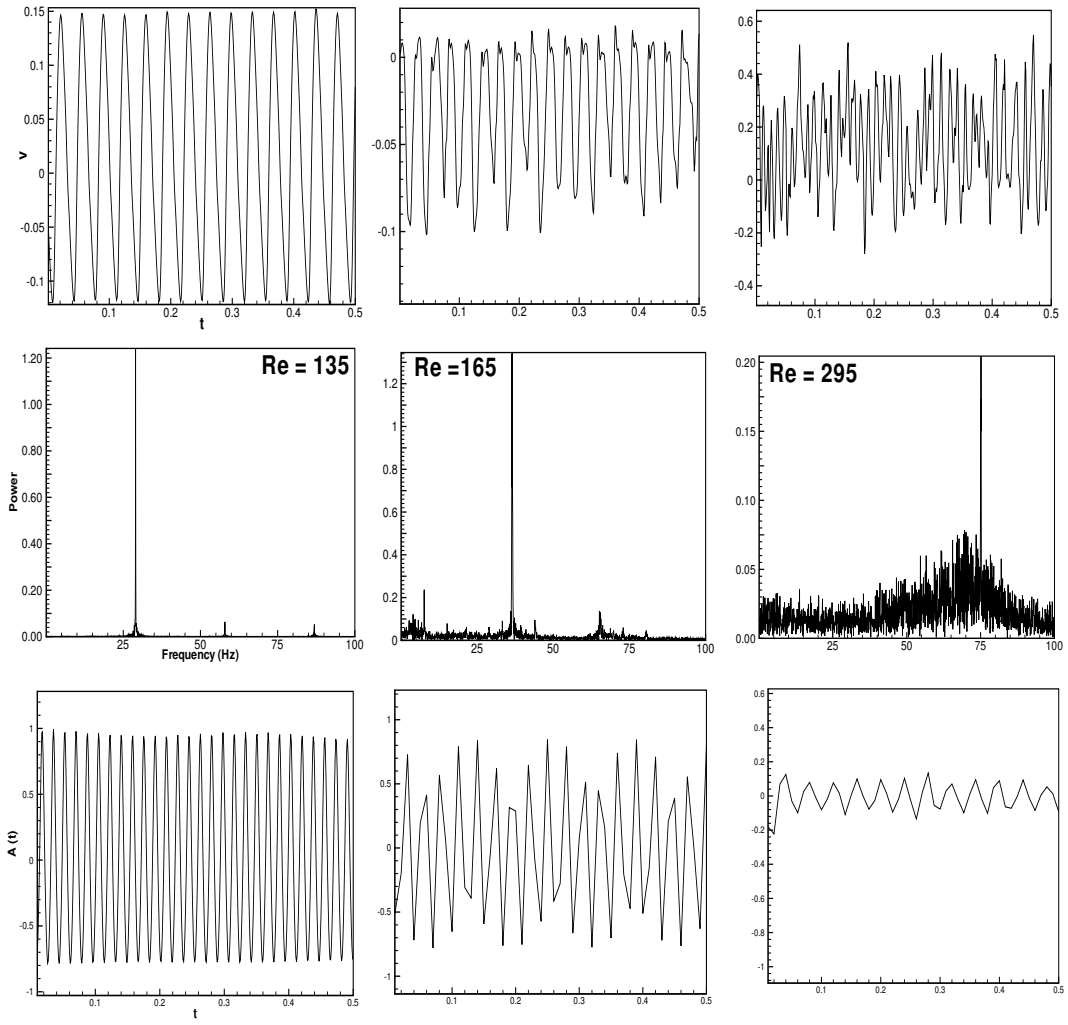

Figure 5.64: Velocity signal (top), power spectra (middle) and autocorrelation function (bottom) for three Reynolds number (Re=135, 165, 295) in the wake of a square cylinder.

5.3.9.1 Poincaré section

This is a qualitative analysis tool that allows one to visualize the unpredictable nature of chaotic flow. Poincaré section systematically reduces the phase space dimensionality. This is accomplished by converting a continuous time evolution into a discrete mapping. The reduced attractor is two-dimensional and is not identical to the original attractor. It however preserves the topological properties of the original attractor from which it has been generated (Bergé *et. al.*, 1986).

In the present study the Poincaré section has been constructed from the time series of velocity by sampling the signal stroboscopically at a particular frequency. A vector

series is defined whose components are $[v(t), v(t+\tau), v(t+2\tau), ...v(t+(m-1)\tau)]$. The time delay, τ and the dimension m need to be properly selected for convergence of solution. In the present work the time series had a length of 2^{14} to 2^{15} points with a time step of 0.001. With the above state vector the trajectory of phase space is constructed with the variables $v(t_s), v(t_s+\tau), t_s$. The Poincaré section is then determined by the successive points of intersection between the trajectory and a plane perpendicular to the axis at equal interval of time $T_s = T_k/4$, where T_k is the fundamental time period of the system corresponding to the dominant frequency.

Figure 5.65 shows the Poincaré sections corresponding to Reynolds number in the range $110 - 610$. The periodic solution at Reynolds number Re=110 and 155 shows a well organized closed curve. The phase space at higher Reynolds number are densely spaced due to additional frequencies. At Re=610 the organized behavior of the Poincaré section breaks down and shows signs of the flow entering the chaotic regime.

5.3.9.2 Lyapunov exponents

The Lyapunov exponent (λ_i) measures the long time-average exponential growth or decay of a infinitesimal perturbations to a phase space trajectory. In operational term these exponents measure the divergence of two neighboring states on the time axis and hence the sensitivity of the system to initial condition. The number of Lyapunov exponent equals the number of independent phase-space dimension. Negative Lyapunov exponent correspond to decay of perturbations towards the attractor. On the other hand, positive hand the positive Lyapunov exponents imply exponential growth of any infinitesimal perturbations on the attractor leading to the chaotic state. An attractor having one positive Lyapunov exponent is termed as a "*strange*" or chaotic attractor.

Different algorithms have been developed to calculate Lyapunov exponents. In the present study the algorithm proposed by Wolf *et al.* (1985) has been implemented to calculate the largest positive Lyapunov exponent from the time series data. Extensive trials with different embedding dimensions were carried out to find the one reliable for the calculation of the Lyapunov exponent.

Figure 5.66 shows the time variation of the Lyapunov exponents at Reynolds numbers 110-610. The number of points used in the time series for each of the Reynolds number is 20000. A zero or negative value value is obtained for non-chaotic attractor. The zero or negative Lyapunov exponent indicates the exponential decay towards the attractor of the trajectories on the phase space when small changes on the initial condi-

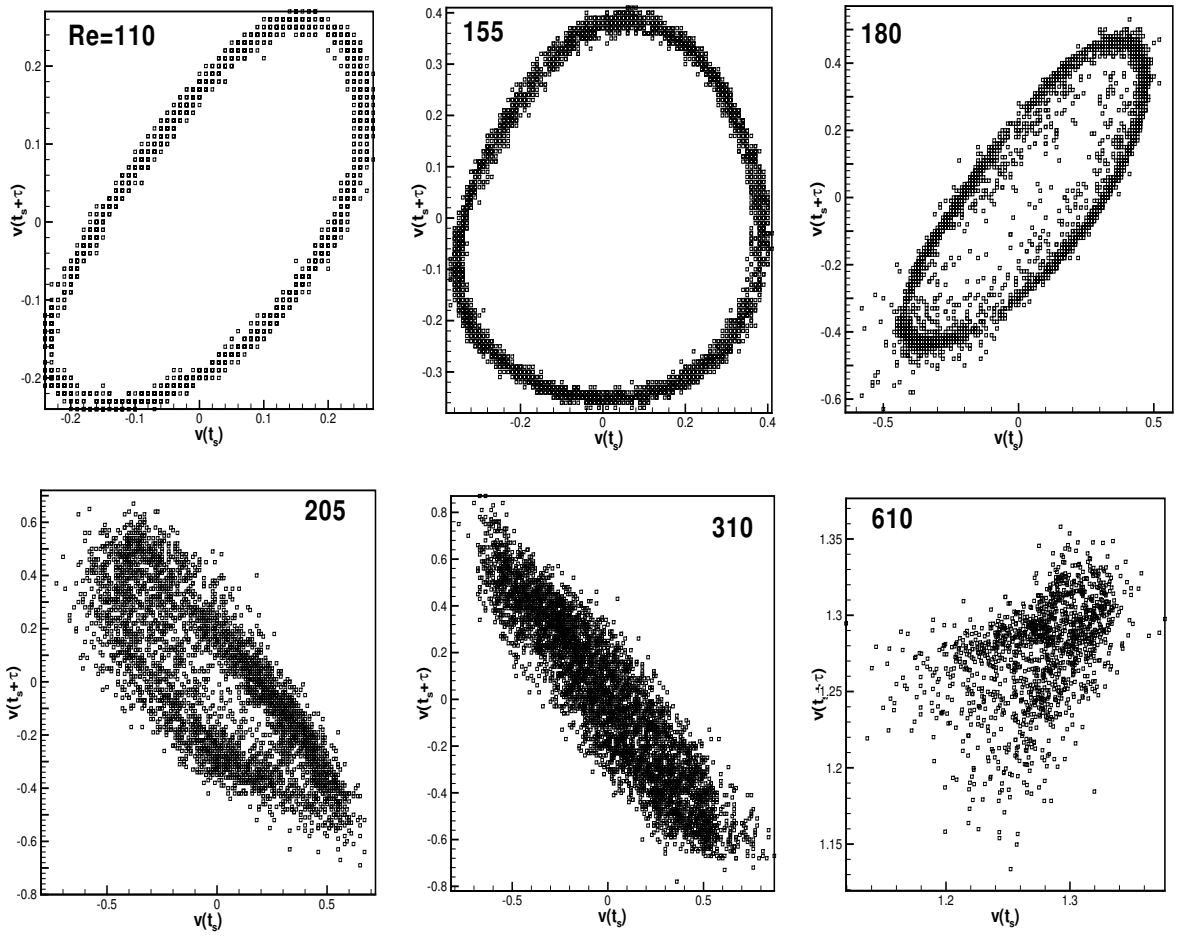

Figure 5.65: Poincaré section of the transverse velocity component at different Reynolds number. The closed orbit at Re=110 and 155 signifies periodic wake whereas the total spreading at a Reynolds number of 610 shows the chaotic nature of flow.

tion occurs. This is seen upto Re=310 from the plot. At Re=610 the Lyapunov value becomes positive which implies flow becomes chaotic.

5.3.10 Flow visualization

The investigation of vortex shedding is important as it is directly related to unsteady forces, structural vibration and turbulent mixing. Figure 5.67 shows the particle traces recorded over a range of Reynolds number (90-285). A Kárman vortex street can be clearly observed over the Reynolds number range. From the images it is observed that greater interaction between alternating vortices starts to appear after Re=110. This is probably responsible for multiple peaks in the power spectra. This observation is also

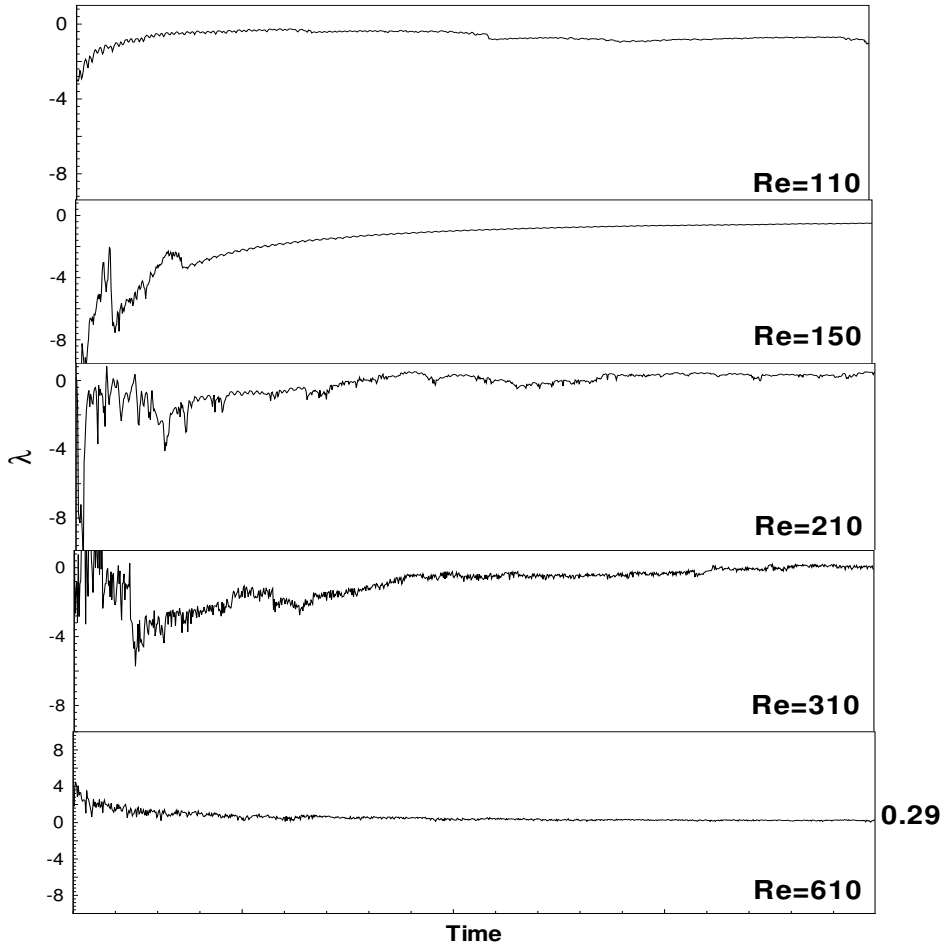

Figure 5.66: Temporal variation of largest Lyapunov exponent λ.

reported by other authors (Saha *et al.* [153], Luo *et al.* [88]). From the images it is also observed that multiple folding of eddies takes place and each eddy is interconnected with each other. Gerrard [45] referred to this pattern as "*fingers*". At higher Reynolds number small scale vortices start appearing within the large scale vortex structure indicating transition to three dimensionality.

5.3.11 Closure

Effect of Reynolds number have been consider in this section. Drag coefficient and Strouhal number shows little dependency on Reynolds number. However the flow structure shows a strong effect on Reynolds number. The Fluctuation level has gone high with increase in Reynolds number. The flow Visualization images shows the effect of Reynolds number clearly. Flow become three dimensional as Reynolds number increases. Power

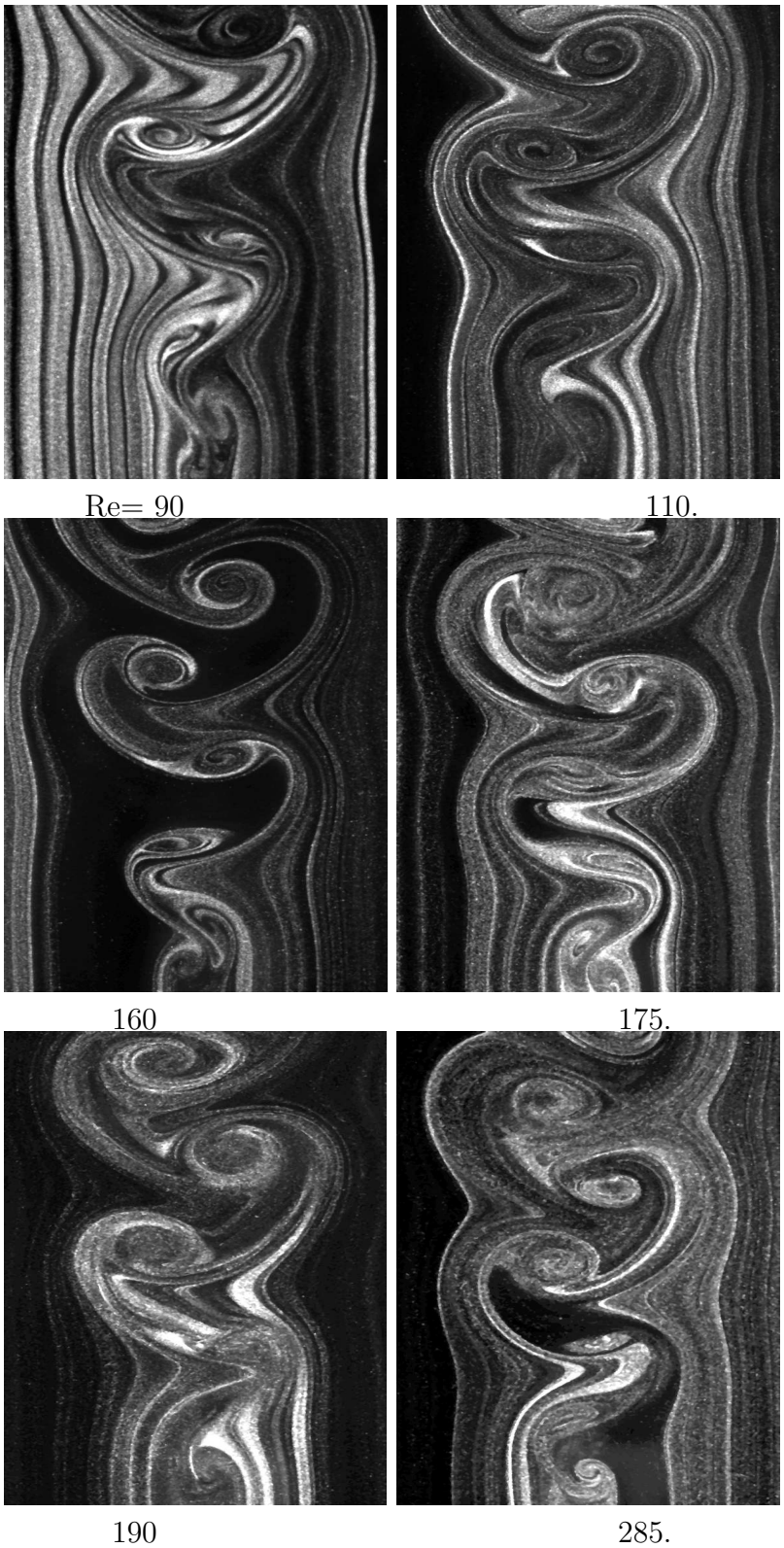

Figure 5.67: Streamwise particle traces from a square cylinder at 0^o cylinder orientation at different Reynolds numbers. AR=28.

spectra also shows that flow become quasi-periodic as Reynolds number increases. Multiple peaks appearing in the spectra which implies energy is shared by other harmonic other than dominant peak frequency. The streamwise velocity fluctuation along cylinder centerline become almost double over the Reynolds number range (Re=165 to 595). The time dependent analysis shows that flow becomes chaotic at Reynolds number of 610.

5.4 Summary

The wake characteristics behind a square cylinder have been studied using PIV, hotwire anemometry and flow visualization. The effect of cylinder orientation with respect to mean flow, effect of aspect ratio and effect of Reynolds number on the wake structure have been investigated. The important observations from this study can be summarized as follows:

(1) Strouhal number and drag coefficient are functions of cylinder orientation. Strouhal number shows an opposite trend with respect to the cylinder orientation compared to that of drag coefficient, i.e. Strouhal is a maximum while the drag coefficient is a minimum at 22.5^o cylinder orientation.

(2) Both Strouhal number and drag coefficient are sensitive to aspect ratio. At higher aspect ratios, the effect of the wall is insignificant. The increase in aspect ratio leads to an increase in Strouhal number and decrease in drag coefficient. The opposite trend for Strouhal number and drag coefficient shows the different roles played by the wake structure on these mean flow behaviour.

(3) Two recirculating bubbles at each side of the central plane of the cylinder are evident in the near field region from the time-averaged stream traces. The size of these recirculation bubbles is a function of cylinder orientation and aspect ratio. The recirculation bubble size is the smallest for 22.5^o cylinder orientation among all the cylinder orientations considered. Similarly, the recirculation zone size is lower for the higher aspect ratio. The smaller recirculation bubble size is an indication of greater wake mixing leading to reduction in the wake deficit and hence lower drag. The velocity magnitude in the immediate downstream of the cylinder confirms the above explanation. The asymmetry of the wake indicates an asymmetric separation process due to cylinder orientation.

(4) The vorticity values (ω_x, ω_y and ω_z) show the contribution of vortical structures. The average vorticity (ω_z) field is more concentrated in the immediate neighborhood of

the cylinder at 22.5^o cylinder orientation. The concentrated contours also move close to the cylinder for the higher aspect ratio. The increased vorticity in the near field region of the cylinder is an indication of greater vortical activity leading to increased mixing and reduction in drag coefficient.

(5) The turbulence intensity plot shows different magnitudes as a function of Reynolds number, aspect ratio and cylinder orientation. The average turbulence intensity is higher at higher aspect ratio. The role played by end conditions or three dimensionality in suppressing the turbulence production at lower aspect ratio is thus revealed. The distribution of the location of turbulence intensity peak in the streamwise direction is an indication of the vortex formation length and correlates with the lower drag at 22.5^o cylinder orientation. The turbulence intensity peak also moves towards the cylinder with an increase in Reynolds number.

(6) The flow visualization images in the streamwise direction show vortical structures and their relative location with respect to each other. The transverse separation is an indication of the interaction between the neighboring vortices of the opposite shear layers. The streamwise separation is an indication of the interaction between the alternate vortices. The role of secondary structures is also evident. The visualization in the spanwise plane indicates the extent of three dimensionality in the flow. The three dimensionality is higher at the lower aspect ratio. Similarly, three dimensionality appears early for the 22.5^o cylinder orientation angle. The appearance of secondary structures are confirmed from the power spectra of the v-velocity fluctuation.

(7) The terms in the kinetic energy budget show their sensitivity to cylinder orientation. The production and diffusion of turbulent kinetic energy in the near field region is a maximum for 22.5^o cylinder orientation and can be attributed to the lower drag values at this orientation.

Chapter 6

Flow past a Square Cylinder at Zero Incidence: Effect of Forced Oscillations

Introduction

Flow past a square cylinder that is oscillated in the streamwise direction is investigated experimentally using PIV and HWA. The interest here is towards active control of the flow field that is likely to result in drag reduction; additionally, the dynamics of the flow phenomena for an oscillating square cylinder at intermediate Reynolds numbers is also of interest. Previous studies have focussed on circular cylinder oscillations. For a circular cylinder, a phase switching mechanism has been observed in the lock-on range. This is absent for a square cylinder, as demonstrated by Ongoren and Rockwell [119] from their flow visualization images. A possible explanation is that the afterbody plays a significant role in creating the phase jump[1]. Compared to free oscillations, forced oscillation helps in regularizing and idealizing every aspect of vortex induced oscillations. The forced oscillation, leads to almost repeatable wake states. Thus, the flow field can be manipulated according to the desired objectives.

Cylinder oscillation provides a coupling between the flow field and the body and usually leads to large correlation length, in the sense that two spatially distinct points maintain a time-independent phase relationship (Blackburn and Henderson [19]). The wake formation is dominated by an absolute instability and there is a close relation between the vortex formation process and the dynamics of the near-wake Kárman vortex street (Cetiner and Rockwell [28]). The basic difference between forced oscillation and

[1] An afterbody refers to the shape of the object beyond the point of separation.

free oscillation is as follows. For forced oscillation, the fluid motion is coupled to the body motion and not *vice-versa*; in free oscillation, the fluid-structure coupling can occur in both directions. The body motion can control the instability mechanism and vortex shedding. Hence, the flow generated by vortex shedding around a vibrating body can have very significant differences from that of a stationary cylinder. The oscillation can be either transverse or inline to the mean flow direction. In the case of inline oscillations, locked-on or quasi-locked states arise for the forcing frequency required is double the vortex shedding frequency (Griffin and Hall [53]). In transverse oscillations, locked states occur close to the shedding frequency.

The term *lock-on* is often used to convey the following idea. The body motion is synchronized with the cycle of vortex shedding. Thus, each vortex is shed when the cylinder is at its mean position in a cycle of oscillation. Two vortices are shed for one complete cycle of cylinder movement. From the view-point of the near-wake, the unsteadiness at lock-on resembles that of a stationary cylinder. For forcing frequencies below that of lock-on, one can expect the shedding frequency to be dominant. At much higher forcing frequencies, the wake is to be expected to contain the signature of the cylinder movement.

The vortex formation in the near-wake determines the wake structure and the forces on the cylinder. Shedding may be symmetric or asymmetric depending on the forcing frequency. The pattern of vortex formation and the associated in-line and transverse force component depend on the Keulegan- Carpenter number[2] ($KC = 2\pi A/B$) and the reduced velocity ($V_r = U/fB$), where A is the amplitude of oscillation, B is the cylinder diameter, and f, the forcing frequency.

For a cylinder at zero angle of incidence, the time-averaged flow field is symmetric about the x-z plane (the plane that carries the cylinder axis). Symmetry of this type breaks down for an oscillating cylinder. This is because the edge (on either side of the symmetry plane) shedding a vortex and moving in the streamwise direction would produce a longer shear layer. In contrast, an edge shedding a vortex but moving in a direction opposed to the main flow would produce a shorter shear layer[3]. Consequently, the time-averaged flow field will reveal an asymmetry in the time-averaged streamline patterns. Asymmetry is expected to be small when the cylinder frequency is close to the vortex shedding frequency. Since a higher amount of energy pumped into the fluid will disturb symmetric interactions, asymmetry is expected to increase with the amplitude

[2]The Keulegan-Carpenter number is also referred to in the literature as Carpenter number.
[3]distances being measured from the mean position of the cylinder.

of oscillation.

The present chapter reports results for a square cylinder with forced oscillations for a reduced velocity ($V_r = U/fB$) range 3 to 15 and a Carpenter number KC < 2. Two Reynolds numbers (Re= 170 and 355) and various amplitudes of oscillation and frequency have been considered. The frequency of oscillations is varied near the vortex shedding frequency (f/f_o =0.5, 1 and 2) and amplitude (A/B) varied from 0.05 to 0.3 taking into account the threshold value of amplitude of oscillation for lock-on (namely A/B=0.05 (Griffin *et al.* [48]).

The detailed study on effect of oscillation has been investigated with respect to the following parameter:
(a) Effect of forcing frequency
(b) Effect of forcing amplitude
(c) Effect of aspect ratio

6.1 Effect of Forcing Frequency

In this section, the effect of forcing frequency on the flow field at a fixed amplitude ($A/B = 0.1$) is presented. The amplitude level is well above the threshold (A/B=0.05) at which lock-on occurs for in-line oscillations (Griffin [51]). Two Reynolds numbers (Re=170 and 355) have been considered. Flow field has been characterized in terms of drag coefficient, Strouhal number, time-averaged velocity field, RMS velocity fluctuations, centerline recovery, vorticity contours, streamline pattern, power spectra and flow visualization.

6.1.1 Drag coefficient and Strouhal number

Drag coefficient has been calculated from the time-averaged velocity profile at a downstream location of $x = 15$ using the momentum balance approach. The total (instantaneous) inline force of an oscillating cylinder has an extra term known as *added mass*. This term comes into existence when there is an acceleration of the body. The added mass contribution to the instantaneous force can be positive or negative depending on the relative direction of body motion with respect to the mean flow. Added mass depends on the type of motion of the body and the fluid, the proximity of other bodies and time. In

unsteady flows, drag is neither equal to its steady state value nor is the added mass equal to its inviscid value (Sarpkaya, 2004). Sarpkaya (1978) has demonstrated experimentally that the added mass coefficient decreases rapidly with increasing reduced velocity (V_r), becomes nearly equal to unity at perfect synchronization, and then becomes negative as (V_r) increases further. In the present study, the quantity reported is the time-averaged drag coefficient and the added mass contribution is not included[4].

Table 6.1 presents the drag coefficient measured at various frequencies of oscillation from the time-averaged mean velocity profile. The amplitude of oscillation is kept constant in these experiments at A/B=0.1. Drag coefficients have been calculated for two Reynolds numbers. The magnitude of C_d decreases with increase in forcing frequency for both lower and higher Reynolds number (Re=170 and 355). These results have been explained against fluid flow measurements in the later sections.

Table 6.1: Drag coefficient as a function of forcing frequency.

f/f_o	Re=170	Re=355
0	1.48	1.41
0.5	1.13	0.78
1.0	0.68	0.83
2.0	1.05	0.58

Table 6.2 presents the Strouhal number data as a function of frequency of oscillation at two Reynolds numbers. Strouhal number has been calculated based on the dominant peak in the spectrum. No significant change in Strouhal number as a function of forcing frequency is observed, although the overall value increases with an increase in Reynolds number. This indicates no lock-on between the cylinder oscillation with the vortex shedding and the vortex shedding frequency is still the dominant mode. However, the oscillation at other frequencies modifies the wake structures leading to reduction in momentum deficit i.e. drag coefficient at higher excitation frequency.

6.1.2 Velocity field

The time-averaged velocity vectors for various oscillation frequencies are shown in Figures 6.1 and 6.2 for two Reynolds number (Re=170, 355). Both x and y-axes have been

[4]Added mass being proportional to fluid density, once can expect it to be small in air, but large in water.

Table 6.2: Strouhal number as a function of forcing frequency.

f/f_o	Re=170	Re=355
0	0.138	0.154
0.5	0.135	0.151
1.0	0.135	0.151
2.0	0.138	0.154

nondimensionalised with the cylinder height. The shaded contours are of resultant velocity. The near field velocity vectors are seen to be affected by the forcing frequency. The zone of velocity deficit reduces due to the cylinder oscillations. The overall shape of the flooded velocity contours is similar at all the cases except at Re=170 and f/f$_o$=2.0. For this condition the drag value has shown marginal increase corresponding to fundamental excitation (Table 6.1). The cylinder continually accelerates and decelerates during its motion in the fluid. The flow entrainment is influenced by the cylinder oscillations which in turn is responsible for a reduction in the recirculation zone size. The shape and size of the flooded velocity contours demonstrates the size of the recirculation zone as a function of excitation frequency. The recirculation zone width reduces with increase in forcing frequency. The effect of excitation on the velocity vector distribution is dependent on the Reynolds number. The near wake structure behind a bluff body is influenced by the overall vortex formation and shedding processes and determines the magnitude of the mean and fluctuating forces on the body. Hence, the velocity vectors reveal the effect of oscillation on both instantaneous and time-averaged forces acting on the cylinder.

Figures 6.3 and 6.4 show the time-averaged u and v- velocity profiles respectively at three x locations (=2, 5 and 10) for Re=170. Both components of velocity have been normalized with the average incoming velocity. The centerline velocity deficit is a minimum at a forcing frequency equal to twice the shedding frequency. The u- velocity at this frequency shows a double-humped profile at x=10. All other u-velocity profiles are U-shaped, as is common for a stationary cylinder in an infinite medium. A simple explanation can be given for the shape realized. When pure Kárman type vortex street is formed for a cylinder that is unforced or subjected to low frequency oscillations, vortices remain on the same side of the wake in which they are shed from the body. The induced velocity at y=0 from this arrangement of vortices is in the upstream direction (negative x direction), which contributes to the centerline velocity defect and produces a U-shaped profile. However, when the centres of vortices cross the wake centerline, (also seen in the instantaneous vorticity contours Figure 6.21) the induced velocity is in the downstream

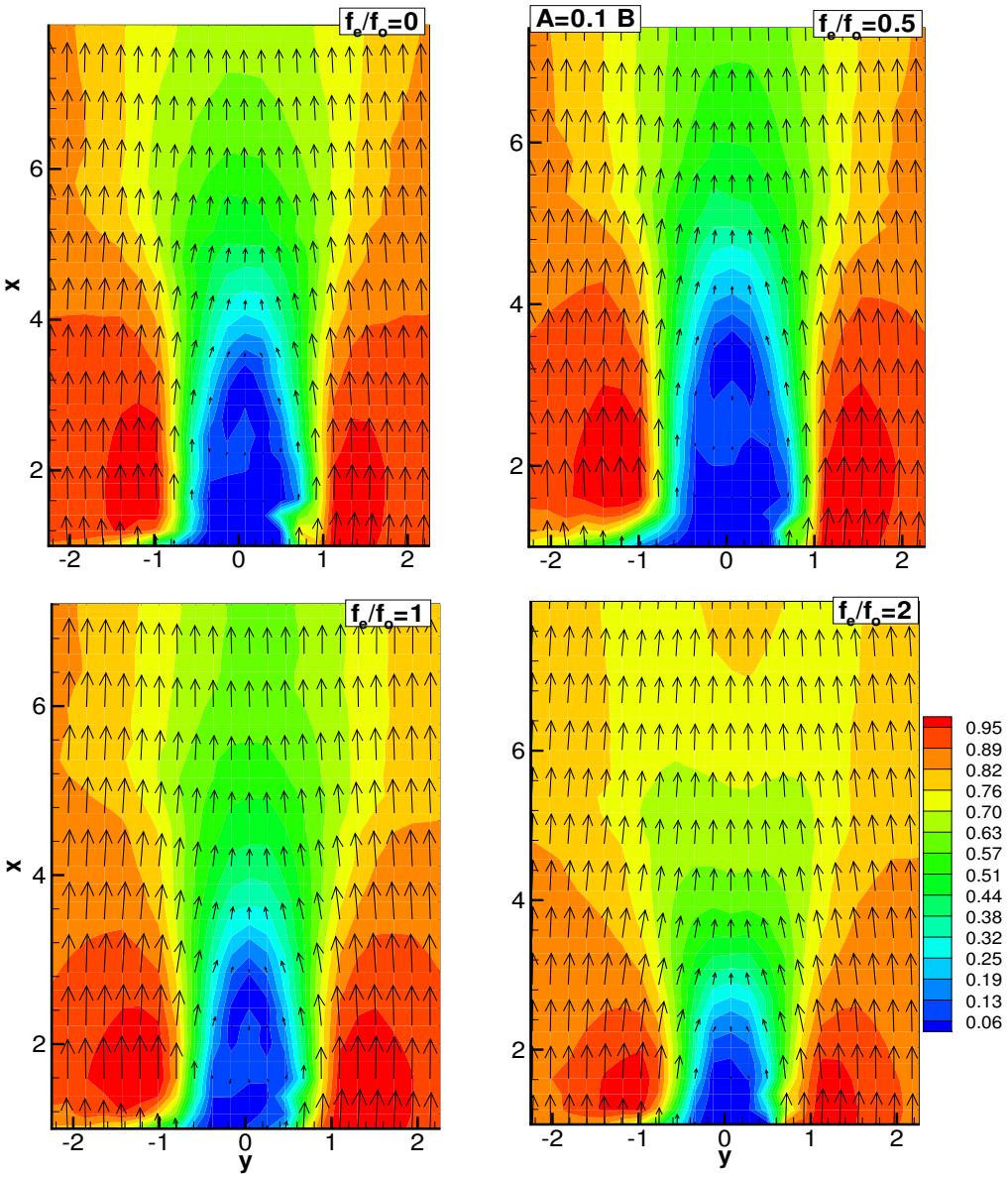

Figure 6.1: Time-averaged non dimensional velocity vectors at various frequencies of oscillation, amplitude ratio (A/B)=0.1, Re=170. The flooded contours represent the absolute velocity magnitude.

direction (positive x direction). Consequently, the induced velocity from a fully formed vortex at $y = 0$ in the downstream direction produces two local maxima of the double-humped profile.

The effect of forcing frequency on the flow field is not significant for the sub-harmonic excitation (f/f_o=0.5). A strong effect of forcing frequency in the near wake is realized at f/f_o= 1 and 2. The v-velocity is also affected significantly at these forcing

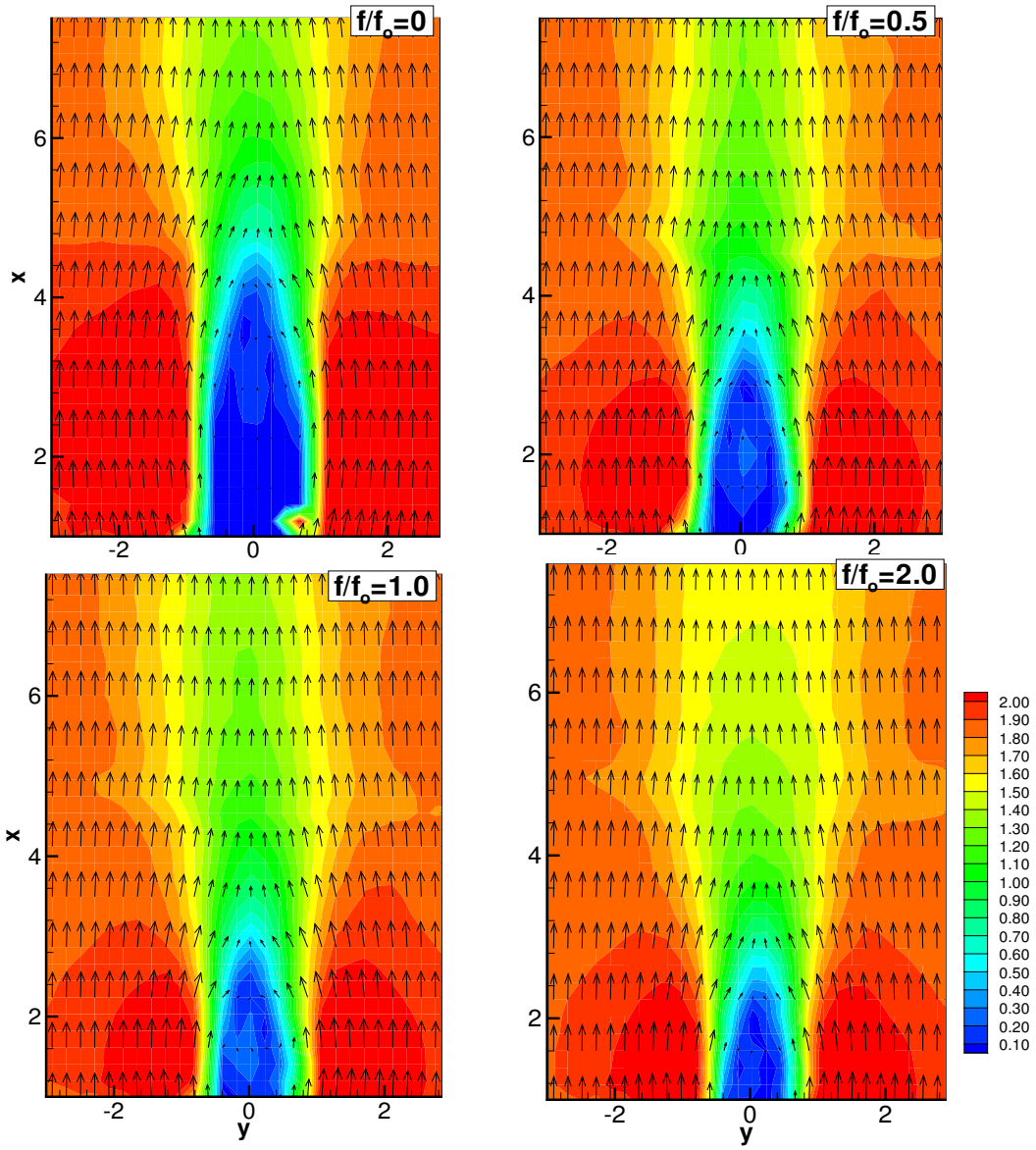

Figure 6.2: Time-averaged non dimensional velocity vectors at various frequencies of oscillation, Re=355 and amplitude of oscillation (A/B)=0.1. The flooded contours represent the absolute velocity magnitude.

frequencies, Figure 6.4. The magnitude of v-velocity increases with increase in the oscillation frequencies and is highest at f/f$_o$=2.0. The increase in v-velocity indicates greater interaction between the vortices of opposite shear layer. This has been confirmed from the instantaneous vorticity plots and visualization images shown in later Sections. The centerline recovery of the streamwise velocity component is faster at these frequencies, as also seen in Figure 6.19. For an excitation frequency, f/f_o=2.0, the development of the

v-velocity is slower in the downstream locations. Figures 6.5 and 6.6 respectively show the u and v- velocity distribution at a higher Reynolds number (Re=355). The u-velocity profile does not show any significant difference at Re=355 compared to Re=170. The v-velocity profiles at higher Reynolds number show higher value compared to the lower Reynolds number indicating the greater interaction between neighboring vortices in the opposite shear layer. The recirculation bubble size in streamwise (x) direction has been

Table 6.3: Recirculation length as a function of forcing frequency.

f/f_o	Re=170	Re=355
0	2.80	2.50
0.5	3.20	2.17
1.0	1.50	1.97
2.0	0.50	1.50

shown in Table 6.3 for different excitation frequency with fixed amplitude (A/B=0.1). The recirculation length shows marginal increase at sub-harmonic excitation (f/f_o=0.5) at Re=170. The continuous drop in the recirculation bubble size confirms the lower drag observed with increase in excitation frequency (see table 6.1).

6.1.3 Time-averaged vorticity contours

Figures 6.7 and 6.8 shows the time-averaged spanwise vorticity (ω_z) contours for various frequency ratios (f/f_o=0, 0.5, 1.0 and 2.0) at a constant amplitude of oscillation (A/B = 0.1). Data for two Reynolds numbers (Re=170 and 355) have been presented. Vortices are subjected to strain fields imposed by the near field vortices. They diffuse and are swept across the wake, while being dissipated by viscosity. With an increase in frequency, the vortices move closer to the cylinder and thus get concentrated in the near-wake. The maximum strength of the vortices, as measured by the vorticity magnitude does not change very much with frequency of oscillation. Vorticity concentration in the near field region has also been observed in the context of circular cylinder oscillations (Gu *et al.* [49]). The concentration of maximum vorticity zone in the near field region for the forcing frequency, f/f_o=2.0 confirms to the relative drop in recirculation zone size in Figures 6.1 and 6.2. A comparison of Figures 6.7 with 6.8 indicate no systematic variation of the maximum vorticity zone with increase in Reynolds number, though the peak vorticity is understandably higher. To a first approximation, one can surmise that the

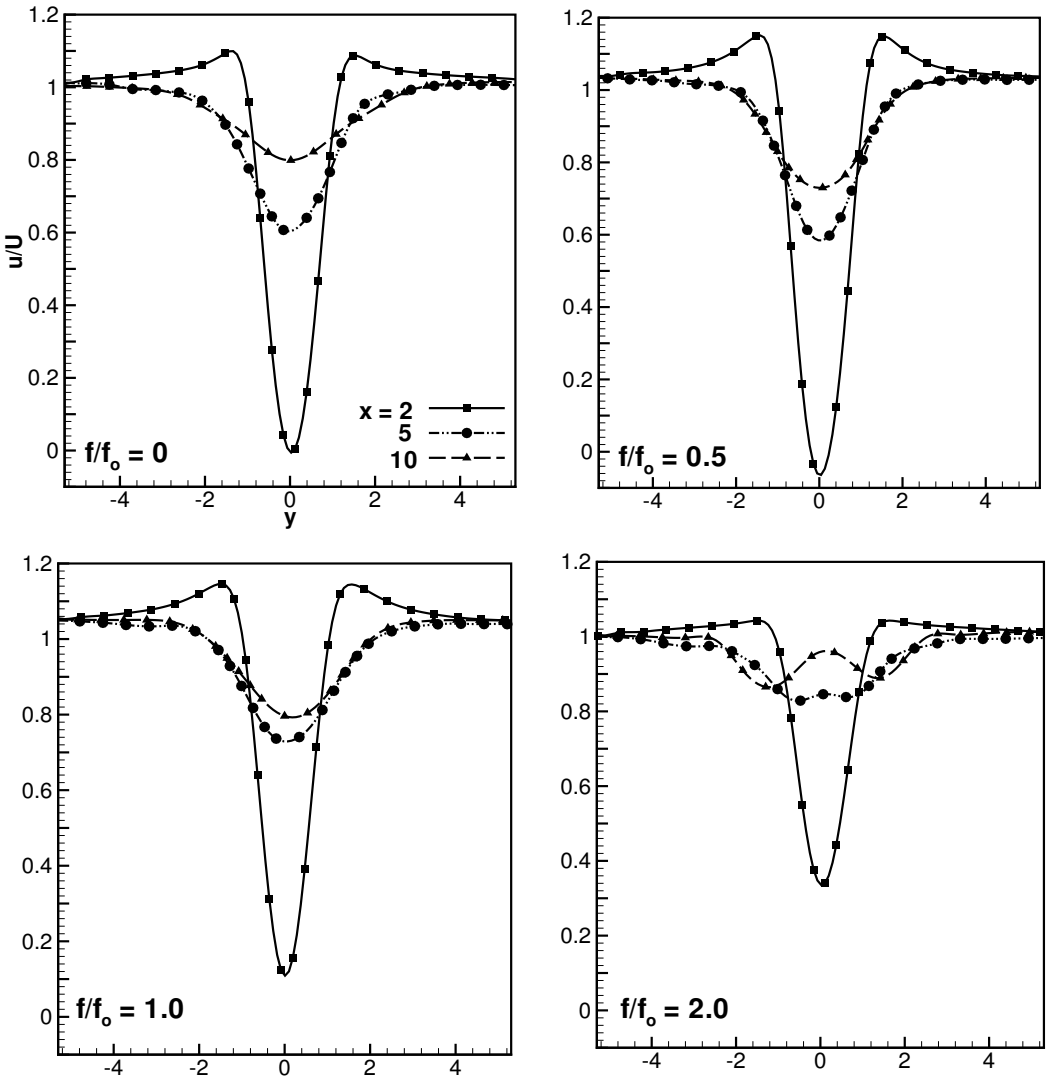

Figure 6.3: Time-averaged u-velocity profiles at various frequencies of oscillation (f/f_o=0, 0.5, 1.0 and 2.0) and three downstream locations (x=2, 5 and 10), Re=170, A/B=0.1.

effects of Reynolds number and frequency on the wake are independent[5]. Additionally, the convective speed of vortices leaving the cylinder (that determines Strouhal number) seem to be invariant with respect to frequency, though a function of Reynolds number. The effect of forced oscillations on flow symmetry is marginal, as seen from vorticity contours. The sizes of two oppositely oriented vortices are similar to each other, though not equal for the frequencies considered.

[5]specifically, the instability characteristics

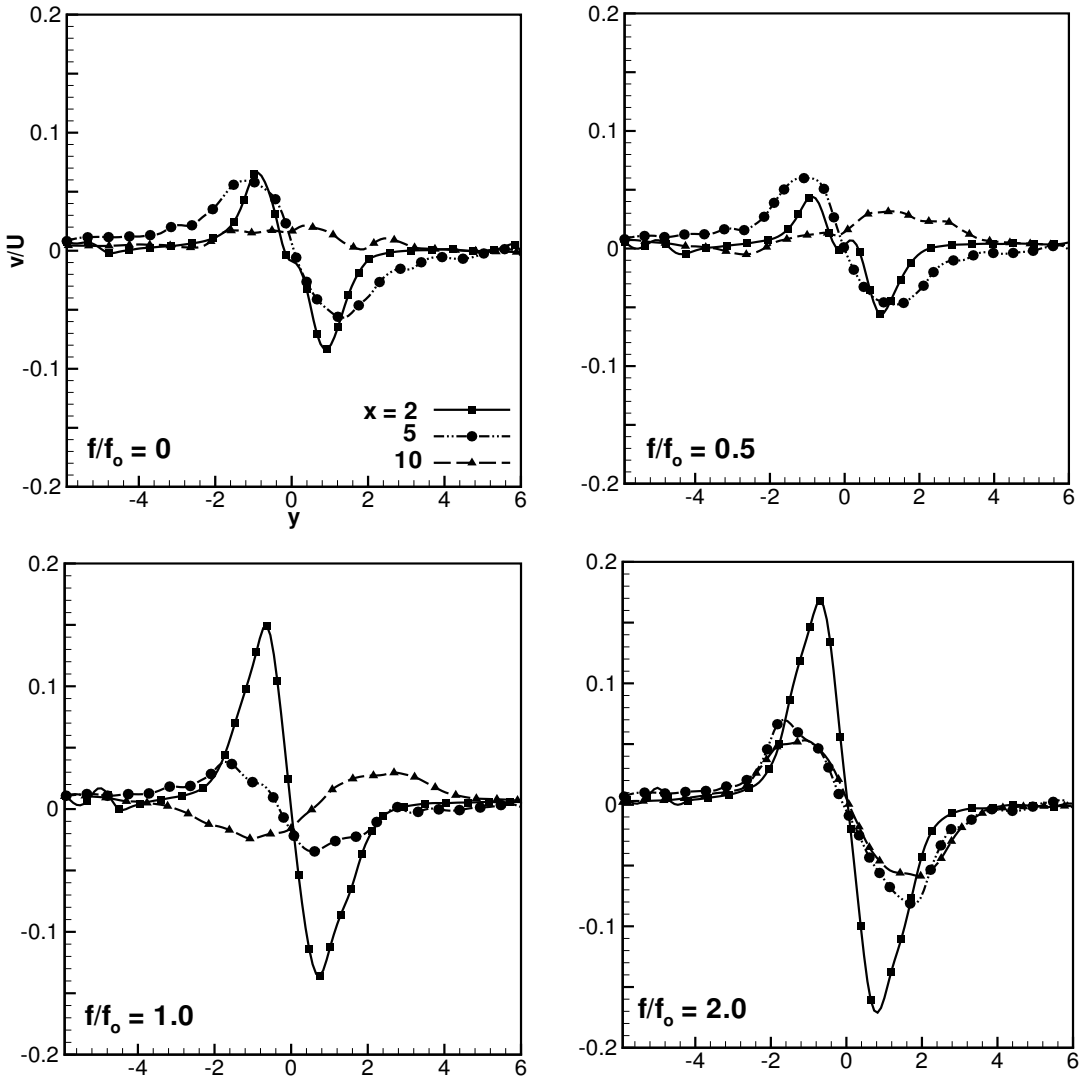

Figure 6.4: Time-averaged v-velocity profiles at various frequencies of oscillation (f/f_o=0, 0.5, 1.0 and 2.0) and three downstream locations (x=2, 5 and 10), Re=170, A/B=0.1.

6.1.4 Time-averaged streamlines

Figures 6.9 and 6.10 show the streamline contours from the time-averaged velocity vectors at the mid-span of the cylinder[6] for Re=170 and 355 respectively. The streamline patterns show that with an increase in excitation frequency, the size of the recirculation bubble reduces. This result has been observed for a circular cylinder by other authors, notably Konstantinidis *et al.* [77]. Zdravkovich [194] pointed out that wakes of a cylin-

[6]As discussed in Chapter 4, 300 PIV image pairs were averaged.

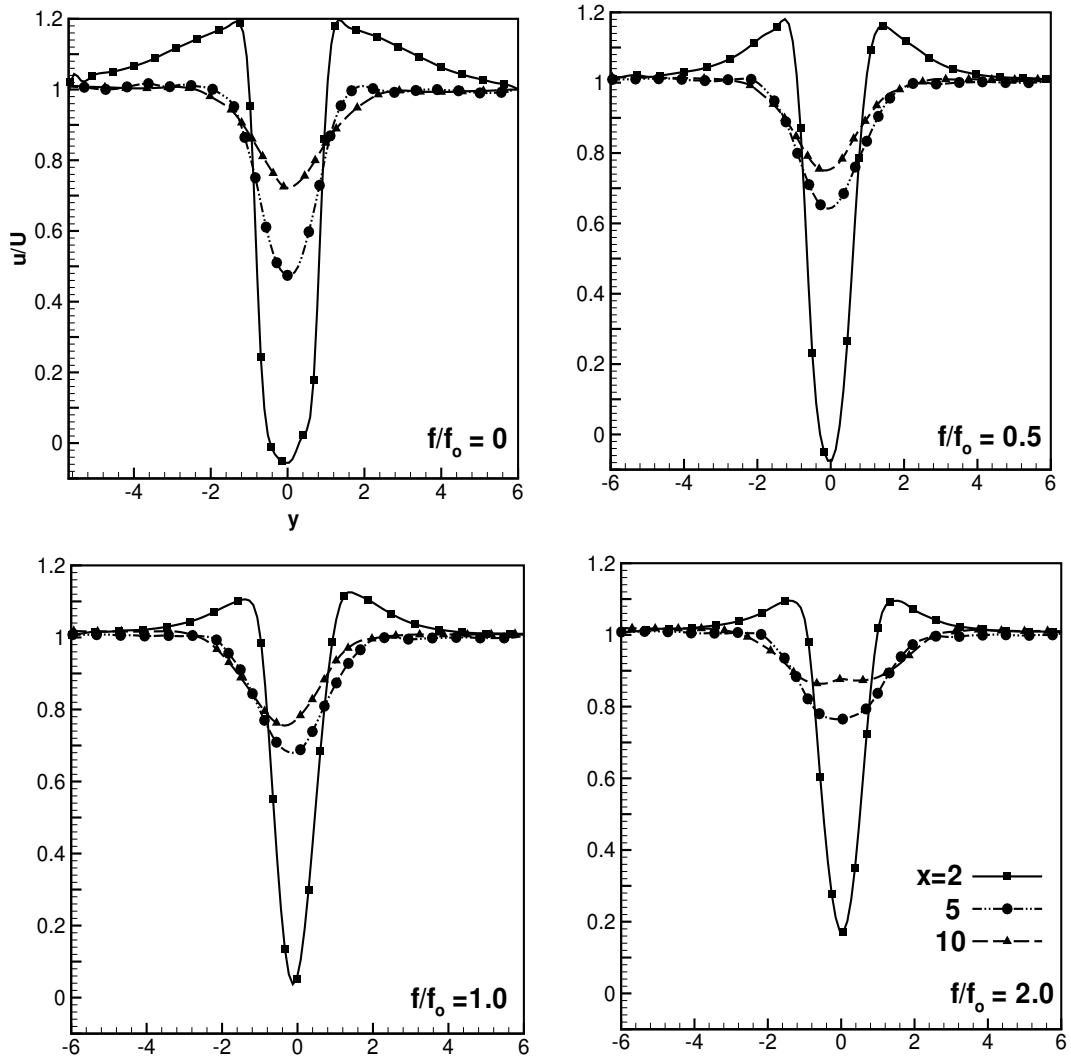

Figure 6.5: Time-averaged u-velocity profiles at various frequencies of oscillation (f/f_o=0, 0.5, 1.0 and 2.0) and three downstream locations (x=2, 5 and 10), Re=355, A/B=0.1.

der forced to oscillate in either the transverse or the streamwise direction share several characteristics, including reduction in vortex formation length and an increase in base pressure. The reduction in vortex formation length in the synchronization range has also been observed for a circular cylinder oscillated in the transverse direction (Krishnamoorthy *et al* [76]). The reduction in vortex formation length indicates directly an increase in the base pressure and hence a reduction in the drag coefficient. At a higher Reynolds number (Re=355) the recirculation bubble is visibly asymmetric. The length of the recirculation bubble, however, decreases with an increase in forcing frequency as

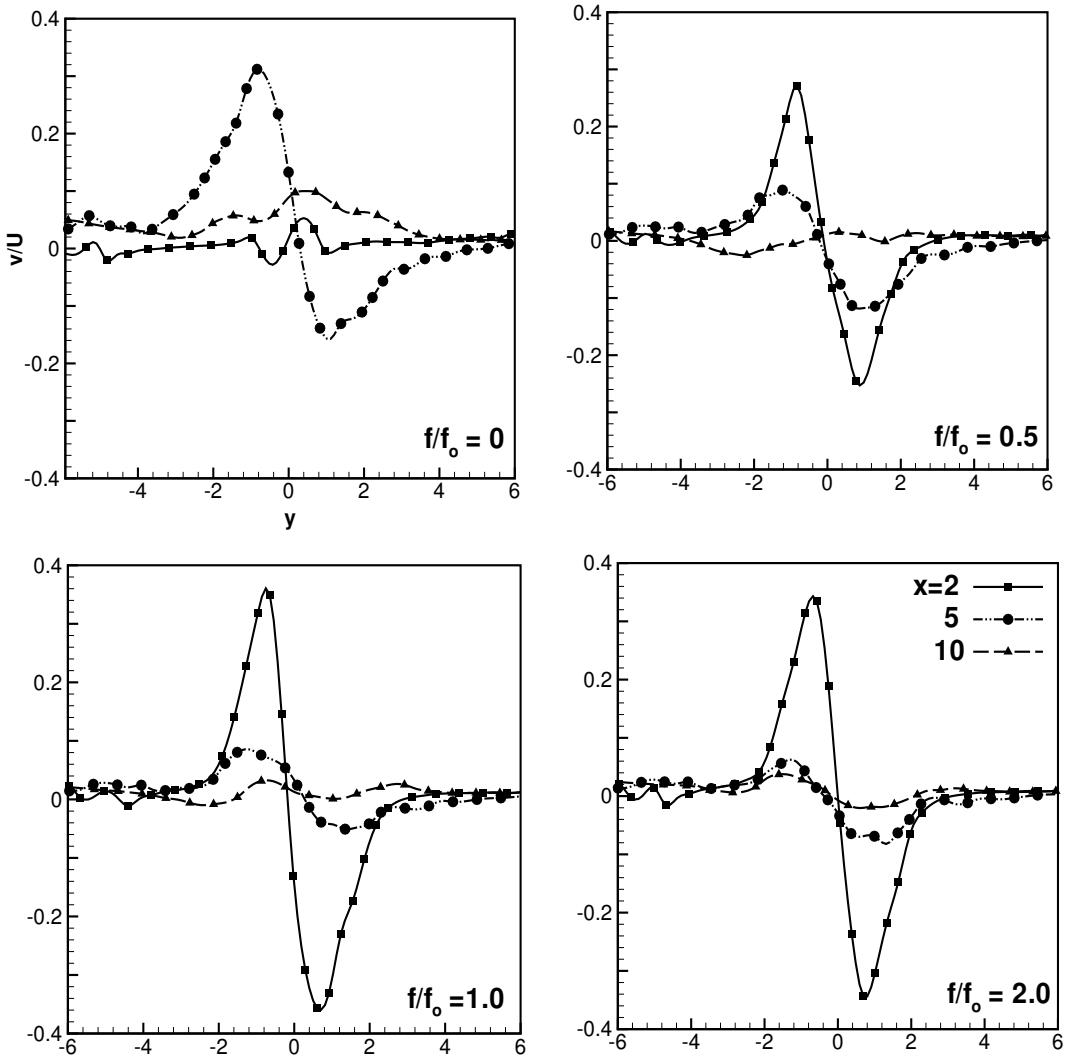

Figure 6.6: Time-averaged v-velocity profiles at various frequencies of oscillation (f/f_o=0, 0.5, 1.0 and 2.0) and three downstream locations (x=2, 5 and 10), Re=355, A/B=0.1.

in the lower Reynolds number experiments (Re=170).

6.1.5 Velocity fluctuations

Figures 6.11 and 6.12 show the spatial distribution of turbulence intensity ($= \sqrt{u'^2 + v'^2}/U$) for two Reynolds numbers of 170 and 355 respectively. RMS values have been normalized with the incoming velocity. With an increase in frequency, the location of maximum turbulence intensity moves closer to the cylinder. There is a strong effect of forcing fre-

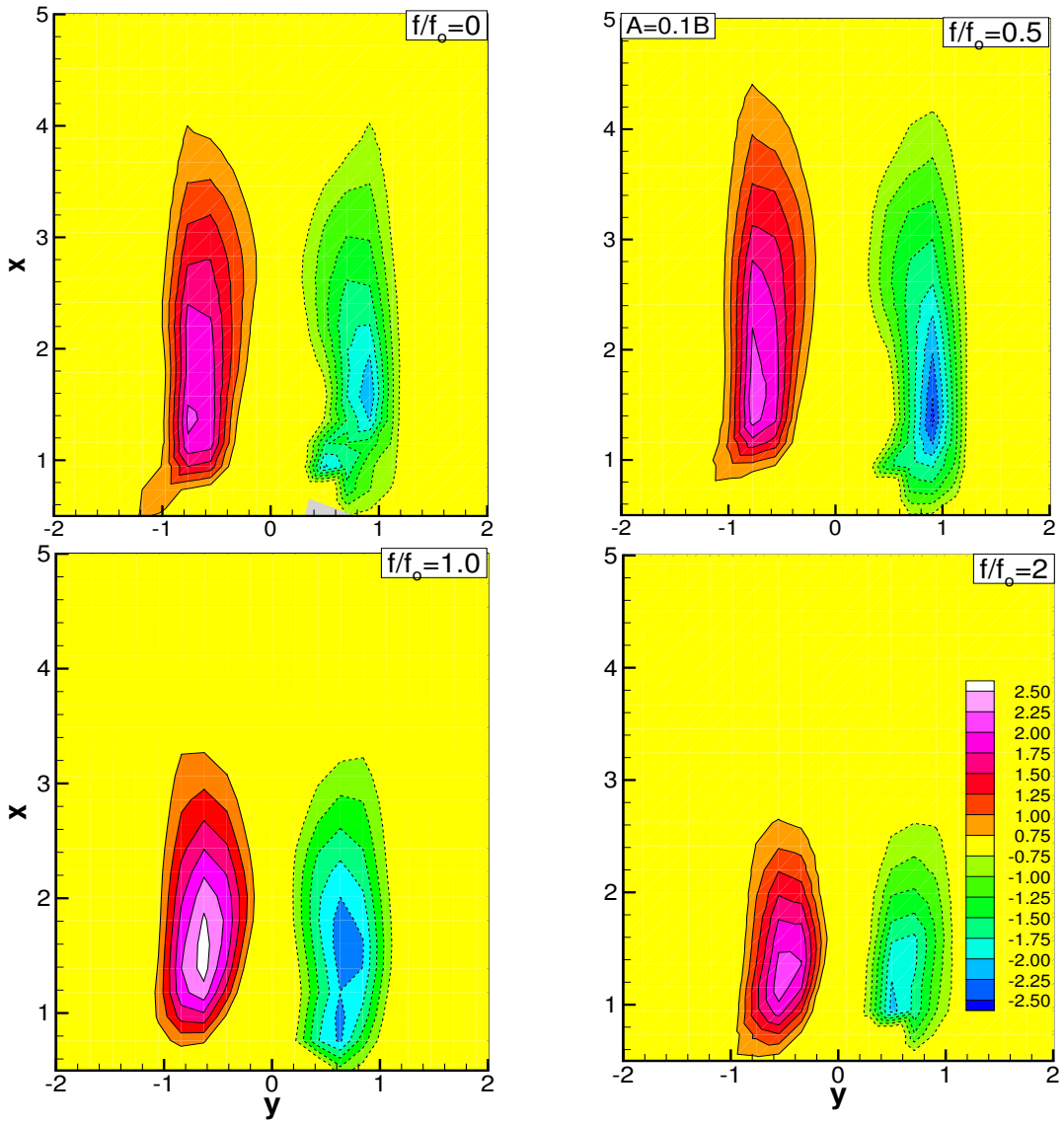

Figure 6.7: Time-averaged vorticity contours (ω_z) at various frequencies of oscillation (f/f_o=0, 0.5, 1.0 and 2.0) for flow past a square cylinder at Re=170 and amplitude of oscillation (A/B)=0.1.

quency on the intensity field, increasing with frequency and reaching a maximum at $f/f_o = 2.0$. The size of the maximum turbulence intensity zone widens in the transverse direction, with an increase in excitation frequency. This observation is to be expected since transport across the wake is governed by advection by the transverse (v) velocity and gradient diffusion by the effective viscosity. A double peak in RMS values appears on each side of the cylinder for f/f_o=2.0; this result was noticed for the time-averaged velocity vectors and streamwise velocity profile as well (Figure 6.1 and 6.3). The dou-

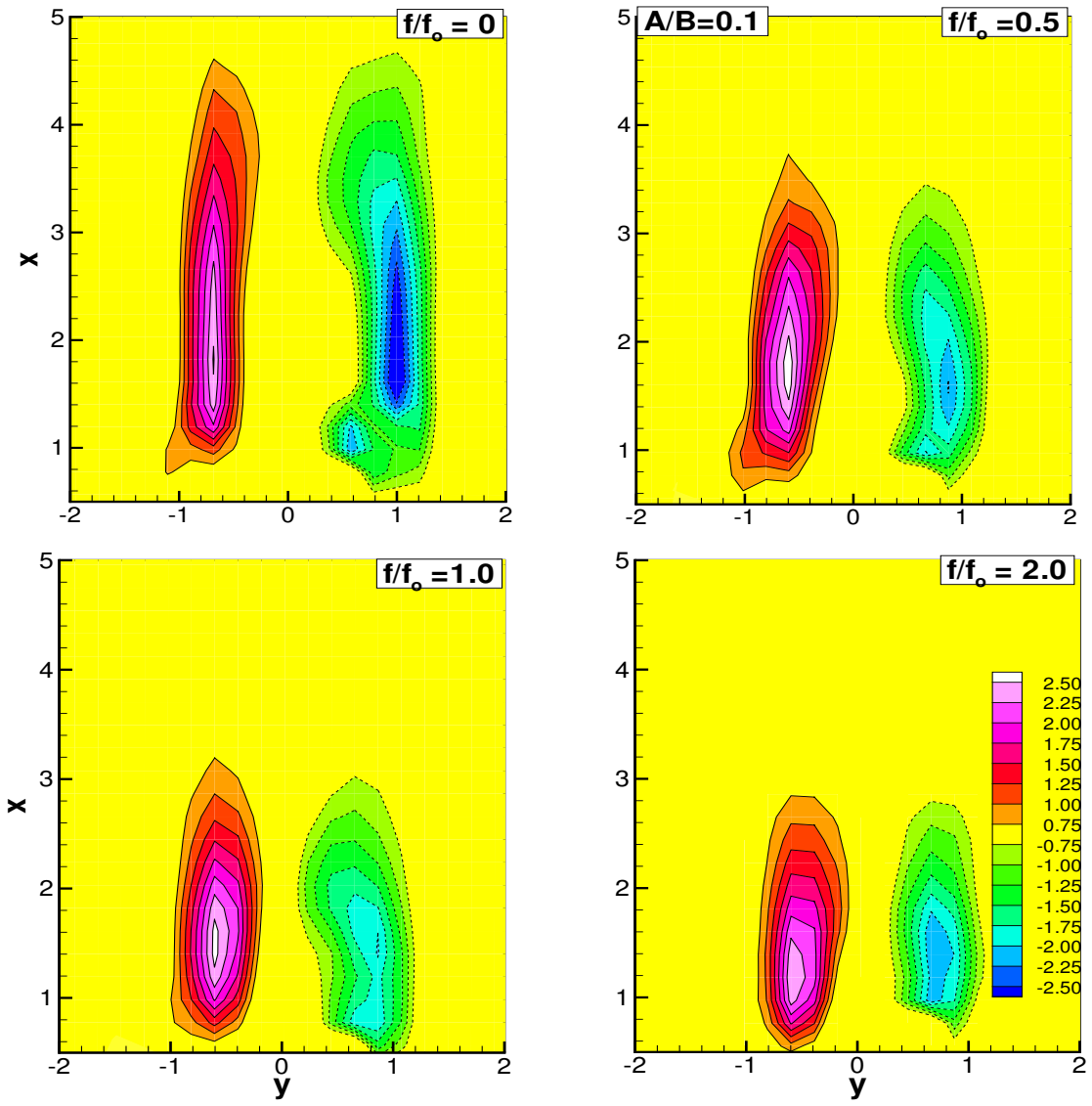

Figure 6.8: Time-averaged vorticity contours (ω_z) at various frequencies of oscillation (f/f_o=0, 0.5, 1.0 and 2.0) for flow past a square cylinder at Re=355 and amplitude of oscillation (A/B)=0.1.

ble peak in turbulence intensity is seen at the lower Reynolds number but not at the higher Reynolds number. This demonstrates the difference in instability characteristics arising from the Reynolds number influence on the separating shear layer. The transverse spreading of the velocity fluctuation field is, however, dependent on the cylinder frequency. The turbulence intensity was also seen to spread more in the transverse direction for higher excitation frequency.

Figure 6.13 shows the development of normalized RMS velocity components along

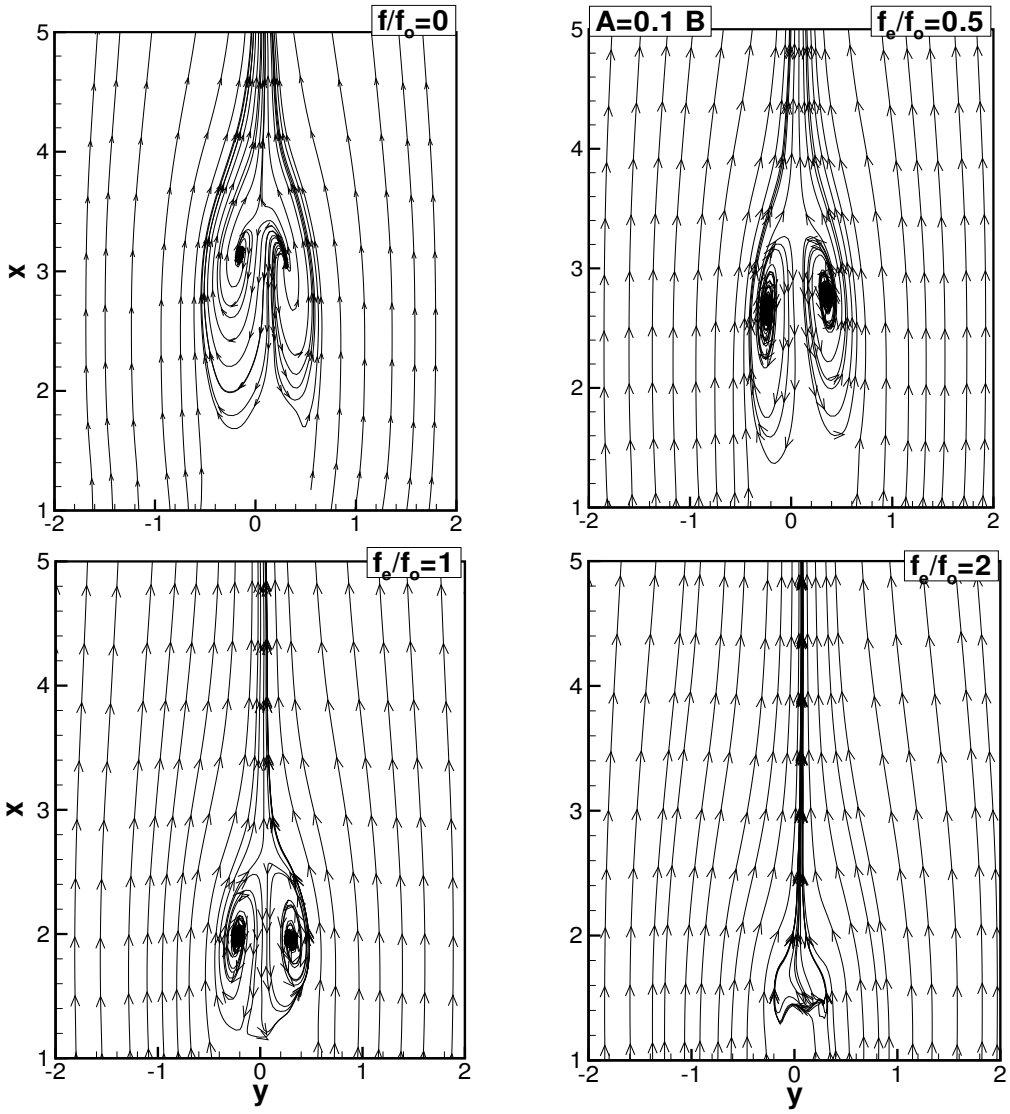

Figure 6.9: Time-averaged streamlines in the wake of a square cylinder at various frequencies of oscillation (f/f_o=0, 0.5, 1.0 and 2.0), perturbation amplitude is unchanged (A/B)=0.1 and Re=170.

the cylinder centerline for various forcing frequencies at Re=170 and 355. A systematic variation in the RMS profiles with forcing frequency is to seen in the near field region. The figure shows RMS values of both u and v velocity peaks at certain x distance from the cylinder and subsequent drops to a small value for each forcing frequency. The downstream location where the peak in the streamwise velocity (u_{rms}) occurs is different from that of the transverse velocity (v_{rms}). Unlike the u_{rms} velocity, the v_{rms} velocity shows a slower decay after attaining the peak value. The position of the peak in the

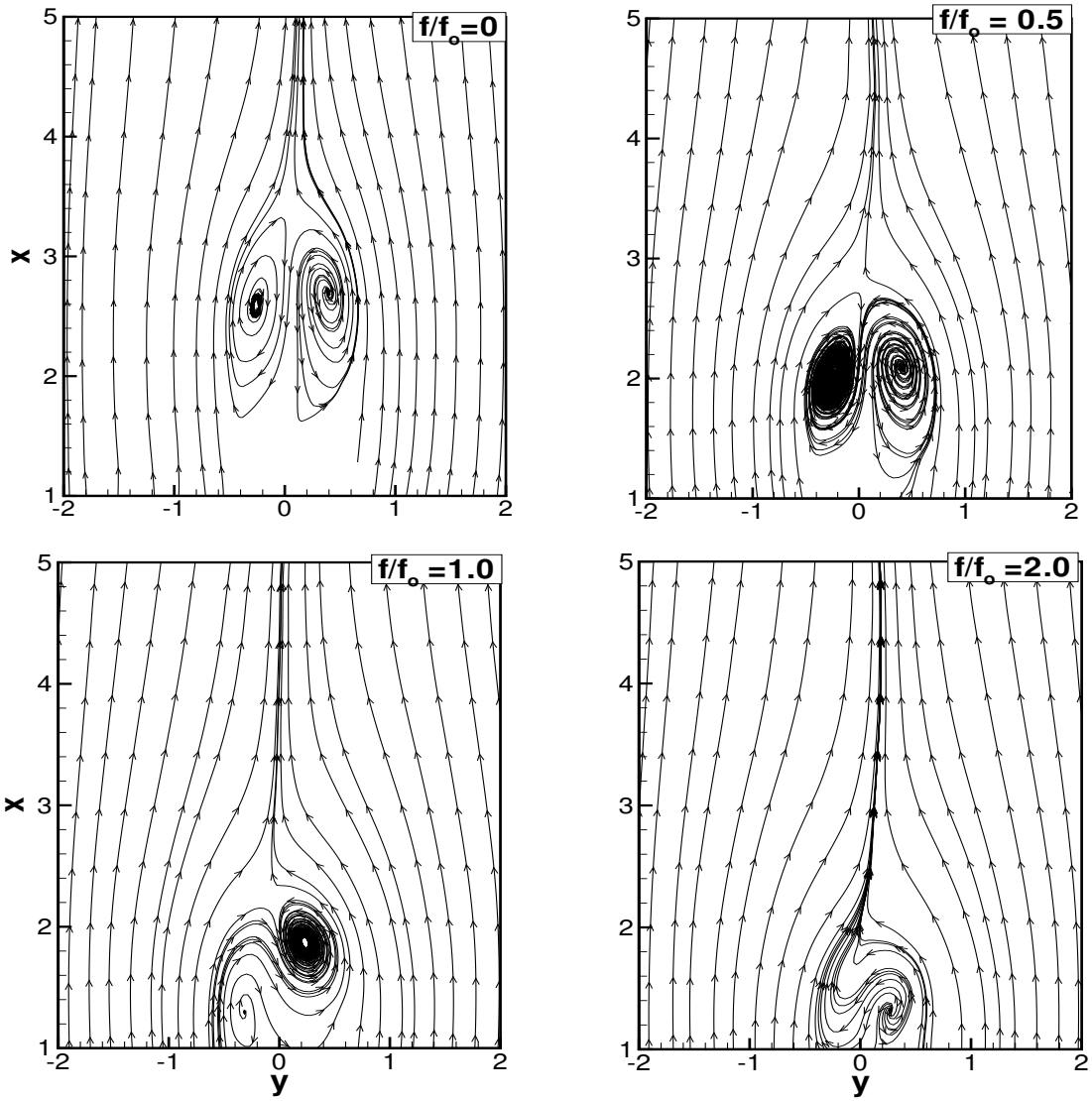

Figure 6.10: Time-averaged streamlines in the wake of a square cylinder at various frequencies (f/f_o=0, 0.5, 1.0 and 2.0); perturbation amplitude is unchanged (A/B=0.1); Re=355.

u_{rms} velocity is a measure of the vortex formation length. The peak magnitude of the velocity fluctuations along the center-line of the cylinder wake increases for both the streamwise and transverse component as the vortex formation length decreases. This suggests that closer the vortices are formed from the downstream edge of the cylinder, the stronger they are, with the magnitudes being higher as well. The overall magnitude of v_{rms} velocity is higher compared to that of u_{rms} and the v_{rms} velocity peak at a later streamwise location. The intensification of the velocity fluctuations in the near wake indicates improved mixing and hence a higher base pressure, followed by a lower drag

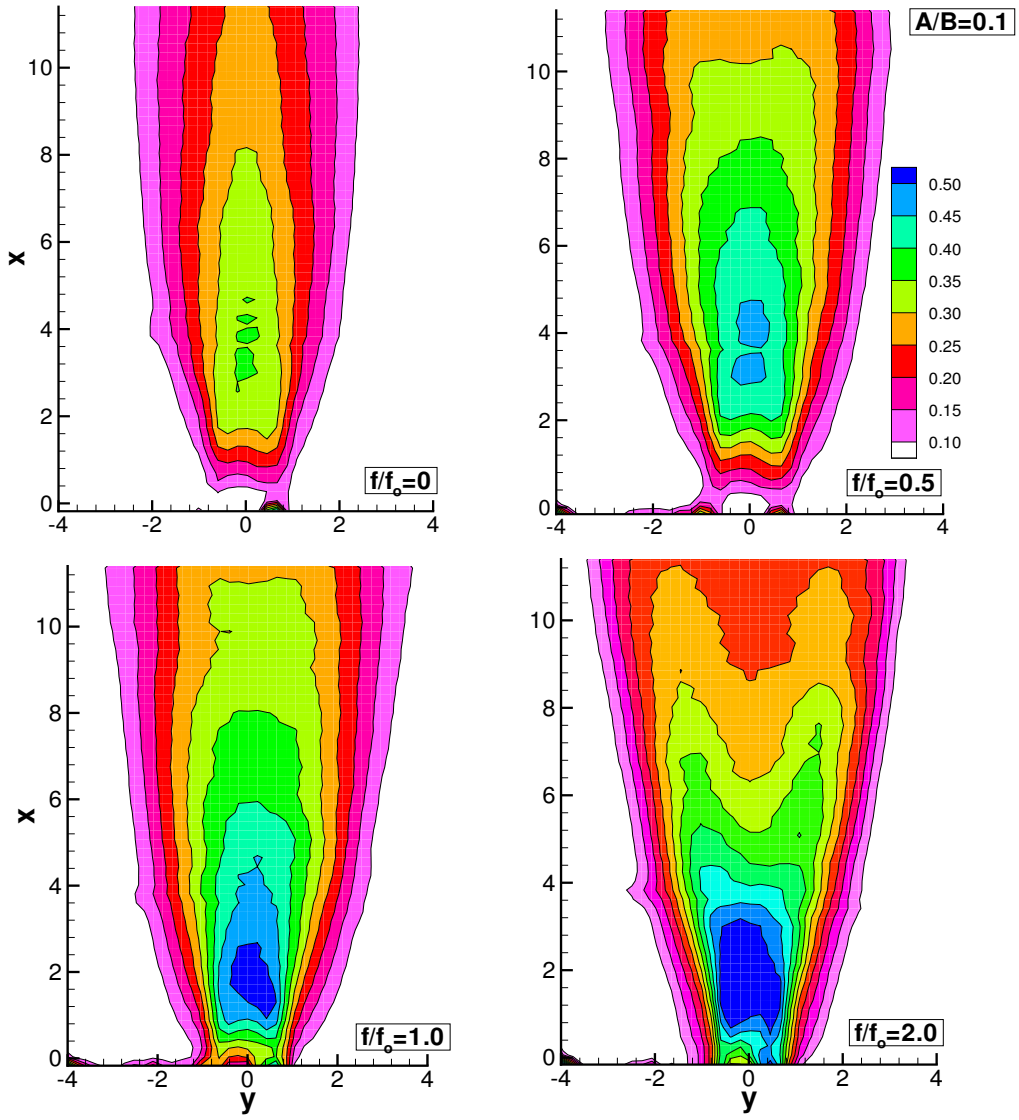

Figure 6.11: Non dimensional contours of turbulent intensity ($= \sqrt{u'^2 + v'^2}/U$) in the wake of an oscillating square cylinder as a function of forcing frequency; Re=170 and amplitude of oscillation (A/B)=0.1.

coefficient.

The position of the maximum in the streamwise RMS velocity moves from $x = 2.3$ in the unperturbed flow to $x = 1.2$ behind the cylinder, when frequency increases from 0 to 2 f_o. A variation in position to this extent was reported by Konstantinidis [77] for a circular cylinder. The variation in the peak amplitude of oscillation with respect to excitation frequency is more pronounced in the streamwise component compared to the transverse component. The increase in intensity of velocity fluctuations can be related

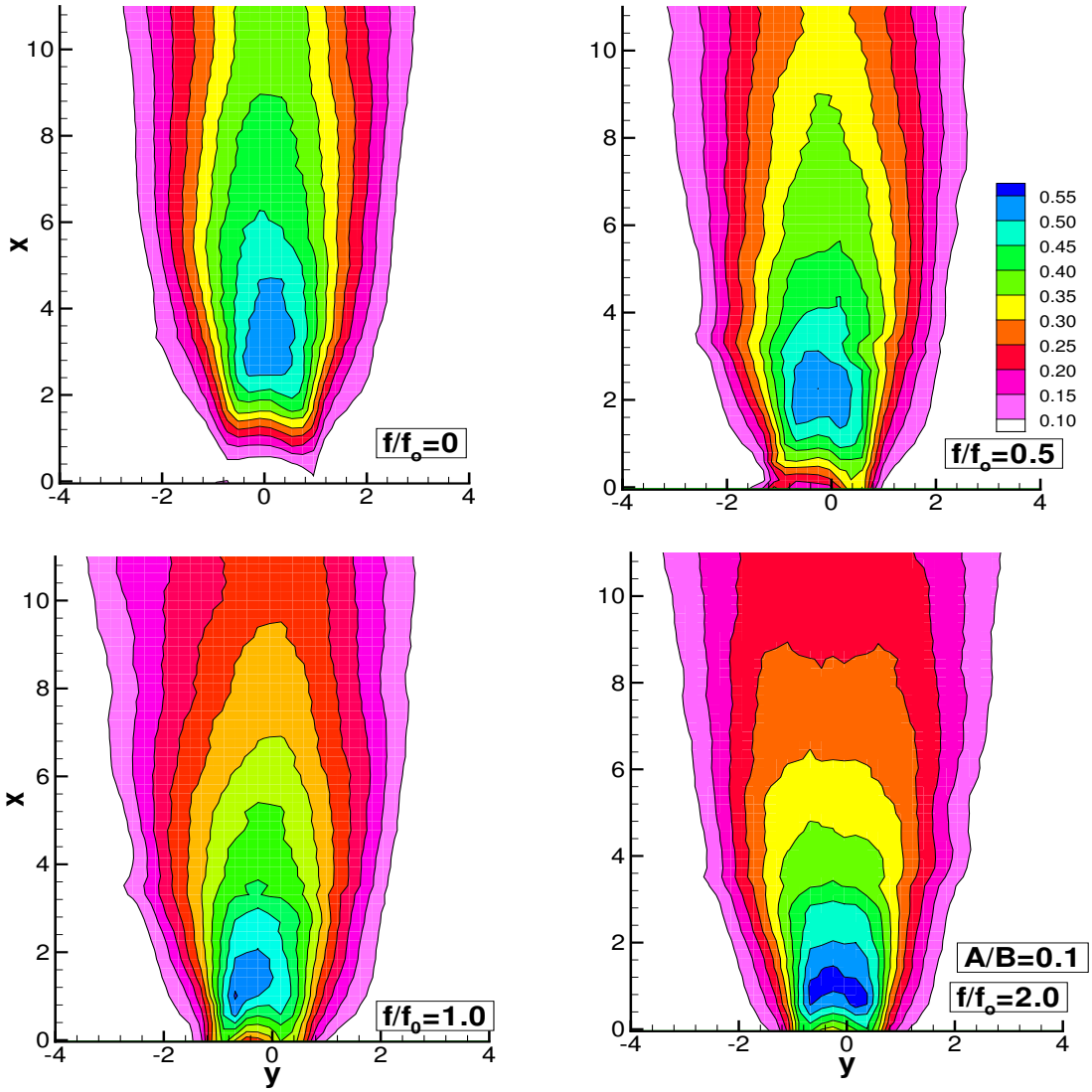

Figure 6.12: Non dimensional contours of turbulent intensity($= \sqrt{u'^2 + v'^2}/U$) in the wake of an oscillating square cylinder as a function of forcing frequency; Re=355 and amplitude of oscillation (A/B)=0.1.

to an increase in the strength of shed vortices, but there is also a dependence on other factors such as the size of the vortices and their arrangement in the vortex street. At higher Reynolds number, the u_{rms} and v_{rms} peak moved upstream to a greater extent compared to that at lower Reynolds number. Overall, the drop in vortex formation length with increase in excitation frequency is clearly evident.

Figures 6.14 and 6.15 show profiles of the streamwise velocity fluctuation (u_{rms}) at four downstream locations (x= 2, 4, 6 and 8) for two Reynolds numbers (Re=170 and

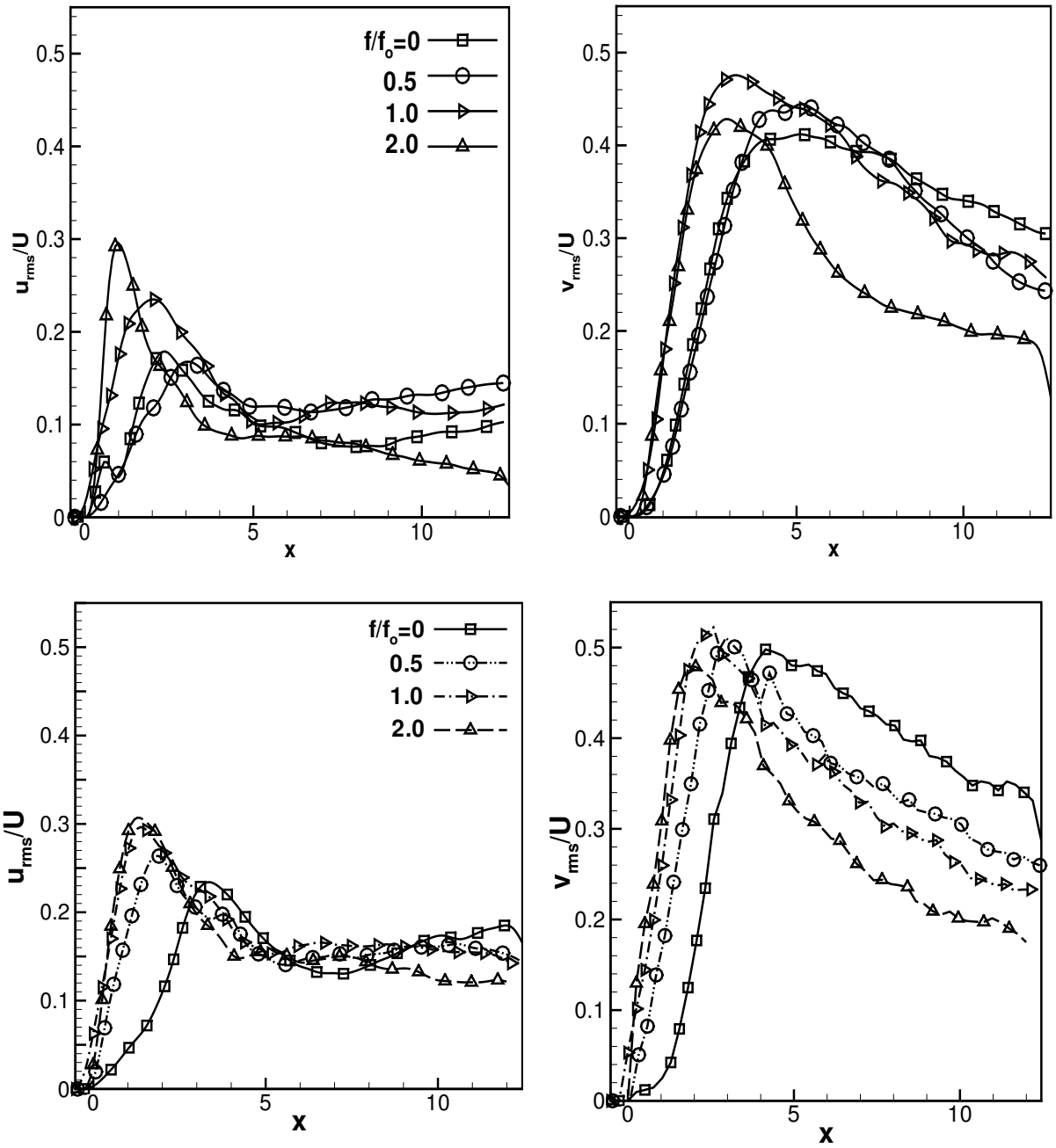

Figure 6.13: Evolution of nondimensional centerline u_{rms} and v_{rms} velocity in the streamwise (x) direction at Re= 170 (Top), 355 (Bottom) for different forcing frequencies (f/f_o=0, 0.5, 1.0 and 2.0) at a constant amplitude of excitation (A/B)=0.1.

355) respectively. Figures 6.16 and 6.17 show the comparison of v_{rms} velocity fluctuation profile. A strong effect of the forcing frequency on velocity fluctuations is seen at x=2. The maximum values of fluctuations, i.e. u_{rms} and v_{rms} value is also dependent on the

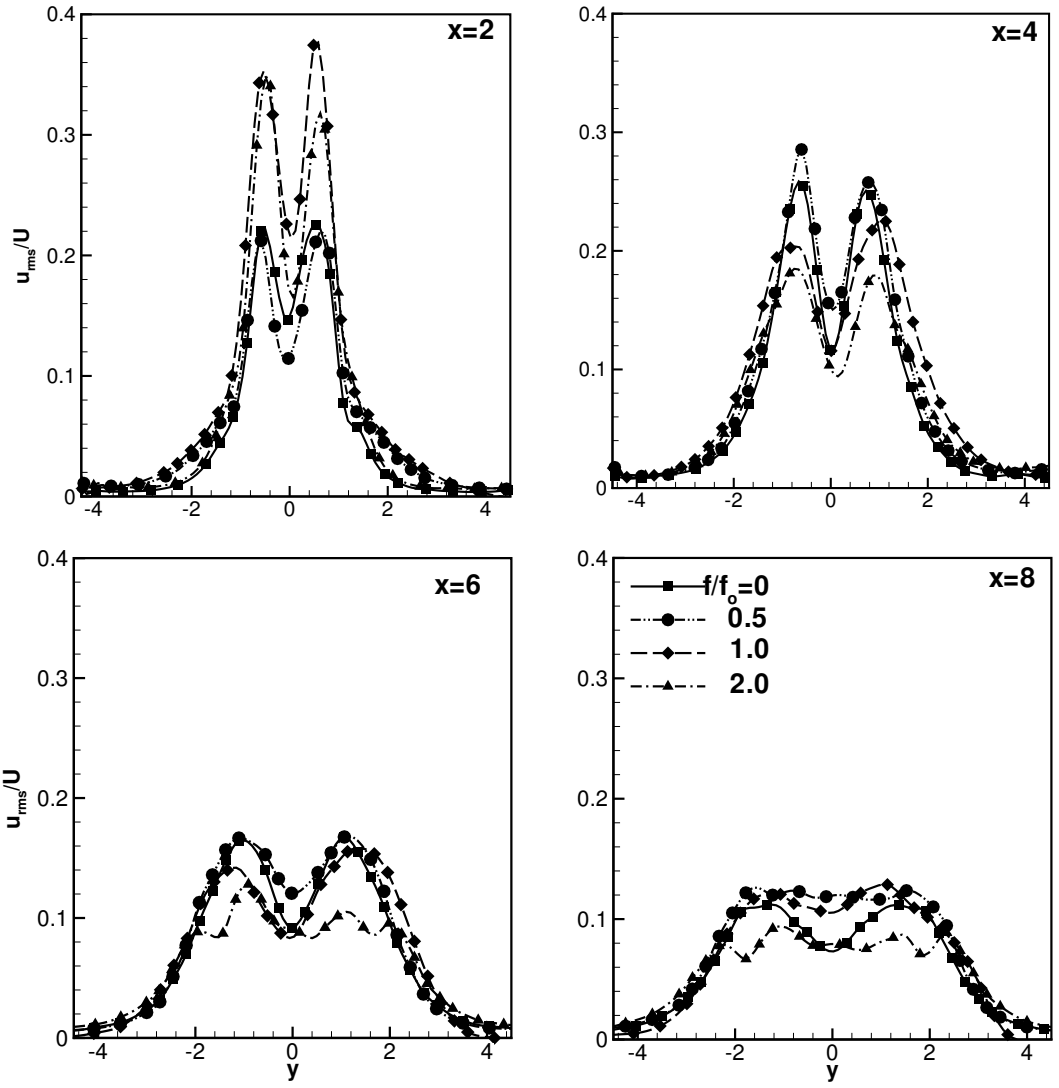

Figure 6.14: Time-averaged nondimensional streamwise (u_{rms}/U) velocity fluctuations at different oscillating frequencies (f/f_o=0, 0.5, 1.0 and 2.0), Re=170.

cylinder frequency. The effect of forcing frequency diminishes rapidly with streamwise distance. The dual peak nature of the u_{rms} velocity in the near field region indicates the roles of the vortices in the opposed shear layers. In the downstream direction, the interaction between these shear layers increases, leading to the disappearance of dual peak. The magnitude of turbulent intensity is generally higher at the higher Reynolds number. The relative magnitude of the RMS velocities at different excitation frequencies is also a function of Reynolds number. The overall higher magnitude of u_{rms} and v_{rms} velocity at f/f$_o$=1.0 and 2.0 indicate greater mixing at these forcing frequencies.

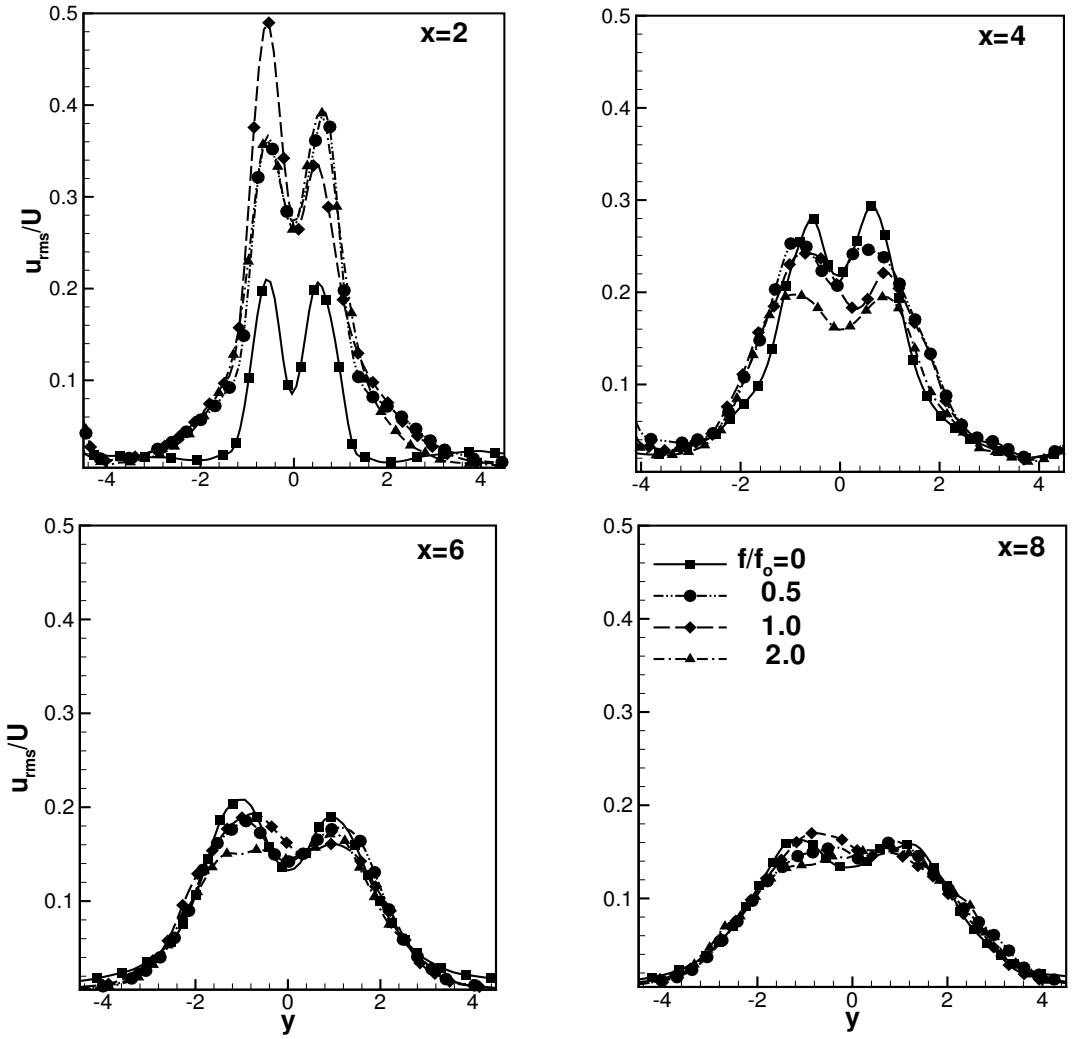

Figure 6.15: Time-averaged nondimensional streamwise (u_{rms}/U) velocity fluctuations at different oscillating frequencies (f/f_o=0, 0.5, 1.0 and 2.0), Re=355.

6.1.6 Centerline recovery

Figure 6.18 shows a comparison of recovery of centerline streamwise velocity with the data reported by Konstantinidis [77] as a function of forcing frequency. The overall trends in the two plots are identical. With an increase in the forcing frequency, the vortex formation region, as measured by the distance over which negative streamwise velocities prevail, is seen to diminish in size.

Figure 6.19 shows the effect of forcing frequency on the variation of the dimensionless time-averaged streamwise velocity along the midplane of the cylinder in the streamwise direction. Two Reynolds numbers (Re= 170 and 355) have been considered.

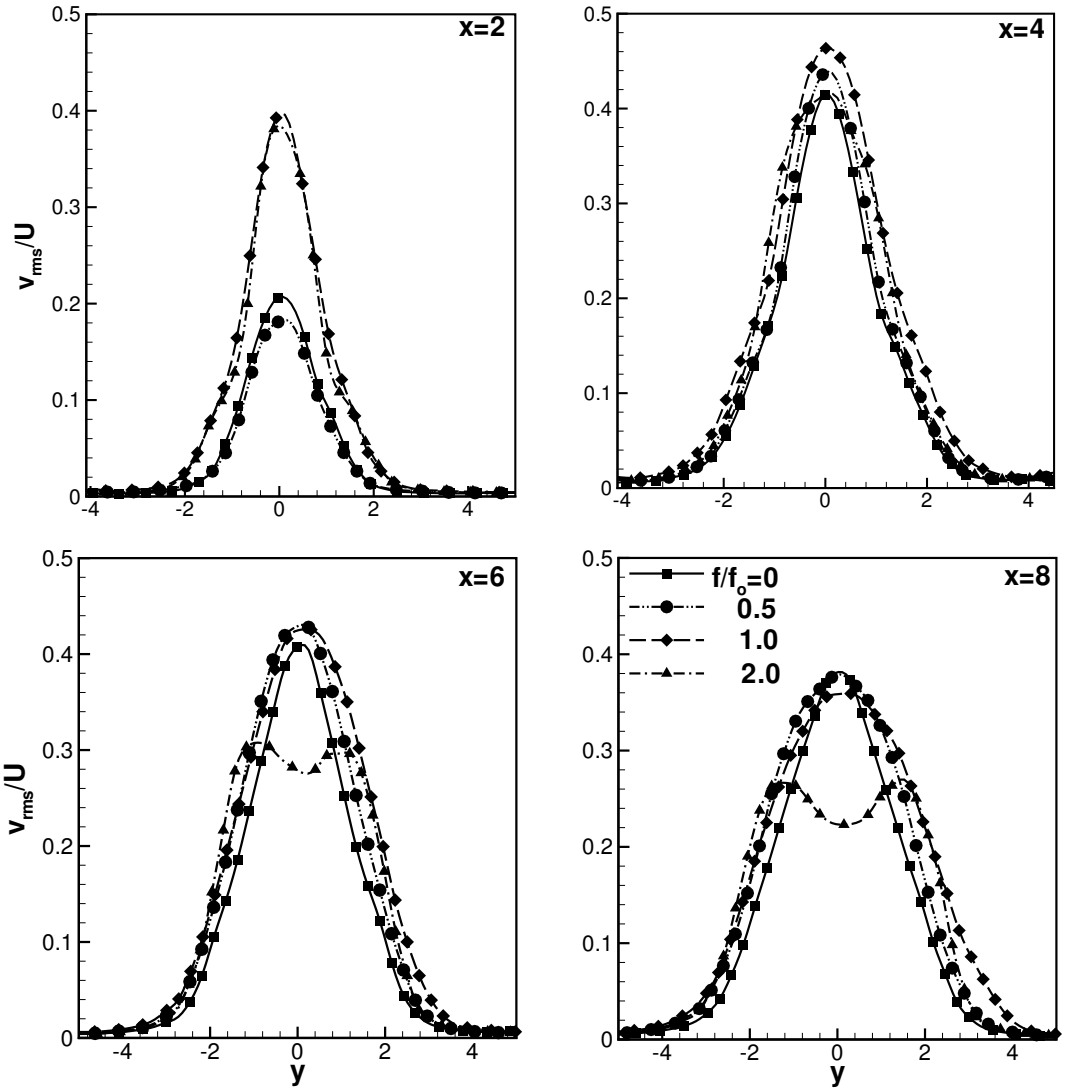

Figure 6.16: Time-averaged nondimensional transverse (v_{rms}/U) velocity fluctuations at different oscillating frequencies (f/f_o=0, 0.5, 1.0 and 2.0), Re=170.

The recovery is directly related to the wake width which in turn depends on entrainment at the edge of the wake. The centerline velocity drops to a minimum value and recovers subsequently for all excitation frequencies. The rate of recovery drops in the downstream region. It is faster in the near field region and is also a function of the excitation frequency. With an increase in frequency, the recovery of centerline velocity is rapid. The PIV data shows that the region of reversed flow decreases in size with an increase in excitation frequency when compared to a stationary cylinder. The centerline recovery is the fastest at f/f_o=2 amongst the excitation frequencies considered, indicating a corresponding minimum in the momentum deficit.

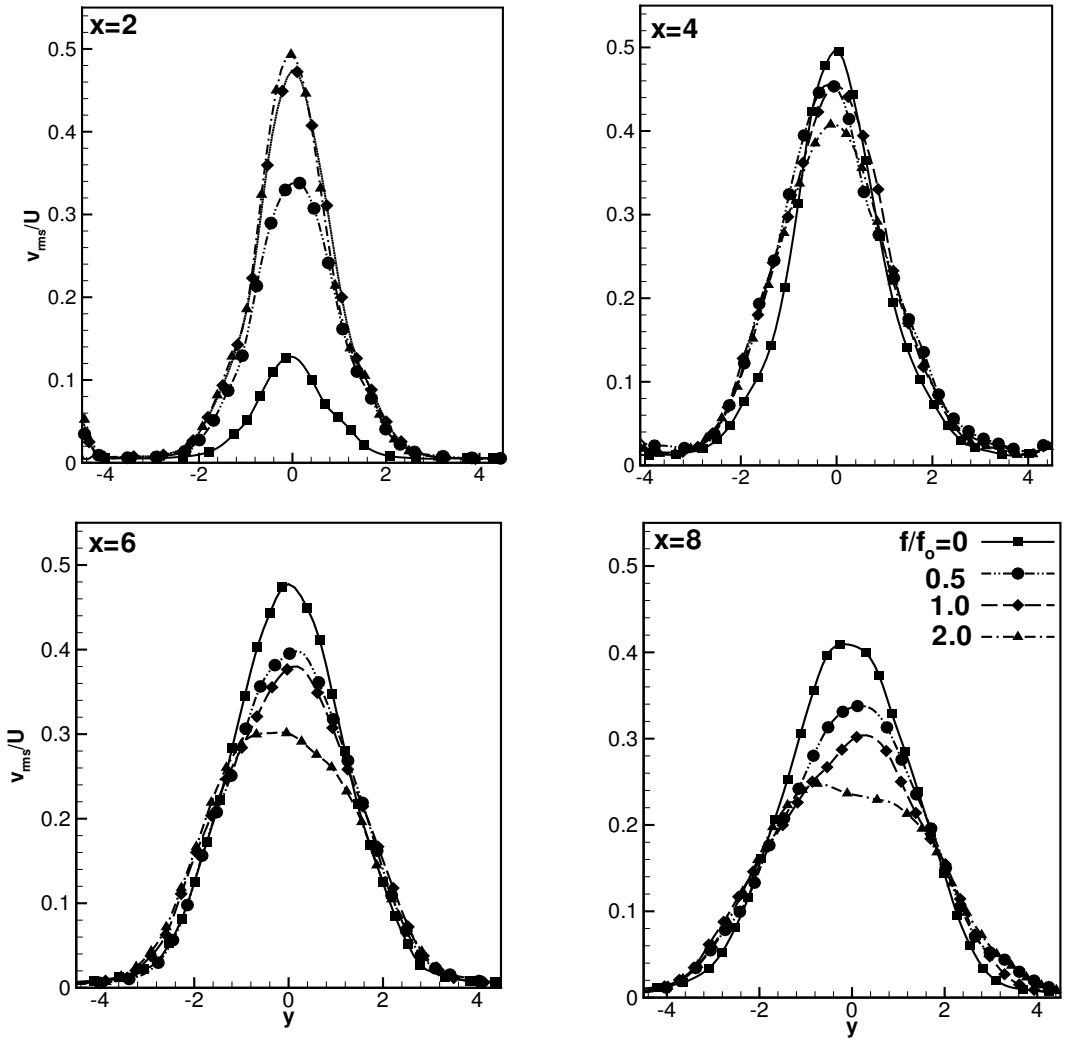

Figure 6.17: Time-averaged nondimensional transverse (v_{rms}/U) velocity fluctuations at different oscillating frequencies (f/f_o=0, 0.5, 1.0 and 2.0), Re=355.

6.1.7 Instantaneous vorticity (ω_z) field

Figure 6.21 shows instantaneous vorticity contours at selected instants of time for different frequencies of oscillation. The Reynolds number considered is 170. As the frequency increases, the near wake vortex pattern changes due to a change in the characteristics of vortex shedding. The vortices grow behind the cylinder and are shed subsequently. The vortex roll up distance after which the vortices shed decreases with increase in frequency. The vortex roll up distance is the lowest at the highest excitation frequency. The alternate vortices shed from the cylinder advect in the downstream direction. The lateral movement of the vortices is maximum for an excitation at f/f_o=2. The vortex shed from one shear layer is drawn towards the other. This process repeats for both

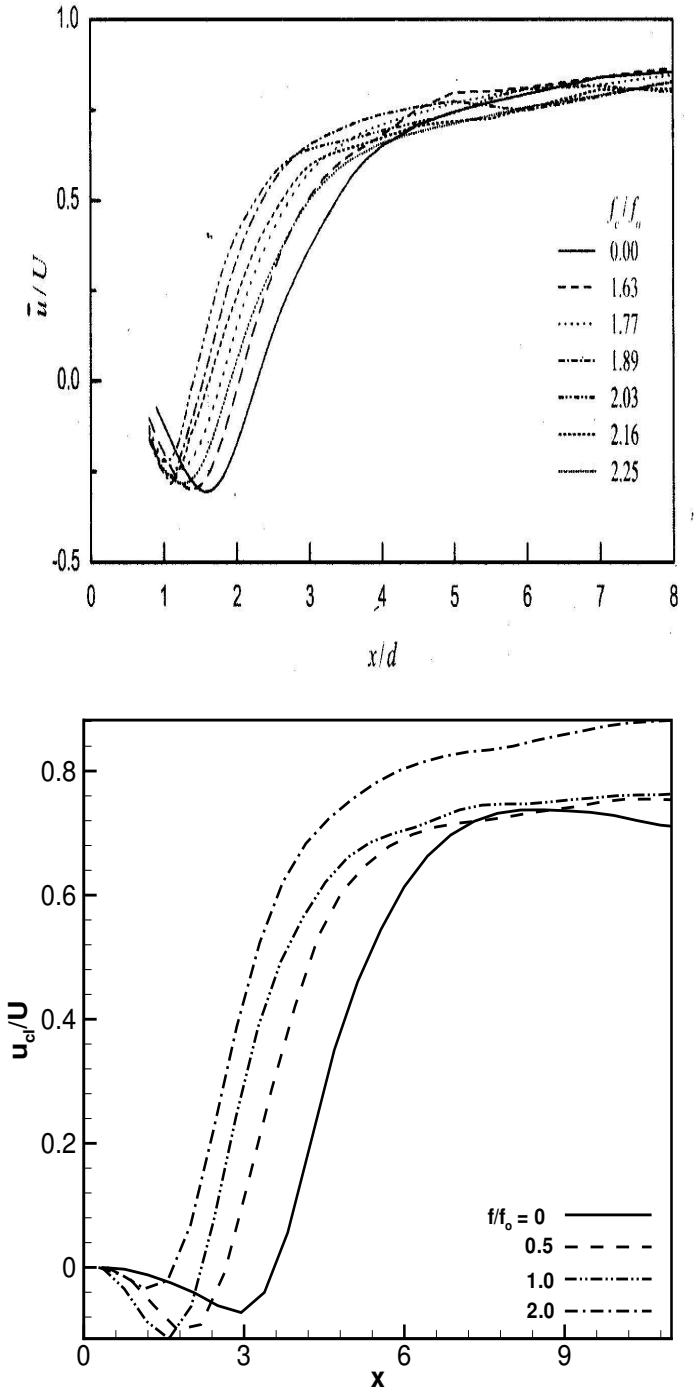

Figure 6.18: Comparison of Centerline recovery of streamwise velocity at various oscillation frequencies with literature (Konstantinidis *et al.* (2003)) and present results (bottom).

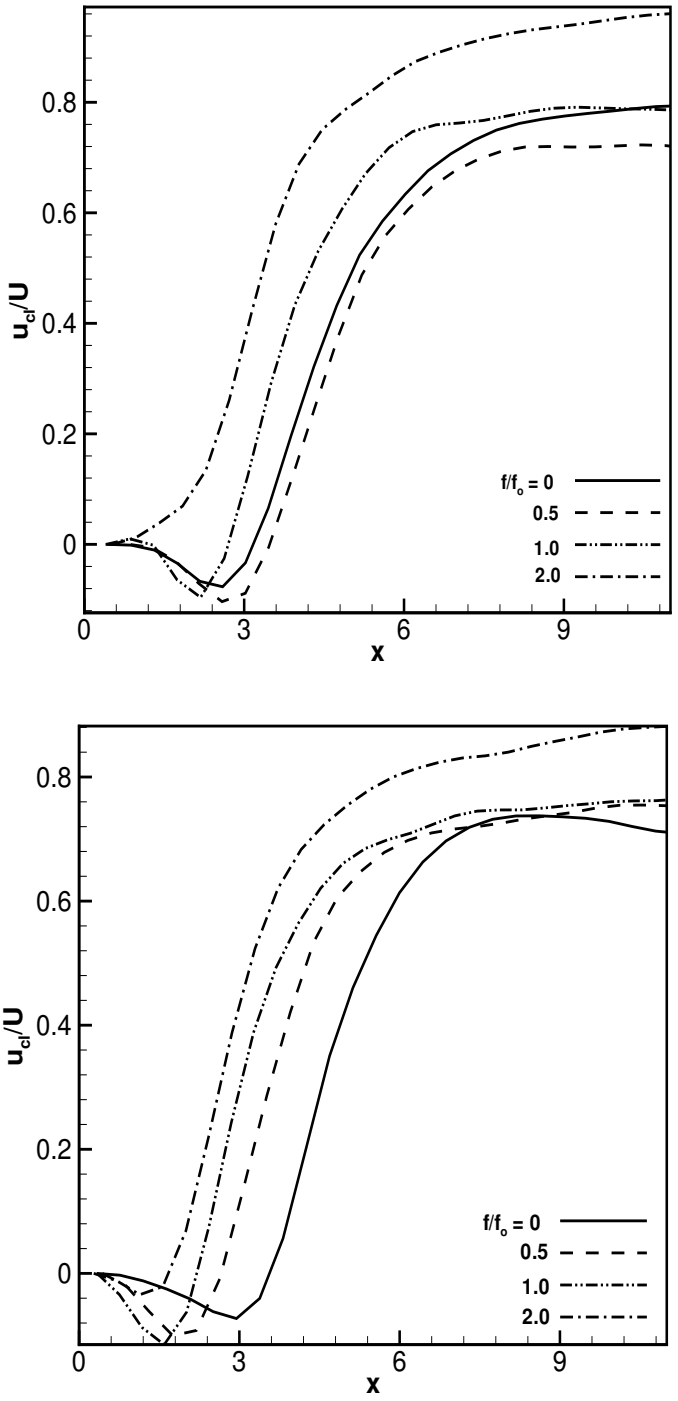

Figure 6.19: Centerline recovery of streamwise velocity at various oscillation frequencies (f/f_o=0, 0.5, 1.0 and 2.0) at constant amplitude of oscillation (A/B)=0.1; Re= 170 (Top), 355 (Bottom).

sides of the shear layer. The dual peak in RMS velocity distribution seen in Figure 6.11 can be attributed to this phenomenon. The larger interaction between the neighboring vortices is responsible for greater mixing and hence lower momentum deficit at f/f_o=2. This vorticity pattern is not realized at the higher Reynolds number of 350 at $f/f_o = 2$, Figure 6.22. However, the vortices are irregular in nature at higher Reynolds number.

Alternate shedding of vortices, typical of a stationary cylinder are referred to the S mode in the literature. The lateral (transverse) movement of vortices is called the P mode, and is often observed for transverse oscillation of the cylinder with respect to the mean flow direction, William and Roshko [186]. In the present experiments, the shedding pattern is predominantly of the S type. At Re=350 and $f/f_o = 2$, a combination of P and S mode is observed.

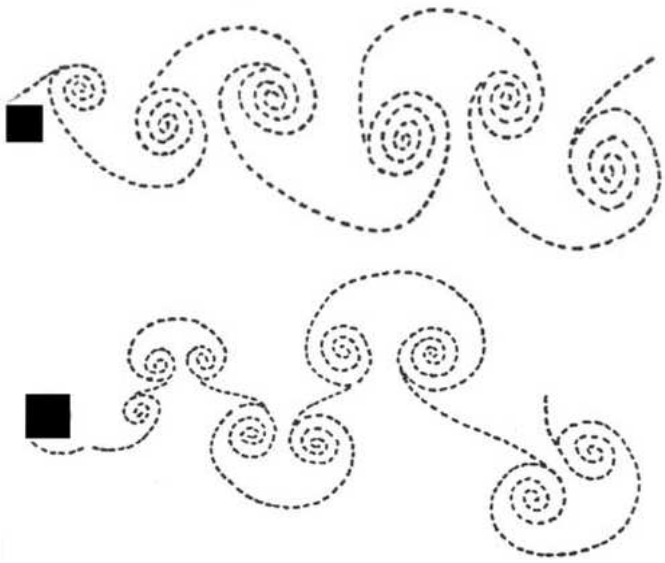

Figure 6.20: Schematic of 2S (top) and 2P (bottom) mode vortex shedding. (after Sarpkaya 2004)

The downstream vortex spacing is an important diagnostic parameter for the state of spatial structure and development of near wake. With an increase in oscillation frequency, the longitudinal wavelength decreases and vortex intensification takes place even outside the near wake. At a higher Reynolds number (Re=350), small scale Kelvin-Helmholtz vortices are embedded within the large scale structure. The small scale concentration of vorticity is seen not only in the shear layer from the cylinder, but eventually spreads over a large scale. With an increase in the forcing frequency, the interaction between small scale and large scale vortices leads to an ill-defined array of vortices.

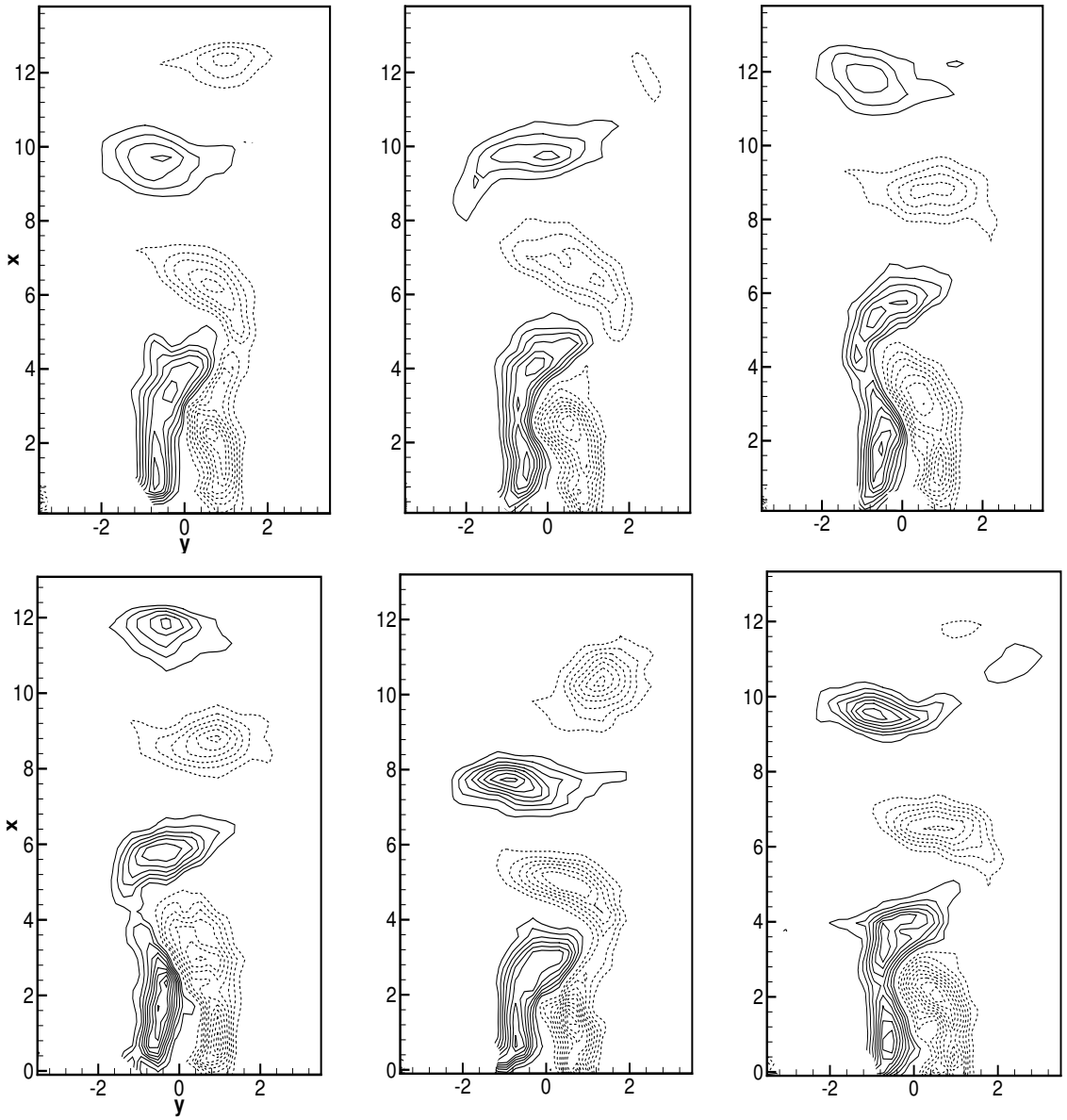

caption in the next page

6.1.8 Power spectra

Figure 6.23 shows power spectra at two Reynolds number for three different nondimensional forcing frequencies. The spectra was obtained from a long-time signal of 20000 points at a sampling rate of 1000 Hz. The spectra have been normalized by their respective areas under the curve. This time record involves at least 300 cycles of cylinder vortex shedding. For low Reynolds number (Re=170), a pure Kárman vortex shedding

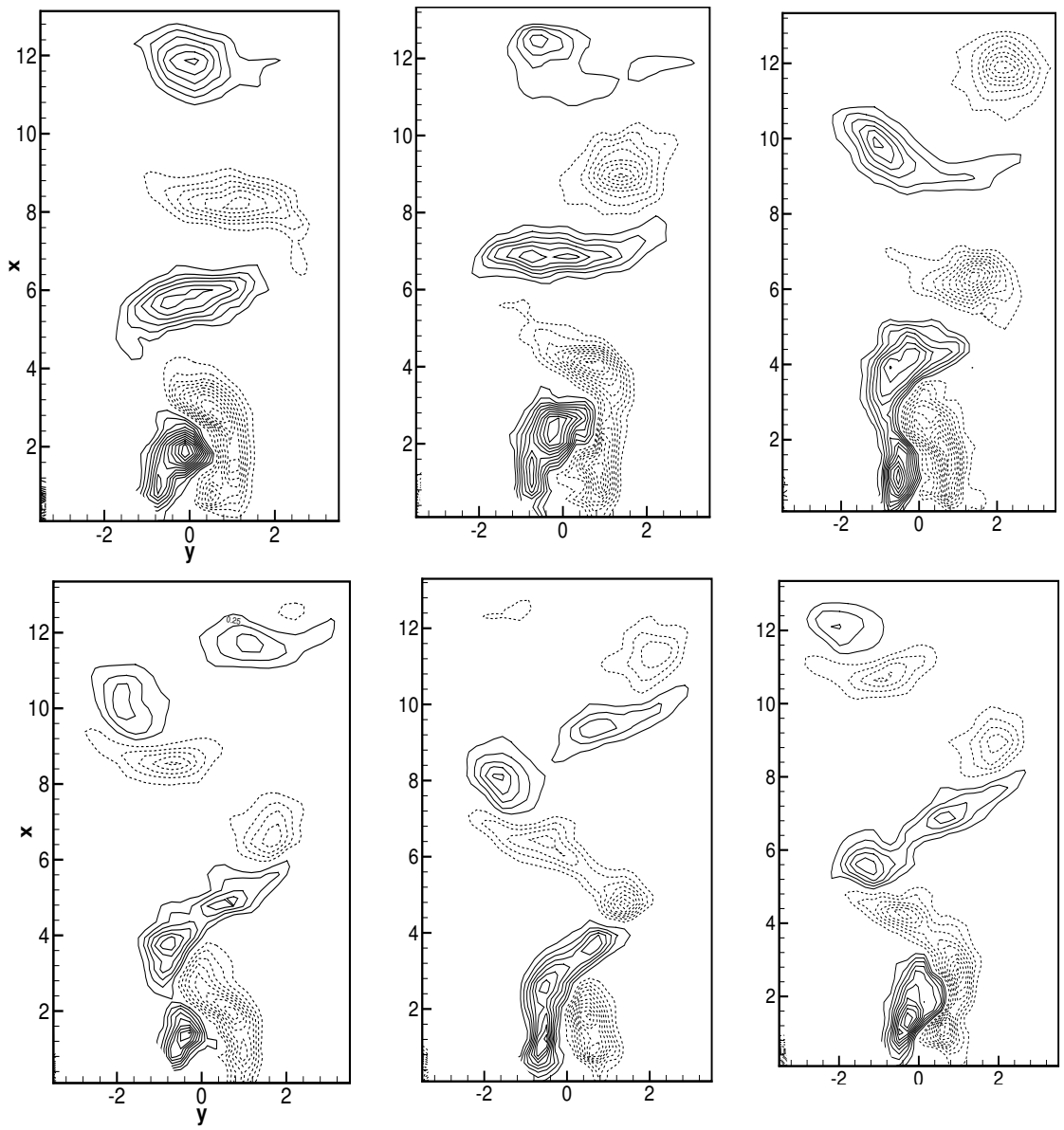

Figure 6.21: Instantaneous spanwise vorticity (ω_z) contours. Stationary cylinder (1st row), f/f_o=0.5 (2nd row), f/f_o=1.0 (3rd row), f/f_o=2.0 (4th row), Re=170, A/B=0.1. $\omega_z(max)$, $\omega_z(min)$ and $\delta\omega_z$=3.0, -3.0, 0.25.

pattern is observed for a stationary cylinder. It corresponds to a single sharply defined peak of vortex shedding in the spectra. With externally applied forcing frequency, additional peaks (*harmonics*) of shedding frequency appear in the spectra. The nonlinear interaction between the forcing signal and vortex shedding frequency generates sum and difference frequencies in each spectrum. The sub-harmonic frequency and additional harmonics for the oscillating cylinder can be understood from the flow visualization images.

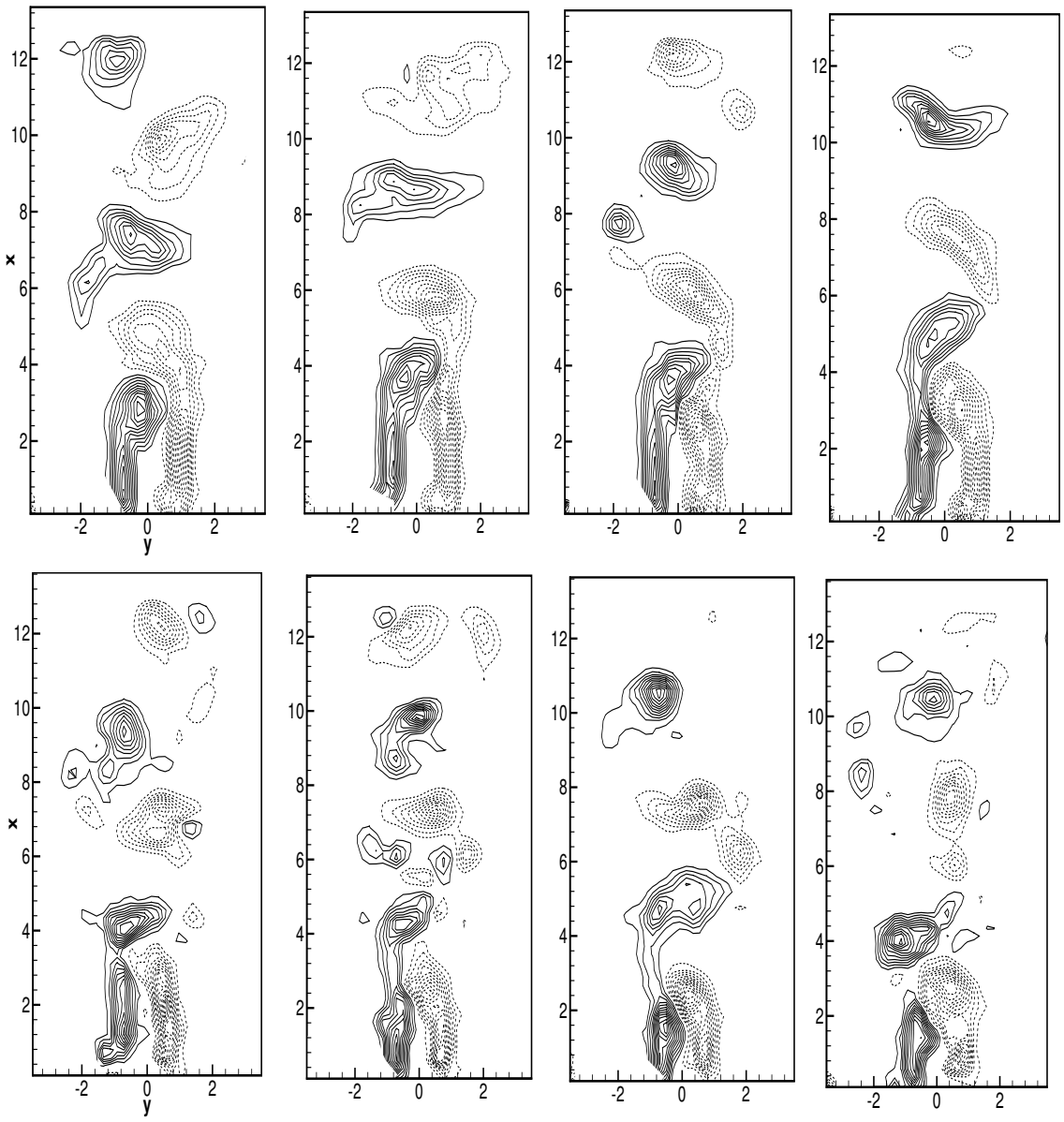

see caption on the next page

Griffin and Ramberg [48] have suggested that a sharply defined spectrum correlates with two dimensionality of the flow field, both for a stationary cylinder and at lock-on. At other frequencies, the appearance of the additional harmonics are probably responsible for the transfer of energy from the streamwise to the transverse modes of fluctuation, leading to an increase in mixing and an additional reason for reduction in the drag coefficient.

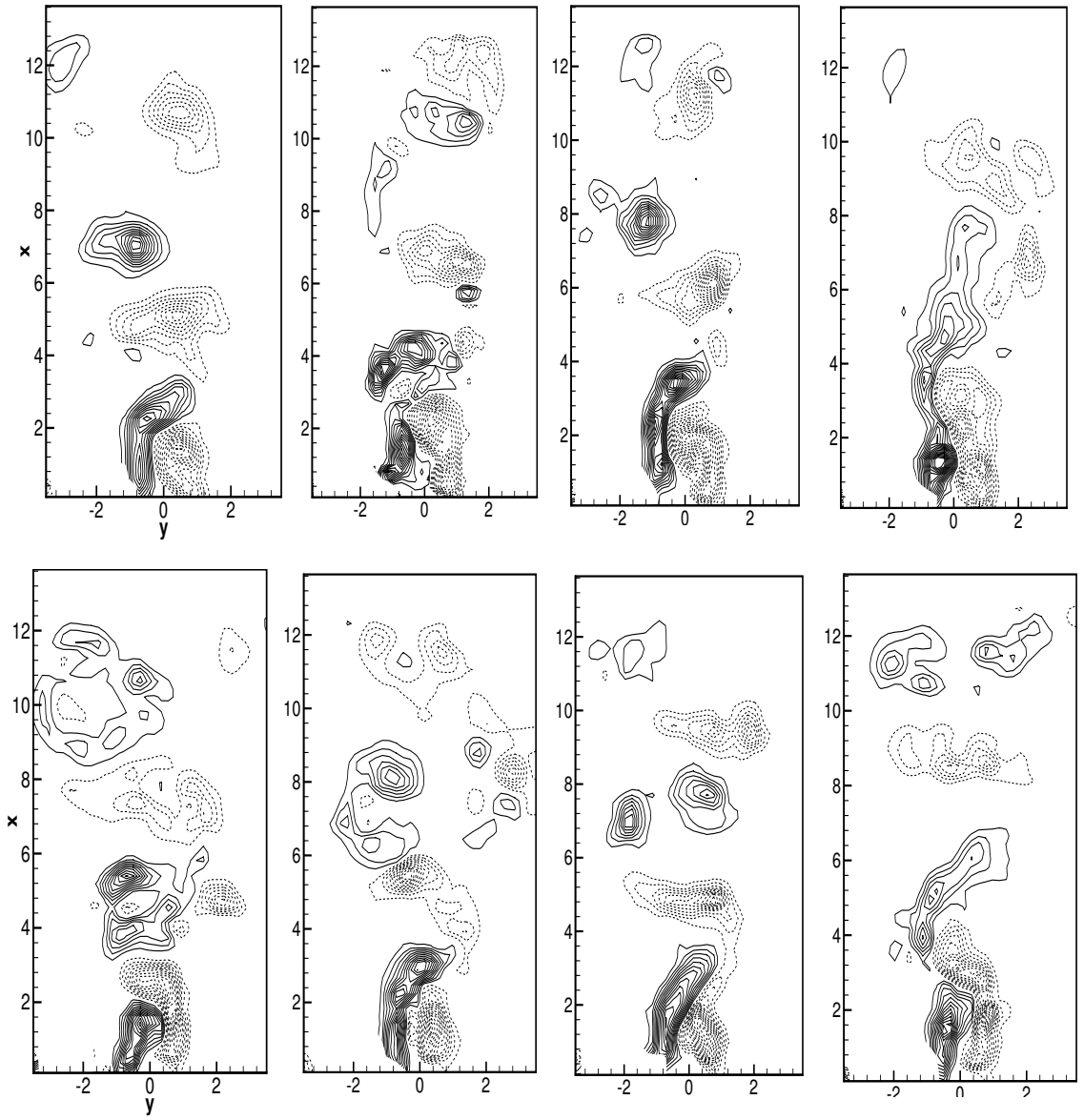

Figure 6.22: Instantaneous spanwise vorticity (ω_z) contours. Stationary cylinder (1st row), f/f_o=0.5 (2nd row), f/f_o=1.0 (3rd row), f/f_o=2.0 (4th row), Re=355, A/B=0.1. $\omega_z(max)$, $\omega_z(min)$ and $\delta\omega_z$=-4.0, 4.0, 0.25.

6.1.9 Flow visualization

Figure 6.24 shows particle traces in the cylinder wake at different forcing frequencies and a Reynolds number of 170. A reference set of images for the stationary cylinder are also presented for comparison. The shedding mechanism is different for an oscillating cylinder when compared to a stationary cylinder (Gerrard [45])). The distance over which

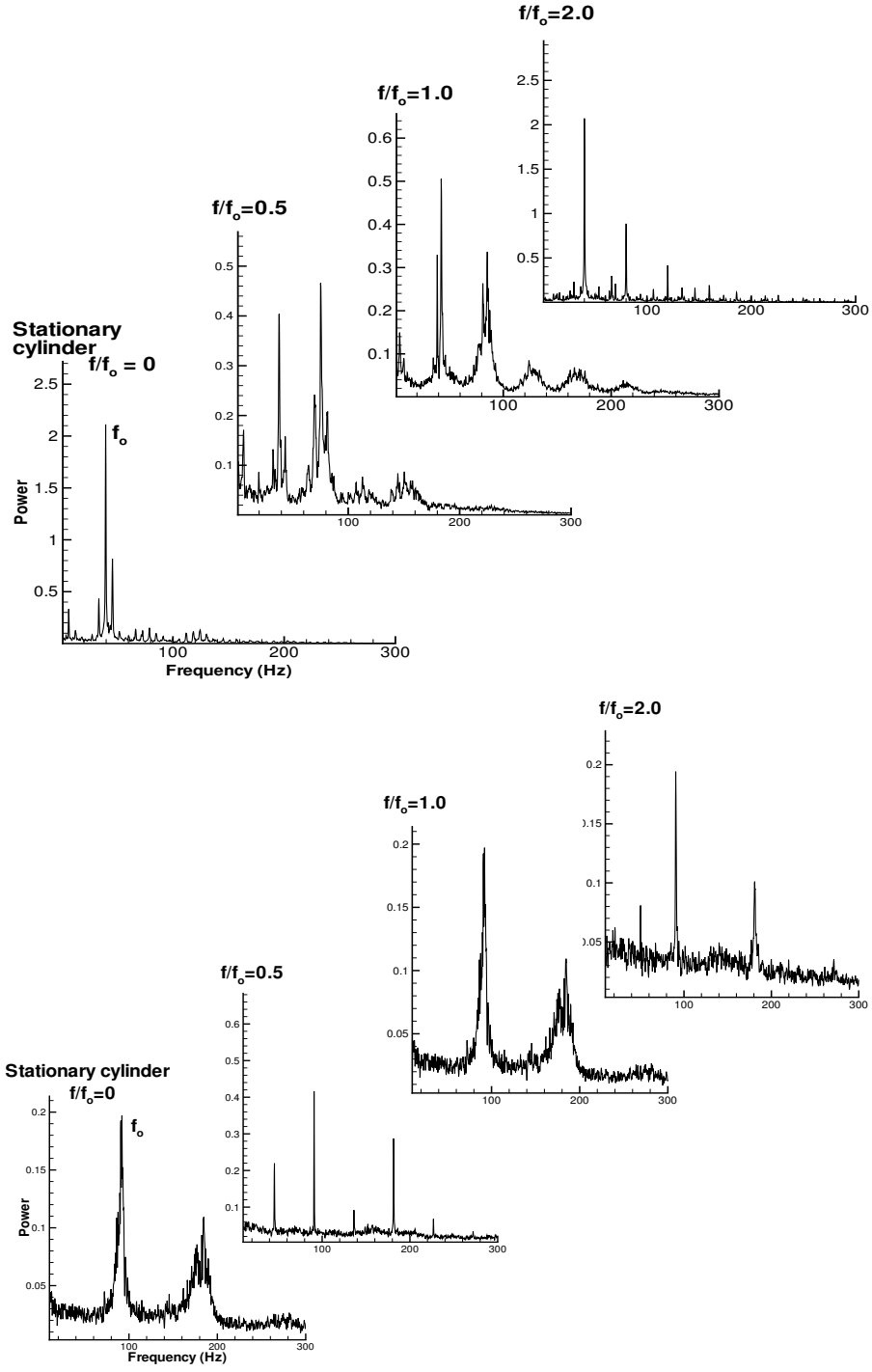

Figure 6.23: Power spectra of the v-component of velocity fluctuation at various frequencies of oscillation; Re= 170 (Top), 355 (Bottom).

a vortex rolls up relative to the cylinder position decreases with an increase in frequency of oscillation as distinctly visible from the images. The distance over which vortices roll up is a measure of shedding frequency and hence Strouhal number. The detachment of the vortex growing on both sides of the cylinder is connected to the displacement of the cylinder under oscillatory conditions. With an increase in oscillating frequency (to f/f_o=1) the pure Kárman vortex structure breaks and two vortices of opposite sign emanate from the cylinder almost simultaneously. The longitudinal distance between vortices decreases. With further increase in frequency (to f/f_o=2) the far wake structure breaks down. A strong three dimensionality starts to appear[7] and the wake width is visibly greater. The increase in the wake width causes a small increase in drag coefficient at this frequency ratio and Re=170, but the overall influence is one of reduction in the time-averaged drag.

6.1.10 Closure

Flow fields obtained for forced inline oscillations with varying forcing frequencies (and a given amplitude) are discussed. A strong effect of forcing frequency in the near-wake flow field is to be seen. The recirculation length and formation length reduce substantially with an increase in frequency and reduce the time-averaged momentum deficit behind the cylinder. The instantaneous vorticity contours show the shear layer roll up distance to be a minimum before separation; hence the longitudinal wavelength of the shed vortices reduce. The time-averaged vorticity contours shows that with an increase in frequency, the large scale vortices move closer to the cylinder. Their concentration near the cylinder leads to higher magnitudes of vorticity. The RMS values of velocity fluctuations cluster around the cylinder as well. Due to improved mixing, the base pressure behind the cylinder reduces leading to reduction in drag coefficient.

6.2 Effect of Forcing Amplitude

In the present section, the effect of amplitude of oscillation on the flow structures have been discussed. The forcing frequency is kept equal to the vortex shedding frequency. With an increase in amplitude, the momentum flux pumped into the near-wake of the cylinder increases. The vortex formation length reduces with an increase in the amplitude. These changes in the near wake vortex formation process cause corresponding

[7] as gaged by the extent of disorganization in the flow field

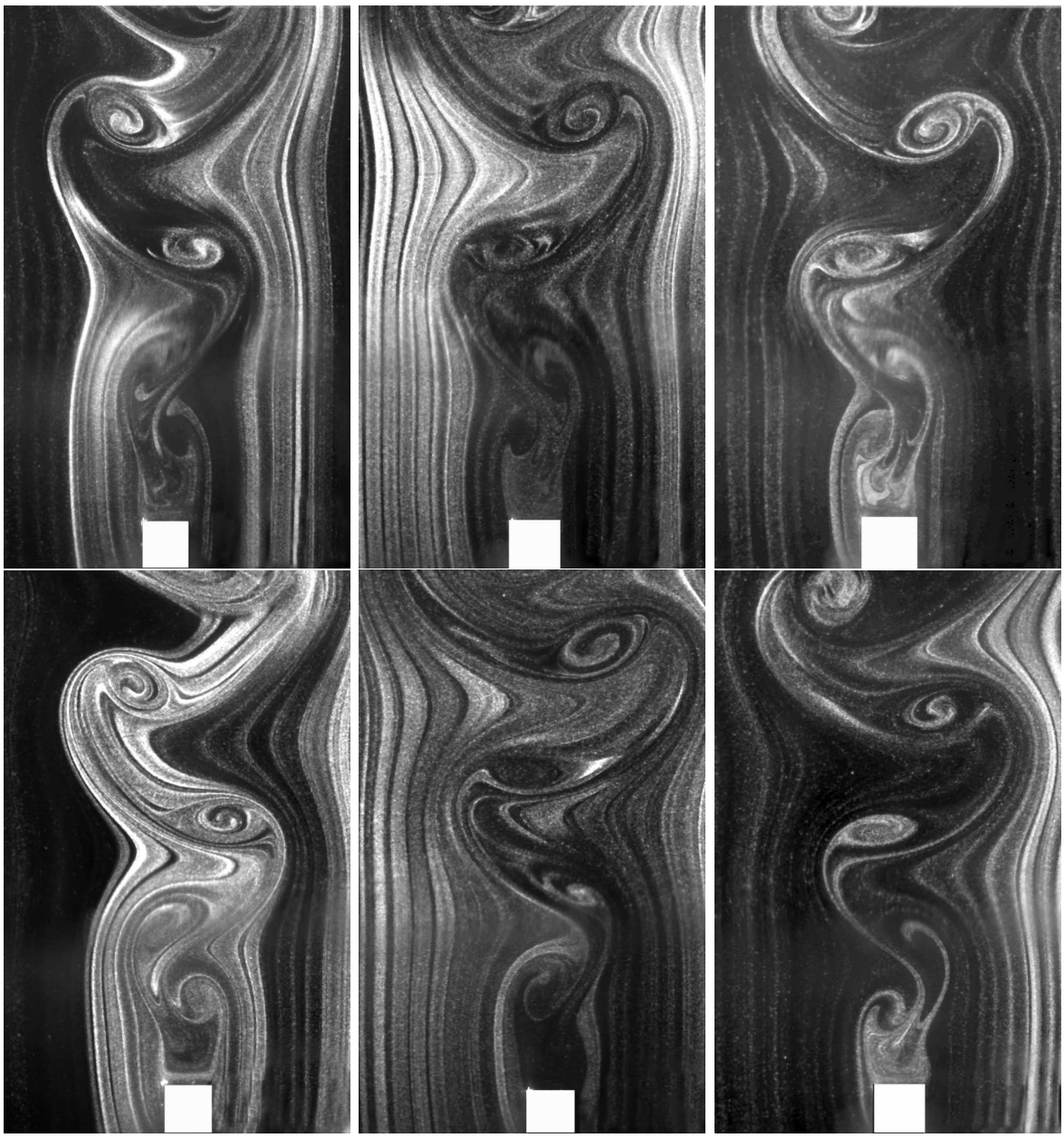

see caption on the next page

changes in the strength or circulation of the shed vortices. The increase in vortex strength can be interpreted as a corresponding increase in the rate of vorticity generation. The details of the effect of forcing amplitude has been elaborated below by means of drag coefficient, Strouhal number, time-averaged velocity field, stream traces, time-averaged vorticity field, velocity fluctuations, instantaneous vorticity field, power spectra and particle trace images.

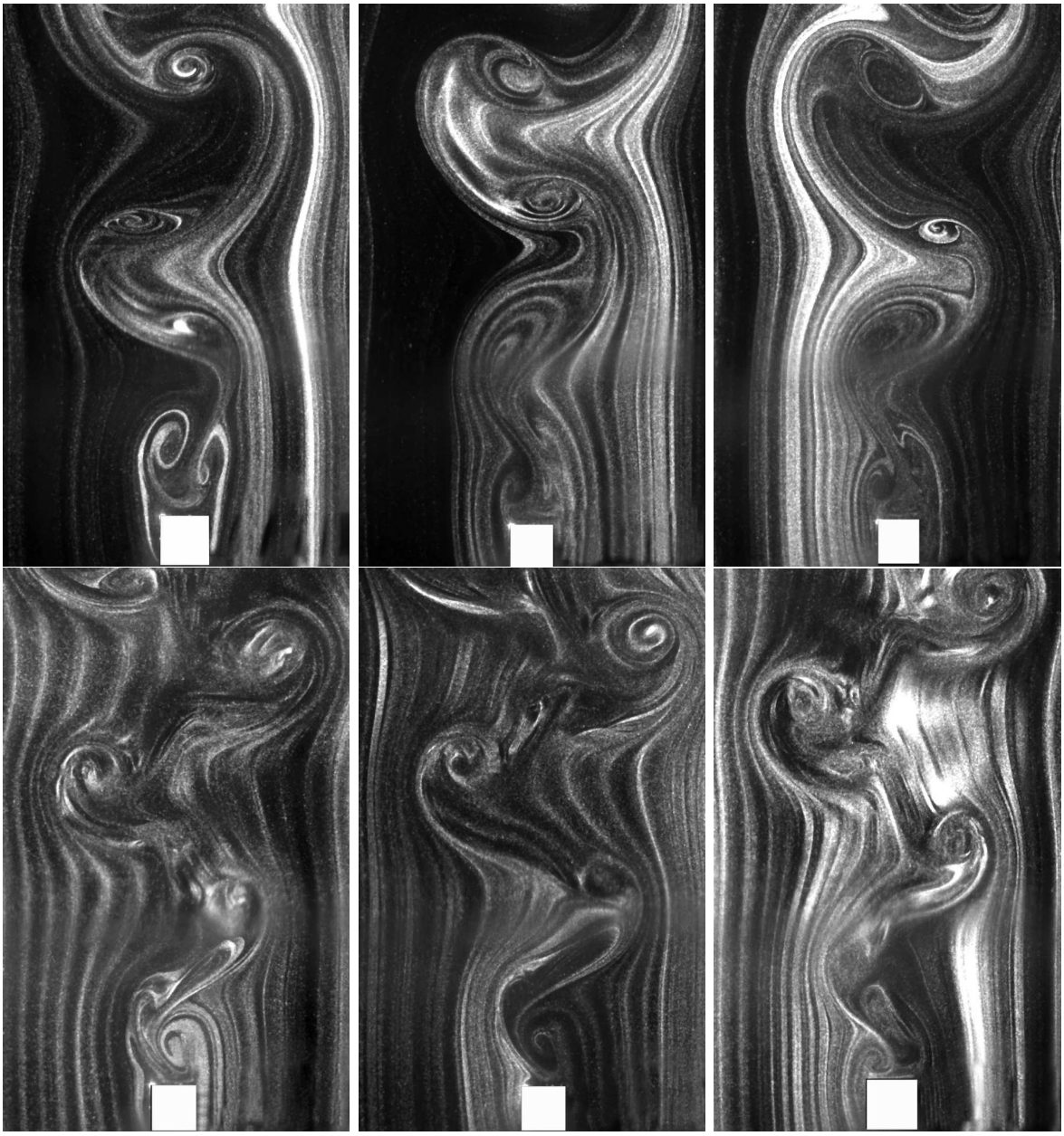

Figure 6.24: Flow visualization images for various cylinder oscillations; Re=170. f/f_o=0 (1st row), 0.5 (2nd row), 1.0 (3rd row) and 2.0 (4th row).

6.2.1 Drag coefficient and Strouhal number

The effect on drag coefficient and Strouhal number as a function of amplitude of excitation has been shown in Table 6.4. Constant Strouhal number is observed at all excitation amplitudes indicating that the amplification of fundamental mode is highest among all other modes and no other harmonics dominates over the vortex shedding with increase

in amplitude of excitation. The drag coefficient drops with increase in amplitude. However, the drop is not continuous i.e. not linearly related to the amplitude of excitation. The drag coefficient saturates after certain amplitude of excitation with minor increase in its value.

Table 6.4: Drag coefficient and Strouhal number as a function of forcing amplitude.

A/B	C_D
0	1.48
0.025	1.71
0.1	0.94
0.17	0.85
0.26	0.81
0.32	1.05

A/B	St
0	0.147
0.025	0.147
0.1	0.147
0.17	0.147
0.26	0.147
0.32	0.147

6.2.2 Time-averaged velocity field

Figure 6.25 shows the time-averaged velocity vectors for various amplitudes of oscillation. The velocity deficit zone reduces with an increase in the amplitude. The streamwise velocity recovery is faster with increase in amplitude of oscillation. With an increase in amplitude, asymmetry in the flow field starts to appear. However, the wake width is not significantly affected. Figure 6.26 shows the average u-velocity profile at different amplitude of excitation. The drop in the wake deficit with increase in excitation frequency is clearly evident indicating the reduction in the mean drag. Figure 6.27 shows the transverse velocity profiles at various amplitudes of oscillation. The transverse velocity profile shows an increase in the magnitude of v-velocity with increase in the excitation amplitude in the near field region. Subsequently, the magnitude of transverse velocity diminishes rapidly with streamwise distance[8] and the v-velocity profile is almost flater at f/f_o=2.0 indicating the developed nature of the wake.

The recirculation bubble size as a function of excitation amplitude has been shown in Table 6.5. The recirculation bubble size drops with increase in excitation amplitude. This is due to the additional momentum applied to the flow by the cylinder motion.

[8]the decay rate being higher at higher amplitudes.

Table 6.5: Recirculation length as a function of forcing amplitude.

A/B	Re=170
0	2.60
0.025	2.43
0.1	1.93
0.17	1.52
0.26	1.5
0.32	1.1

6.2.3 Time-averaged stream traces

Figure 6.28 shows the streamline plot derived from the time-averaged velocity field. The size of the recirculation zone reduces with an increase in the amplitude of oscillation. When compared to the effect of forcing frequency on recirculation length, the effect of amplitude is less prominent. Simultaneously, an asymmetry in the flow field starts to appear; this is also seen in the time-averaged velocity profiles. The increase in amplitude of oscillation makes the flow field more asymmetric due to a distortion in the phase relationship between cylinder movement and the vortex shedding cycle. A strong coupling between oppositely oriented vortices is the responsible for the asymmetry in the time-averaged data.

6.2.4 Time-averaged vorticity field

The time-averaged spanwise vorticity contours for various oscillation amplitudes are shown in Figure 6.29. Asymmetry in vortex shedding starts to appear in the vorticity contours with an increase in the oscillation amplitude. The maximum vorticity magnitude is also different in the opposite shear layer. An upstream migration of the large scale vortex structure is to be seen; this has been observed earlier by Ongoren *et al.* [115] for transverse oscillation experiments with cylinders of circular, square and triangle cross-sections.

The effect of cylinder amplitude on the flow field can be understood from the following idealized context. Consider a situation where a cylinder moves in an infinite fluid and the superimposed flow is zero. For a square cylinder with inline oscillations, two fixed stagnation point at the front and back of the cylinder are available. The resulting vortex generation process can be described as follows. As the oscillating cylinder moves in

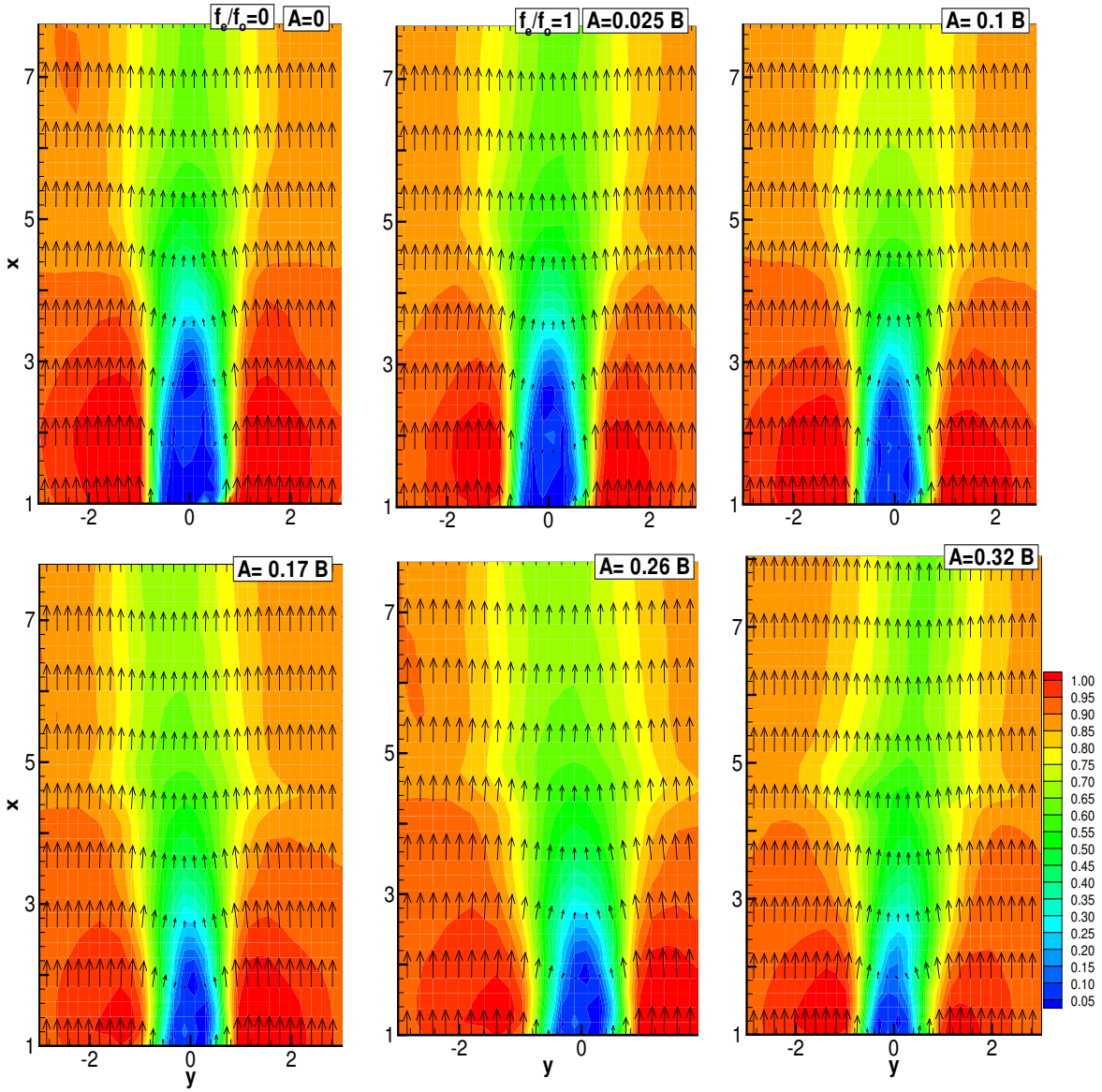

Figure 6.25: Time-averaged velocity vectors for various amplitudes of oscillation (A/B=0, 0.025, 0.1, 0.17, 0.26 and 0.32); Re=170, f/f_o=1.0.

the forward direction, two boundary layers develop on the cylinder wall. The separating flow creates two counter rotating vortices of equal magnitude and strength, resulting in geometrically similar vortex fields. The creation of vortices stops when the maximum forward location of the cylinder is reached and the cylinder starts its backward motion.

The vortex formation process is now repeated on the other side of the cylinder. In addition, the backward motion of the cylinder causes a splitting of the vortex pair, produced earlier by the forward motion, till, finally, flow reversal occurs. Thus, cylinder

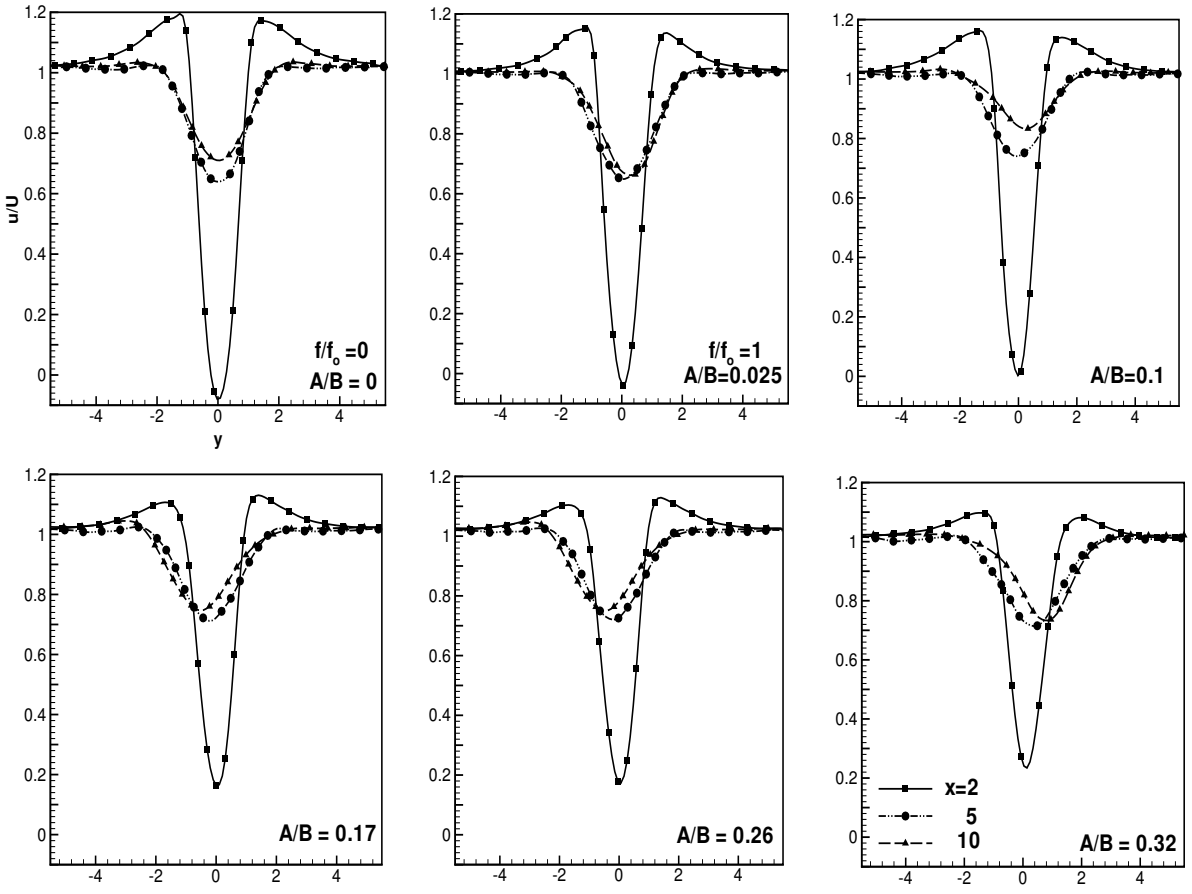

Figure 6.26: Time-averaged streamwise velocity profiles for various amplitudes of oscillation; Re=170, f/f_o=1.0.

oscillation creates a strong damping effect in the near flow field and a concentration of vortices in the near wake of the cylinder. Higher the amplitude of oscillation, larger is the damping effect. One can now expect the superimposed flow to modulate the vortex generation process described above, but the influence of increasing amplitude is clear. The origin of asymmetry to oscillation amplitude can now be traced to the fact that the forward and rear halves of the cylinder respond differently to the incoming flow.

6.2.5 Velocity fluctuations

Figure 6.30 shows the nondimensional turbulent intensity field $(((u_{rms}^2 + v_{rms}^2)^{0.5}/U))$ at various amplitudes of oscillation. The turbulent intensity near the cylinder increases as more positive energy enters the flow field from cylinder excitation. The maximum

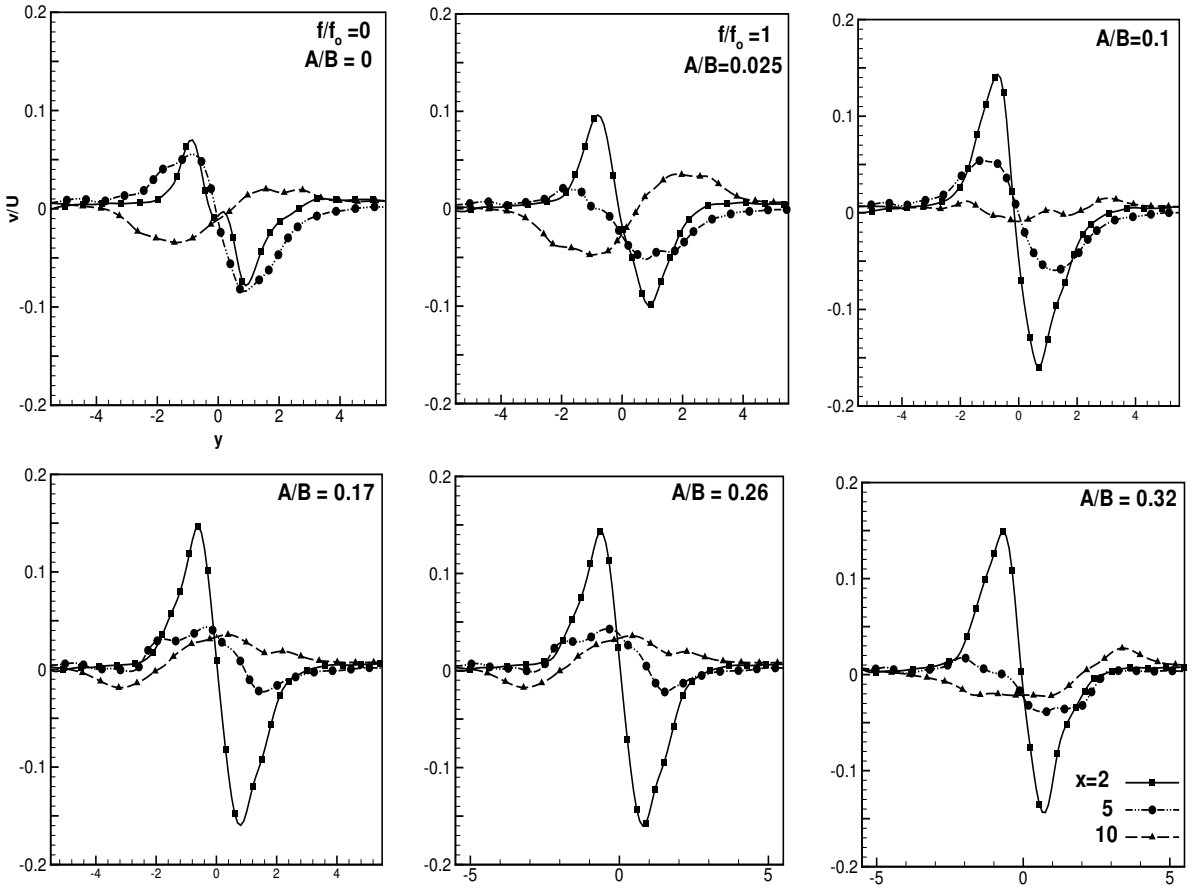

Figure 6.27: Time-averaged transverse velocity profiles for various amplitudes of oscillation; Re=170, f/f_o=1.0.

intensity value moves towards the cylinder with increase in excitation amplitude. The degree of asymmetry increases with an increase in amplitude. The transverse spacing is restricted for all the amplitudes considered, unlike experiments where the excitation frequency was increased.

Figure 6.31 shows the streamwise and transverse velocity fluctuations (u_{rms}, v_{rms}) along the cylinder centerline at various amplitudes of oscillation. With the increase in amplitude of excitation, the peak RMS value increases. The v_{rms} magnitude is higher when compared to the u_{rms} value for all amplitudes. From the RMS profiles, it is to be observed that peak magnitude of v_{rms} does not change significantly with amplitude. The u_{rms} magnitude changes sharply with an increase in amplitude. The position of the peak value moves upstream with an increase in amplitude. There is a sharp reduction in u_{rms} and v_{rms} after attaining its peak value. The rate of decay for u_{rms} is higher

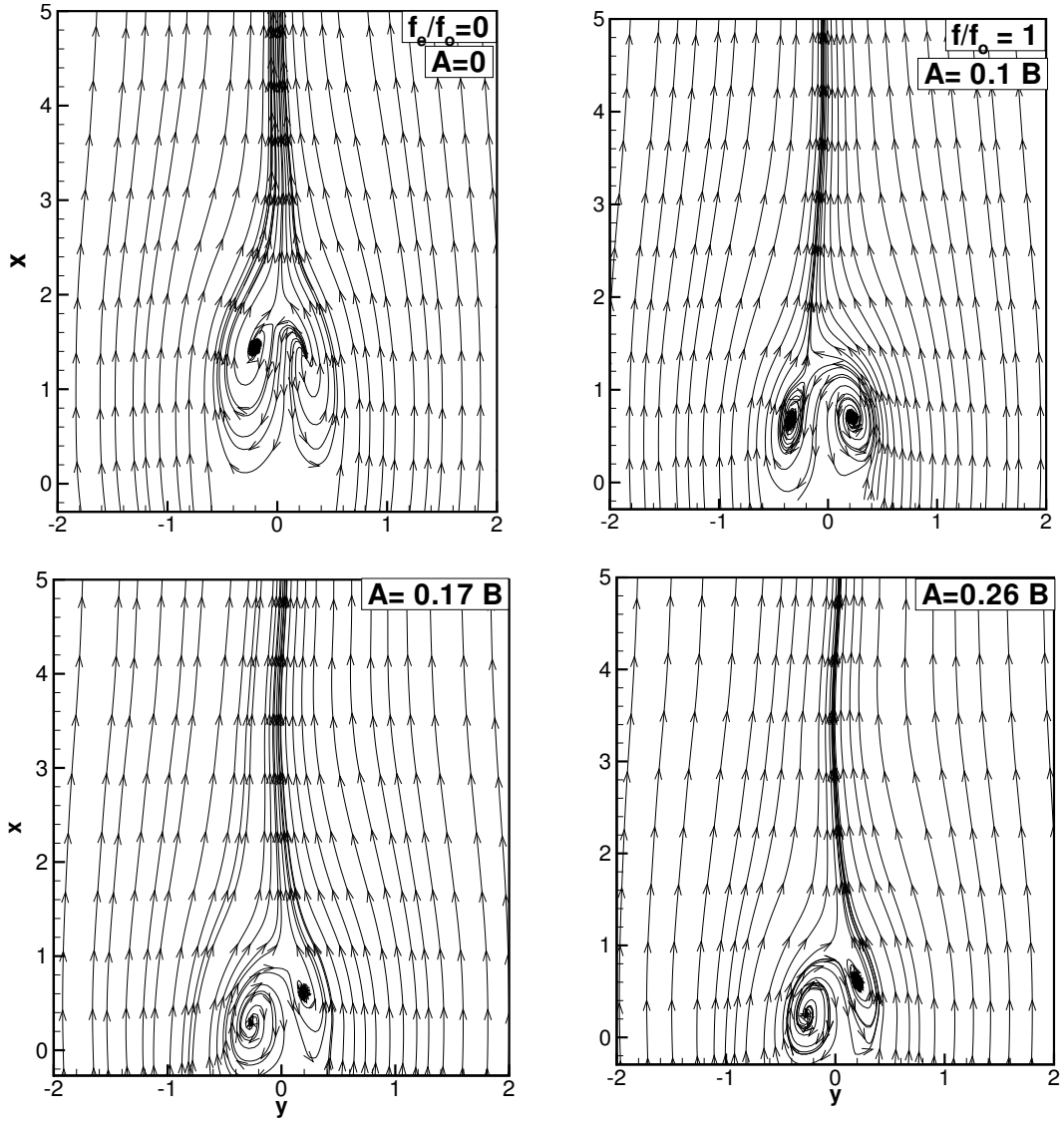

Figure 6.28: Time-averaged stream traces for various amplitudes of oscillation (A/B=0, 0.1, 0.17 and 0.26) at a constant forcing frequency (f/f_o=1.0); Re=170.

when compared to v_{rms}. The magnitude of v_{rms} peak is less sensitive to the amplitude of excitation compared to that of u_{rms}. The in-line nature of oscillation can be attributed to the higher sensitiveness of u_{rms} compared to that of v_{rms}.

Figure 6.32 and Figure 6.33 show the streamwise and transverse velocity fluctuation profiles at four downstream locations (x=2, 4, 6 and 8) and five amplitudes of oscillation. Similar to the effect of forcing frequency, the near wake shows a strong effect of amplitude. The effect of amplitude diminishes after x=2 (outside the near wake). The reduction in the peak magnitude of u_{rms} is higher in the near field region. In contrast, the v_{rms}

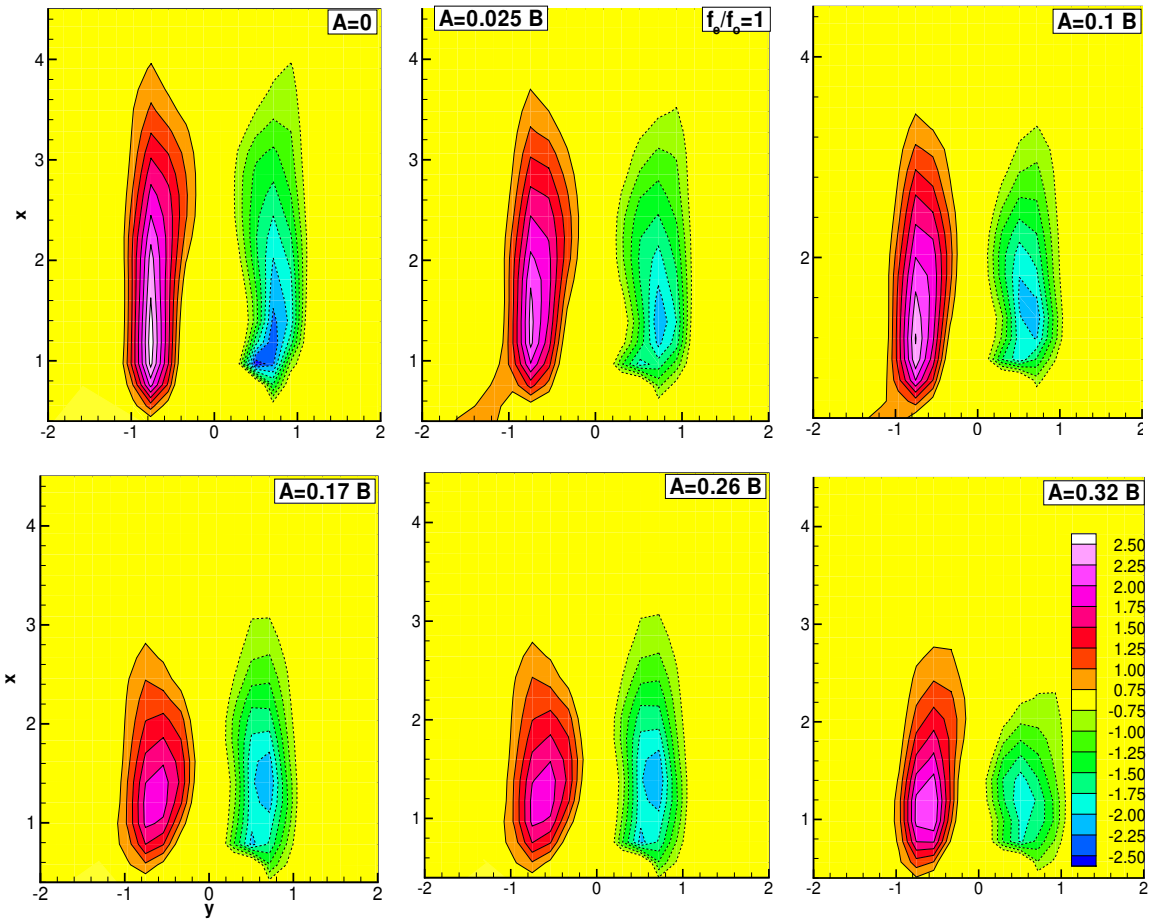

Figure 6.29: Time-averaged vorticity contours for various amplitudes of oscillation at forcing frequency, f/f_o=1.0; Re=170.

peak shows a larger fall in the downstream region, i.e. beyond the recirculation bubble. There is a systematic increase in fluctuation level with an increase in amplitude for both streamwise and transverse velocity fluctuations. The maxima in both components of velocity fluctuations occur at the highest amplitude considered.

6.2.6 Instantaneous flow field

Figure 6.34 shows the instantaneous vorticity contours for various amplitudes of oscillation. A significant change in the wake structure takes place as the forcing amplitude increases. At a low amplitude, the structure is more or less similar to the natural case of a stationary cylinder. With an increase in amplitude to an intermediate level, the vortices are seen to be rearranged. Vortex formation occurs much closer to the cylinder body. The length of the elongated vortex attached to one side of the cylinder decreases

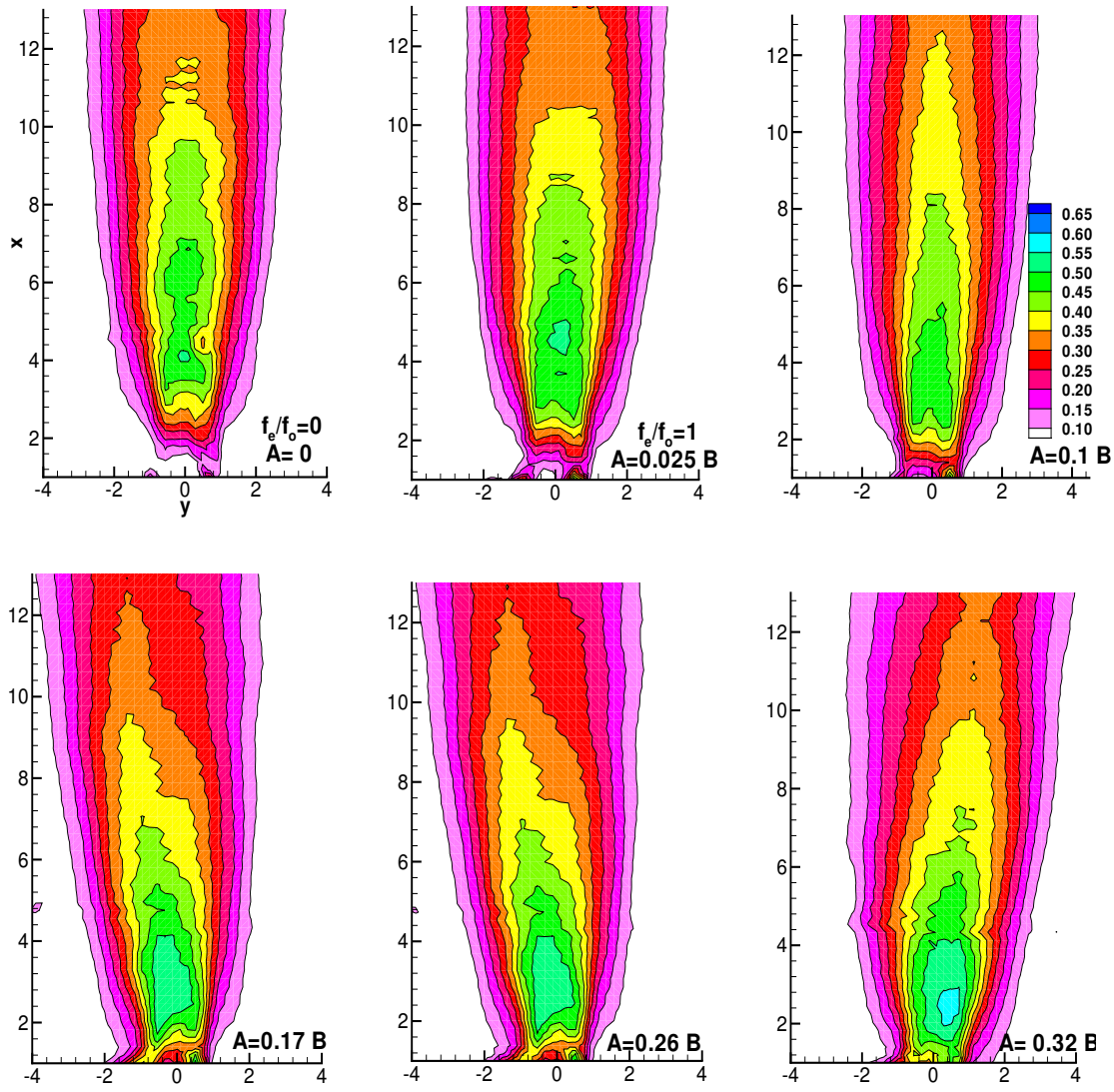

Figure 6.30: Contour of turbulence intensity $((u_{rms}^2 + v_{rms}^2)^{0.5}/U)$ for various amplitudes of oscillation at forcing frequency, f/f$_o$=1.0; Re=170.

with an increase in amplitude before shedding from the cylinder. This behavior of vortex separation is also observed when frequency is increased.

The flow separation mechanism differs for oscillation experiments from stationary in the following manner. The centroid of the vortices cross the centerline at a higher amplitude of oscillation. This is in contrast to the undisturb natural wake of a stationary cylinder where the vorticity shed from one side remains on the same side. In the former, the spacing between vortices becomes irregular at higher amplitude. The convection speed of the vortices is smaller when compared to the stationary cylinder. It causes

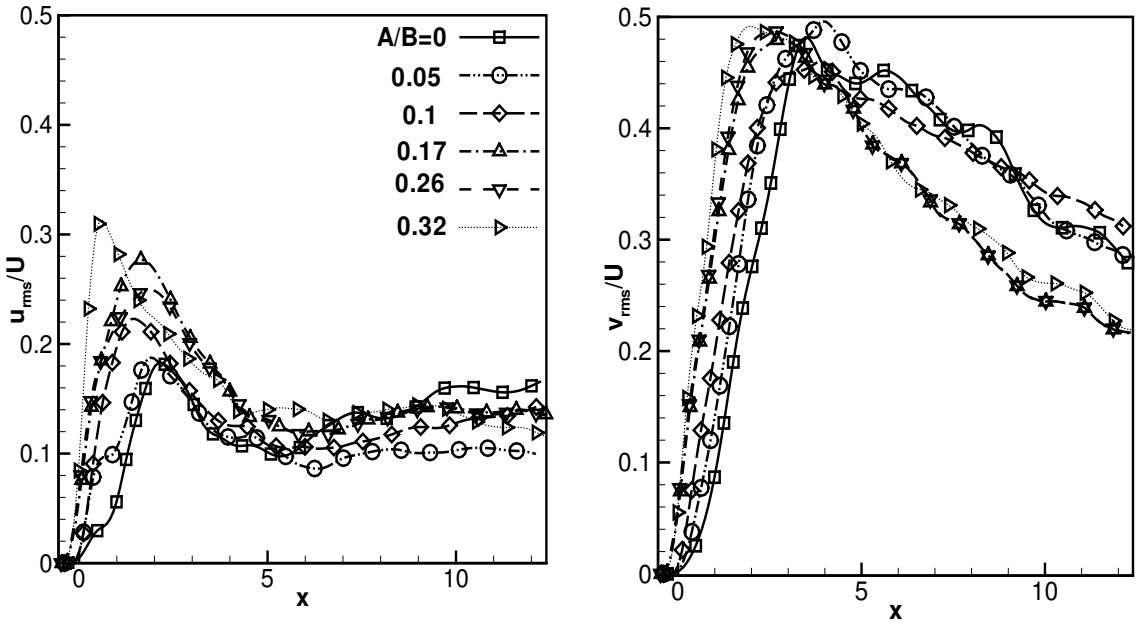

Figure 6.31: Profiles of centerline RMS velocity as a function of the amplitude of oscillation for fundamental excitation frequency (f/f_o=1.0); Re=170.

the longitudinal distance between two vortices of opposite sign to decrease, leading to the appearance of multiple modes by greater interaction between the vortices. This distance monotonically decreases with increase in amplitude of oscillation. Hence, there is a greater probability of vortex merging and the appearance of sub-harmonics at higher amplitude.

6.2.7 Centerline recovery

The effect of perturbation amplitude on centerline velocity recovery is shown in Figure 6.35. The centerline velocity is non-dimensionalised with the incoming free stream velocity. The perturbation frequency is set to be equal to the vortex shedding frequency. With an increase in the amplitude, recovery is faster and the centerline velocity attains an asymptotic value. The recirculation length denoted by the size of the near wake where the u-velocity is negative, decreases with an increase in amplitude. This trend has also been observed in transverse oscillation experiments of Konstantinidis *et al.* [77]. The size of the recirculation zone depends on the lowering of the base pressure which is ultimately related to drag coefficient. At a higher amplitude, the two oppositely oriented vortices come closer to the cylinder resulting in early interaction between vortices of opposite sign. The interaction of coherent structures is governed by tearing and pairing

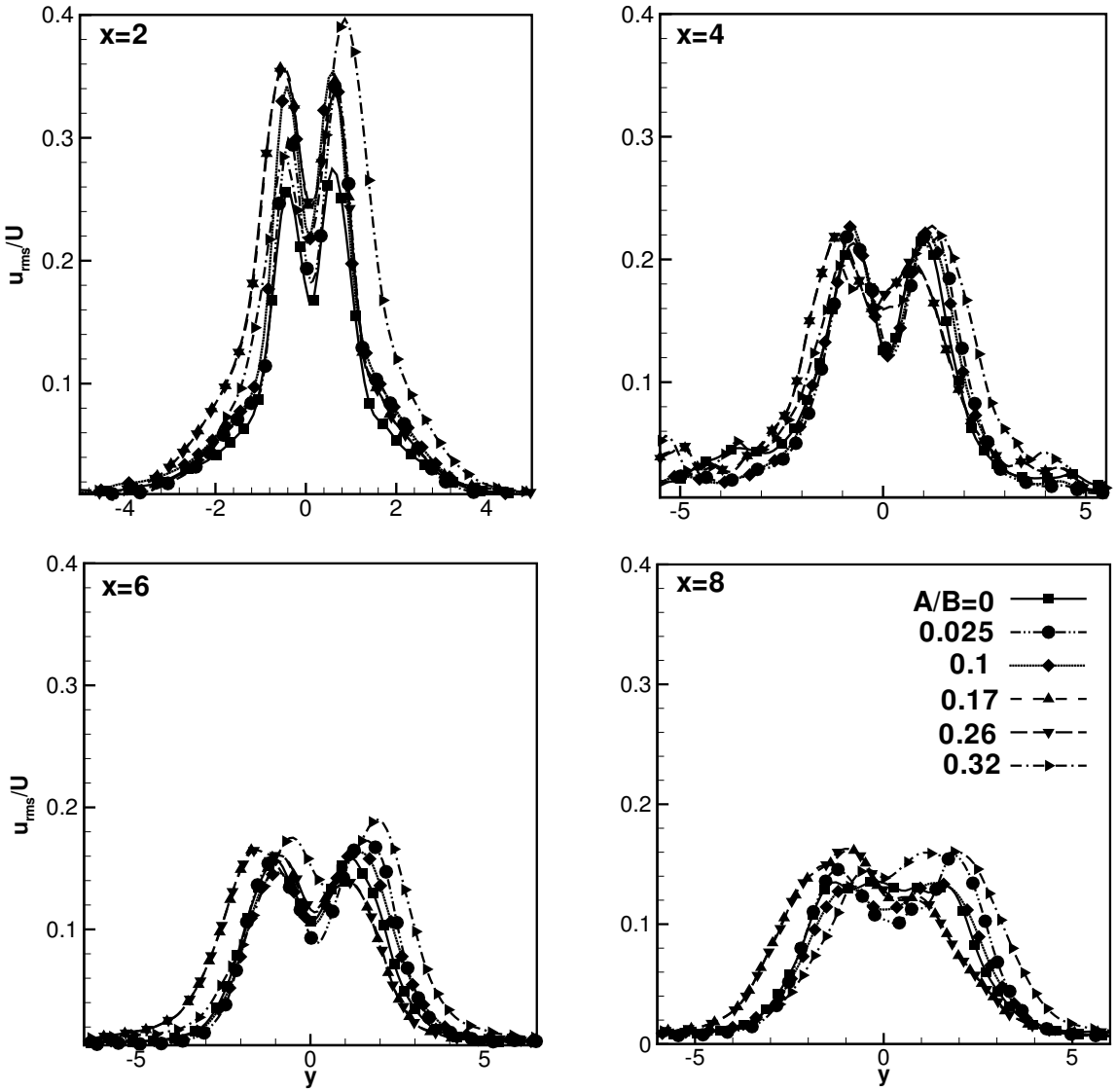

Figure 6.32: The u_{rms} velocity profiles for various amplitudes of oscillations at fundamental excitation (f/f$_o$=1.0); Re=170.

of vortices (Hussain, 1986), but the net effect is a raised base pressure and a lowered drag coefficient.

6.2.8 Power spectra

Figure 6.36 shows the power spectra of velocity signals in the near wake at different amplitudes of oscillation. Spectra have been calculated based on v component of velocity

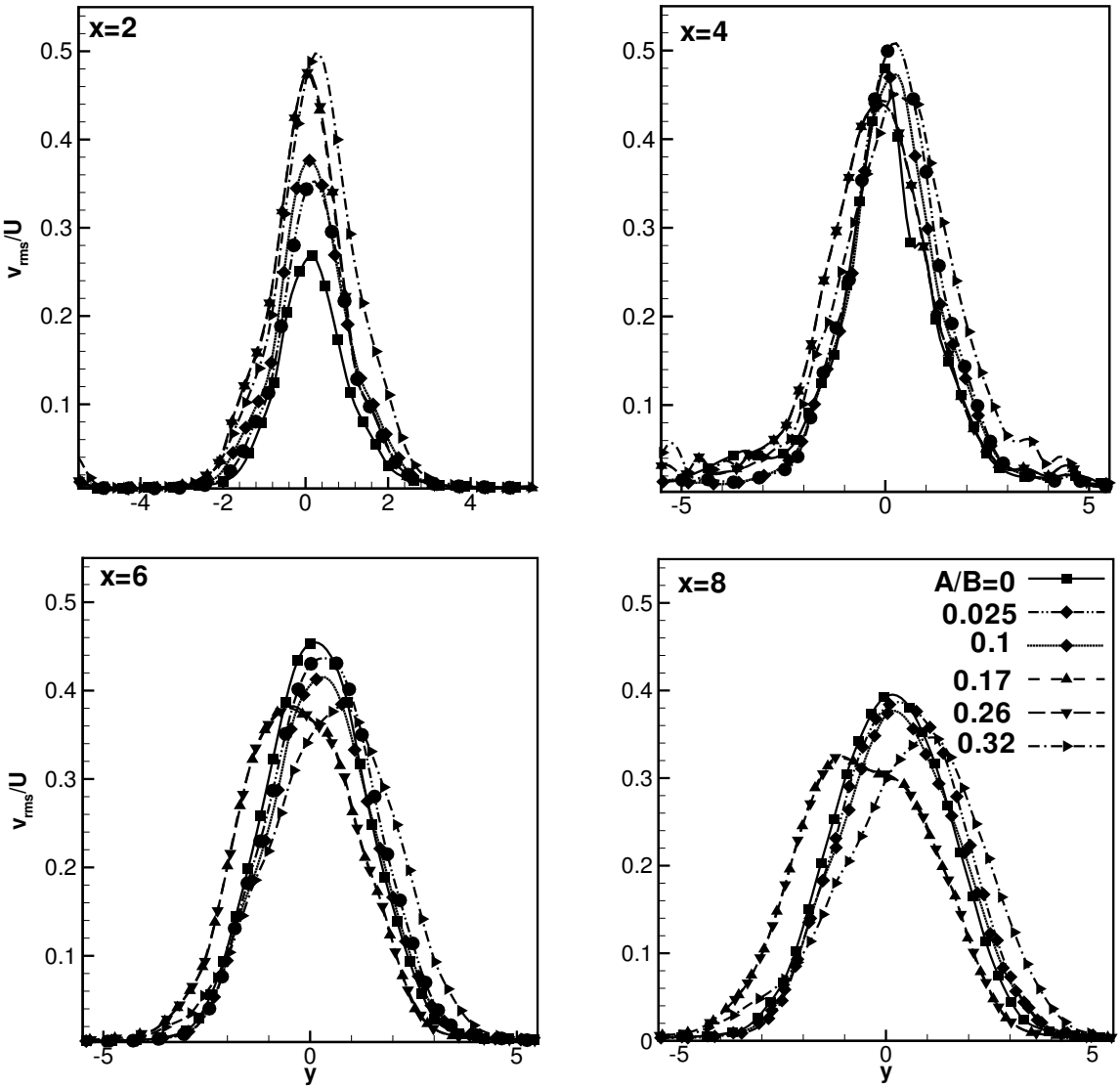

Figure 6.33: The v_{rms} velocity profiles for various amplitudes of oscillations at fundamental excitation (f/f_o=1.0), Re=170.

(at $x/B = 5$ and $y/B = 1$) and normalized with the area under the curve. Multiple frequencies in harmonics of vortex shedding start appearing with an increase in the amplitude of oscillation. After a particular amplitude, the flow field is dominated by the forcing frequency and only one dominant peak is seen in the power spectra. It can then be expected that the flow tends to become increasingly two dimensional at higher amplitudes. Here, two oppositely oriented vortices come closer and move parallel to the centerline. This process can explain a single dominant peak seen in the spectra. The

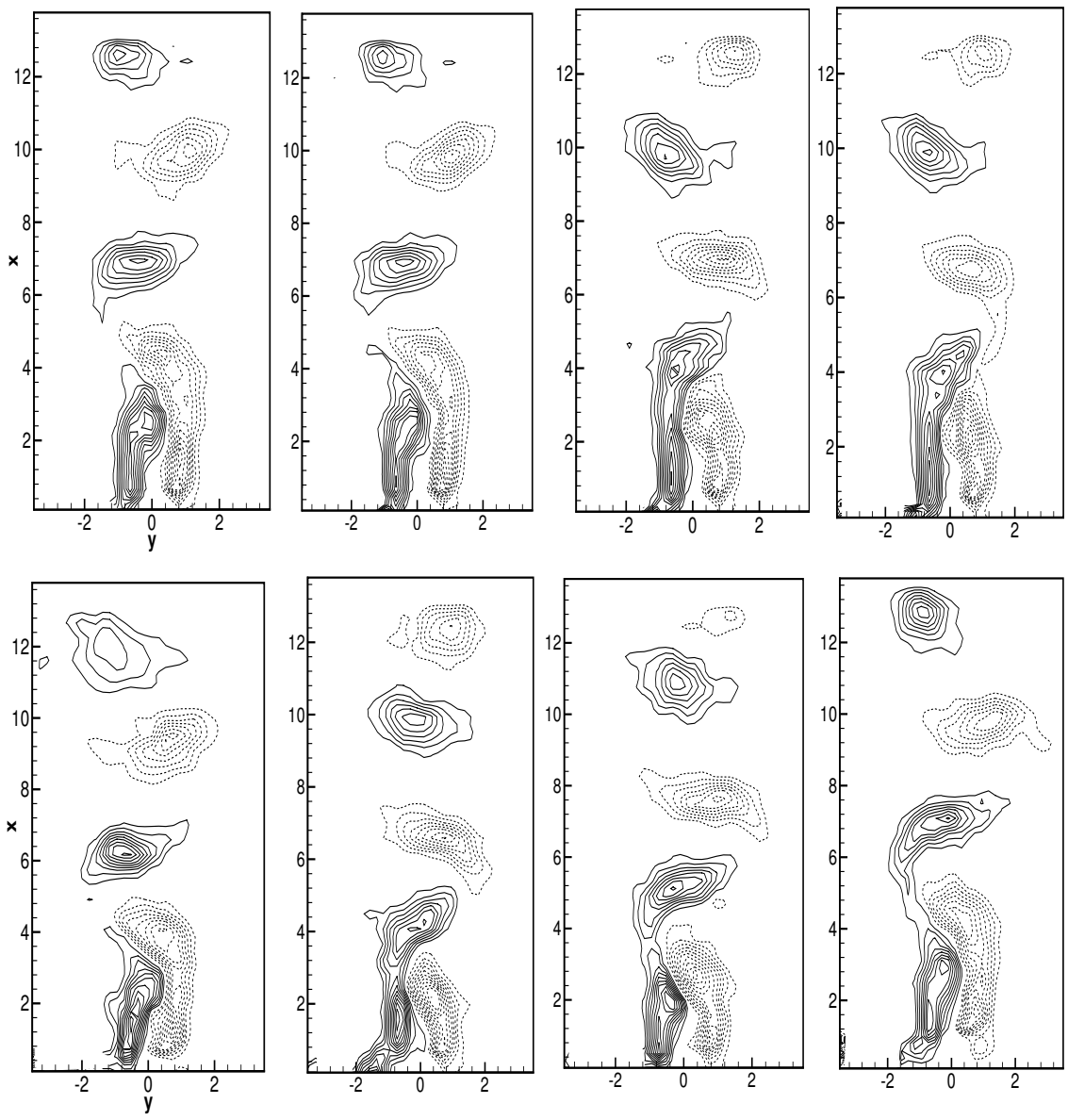

see caption on the next page

absence of harmonics at higher amplitude indicates the delay in the appearance of three dimensionality at higher amplitude.

6.2.9 Particle traces

Figure 6.38 show particle traces for various amplitudes of oscillation at a forcing frequency equal to vortex shedding frequency at Re=170. Each row is a time sequence of images for each amplitude. The images has been arranged on the basis of the cylinder

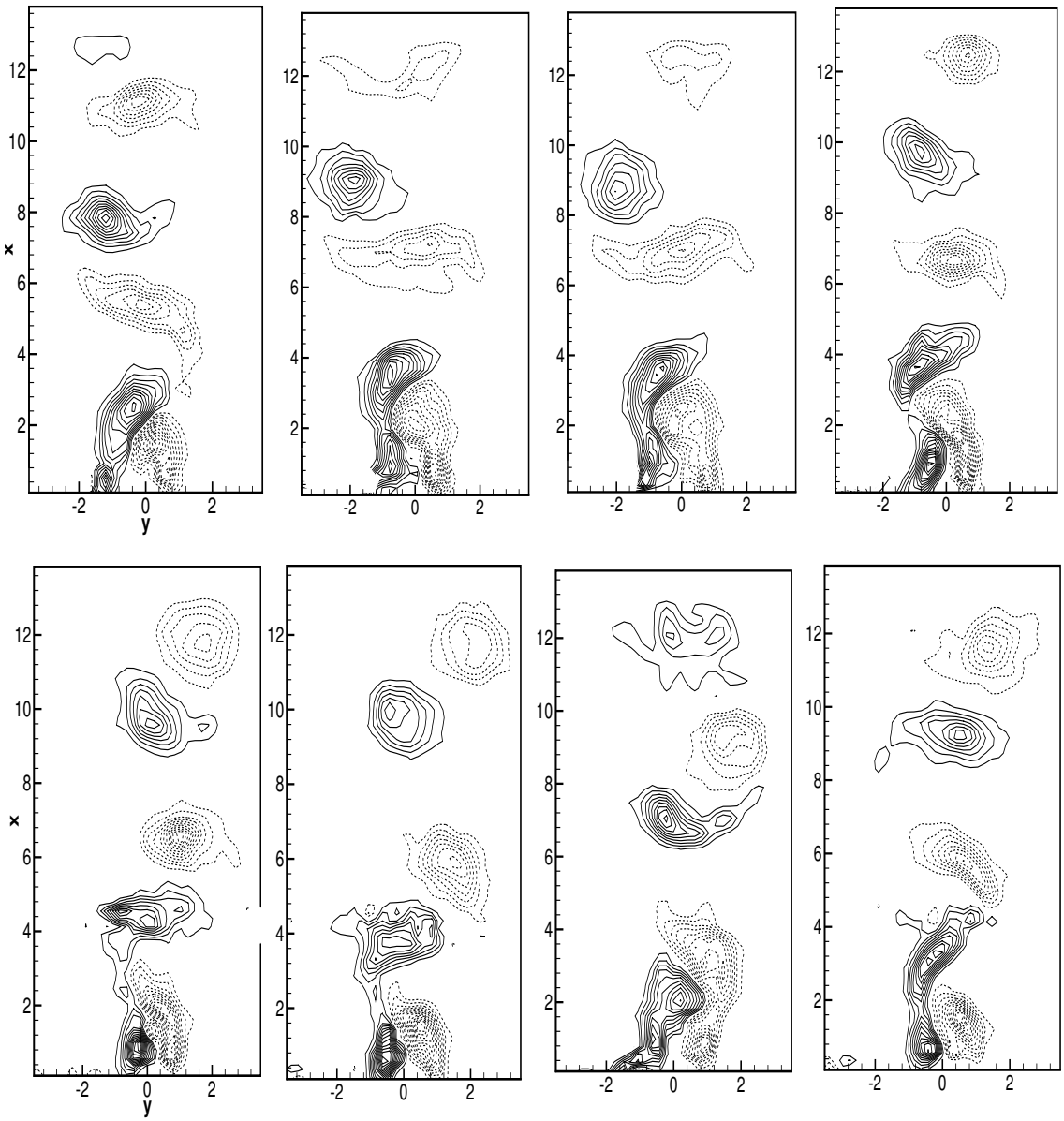

Figure 6.34: Instantaneous spanwise vorticity (ω_z) contours at different amplitudes of oscillation, A/B= 0 (1st row), 0.025 (2nd row), 0.26 (3rd row) and 0.32 (4th row), Re=170. $\omega_z(max)$, $\omega_z(min)$ and $\delta\omega_z$=4.0, -4.0, 0.25.

position as it is not possible to capture a continuous time sequence with the available camera speed of 8 Hz. As in the experiments with a stationary cylinder, the shedding pattern is found to be in $2S$ mode (Figure 6.20). The $2S$ mode is characterized by the shedding of a single vortex in each half cycle, analogous to Kárman vortex shedding. In the presence of oscillations, the shedding pattern is more organized and increases the correlation length over which the phase relationship is preserved. Vortex shedding

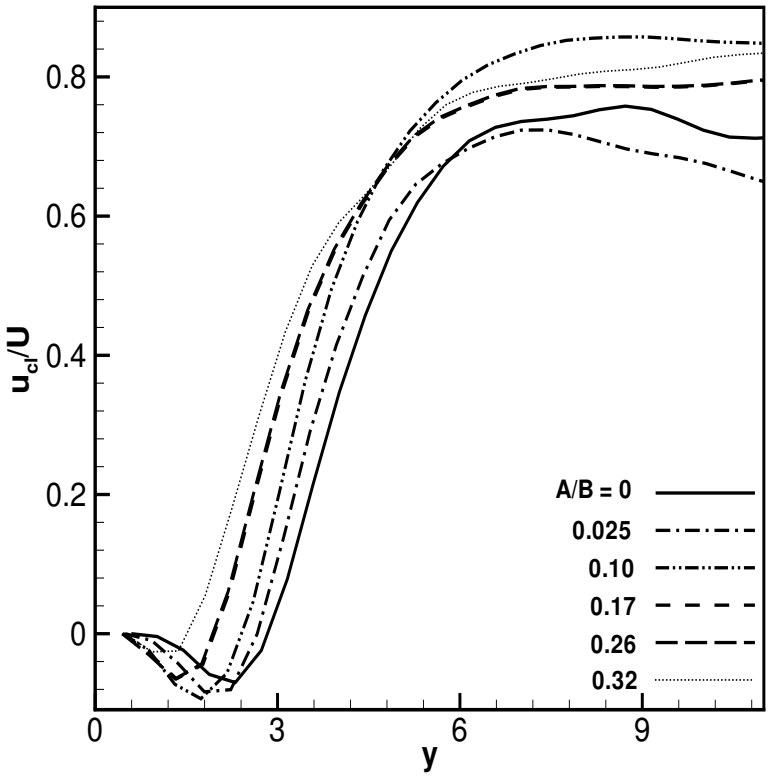

Figure 6.35: Centerline recovery of time-averaged streamwise velocity for various amplitudes of oscillation; Frequency (f/f_o)=1.0; Re=170.

is initiated closer to the cylinder and the spacing between two consecutive vortices of opposite sign reduces with an increase in amplitude. The vortex formed on one side of the cylinder is shed when the cylinder is near the maximum displacement position.

6.2.10 Closure

The effect of amplitude of oscillation on the flow field is studied. The frequency of oscillation is kept constant at the vortex shedding frequency of a stationary cylinder. The time-averaged flow field is affected in the near wake due to an increase in the amplitude. The time-averaged velocity profiles show asymmetry with increase in perturbation amplitude. Asymmetry is also seen in the contours of RMS velocity. The peak value of RMS velocity increases with excitation amplitude. The peak RMS value moves upstream towards the cylinder with an increase in the amplitude. The effect of increasing the amplitude at a given frequency leads to a reduction of the length of the recirculation

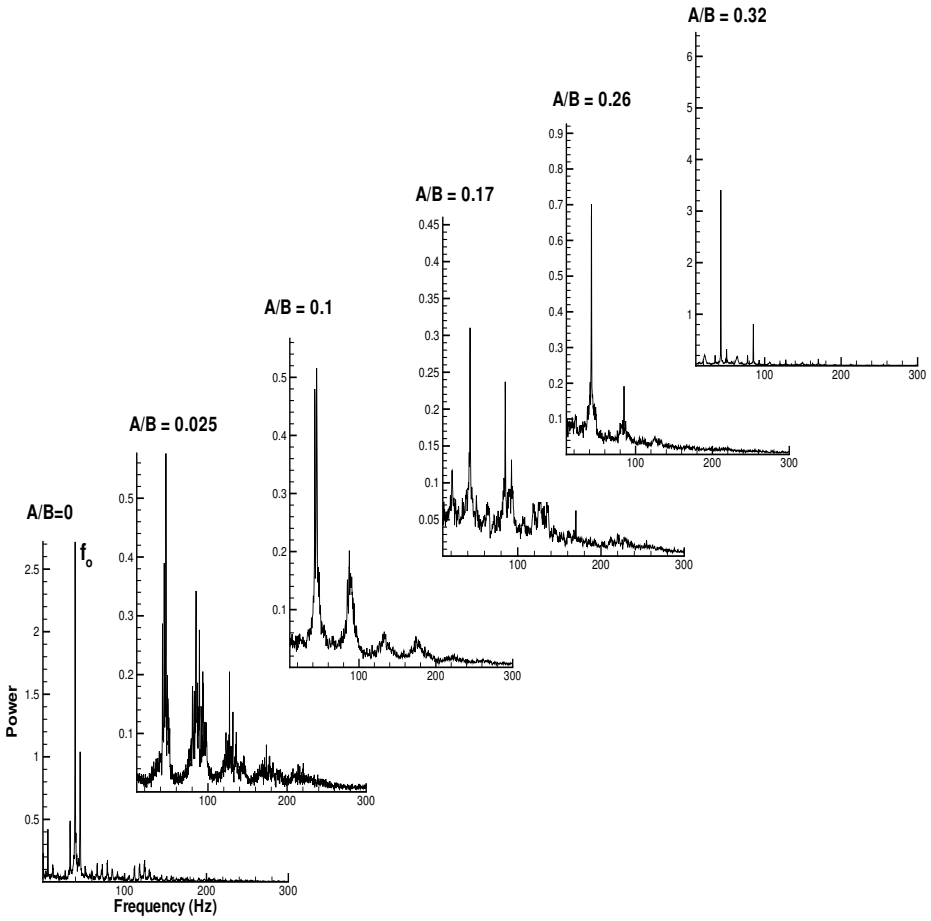

Figure 6.36: Power spectra for various amplitudes of oscillation at fundamental excitation (f/f_o=1.0); Re=170.

bubble and the vortex formation region. From the spectra, the flow field appears to be better organized and two dimensional at the highest amplitude considered.

6.3 Effect of Aspect Ratio

A limited study is carried out to investigate the effect of aspect ratio on the near wake of a cylinder under oscillatory conditions. While the aspect ratio considered in earlier Sections were 28, the aspect ratio in the present discussion has been set equal to 16. For definiteness, a Reynolds number of 170 is considered. The effects of frequency as well as amplitude of oscillation are investigated.

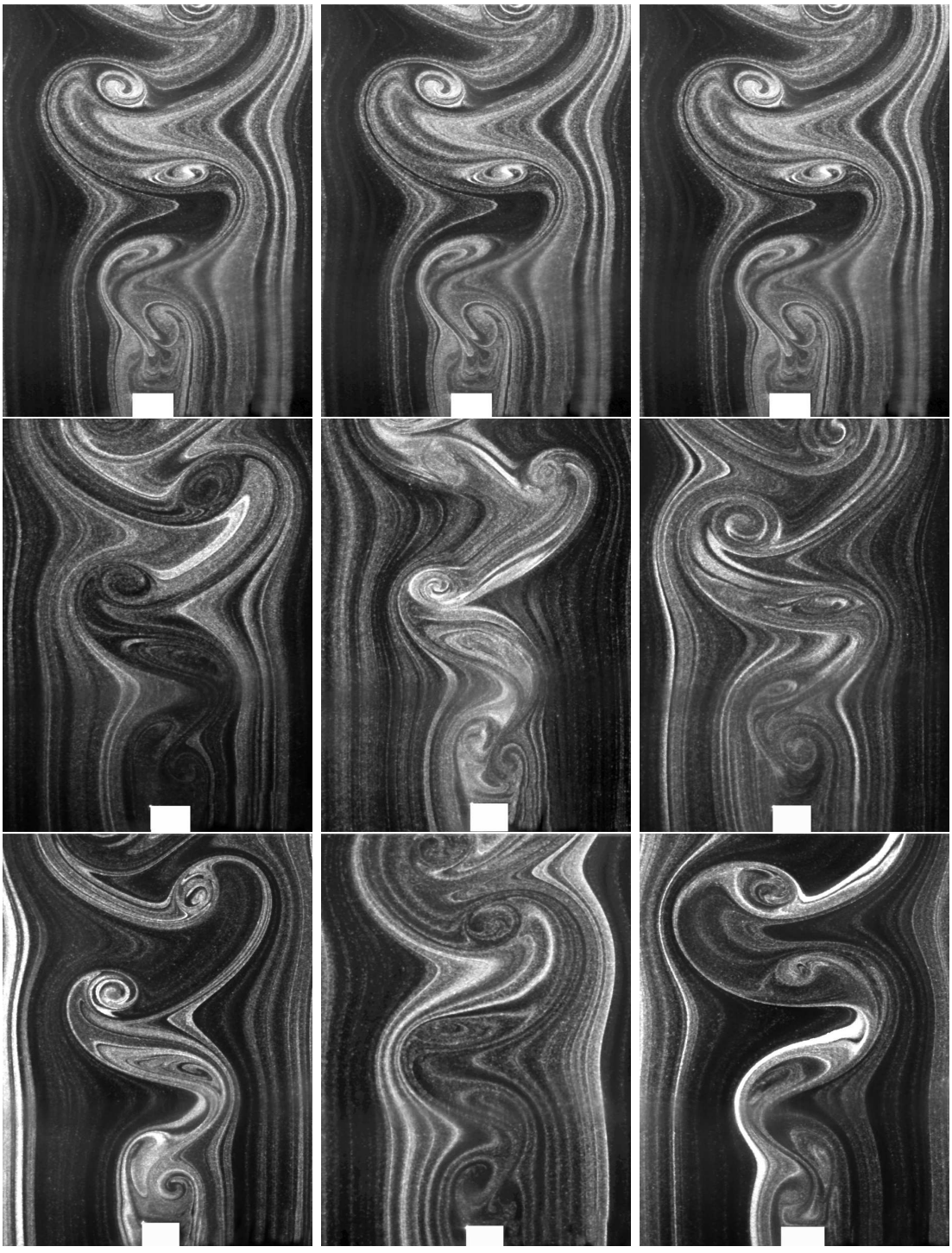

Figure 6.37: Time sequence of flow visualization images for various amplitudes of oscillation; A/B= 0 (1st row), 0.025 (2nd row), 0.1 (3rd row), Re=170, f/f_o=1.0.

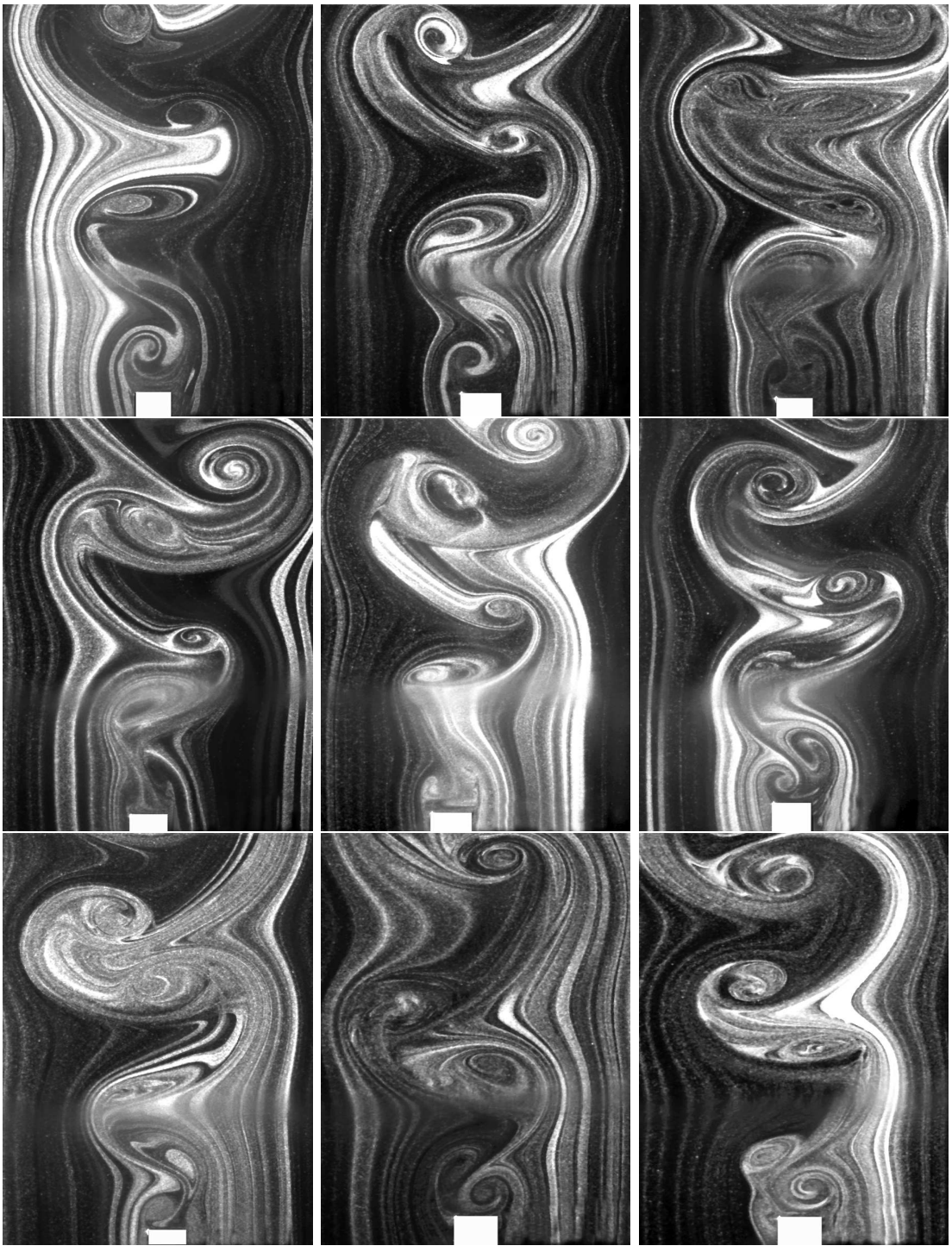

Figure 6.38: Time sequence of flow visualization images for various amplitudes of oscillation; A/B=0.17 (1st row), 0.26 (2nd row), 0.32 (3rd row), Re=170, f/f_o=1.0.

Table 6.6: Comparison of drag coefficient as a function of forcing frequency (left) and amplitude (right) for two aspect ratio (AR=16 and 28) at Re=170

f/f_o	AR=16	AR=28
0	2.42	1.48
0.5	2.61	1.13
1.0	1.51	0.68
2.0	2.02	1.05

A/B	AR=16	AR=28
0	2.34	1.48
0.05	2.55	-
0.1	1.91	0.94
0.17	1.72	0.85
0.23	1.34	0.81
0.27	1.21	-

Table 6.6 summarize the time-averaged drag coefficient data for two aspect ratio 16 and 28 for various frequencies and amplitudes of oscillation. In the study of the effect of frequency, the amplitude is kept constant at 0.1. In the second set of experiments, the forcing frequency is that of vortex shedding, while the amplitude is varied. The overall drag coefficient is lower at higher aspect ratio for both unexcited and excited cylinder. A minimum in drag coefficient is seen for a frequency ratio f/f_o=1.0 for both the aspect ratios. This indicates that the end conditions due to the aspect ratio difference does not alter the effect of cylinder oscillation. The magnitude of drag coefficient is uniformly higher when compared to the higher aspect ratio experiments[9]. The drag coefficient diminishes rapidly with an increase in the amplitude of oscillation.

Figure 6.39 and Figure 6.40 shows the time-averaged velocity vectors on the cylinder mid-plane at different frequencies and amplitude ratios respectively. With an increase in either the frequency of oscillation or the amplitude, the length of recirculation region decreases. The decreasing trend in C_D with an increase in the frequency ratio as well as amplitude can be correlated with this change in the flow distribution.

Figure 6.41 and Figure 6.42 show the time-averaged spanwise (ω_z) vorticity contours for various frequencies and amplitudes. With an increase in the forcing frequency, the vortices concentrate near the rear surface of the cylinder. Similar trends are to be observed at higher aspect ratio (AR=28). However, the strength of the vorticity is higher at lower aspect ratio compared to that at higher aspect ratio (see Figure 6.7 and Figure 6.41) . The high vorticity may be related to the effect of the end condition due to the low aspect ratio. The comparison of Figure 6.29 with Figure 6.42 indicate similar effect of excitation amplitude at both aspect ratios. The near field vorticity level is higher at lower aspect ratio due to the greater effect of end wall conditions.

[9]This effect of aspect ratio on drag coefficient was seen for a stationary cylinder as well.

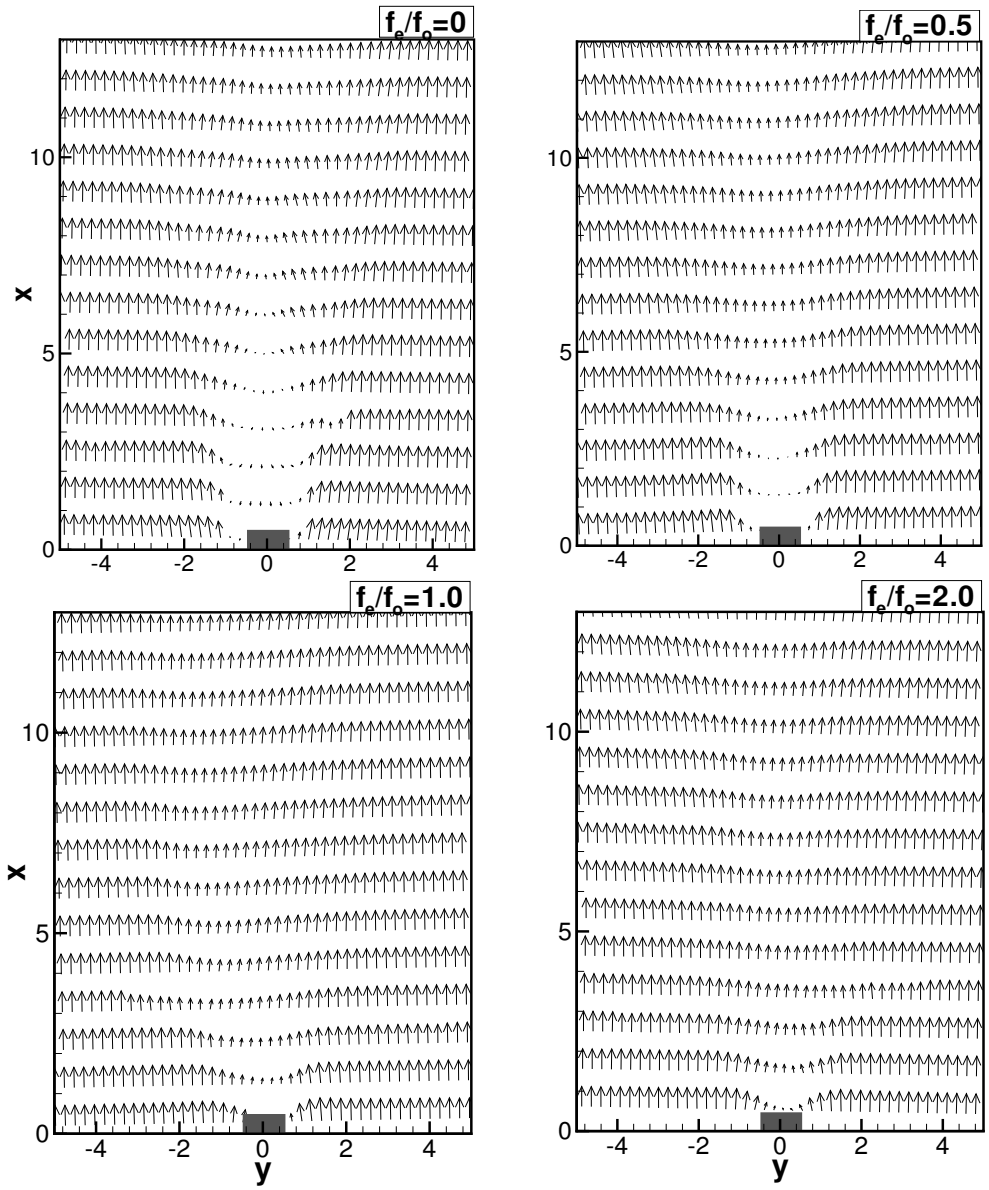

Figure 6.39: Time-averaged velocity vectors at various frequencies of oscillation; Re=170 and amplitude of oscillation (A/B)=0.1. Aspect ratio(AR)=16.

Figure 6.43 and Figure 6.44 present the effect of frequency and amplitude of oscillation on the evolution of the centerline streamwise velocity component. Velocity values are normalized with the free stream velocity (=U). Both frequency and amplitude have similar effect on the centerline velocity. The recovery is rapid and the size of the recirculation bubble diminishes with increase in frequency as well as amplitude.

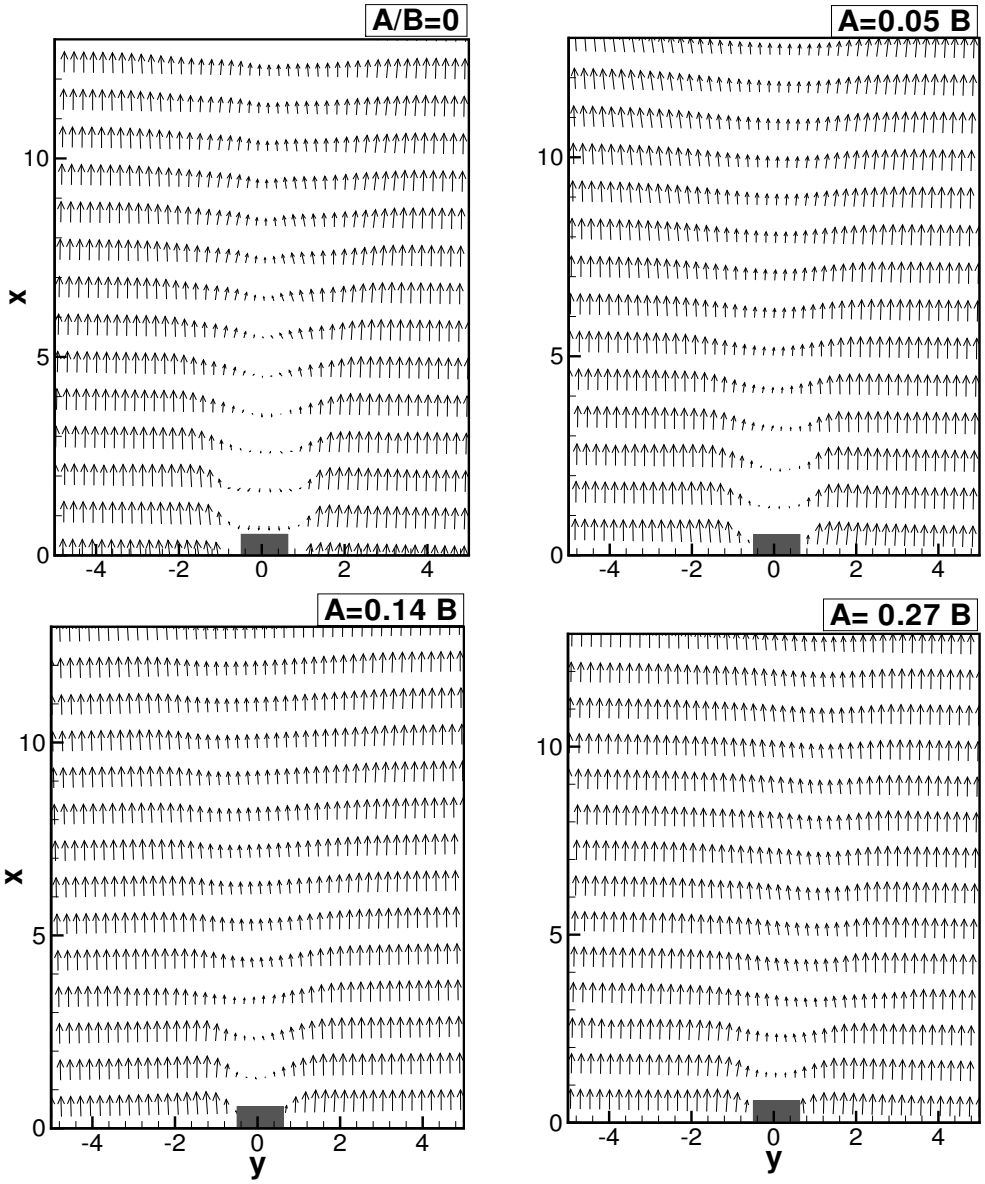

Figure 6.40: Time-averaged velocity vectors at various amplitudes of oscillation; Re=170 and f/f_o=1. AR=16

The asymptotic centerline velocity is reached within the measurement plane at high frequencies and amplitudes. The comparison of Figures 6.43 and 6.44 with Figures 6.19 and 6.35 indicates greater receptivity of oscillation with respect to the frequency and amplitude of oscillation compared to the stationary cylinder at low aspect ratio case. In summary, the near wake flow patterns of an oscillating cylinder respond strongly to frequency and oscillation amplitude but only weakly to aspect ratio.

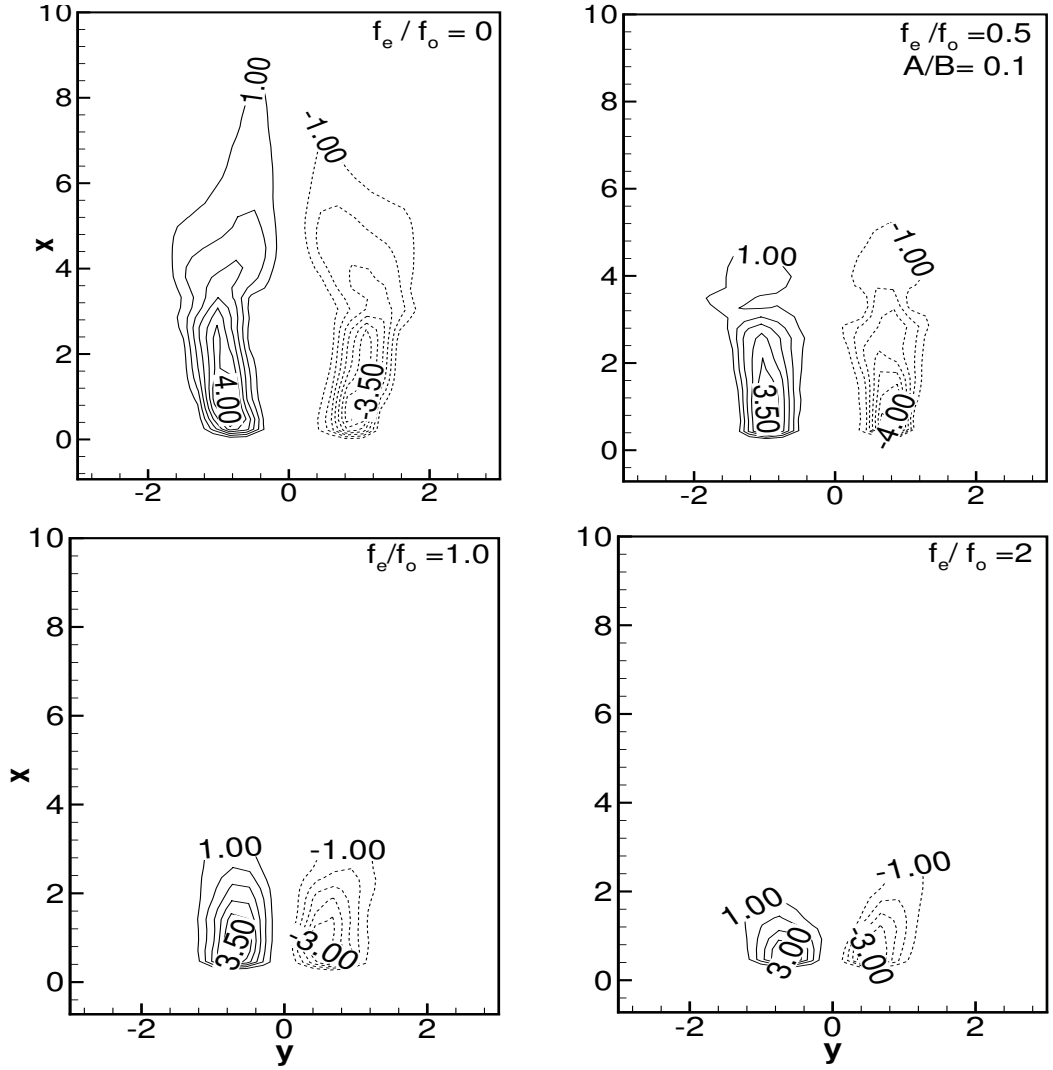

Figure 6.41: Time-averaged spanwise vorticity contours (ω_z) for various forcing frequencies (f/f_o=0, 0.5, 1.0 and 2.0), at Re=170 and amplitudes (A/B)=0.1. Aspect ratio (AR)=16.

6.4 Summary

The effect of forced oscillation of a square cylinder mounted in a free stream at zero incidence has been studied. The cylinder is oscillated in-line, i.e. in the mean flow direction. The wake sensitivity to the oscillation frequency and amplitude of oscillation are investigated. The frequency of oscillation is set to f/f_o=0, 0.5, 1.0 and 2.0. Here f_o is the vortex shedding frequency of a stationary cylinder. The amplitude of oscillation is set in the range of (0-0.32) of the cylinder size. The effect of cylinder aspect ratio is investigated by comparing the results for two aspect ratios, i.e. AR=16 and 28. The

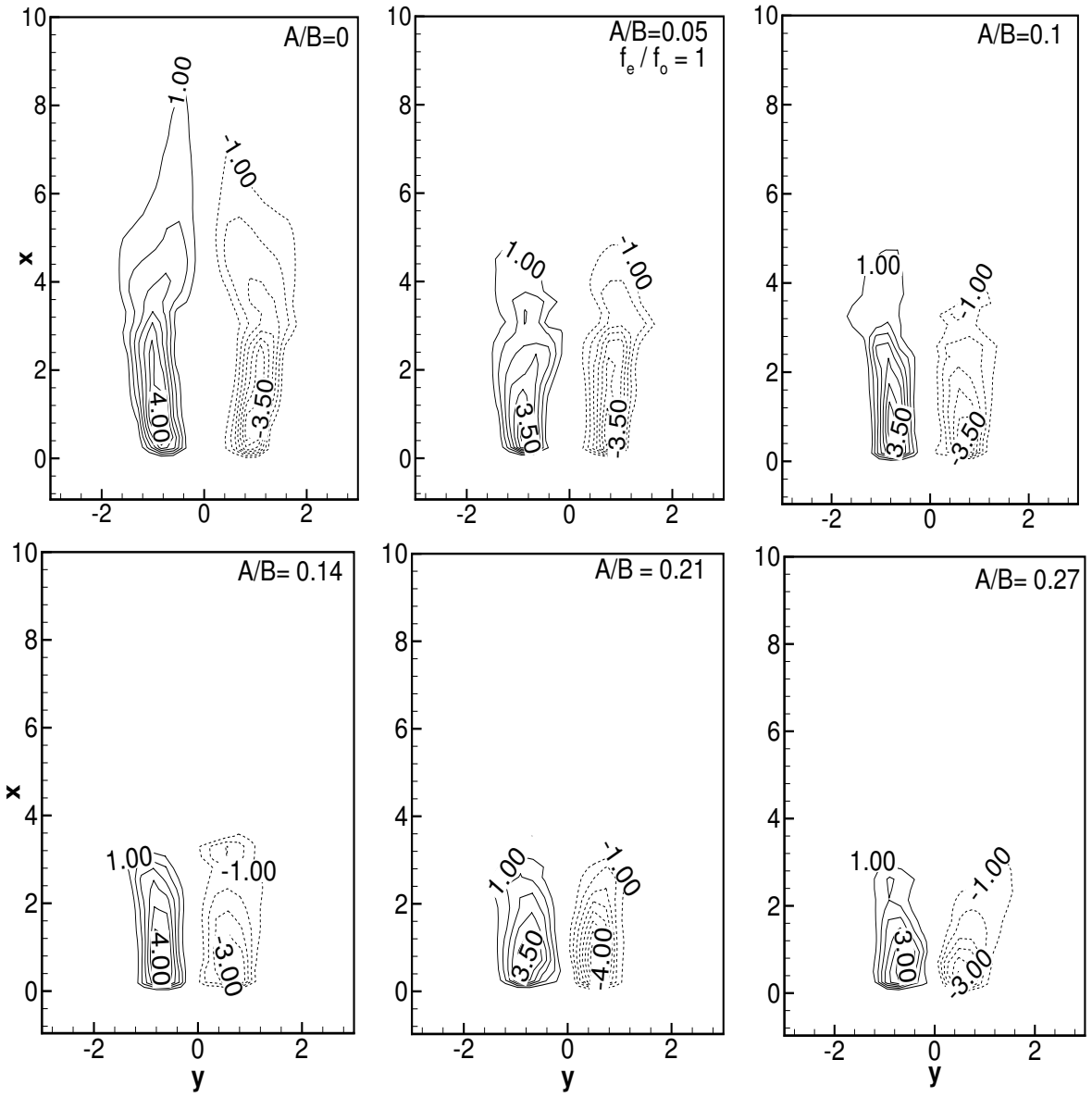

Figure 6.42: Time-averaged spanwise vorticity contours (ω_z) at various amplitudes of oscillation (A/B=0, 0.05, 0.1, 0.14, 0.21 and 0.27), Re=170 and f/f_o=0.1. Aspect ratio (AR)=16.

observations of the study can be summarized as follows:

(1) The momentum deficit in the wake reduces due to cylinder oscillation. The largest drop in momentum deficit is observed at the oscillation frequency, f/f_o=1.0 and 2.0 at the excitation amplitude equal to 0.1 times the cylinder dimension. The increase in the excitation amplitude at the fundamental also leads to reduction in the momentum deficit. However, the relative drop in the magnitude of momentum deficit reduces at

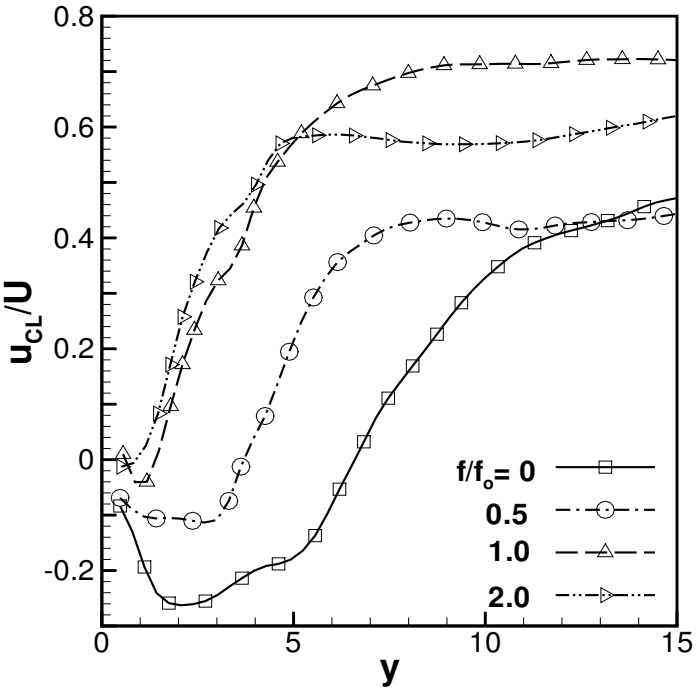

Figure 6.43: Centerline recovery of streamwise velocity at various oscillation frequencies (f/f$_o$=0, 0.5, 1.0 and 2.0) at constant amplitude of oscillation (A/B)=0.1; Re=170; AR=16.

very high oscillation amplitude.

(2) The size of the recirculation bubble is sensitive to both oscillation amplitude and frequency. There is a reduction in the size of the recirculation bubble with an increase in the excitation frequency and its amplitude. The x-location of the minimum centerline velocity in the zone of flow reversal also moves closer to the cylinder. The asymmetry of the recirculation bubbles increases at higher Reynolds number and at higher amplitude of oscillation. This is attributed to the phase relationship of vortex shedding with respect to the motion of the cylinder.

(3) The size of the average vorticity contour reduces for the oscillating cylinder compared to the stationary cylinder. Both the oscillation frequency and amplitude of oscillation have a similar effect on the vorticity contours. The relative size of the vorticity contours follows an identical trend as the recirculation bubble. The high value of vorticity in the near field region has also been observed in previous studies on an oscillating circular cylinder. This is also an indication that vortex formation length reduces for the oscillating cylinder. The centerline u_{rms} variation in the streamwise direction confirms

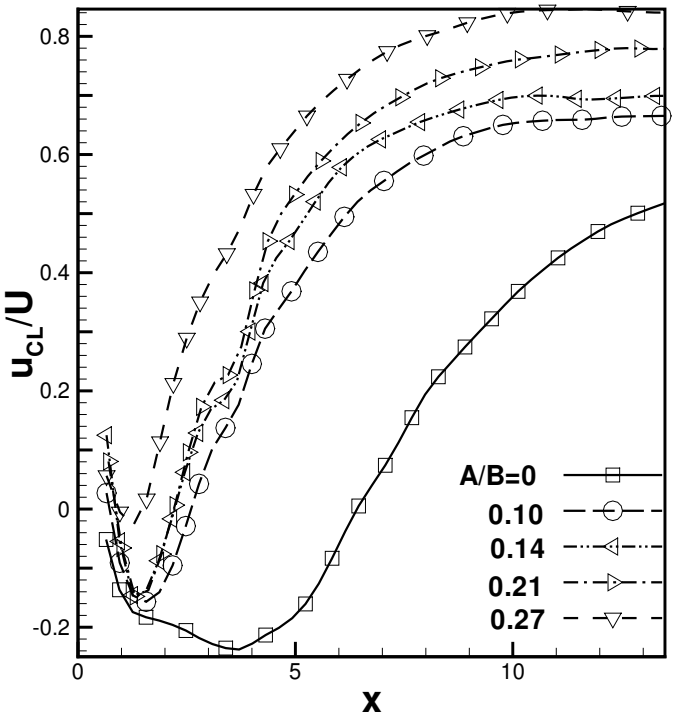

Figure 6.44: Centerline recovery of streamwise velocity for various amplitude of oscillation; Frequency(f/f_o)=1.0; Re=170; AR=16.

the drop in the vortex formation length for an increase in excitation frequency and amplitude.

(4) The changes in turbulence intensity demonstrate the wake unsteadiness or instability when the stationary and oscillating cylinder are compared. The near field region is more sensitive to the cylinder oscillation than the far field region. The turbulence intensity in the near field increases with an increase in frequency and amplitude of oscillation.

(5) The power spectra do not show the lock-on regime of the cylinder wake for the excited flow. However, multiple peaks are visible at intermediate amplitudes of excitation and there is a clear dominant peak at high amplitudes indicating two dimensional vortex shedding. The flow visualization images also show clear vortex shedding and the changes in the size of the vortex formation length. The merging and greater transverse motion of the neighboring vortices explain the appearance of secondary flow and additional peak in the power spectra.

(6) The overall effect of excitation is mildly altered by the aspect ratio of the

cylinder. There is a larger concentration of vorticity for the lower aspect ratio compared to the higher aspect ratio. This is due to a greater wall influence at the lower aspect ratio.

Chapter 7

Conclusions and Scope of Future Work

An experimental study of flow past stationary and oscillating square cylinders at intermediate range of Reynolds number is reported. Measurement techniques are based on PIV, HWA and flow visualization. The Reynolds number range considered is 90-610. The effects of cylinder orientation and aspect ratio on the wake structure have been studied for the stationary cylinder. In the second set of experiments, the cylinder is oscillated using an electro-magnetic actuator at around the vortex shedding frequency of the equivalent stationary cylinder. The flow patterns have been mapped for various frequencies and amplitudes of oscillation. Major conclusions arrived at from the study are presented below.

7.1 Stationary Square Cylinder

1. Drag coefficient and Strouhal number: Flow characteristics and all related parameters are seen to be affected by the cylinder orientation. Among the angles studied, a minimum in drag coefficient is seen to occur at 22.5^o. At this orientation the Strouhal number is a maximum.

2. Symmetry: For orientations other than 0 and 45^o, the wake is asymmetric. The v-velocity profile clearly brings out the wake asymmetry. The roll up of the shorter shear layer governs wake unsteadiness and hence Strouhal number. The loss of symmetry of the wake increases the transverse velocity, increases the base pressure and lowers the drag. This factor is counter-balanced by an increase in blockage itself, but the minimum in the drag coefficient at an orientation of 22.5^o reveals that the former has overall stronger influence at small cylinder angles. Stronger

three dimensionality of the flow field at this angle additionally contributes to higher base pressure and lower drag.

3. Aspect ratio: Drag coefficient and Strouhal number are seen to be strong function of aspect ratio for the range of Reynolds number studied. Strouhal number increases with increase in aspect ratio and drag coefficient decreases with an increase in aspect ratio. For both aspect ratios, a minimum in drag coefficient is found at 22.5^o. For this orientation, Strouhal number is a maximum. The centerline recovery of streamwise velocity is faster for the high aspect ratio (AR=28) when compared to low aspect ratio (AR=16). The size of the recirculation bubble is lower at the higher aspect ratio.

4. Flow visualization: The visualization pictures show that the separation distance between the alternating Kárman vortices are function of both aspect ratio and cylinder orientation. The multiple modes in the power spectra indicate the modification of vortex shedding process and appearance of secondary vortical structure. From images of secondary flow, it is seen that flow three dimensionality is stronger for AR=16 compared to AR=28.

5. Reynolds number: Drag coefficient and Strouhal number show only a dependence on Reynolds number. However the flow structure is strongly affected. The fluctuation levels increase with an increase in Reynolds number. Flow become strongly three dimensional as well, as Reynolds number increases. Multiple peaks appearing in the power spectra (around the vortex shedding frequency) indicate energy transfer among discrete modes in the flow field. The streamwise velocity fluctuation along the cylinder centerline doubles in magnitude over the Reynolds number range of 165 to 595.

7.2 Oscillating Square Cylinder

1. Frequency: A strong effect of forcing frequency (around the vortex shedding frequency) in the near-wake flow field is uniformly to be seen in the measured data. The recirculation length and formation length reduce substantially with an increase in frequency and diminish the time-averaged drag force acting on the cylinder. The instantaneous vorticity contours show the shear layer elongation to be a minimum before separation; hence the longitudinal wavelength of the shed vortices reduces. The time-averaged vorticity contours show that with an increase in frequency, the large scale vortices move closer to the cylinder. The RMS values of velocity fluctuations cluster around the cylinder as well. By a mechanism of improved mixing,

they can result in pressure equalization and a further reduction in drag coefficient.

2. Amplitude: The effect of amplitude of oscillation on the flow details has been studied when the forcing frequency is kept at the vortex shedding frequency of the stationary cylinder. The time-averaged flow field shows a nominal effect of increase in amplitude but the instantaneous flow field changes significantly with amplitude. The time-averaged velocity profiles show asymmetry with increase in the perturbation amplitude. Asymmetry is related to the phase difference between the vortex shedding mechanism and the cylinder motion. Asymmetry is also seen in the contours of RMS velocity. The peak value of RMS velocity increases with amplitude. The peak RMS value also moves upstream with an increase in the amplitude. The effect of increasing the amplitude at a given frequency leads to a reduction of the length of the recirculation bubble.

3. Aspect ratio: A limited study has been carried out at an aspect ratio of 16. The effect of forcing frequency and amplitude are identical to the flow field as seen for the higher aspect ratio. With increase in frequency and amplitude of oscillation the recirculation length reduces. Hence a diminishing trend in drag coeffient is seen. The vortices are concentrated near the cylinder with increase in frequency and amplitude of oscillation. The maximum magnitude of spanwise vorticity is higher at the lower aspect ratio as compare to the higher (AR=28).

7.3 Future Work

The following topics are suggested as future work of interest.

1. Use a stereoscopic version of PIV to estimate spanwise velocities along the cylinder length. Three dimensionality is better understood with this approach.

2. Experiments reported in the present study can be closely validated against numerical simulation since inflow and other boundary condition are fully known.

3. The influence of a feedback control system to control cylinder oscillations on flow control within the wake is a topic of considerable importance.

4. Extending the ranges of parameters such as aspect ratio, Reynolds number, frequency ratio, amplitude ratio and orientation will strengthen the conclusions arrived at in the present work.

References

[1] Adrian, R. J. and Yao, C. S., (1985), Pulsed Laser Technique Application to Liquid and Gaseous Flows and the Scattering Power of Seed Materials, *Applied Optics*, Vol.24, No. 1, pp. 44-52.

[2] Adrian, R. J., (1986), Multi-point Optical Measurements of Flow Simultaneous Vectors in Unsteady Flow- a Review. *Int. J. Heat and Fluid flow*, Vol. 7, No.2, pp. 127-145.

[3] Adrian, R. J., (1997), Dynamic Ranges of Velocity and Spatial Resolution of Particle Image Velocimetry, *Meas. Sci. Techonol.*, Vol. 8, pp. 1393-1398.

[4] Atta, C. W. V., (1987), Ordered and Chaotic Vortex Streets Behind Circular Cylinders at Low Reynolds Numbers, *J. Fluid Mech.*, Vol. 174, pp. 113-133.

[5] Antonia, R. A. and Rajagopalan, S., (1990), Determination of Drag of a Circular Cylinder, em AIAA Journal, Vol. 28, No. 10, pp. 1834-1835.

[6] Adrian, R. J., (1991), Particle Imaging Techniques for Experimental Fluid Mechanics, *Annu. Rev. Fluid Mech.*, Vol. 23, pp. 261-304.

[7] Adrian, R. J., (2005), Twenty Years of Particle Image Velocimetry, *Expts. Fluids*, Vol. 39, pp. 159-169.

[8] Abrahamson, S. and Lonnes, S., (1995), Uncertainty in Calculating Vorticity from 2D Velocity Fields Using Circulation and Least-Square Approaches, *Expts. Fluids.*, Vol. 20, pp. 10-20.

[9] Antonia, R. A. and Rajagopalan, S., (1989), Determination of Drag of a Circular Cylinder, *AIAA Journal*, Vol. 28, No. 10, pp. 1833-1834.

[10] Blackwelder, R. F., Liu, D. and Jeon W., (1998), Velocity Perturbations Produced by Oscillating Delta Wing Actuators in the Wall Region, *J. Expt. Thermal and Fluid Science*, Vol. 16, pp. 32-40.

[11] Bergé, P., Pomeau, Y. and Vidal, C., (1986),*Order Within Chaos*, Wiley, New York.

[12] Boillot, A. and Prasad, A. K., (1996), Optimization Procedure for Pulse Separation in Cross-Correlation PIV, *Expts. Fluids*, Vol. 21, pp. 87-93.

[13] Bearman, P. W., (1997), Near Wake Flows Behind Two-and Three-Dimensional Bluff Bodies, *J. Wind Engg. Ind. Aerodyn.*, Vol. 69-71, pp. 33-54.

[14] Brede, M., Eckelmann, H. and Rockwell, D., (1996), On Secondary Vortices in the Cylinder Wake, *Phys. Fluids*, Vol. 8(8), pp. 2117-2123.

[15] Belmont, M. R. and Jordon, S. P. V., (2000), Generalised Cross-Correlation Functions for Engineering Applications. Application to Experimental Data, *Expts. Fluids.*, Vol. 29, pp. 461-467.

[16] Blackburn, H. and Henderson, R., (1996), Lock-in Behavior in Simulated Vortex Induced Vibration, *Expt. Thermal and Fluid Science*, Vol.12, pp. 184-189.

[17] Bearman, P. W. (1984), Vortex Shedding from Oscillating Bluff Bodies, *Annu. Rev. Fluid Mech.*, Vol.16, pp. 195-222.

[18] Berger, E. (1967), Suppression of Vortex Shedding and Turbulence Behind Oscillating Cylinders, *The Physics of Fluids supplement*, Vol.10 , pp. S191-S193.

[19] Blackburn, H. M. and Henderson, R. D., (1999), A Study of Two-Dimensional Flow Past an Oscillating Cylinder, *J. Fluid Mech.*, Vol. 385, pp. 255-286.

[20] Bruun, H. H., (1995), Hot-Wire Anemometry, Principles and Signal Analysis, Oxford University Press, USA.

[21] Cheng, L., Zhou, Y. and Zhang, M. M., (2003), Perturbed Interaction Between Vortex Shedding and Induced Vibration, *J. Fluids and Structures*, Vol. 17, pp. 887-901.

[22] Carberry, J. and Sheridan, J., (2001), Forces and Wake Modes of an Oscillating Cylinder, *J. Fluids and Structures*, Vol. 15, pp. 523-532.

[23] Chew, Y. T. and Simpson, R. L., (1988), An Explicit Non-Real Time Data Reduction Method of Triple Sensors Hot-Wire Anemometer in Three-Dimensional Flow, *ASME J. Fluids Engg.*, Vol. 110, pp. 110-119.

[24] Chua, L. P., Li, H. S. and Zhang, H., (2000), Calibration of Hot-Wire for Low Speed Measurements, *Int. comm. Heat Mass Transfer*, Vol. 27, No. 4, pp. 507-516.

[25] Chen, J. M. and Liu, C. H., (1999), Vortex Shedding and Surface Pressure on a Square Cylinder at Incidence to a Uniform Air Stream, *Int. J. Heat and Fluid Flow*, Vol. 20, pp. 592-597.

[26] Chung, Y. J. and Kang, S. H., (2000), Laminar Vortex Shedding from a Trapezoidal Cylinder with Different Ratios, *Phys. Fluids.*, Vol. 12, No. 5, pp. 1251-1254.

[27] Chen, Y. T. and Du, R. K., (2003), Effect of Velocity Fluctuations on Heat Transfer Enhancement, *Expts. Fluids*, Vol.34, No. 5, pp. 1432-1114.

[28] Cetiner, O. and Rockwell, D., (2001), Stream wise Oscillations of a Cylinder in a Steady Current. Part 1. Locked-on States of Vortex Formation and Loading, *J. Fluid Mech.*, Vol. 427, pp. 1-28.

[29] Cheng, L., Zhou, Y. and Zhang, M. M.,(2003), Perturbed Interaction Between Vortex Shedding and Induced Vibration, *J. Fluids and Structures*, Vol. 17, pp. 887-901.

[30] Chang, L. and Hsieh, S. C., (2003), Convection Velocity of Vortex Structures in the Near Wake of a Circular Cylinder, *ASCE J. Engg. Mech.*, Vol. 129, No. 10, pp. 1108-1118.

[31] Durão, D. F. G., Heitor, M. V. and Pereira, J. C. F., (1988), Measurements of Turbulent and Periodic Flows Around a Square Cross-Section Cylinder, *Expts. Fluids*, Vol. 6, pp. 298-304.

[32] Davis, R. W. and Moore, E. F., (1984), A Numerical Study of Vortex Shedding from Rectangles, *J. Fluid Mech.*, Vol. 116, pp. 475-506.

[33] Dutta, S., Muralidhar, K. and Panigrahi, P. K., (2003), Influence of the Orientation of a Square Cylinder on the Wake Properties, *Expts. Fluids*, Vol. 34, pp. 16-23.

[34] Dutta, S., Muralidhar, K. and Panigrahi, P. K., (2006), Experimental Investigation of Flow Behind an Oscillating Square Cylinder at Low Reynolds Numbers, *Int. Conference in Marine Hydrodynamics (MAHY 2006)*, Visakhapatnam, India.

[35] Dutta, S., P. K. Panigrahi and K. Muralidhar, (2005), Structure of Low Reynolds Number Flow Behind a Prism of Square Cross-Section at Various Orientations, 50^{th} *Congress of ISTAM (An International meet)*, IIT-Kharagpur, India.

[36] Dutta, S. and P. K. Panigrahi, (2005), Laser Sheet Visualization of Flow Past Square Cylinder: Effect of Orientation and External Excitation, 32^{nd} *National conference on Fluid Mechanics and Fluid Power (FMFP)*, Osmanabad, India.

[37] Deaconu, S. and Coleman, H. W., (2000), Limitations of Statistical Design of Experimental Approaches in Engineering Testing, *Transaction ASME J. Fluid Engg.*, Vol. 122, pp. 254-259.

[38] Davis, R. W., Moore, E. F. and Purtell, L. P., (1984), A Numerical-Experimental Study of Confined Flow Around Rectangular Cylinders,*Phys. Fluids*, Vol. 23, pp. 46-59.

[39] Stäger, R. and Eckelmann, H., (1991), The Effect of End plates on the Shedding Frequency of Circular Cylinders in the Irregular Range, *Phys. Fluids*, Vol. 3(9), pp. 2116- 2121.

[40] Eisenlohr, H. and Eckelmann, H., (1988), Vortex Splitting and Its Consequences in the Vortex Street Wake of Cylinder at Low Reynolds Number, *Phys. Fluids* , Vol. 1, No. 2, pp. 189-192.

[41] Facchinetti, M. L., Langre, E. D. and Biolley, F., (2004), Coupling of Structure and Wake Oscillators in Vortex-Induced Vibrations, *J. Fluids and Structures*, Vol.19, pp. 123-140.

[42] Foucaut, J. M. and Stanislas, M., (2002), Some Consideration on the Accuracy and Frequency Response of Some Derivative Filters Applied to Particle Image Velocimetry Vector Fields, *Meas. Sci. Technol.*, Vol. 13, pp. 1058-1071.

[43] Franke, R., Rodi, W. and Schönung, B., (1990), Numerical Calculation of Laminar Vortex Shedding Flow Past Cylinders, *J. Wind Engg. Ind. Aerodyn.*, Vol. 35, pp. 237-257.

[44] Guezennec, Y. G. and Kirtsis, N., (1990), Statistical Investigation of Errors in Particle Image Velocimetry, *Expts. Fluids*, Vol. 10, pp. 138-146.

[45] Gerrard J.H. (1966), The Mechanics of the Formation Region of Vortices Behind Bluff Bodies,*J. Fluid Mech.*, Vol. 25, pp. 401-413.

[46] Gerrard, J. H., (1997), Numerical Study of the Instability in the Near Wake of the Circular Cylinder at Low Reynolds Number, *J. Fluids and structures*, Vol. 11, pp. 271-291.

[47] Gerich, D. and Eckelmann, H., (1982), Influence of End Plates and Free Ends on the Shedding Frequency of Circular Cylinders, *J. Fluid Mech.*, Vol. 122, pp. 109-121.

[48] Griffin, O. M. and Ramberg, S. E., (1976), Vortex Shedding from a Cylinder Vibrating in Line With an Incident Uniform Flow, *J. Fluid Mech.*, Vol. 75, Part 2, pp. 257-271.

[49] Gu, W., Chyu, C. and Rockwell, D., (1994), Timing of Vortex Formation from an Oscillating Cylinder, *Phys. Fluids*, Vol. 6, No.11, pp. 3677-3682.

[50] Goldstein, R. J. (Editor), (1997), Fluid Mechanics Measurements, 2^{nd} edition, Hemisphere Publishing Corporation, New York.

[51] Griffin, O. M., (1981), Universal Similarity in the Wakes of Stationary and Vibrating Bluff Structures, *Trans. ASME J. Fluids Engg.*, Vol. 103, pp. 52-57.

[52] Guilmineau, E. and Queutey, P., (2002), A Numerical Simulation of Vortex Shedding from an Oscillating Circular Cylinder, *J. Fluids and Structures* , Vol. 16(6), pp. 773-794.

[53] Griffin, O. M. and Hall, M. S., (1991), Review- Vortex Shedding Lock-on and Flow Control in Bluff Body Wakes, *Transactions ASME J. Fluids Engg.*, Vol. 113, pp. 526-537.

[54] Guzmán, A. M. and Amon, C. H., (1996), Dynamical Flow Characterization of Transitional and Chaotic Regimes in Converging-Diverging Channels, *J. Fluid Mech.*, Vol. 321, pp. 25-57.

[55] Hussain, A. K. M. F., (1986), Coherent Structures and Turbulence, *J. Fluid Mech.*, Vol. 173, pp. 303-356.

[56] Henderson, R. D., (1995), Details of the Drag Curve Near the Onset of Vortex Shedding, *Phys. Fluids*, Vol. 7, No. 9, pp. 2102-2104.

[57] Hu, H., Saga, T., Kobayashi, T., Okamoto, K. and Taniguchi, N., (1998), Evaluation of the Cross Correlation Method by Using PIV Standard Images, *Journal of Visualization*, Vol. 1, No. 1, pp. 87-94.

[58] Hammache, M. and Gharib, M., (1991), An Experimental Study of the Parallel and Oblique Vortex Shedding from Circular Cylinders, *J. Fluid Mech.*, Vol. 232, pp. 567-590.

[59] Hwang, R. R. and Sue, Y. C., (1997), Numerical Simulation of Shear Effect on Vortex Shedding Behind a Square Cylinder, *Int. J. Numer. Methods Fluids*, Vol. 25, pp. 1409-1420.

[60] Henderson, R. D. and Barkley D., (1996), Secondary Instability in the Wake of a Circular Cylinder, *Phys. Fluids*, Vol. 8, No. 6, pp. 1683-1685.

[61] Hammache, M. and Gharib, M., (1989), A Novel Method to Promote Parallel Vortex Shedding in the Wake of Circular Cylinders, *Phys. Fluids* , Vol. 1, No. 10, pp. 1611-1614.

[62] Hart, D. P., (2000), PIV Error Correction, *Expts. Fluids*, Vol. 29, pp. 13-22.

[63] Huang, H., Dabiri, D. and Gharib, M., (1997), On Errors of Digital Particle Image Velocimetry, *Meas. Sci. Technol.*, Vol. 8, pp. 1427-1440.

[64] Imaichi, K. and Kazuo, O., (1983), Numerical Processing of Flow Visualization Pictures-Measurement of Two Dimensional Vortex Flow, *J. Fluid Mech.*, Vol. 129, pp. 283-311.

[65] Jeon, D. and Gharib, M., (2001), On Circular Cylinders Undergoing Two-Degree-of-Freedom Forced Motions, *J. Fluids and Structures*, Vol. 15, pp. 533-541.

[66] Jauvtis, N. and Williamson, C. H. K., (2003), Vortex- Induced Vibration of a Cylinder with Two Degrees of Freedom , *J. Fluids and Structures*, Vol. 17, pp. 1035-1042.

[67] Jakobsen, M. L., Dewhirst, T. P. and Greated, C. A., (1997), Particle Image Velocimetry for Predictions of Acceleration Fields and Force Within Fluid Flows, *Meas. Sci. Technol.*, Vol. 8, pp. 1502-1516.

[68] Jorgensen, F. E., (2002), How to Measure Turbulence With Hot-Wire Anemometers- A Practical Guide, *Dantec Dynamics*, Denmark.

[69] König, M., Eisenlohr, H. and Eckelmann H., (1990), The Fine Structure in the Strouhal Number Relationship of the Laminar Wake of a Circular Cylinder, *Phys. Fluids*, Vol. 2, No. 9, pp. 1607-1614.

[70] Kostas, J., Soria, J. and Chong, M. S., (2002), Particle Image Velocimetry of a Backward Facing Step Flow, *Expts Fluids*, Vol. 33, pp. 838-853.

[71] Kasagi, N. and Matsunaga, A., (1995), Three-Dimensional Particle- Tracking Velocimetry Measurement of Turbulence Statistics and Energy Budget in a Backward-Facing Step Flow, *Int. J. Heat and Fluid flow*, Vol. 16, pp. 477-485.

[72] Keane, R. D. and Adrian, R. J., (1990), Optimization of Particle Image Velocimeters. Part I: Double-Pulsed System, *Meas. Sci. Technol.*, Vol. 1, pp. 1202-1215.

[73] Knisely, C. W., (1990), Strouhal Numbers of Rectangular Cylinders at Incidence: A Review and New Data, *J. Fluids Struct.*, Vol. 4, pp. 371-393.

[74] Karniadakis, G. E., Mikic, B. B. and Patera, A. T., (1988), Minimum -Dissipation Transport Enhancement by Flow De-stabilization-Reynolds' Analogy Revisited, *J. Fluid Mech.*, Vol. 192, pp. 365-391.

[75] Kähler, C. J., Sammler, B. and Kompenhans, J., (2002), Generation and Control of Tracer Particles for Optical Flow Investigation in Air, *Expts. Fluids*, Vol. 33, pp. 736-742.

[76] Krishnamoorthy, S., Price, S. J. and Paidoussis, M. P., (2001), Cross-Flow Past an Oscillating Circular Cylinder: Synchronization Phenomena in the Near Wake, *J. Fluids and Structures*, Vol. 15, pp. 955-980.

[77] Konstantinidis, E., Balabani, S. and Yianneskis, M., (2003), The Effect of Flow Perturbations on the Near Wake Characteristics of a Circular Cylinder, *J. Fluids and Structures*, Vol. 18, pp. 367-386.

[78] Kiya, M., Ishikawa, H. and Sakamoto, H., (2001), Near-Wake Instabilities and Vortex Structures of Three-Dimensional Bluff Bodies: a Review, *J. Wind Engg. Ind. Aerodyn.*, Vol. 89, pp. 1219-1232.

[79] Keane, R. D. and Adrian, R. J., (1992), Theory of Cross-Correlation Analysis of PIV Images, *Appl. Sci. Research*, Vol. 49, pp. 191-215.

[80] Konstantinidis, E., Balabani, S. and Yianneskis, (2005), Conditional Averaging of PIV Plane Wake Data Using a Cross-Correlation Approach, *Expts. Fluids*, Vol. 39, pp. 38-47.

[81] König, M., (1992), Visualization of the Spanwise Cellular Structure of the Laminar Wake of Wall-Bounded Circular Cylinders, *Phys. Fluids*, Vol. 4,No. 5, pp. 869-872.

[82] Kim, J. and Choi, H., (2005), Distributed Forcing of Flow Over a Circular Cylinder, *Phys. Fluids*, Vol. 17, pp. 1-16.

[83] Kim, K., Lee, M.B., Yoon, S.Y., Boo, J.S. and Chun, H. H., (2002), Phase Averaged Velocity Field in the Near Wake of a Square Cylinder Obtained by a PIV Method, *J. Visualization*, Vol. 5, No. 1, pp. 29-36.

[84] Kline, S. J., (1985), The Purpose of Uncertainty Analysis, *Trans. ASME J. Fluid Engg.*, Vol. 107, pp. 153-160.

[85] Karniadakis, G. E. and Traintafyllou, G., (1992), Three-Dimensional Dynamics and Transition to Turbulence in the Wake of Bluff Objects, *J. Fluid Mech.*, Vol. 238, pp. 1-30.

[86] Lee, T. and Budwig, R., (1991), A Study of the Effect of Aspect Ratio on Vortex Shedding Behind Circular Cylinders, *Phys. Fluids*, Vol. 3(2), pp. 309-315.

[87] Lee, B. E., (1975), The Effect of Turbulence on the Surface Pressure Field of a Square Prism, *J. Fluid Mech.*, Vol. 69, part. 2, pp. 263-282.

[88] Luo, S. C., Chew, Y.T. and Ng, Y. T., (2003), Characteristics of Square Cylinder Wake Transition Flow, *Phys. Fluids*, Vol 15(9), pp. 2549-2559.

[89] Lyn, D. A. and Rodi, W., (1994), The Flapping Shear Layer Formed by Flow Separation from the Forward Corner of a Square Cylinder, *J. Fluid Mech.*, Vol. 267, pp. 353-376.

[90] Liu, X. and Thomas, F. O., (2004), Measurement of the Turbulent Kinetic Energy Budget of a Planar Wake Flow in Pressure Gradients, *Expts. Fluids*, Vol. 37, pp. 469-482.

[91] Lin, J. C., Towfighi, J. and Rockwell, D., (1995), Instantaneous Structure of the Near Wake of a Circular Cylinder: On the Effect of Reynolds Number, *J. Fluids and Structures*, Vol. 9, pp. 409-418.

[92] Lin, J. C., Vorobieff, P. and Rockwell, D., (1995), Three Dimensional Patterns of Streamwise Vorticity in the Turbulent Near Wake of a Cylinder, *J. Fluids and Structures*, Vol. 9, pp. 231-234.

[93] Lourenco, L. M., Gogineni, S. P. and Lasalle, R. T., (1994), On-Line Particle Image Velocimeter: an Integrated Approach, *Appl. Optics*, Vol. 33, No. 13, pp. 2465-2470.

[94] Lourenco, L. and Krothapalli, A., (1995), On the Accuracy of Velocity and Vorticity Measurements with PIV, *Expts. Fluids.*, Vol. 18, pp. 421-428.

[95] Lu, X. Y. and Dalton C., (1996), Calculation of the Timing of Vortex Formation from an Oscillating Cylinder, *J. Fluids and Structures* , Vol. 10, pp. 527-541.

[96] Lee, T. and Budwig, R., (1991), Two Improved Method for Low Speed Hot-Wire Calibration, *Meas. Sci. Technol.*, Vol. 2, pp. 643-646.

[97] Li, G. and Humphrey, J. A. C., (1995), Numerical Modeling of Confined Flow Past a Cylinder of Square Cross-Section at Various Orientations, *Int. J. Numer. Meth. Fluids*, Vol. 20, pp. 1215-1236.

[98] Melling, A., (1997), Tracer Particles and Seeding for Particle Image Velocimetry, *Meas. Sci. Technol.*, Vol. 8, pp. 1406-1416.

[99] Meinhart, C. D., Wereley, S. T. and Satiago, J. G., (2000), A PIV Algorithm for Estimating Time Averaged Velocity Fields, *ASME J. Fluid Engg.*, Vol. 122, pp. 285-289.

[100] Moffat, R. J., (1988), Describing the Uncertainties in Experimental Results, *Expt. Therm. Fluid Sci.*, Vol. 1, pp. 3-17.

[101] Mittal, R. and Balachandran, S., (1995), Effect of Three Dimensionality on the Lift and Drag of Nominally Two-Dimensional Cylinders, *Phys. Fluids*, Vol. 7, No. 8, pp. 1841-1865.

[102] Matsumoto, M., (1999), Vortex Shedding of Bluff Bodies: A Review, *J. Fluids and Structures*, Vol. 13, pp. 791-811.

[103] Monkewitz, P. A., (1996), Phase Dynamics of Karman Vortices in Cylinder Wakes, *Phys. Fluids*, Vol. 8, No. 1, pp. 91-96.

[104] Mittal, R. and Balachandran, S., (1995), Generation of Streamwise Vorticity Structures in Bluff Body Wakes, *Phys. Rev. Lett.*, Vol. 75, No. 7, pp. 1300-1303.

[105] Martinuzzi, R. J., Bailey, S. C. C. and Kopp, G. A., (2003), Influence of Wall Proximity on Vortex Shedding from a Square Cylinder, *Expts. Fluids*, Vol. 34, pp. 585-596.

[106] Nishihara, T., Kaneko, S. and Watanabe, T., (2005), Characteristics of Fluid Dynamic Forces Acting on a Circular Cylinder Oscillated in the Streamwise Direction and Its Wake Patterns, *J. Fluids and Structures*, Vol. 20, pp. 505-518.

[107] Nogueira, J., Lecuona, A. and Rodriguez, P. A., (1997), Data Validation, False Vectors Correction and Derived Magnitudes Calculation on PIV Data, *Meas. Sci. Technol.*, Vol.8, pp. 1493-150.

[108] Norberg, C., (1993), Flow Around Rectangular Cylinders: Pressure Forces and Wake Frequencies, *J. Wind Engg. Ind. Aerodyn.*, Vol 49, pp. 187-196.

[109] Nishioka, M., and Sato, H., (1974), Measurements of Velocity Distribution in the Wake of a Circular Cylinder at Low Reynolds Number, *J. Fluid Mech.*, Vol. 65, part 1, pp. 97-112.

[110] Norberg, C., (2003), Fluctuating Lift on a Circular Cylinder: Review and New Measurements, *J. Fluids and Structures*, Vol. 17, pp. 57-96.

[111] Nobari, M. R. H. and Naderan, H., (2005), A Numerical Study of Flow Past a Cylinder with Cross Flow and Inline Oscillation, *Computers and Fluids*, (in press).

[112] Norberg, C., (1994), An Experimental Investigation of the Flow Around a Circular Cylinder: Influence of Aspect Ratio, *J. Fluid Mech.*, Vol. 258, pp. 287-316.

[113] Obasaju, E. D.. Bearman, P. W. and Graham, J. M. R., (1988), A Study of Forces, Circulation Patterns Around a Circular Cylinder in Oscillating Flow, *J. Fluid Mech.* , Vol. 196, pp. 467-494.

[114] Okajima, A., Matsumoto, T. and Kimura, S., (1998), Force Measurements and Flow Visualization of Circular and Square Cylinders in Oscillatory Flow, *JSME Int. Journal*, Vol. 41(4), pp. 796-805.

[115] Ongoren, A. and Rockwell, D., (1988), Flow Structure from an Oscillating Cylinder, Part 2. Mode Competition in the Near Wake, *J. Fluid Mech.*, Vol. 191, pp. 225-245.

[116] Okajima, A., (1982), Strouhal Numbers of Rectangular Cylinders, *J. Fluid Mech.*, Vol. 123, pp. 379-398.

[117] Okajima, A., (1990), Numerical Simulation of Flow Around Rectangular Cylinders, *J. Wind Engg. Ind. Aerodyn.*, Vol. 33, pp. 171-180.

[118] Okamoto, K., Nishio, S., Saga, T. and Kobayashi, T., (2000), Standard Images for Particle Image Velocimetry, *Meas. Sci. Technol.*, Vol. 11, pp. 685-691.

[119] Ongoren, A. and Rockwell, D., (1988), Flow Structure from an Oscillating Cylinder. Part 1. Mechanisms of Phase Shift and Recovery in the Near Wake, *J. Fluid Mech.*, Vol. 191, pp. 197-223.

[120] Okajima, A., Yasuda, T. and Iwasaki, T., (1999), Flow Visualization of In-Line Oscillation of a Cylinder with Circular or Rectangular Section, 3^{rd} *Joint conference ASME/JSME.*

[121] Oudheusden, B. W. V., Scarano, F., Hinsberg, N. P. V. and Watt, D. W., (2005), Phase Resolved Characterization of Vortex Shedding in the Near Wake of a Square-Section Cylinder at Incidence, *Expts. Fluids*, Vol. 39, pp. 86-98.

[122] Obasaju, E. D., (1983), An Investigation of the Effect of Incidence on the Flow Around a Square Section Cylinder, *Aero Q.*, Vol. 34, pp. 243-259.

[123] Perry, A. E., (1982),*Hot-Wire Anemometry*, Oxford University Press, USA.

[124] Perry, A. E., Chong, M. S. and Lim, T. T., (1982), The Vortex Shedding Process Behind Two Dimensional Bluff Bodies, *J. Fluid Mech.*, Vol. 116, pp. 77-90.

[125] Prasad, A. K., (2000), Particle Image Velocimetry: Review Article, *Current science*, Vol. 79, No. 1, pp. 51-60.

[126] Prasad, A. K., Adrian, R. J., Landreth, C. C. and Offutt, P. W., (1992), Effect of Resolution on the Speed and Accuracy of Particle Image Velocimetry Interrogation, *Expts. Fluids*, Vol.13, pp. 105-116.

[127] Panigrahi, P. K. and Acharya, S., (2005), Excited Turbulent Flow Behind a Square Rib ,*J. Fluids and Structures*, Vol. 20, pp. 235-253.

[128] Panigrahi, P. K. and Acharya, S., (2004), The Flow Over a Surface Mounted Rib Turbulator Under Single-Mode and Dual-Mode Excitation, *J. Wind Engg. Ind. Aerodyn.*, Vol. 92, pp. 1219-1244.

[129] Panigrahi, P. K., Schroeder, A. and Kompenhans, J., (2005), Turbulent Structures and Budgets Behind Permeable Ribs, 6^{th} *Int. symposium on PIV, Pasadena.*

[130] Piirto, M., Saarenrinne, P., Eloranta, H. and Karvinen, R., (2003), Measuring Turbulence Energy with PIV in a Backward Facing Step Flow, *Expts. Fluids*, Vol. 35, pp. 219-236.

[131] Raffel, M., Willert, C. E. and Kompenhans, J., (1998), Particle Image Velocimetry, A Practical Guide, *Springer publication.*

[132] Robichaux, J., Balachandar, S. and Vanka, S. P., (1999), Three-Dimensional Floquet Instability of the Wake of a Square Cylinder, *Phys. Fluids*, Vol.11, No. 3, pp. 560-578.

[133] Rockwell, D., (2000), Imaging of Unsteady Separated Flows: Global Interpretation with Particle Image Velocimetry, *Expts. Fluids (Suppl.)*, pp. S255-S273.

[134] Roussopoulos, K., (1993), Feedback Control of Vortex Shedding at Low Reynolds Numbers, *J. Fluid Mech.*, Vol. 248, pp. 267-296.

[135] Robichaux, J., Balachandar, S. and Vanka, S. P., (1999), Three-Dimensional Floquet Instability of the Wake of Square Cylinder,*Phys. Fluids*, Vol. 11, No. 3, pp. 560-578.

[136] Rajagopalan, S. and Antonia, R. A., (1997), Flow Around a Circular Cylinder -Structure of the Near Wake Shear Layer, *Expts. Fluids* , Vol. 38, pp. 393-402.

[137] Stäger, R. and Eckelmann, H., (1991), The Effect of End Plates on the Shedding Frequency of Circular Cylinders in the Irregular Range, *Phys. Fluids*, Vol. 3, No. 9, pp. 2116-2121.

[138] H. Schlichting, (1979), Boundary-layer theory, *Mcgraw-Hill Publisher, U.S.A.*

[139] Szepessy, S. and Bearman, P. W., (1992), Aspect Ratio and End Plate Effects on Vortex Shedding from a Circular Cylinder, *J. Fluid Mech.*, Vol. 234, pp. 191-217.

[140] Sohankar, A., Norberg, C. and Davidson, L., (1999), Simulation of Three-Dimensional Flow Around a Square Cylinder at Moderate Reynolds Numbers, *Phys. Fluids*, Vol 11, No.2, pp. 288-306.

[141] Sohankar, A., Norberg, C. and Davidson, L., (1998), Low-Reynolds-Number Flow Around a Square Cylinder at Incidence: Study of Blockage, Onset of Vortex Shedding and Outlet Boundary Condition, *Int. J. Numer. Meth. Fluids*, Vol. 26, pp. 39-56.

[142] Saha, A. K., Biswas, G. and Muralidhar, K., (2003), Three-Dimensional Study of Flow Past a Square Cylinder at Low Reynolds Numbers, *Int. J. Heat Fluid Flow*, Vol. 24, pp. 54-66.

[143] Saha, A. K., (2004), Three-Dimensional Numerical Simulation of the Transition of Flow Past a Cube. *Phys. Fluids*, Vol. 16, pp. 1630-1646.

[144] Sarpkaya, T., (2004), A Critical Review of the Intrinsic Nature of Vortex- Induced Vibrations, *J. Fluids and Structures*, Vol. 19, pp. 389-447.

[145] Sarpkaya, T., (1979), Vortex Induced Oscillations-a Selective Review, *J. Applied Mechanics*, Vol. 46, pp. 241-255.

[146] Sharma, A., (2003), Numerical Investigation of the Unconfined and Channel-Confined Flow Across a Square Cylinder with Forced and Mixed Convection Heat Transfer, Ph.D. Thesis, Indian Institute of Technology Kanpur, India.

[147] Saha, A. K., (1999), Dynamical Characteristics of the Wake of a Square Cylinder at Low and High Reynolds Numbers, Ph.D. Thesis, Indian Institute of Technology Kanpur, India.

[148] Sung, J. and Yoo, J. Y., (2003), Near Wake Vortex Motion Behind a Circular Cylinder at Low Reynolds Number, *J. Fluids and Structures* , Vol. 17, pp. 261-274.

[149] Stansby, P. K., (1974), The Effect of End Plates on the Base Pressure Coefficient of a Circular Cylinder, *Aeronautical Journal*.

[150] Suzuki, K. and Inaoka, K., (1998), Flow Modification and Heat Transfer Enhancement with Vortices, *Int. J. Transport Phenomena*, Vol. 1, pp. 17-30.

[151] Sousa, J. M. M., (2004), DPIV Study of the Effect of a Gable Roof on the Flow Structure Around a Surface-Mounted Cubic Obstacle ,*Expts. Fluids*, Vol. 37, pp. 409-418.

[152] Saha, A. K., Muralidhar K. and Biswas, G., (2000), Transition and Chaos in Two Dimensional Flow Past a Square Cylinder, *J. Engg. Mech.*, Vol. 126, No. 5, pp. 523-532.

[153] Saha, A. K., Muralidhar K. and Biswas, G., (2003), Investigation of Two and Three Dimensional Models of Transitional Flow Past a Square Cylinder, *J. Engg. Mech.*, Vol.129, No. 11, pp. 1320-1329.

[154] Stanislas, M. and Monnier, J. C., (1997), Practical Aspects of Image Recording in Particle Image Velocimetry, *Meas. Sci. Technol.*, Vol. 8, pp. 1417-1426.

[155] Soria, J., (1996), An Investigation of the Near Wake of a Circular Cylinder Using a Video-Based Digital Cross Correlation Particle Image Velocimetry Technique, *Expt. Fluid and Thermal Sci.*, Vol. 12, pp. 221-233.

[156] So, R. M. C., Liu, Y., Cui, Z. X., Zhang, C. H. and Wang, X. Q., (2005), Three-Dimensional Wake Effects on Flow Induced Forces, *J. Fluids and Structures*, Vol. 20, pp. 373-402.

[157] Schenck, T. and Jovanović, J., (2002), Measurement of the Instantaneous Velocity Gradients in Plane and Axisymmetric Turbulent Wake Flows, *ASME J. Fluids Engg.*, Vol. 124, pp. 143-153.

[158] Tao, J. S., Huang, X. Y. and Chan W. K., (1996), A Flow Visualization Study on Feedback Control of Vortex Shedding from a Circular Cylinder, *J. Fluids and Structures*, Vol.10, pp. 965-970.

[159] Tanida, Y., Okajima, A. and Watanabe, Y., (1973), Stability of a Circular Cylinder Oscillating in Uniform Flow or in a Wake, *J. Fluid Mech.*, Vol. 61(4), pp. 769-784.

[160] Towfighi, J. and Rockwell, D., (1994), Flow Structure from an Oscillating Non-Uniform Cylinder: Generation of Patterned Vorticity Concentrations, *Phys. Fluids*, Vol. 6(2), pp. 531-536.

[161] Tsutsui, T., Igarashi, T. and Nakamura, H., (2001), Drag Reduction and Heat Transfer Enhancement of a Square Prism, *JSME Int. Journal*, Vol. 44, No. 4, pp. 575-583.

[162] Thompson, M. C., Leweke, T. and Williamson, C. H. K., (2001), The Physical Mechanism of Transition in Bluff Body Wakes, *J. Fluids and Structures*, Vol. 15, pp. 607-616.

[163] Tamura, T. and Kuwahara, K., (1990), Numerical Study of Aerodynamic Behavior of a Square Cylinder. *J. Wind Engg. Ind. Aerodyn.*, Vol. 33, pp. 161-170.

[164] Townsend, A. A., (1949), The Fully Developed Turbulent Wake of a Circular Cylinder, *Aust. J. Sci Res.*, Vol. 2, pp. 451-468.

[165] Unal, M. F., Lin, J. C. and Rockwell, D., (1997), Force Prediction by PIV Imaging: A Momentum Based Approach, *J. Fluids and Structures*, Vol. 11, pp. 965-971.

[166] Unal, M. F. and Rockwell, D., (1988), On Vortex Formation from a Cylinder. Part 1. The Initial Instability, *J. Fluid Mech.*, Vol. 190, pp. 491-512.

[167] Vickery, B. J., (1966), Fluctuating Lift and Drag on a Long Cylinder of Square Cross-Section in a Smooth and in a Turbulent Stream, *J. Fluid Mech.*, Vol. 25, part. 3, pp. 481-494.

[168] Vittori, G., (1993), Quasi periodicity and Phase Locking Route to Chaos in the 2D Oscillatory Flow Around a Circular Cylinder, *Phys. Fluids*, Vol. 5, No. 8, pp. 1866-1868.

[169] Willert, C. E. and Gharib, M., (1991), Digital Particle Image Velocimetry, *Expts. Fluids*, Vol.10, pp. 181-193.

[170] Westerweel, J., (1997), Fundamental of Digital Image Velocimetry, *Meas. Sci. Technol.*, Vol. 8, pp. 1379-1392.

[171] Wernet, M. P., (2000), Application of DPIV to Study Both Steady and Transient Turbomchinery Flows, *Optics and Laser Technol.*, Vol. 32, pp. 497-525.

[172] Williamson, C. H. K., (1996), Three-Dimensional Wake Transition, *J. Fluid Mech.*, Vol. 328, pp. 345-407.

[173] Williamson, C. H. K., (1996), Vortex Dynamics in the Cylinder Wake, *Annu. Rev. Fluid Mech.*, Vol. 28, pp. 477-539.

[174] Westerweel, J., (2000), Theoretical Analysis of the Measurement Precision in Particle Image Velocimetry, *Expts. Fluids (Suppl.)*, pp. s3-s12.

[175] Williamson, C. H. K., (1997), Advances in Our Understanding of Vortex Dynamics in Bluff Body Wakes, *J. Wind Eng. Ind. Aerodyn.*, Vol. 69-71, pp. 3-32.

[176] Westerweel, J., (1994), Efficient Detection of Spurious Vectors in Particle Image Velocimetry Data, *Expts. Fluids*, Vol. 16, pp. 236-247.

[177] Wen, C. Y., Yeh, C. L., Wang, M. J. and Lin, C. Y., (2004), On the Drag of Two Dimensional Flow About a Circular Cylinder, *Phys. Fluids*, Vol. 16, No 10, pp. 3828-3831.

[178] Williamson, C. H. K., (1989), Oblique and Parallel Modes of Vortex Shedding in the Wake of Circular Cylinder at Low Reynolds Numbers, *J. Fluid Mech.*, Vol. 206, pp. 579-627.

[179] Williamson, C. H. K., (1996), Mode A Secondary Instability in Wake Transition, *Phys. Fluids*, Vol. 8, No. 6, pp. 1680-1682.

[180] Williamson, C. H. K. and Prasad, A., (1993), Wave Interactions in the Far Wake of a Body, *Phys. Fluids*, Vol. 5, No. 7, pp. 1854-1856.

[181] Wolf, A., Swift, J. B., Swinney, H. L. and Vastano, J. A., (1985), Determining Lyapunov Exponent from a Time Series, *Physica 16D*, Vol. 16, pp. 285-317.

[182] Wu, J., Sheridan, J., Welsh, M. C., Hourigan, K. and Thompson, M., (1994), Longitudinal Vortex Structures in a Cylinder Wake, *Phys. Fluids* , Vol. 6, No. 9, pp. 2883-2885.

[183] Wolochunk, M. C., Plesniak, M. W. and Braun, J. E., (1996), The Effect of Turbulence and Unsteadiness on Vortex Shedding from Sharp-Edged Bluff Bodies, *Transactions of ASME*, Vol. 118, pp. 18-25.

[184] White, F.M., (1991), Viscous Fluid Flow, 2_{nd} Edition, Mcgraw-Hill International, New York.

[185] Williamson, C. H. K., (1988), Defining a Universal and Continuous Strouhal Number Relationship for the Laminar Vortex shedding of a Circular Cylinder, *Phys. Fluids*, Vol. 31, No. 10, pp. 2742-2744.

[186] Williamson, C. H. K. and Roshko, A., (1988), Vortex Formation in the Wake of an Oscillating Cylinder, *J. Fluids and Structures*, Vol. 2, pp. 355-381.

[187] Williamson, C. H. K., (2004), Vortex-Induced vibrations, *Annu. Rev. Fluid Mech.*, Vol. 36, pp. 413-455.

[188] Wolfe, D. and Ziada, S., (2003), Feedback Control of Vortex Shedding from Two Tandem Cylinders , *J. Fluids and Structures* , Vol. 17, pp. 579-592.

[189] Williams, D. R., Mansy, H. and Amato, C., (1992), The Response and Symmetry Properties of a Cylinder Wake Subjected to Localized Surface Excitation, *J. Fluid Mech.*, Vol. 234, pp. 71-96.

[190] Yang, S. J., Cheng T. R. and Fu, W. S., (2005), Numerical Simulation of Flow Structures Around an Oscillating Rectangular Cylinder in a Channel Flow, *Comput. Mech.*, Vol. 35, pp. 342-351.

[191] Zhang, H. Q., Fey, U. and Noack, B. R., (1995), On the Transition of the Cylinder Wake, *Phys. Fluids*, Vol. 7, No. 4, pp. 779-794.

[192] Zdravkovich, M. M., (2003), Flow Around Circular Cylinders. Vol. 2: Application, *New York: Oxford University Press.*

[193] Zdravkovich, M. M., (1997), Flow Around Circular Cylinders. Vol. 1, *New York: Oxford University Press.*

[194] Zdravkovich, M. M., (1996), Different Modes of Vortex Shedding: an Overview, *J. Fluids and Structures* , Vol. 10, pp. 427-437.

[195] Zhang, M. M., Zhou, Y. and Cheng, L., (2003), Spring Supported Cylinder Wake Control, *AIAA Journal*, Vol 41, pp. 1500-1506.

[196] Zhang, M. M., Zhou, Y. and Cheng L., (2005), Closed-Loop-Manipulated Wake of a Stationary Square Cylinder, *Expts. Fluids*, Vol. 39, pp. 75-85.

[197] Zhang, M. M., Cheng, L. and Zhou, Y., (2004), Closed-Loop-Controlled Vortex Shedding and Vibration of a Flexibly Supported Square Cylinder Under Different Schemes, *Phys. Fluids*, Vol. 16, No.5, pp. 1439-1448.

[198] Zdravkovich, M. M., (1982), Modification of Vortex Shedding in the Synchronization Range, *J. Fluids Engg.*, Vol. 104, pp. 513-517.

Appendix A

Feedback Control

Control of vortex shedding from a bluff body and vortex induced structural vibration is of fundamental interest and of practical significance. Various schemes have been implemented in the literature for feedback. The choice of the transfer function is crucial for the effectiveness of a feedback signal (Zhang *et al.* [196]). For objects that are set in motion by the unsteady forces, literature shows that a control system will best perform when a combination of flow field information and body motion is used for control. Preliminary results obtained on controlling vortex shedding from a square cylinder using a feedback control system are reported in the present Appendix. Flow visualization images from the present experiments show that feedback-driven oscillation of the cylinder suppresses the vortex street, but differences with respect to the flow patterns for forced oscillations are minimal.

Control scheme and experimental details

Experiments were conducted with the hardware used for oscillation experiments at a Reynolds number of 175. The feedback loop consisted of the hotwire probe, phase shifter available in labVIEW, a power amplifier and electromagnetic actuators (dynamic shakers). The experiment was conducted in the following manner. A hotwire probe was placed at x=5 downstream and y=1.2 off set location. A long hotwire signal (60000 points) at a sampling rate of 1000 samples per second was collected in the near wake of a stationary cylinder. This data was subsequently used for generating the feedback signal for the oscillating the cylinder[1]. A clear peak was seen in the power spectrum of

[1]It was not possible to perform hotwire and PIV measurement simultaneously.

the hotwire signal. The signal was low-passed filtered at a cutoff frequency of 100 Hz to remove the high frequency noise. The signal was amplified to the level acceptable to the actuator. A phase shift was given to the filtered signal before sending it to the actuator. By placing the time series of the filtered and amplified signal in a loop, it was possible to run the experiment for a long period of time. The schematic layout of the feedback circuit is shown in Figure A.1. The front panel and the block diagram for implementing labVIEW software are shown in Figure A.2. Results discussed below are for a phase shift of 180^o. The amplitude of oscillation is practically constant in the oscillation experiments with and without feedback.

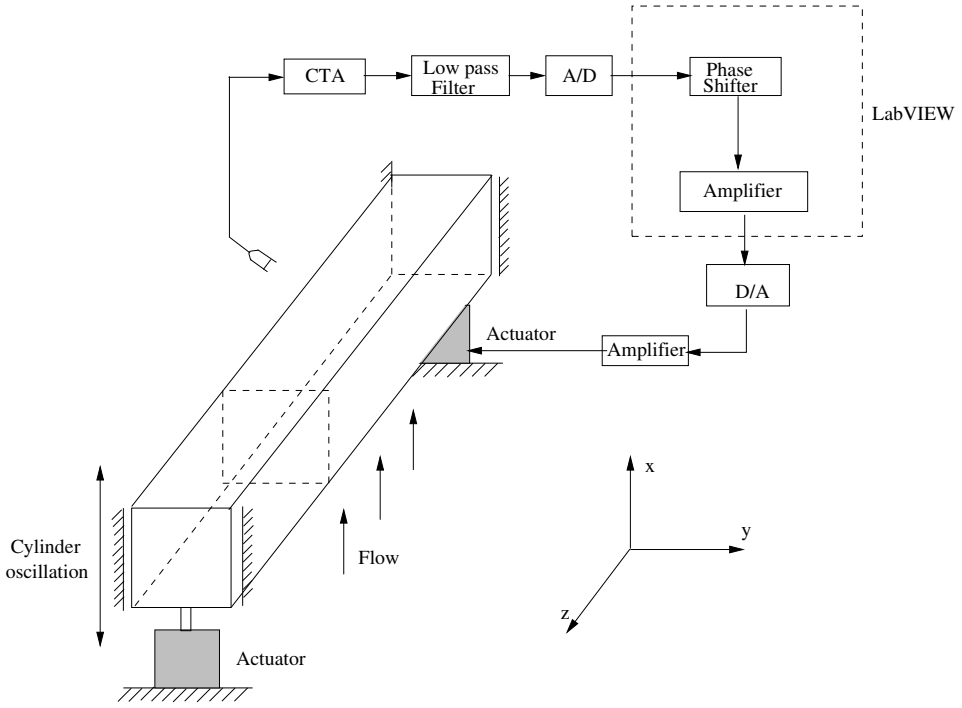

Figure A.1: Schematic drawing of the experimental arrangement with feedback.

Performance of feedback control

Flow patterns are compared in terms of the time-averaged and instantaneous quantities recorded in feedback experiments against wakes of a stationary cylinder and an oscillating cylinder in an open loop configuration. Figure A.3 shows the u velocity signal as a function of time for stationary and oscillating cylinder with feedback. The magnitude of velocity fluctuation is seen to be reduced substantially with feedback. Furthermore, the spectral characteristics of the signal was also seen to be affected.

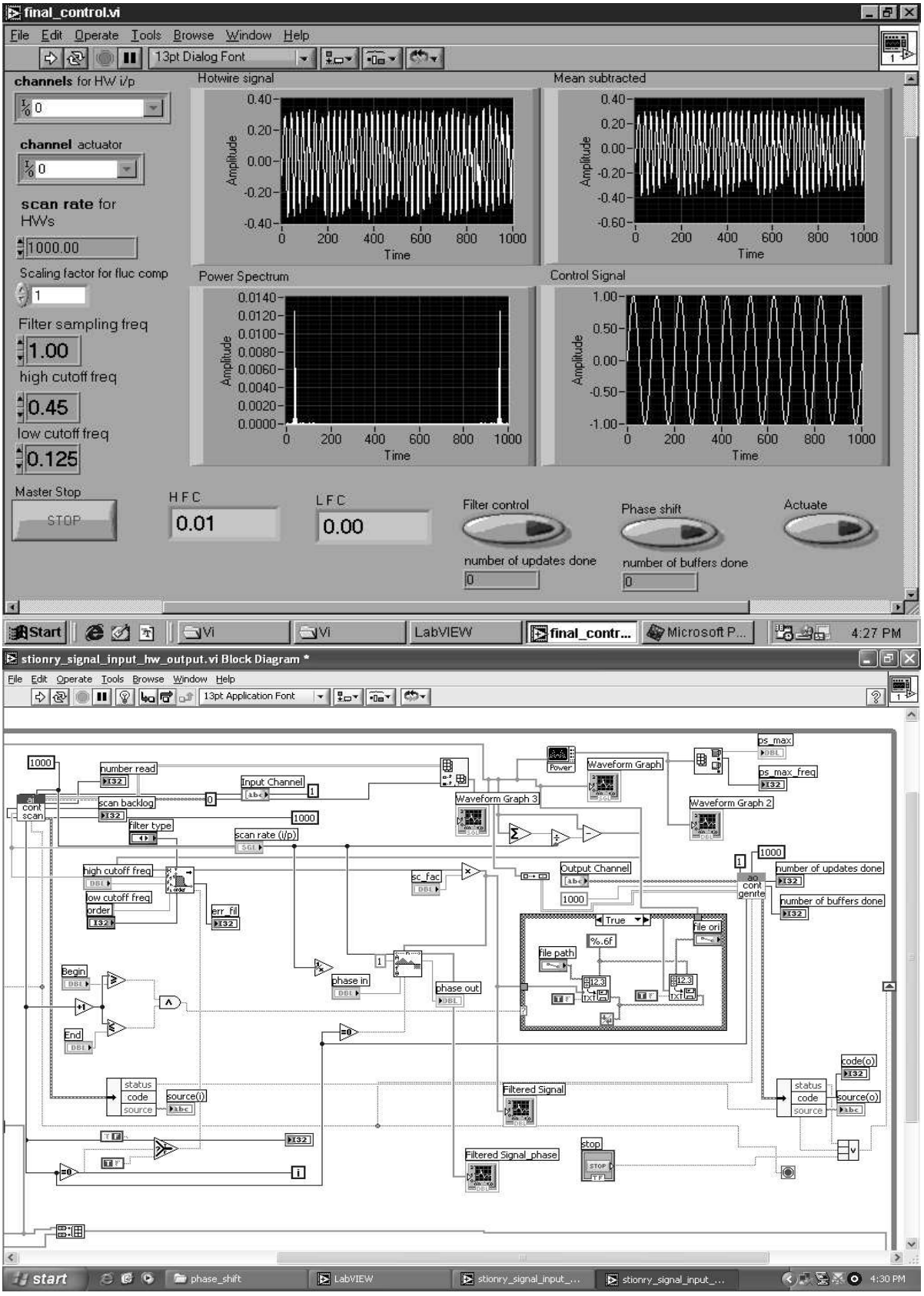

Figure A.2: Front panel and block diagram of labVIEW for feed back control loop

Figure A.4 shows the time-averaged velocity vectors for stationary and oscillating cylinders, with and without feedback. A distinct change in the near wake velocity vector distribution is seen. The recirculation zone is quite small for the open loop system. With the feedback-driven oscillation, it is seen to be increased. Thus, for the choice of parameters, feedback does not appear to have a beneficial effect in diminishing drag coefficient beyond the value for forced oscillations.

Figure A.5 shows the time-averaged and fluctuating velocity components in the wake when the cylinder is stationary, oscillatory and oscillatory with feedback. Measurements at the location x=4 are reported. The mean velocity deficit is higher for the stationary cylinder when compared to the perturbed. The velocity deficit for the closed loop experiment is higher when compared to forced oscillations. Thus, the present set of parameters, the control function (namely a phase shift of 180^o) is not effective in reducing the time-averaged drag coefficient. In contrast, the instantaneous flow visualization images (Figure A.10) show vortex shedding to be destroyed with feed back. The strength of the fluctuations also diminish, as seen from the time traces of the velocity signal. The magnitudes of u_{rms} and v_{rms} are quite close for experiments with and without feedback.

Figure A.6 shows the time-averaged spanwise (ω_z) vorticity contours for a stationary cylinder, open loop control and and feedback controlled oscillations. For the open loop, the vortices move close to the cylinder and the concentration of vortices near the cylinder increases. With feedback control oscillation the concentration near the cylinder marginally reduces, indicating that feedback negates some of the beneficial aspects of forced cylinder oscillation with respect to the time-averaged drag coefficient.

Figure A.7 shows the instantaneous vorticity contours for stationary and oscillating cylinders (with and without feed back) at selected instants of time. When there is no perturbation, the vortices display the pattern of a K*á*rman vortex street. With perturbation, the vortices get distorted. The vortices are shed very near the cylinder. The longitudinal spacing decreases. With feedback controlled oscillations, the periodic structure is disrupted. Experiments showed that the structure thus generated is not continuous and appears intermittently.

Figure A.8 shows the centerline recovery of streamwise velocity for stationary and oscillating cylinders, with and without feedback. The centerline velocity drops to a minimum value and then increases with entrainment of flow from outside the wake. The recovery is faster in the near field region and reaches an asymptotic value at around x=7. The rate of velocity recovery is seen to be high for the open loop system when compared to

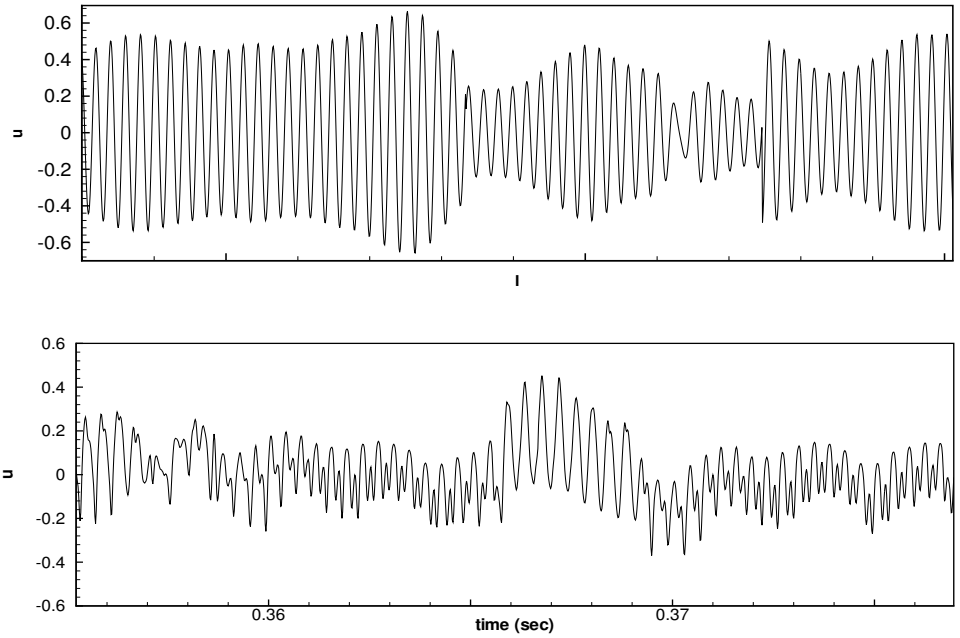

Figure A.3: Typical time histories of the streamwise flow velocity u with (lower trace) and without (upper trace) perturbation. Time scales for the two traces are identical. Re=175.

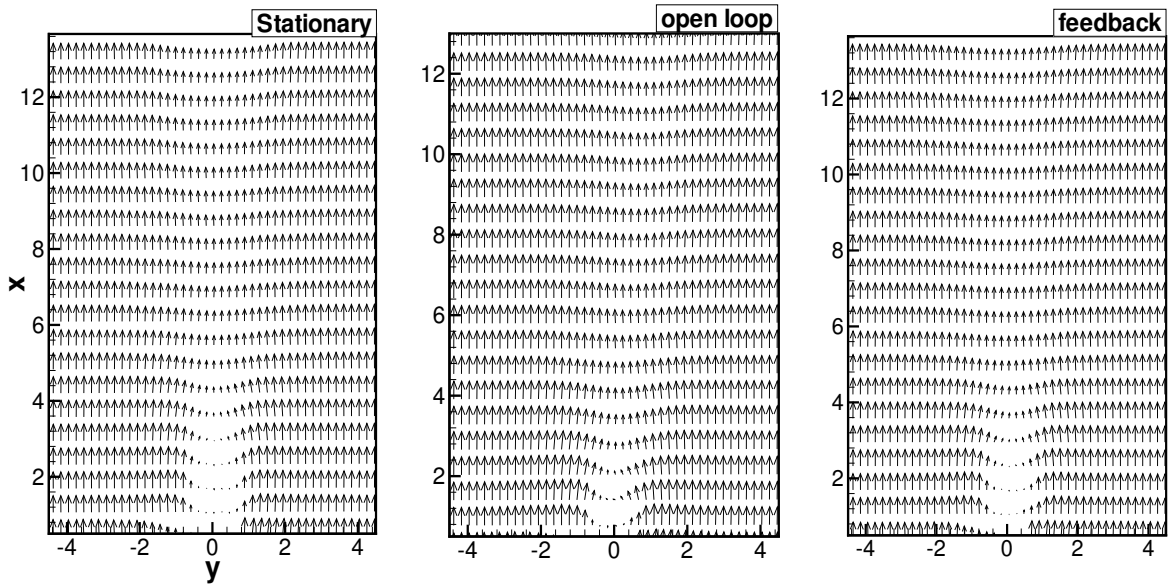

Figure A.4: Time-averaged vorticity contours for stationary and oscillating cylinder (with and without feedback) at Re=175.

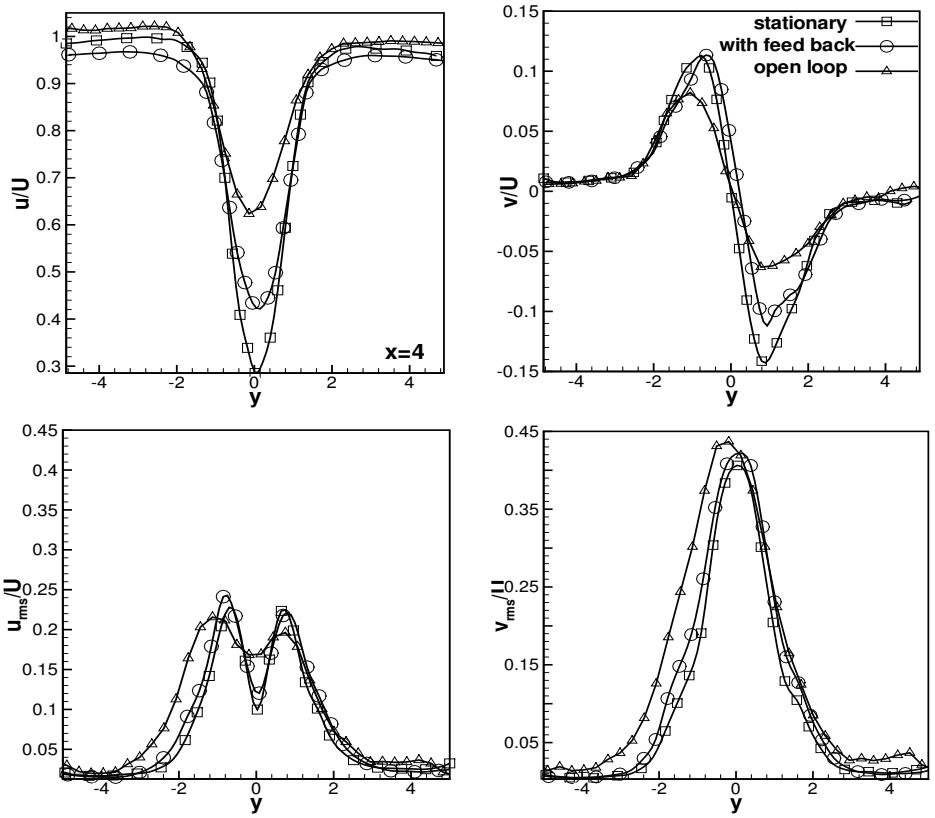

Figure A.5: Comparison of time-averaged velocities u and v, velocity fluctuations u_{rms} and v_{rms} for stationary and oscillating cylinders (with and without feedback) at a downstream location of x=4, Re=175.

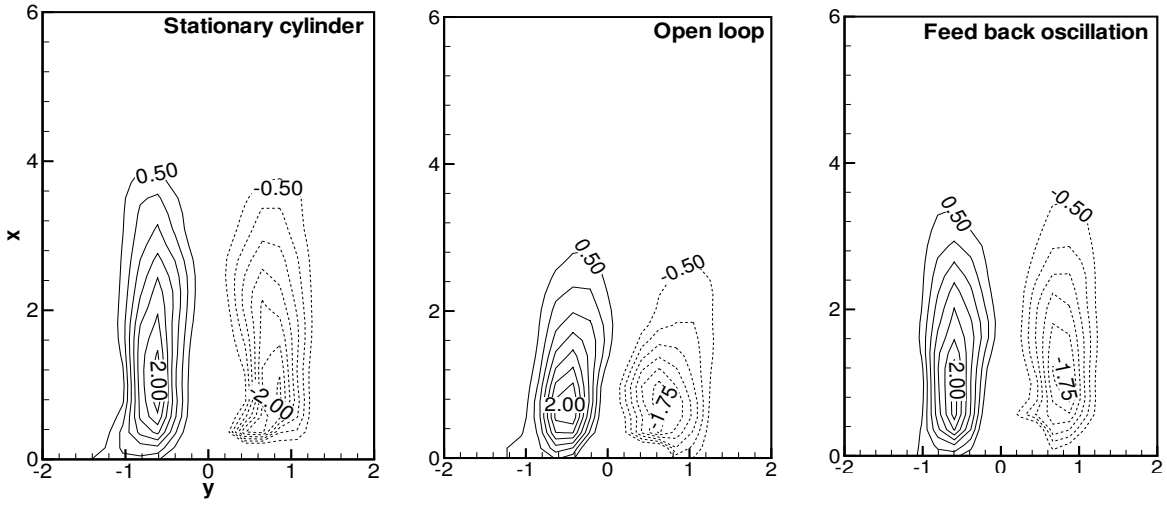

Figure A.6: Time-averaged vorticity contours for stationary, and oscillating cylinder (with and without feedback)

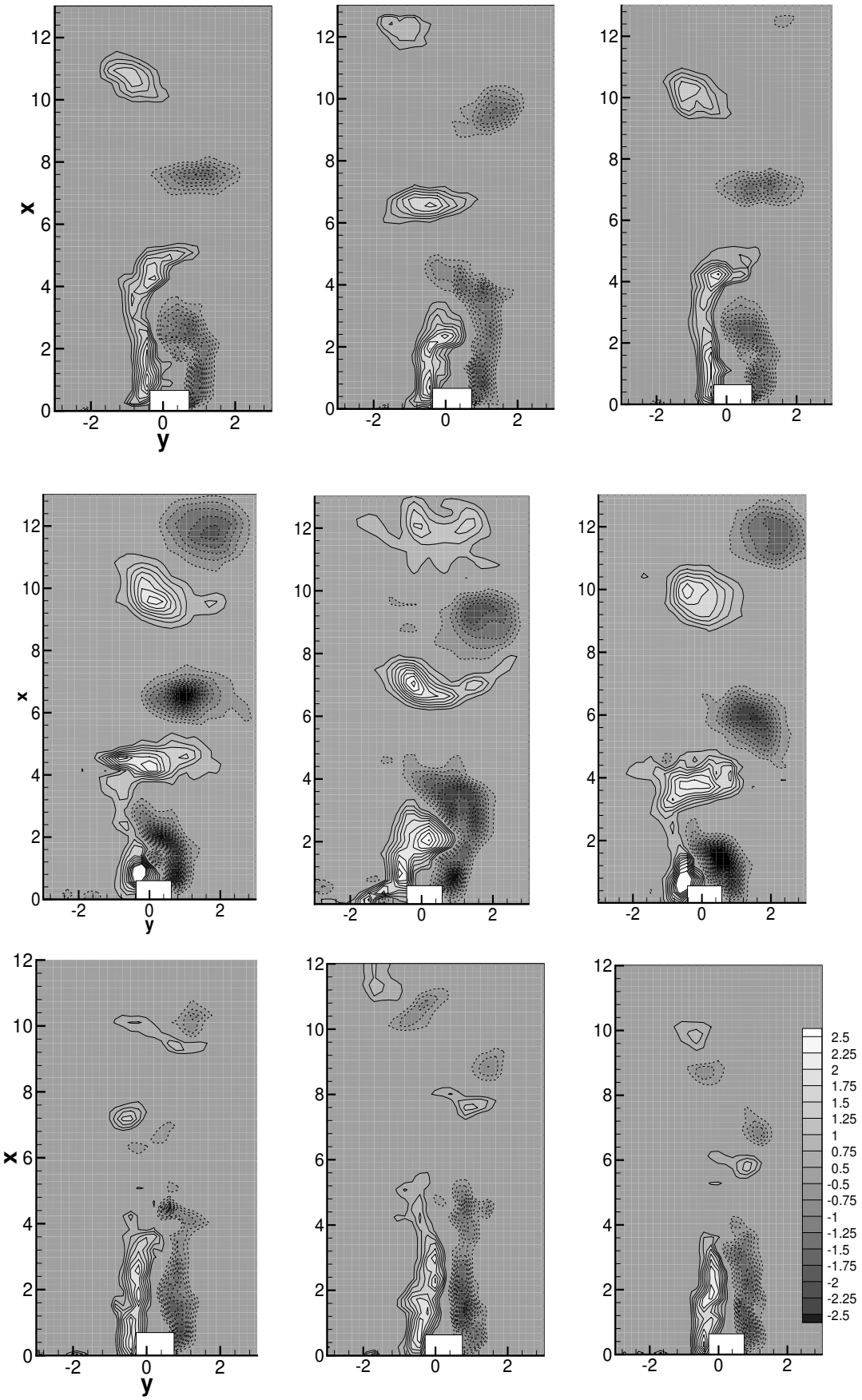

Figure A.7: Instantaneous spanwise vorticity contours for a stationary cylinder (top row), oscillating cylinder without feedback (middle row) and cylinder with feedback (bottom row) cylinder at Re=175.

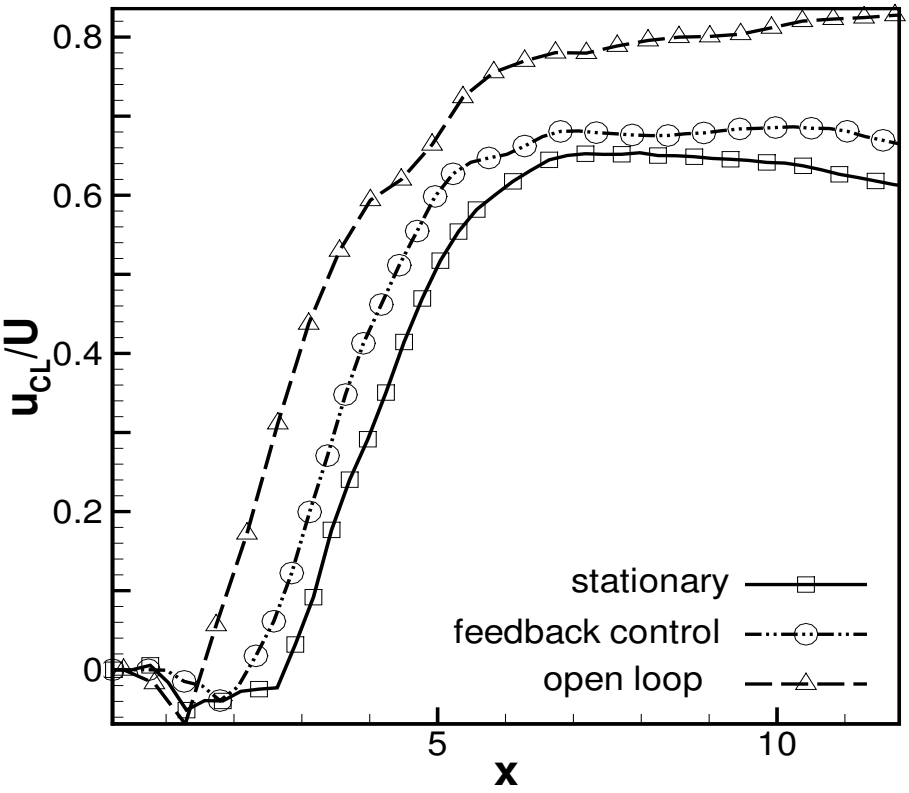

Figure A.8: Centerline recovery of streamwise velocity for stationary and oscillating cylinder (with and without feedback).

the stationary and feedback control experiments. Figure A.9 shows the nondimensional u_{rms} and v_{rms} contours for stationary and oscillating cylinder. For open loop oscillation the flow field becomes asymmetric. The magnitude of fluctuations are also high near the cylinder for the open loop arrangement when compared to the experiment with feedback. With feedback control, the flow field becomes increasingly symmetric.

Figure A.10 shows the particle traces for stationary and the oscillation experiments. The top row shows a sequence of three instantaneous images for a stationary cylinder. Pure Karman vortex shedding flow pattern is seen from the images. With oscillation at the vortex shedding frequency, vortex shedding is governed by the amplitude of oscillation of the cylinder. Vortices are shed from very near the cylinder. With the application of feedback to the actuator, vortex shedding is fully distorted and the wake size reduces significantly. This pattern was not continuously seen with feedback. Intermittently the vortex shedding such as that for a stationary cylinder was also seen.

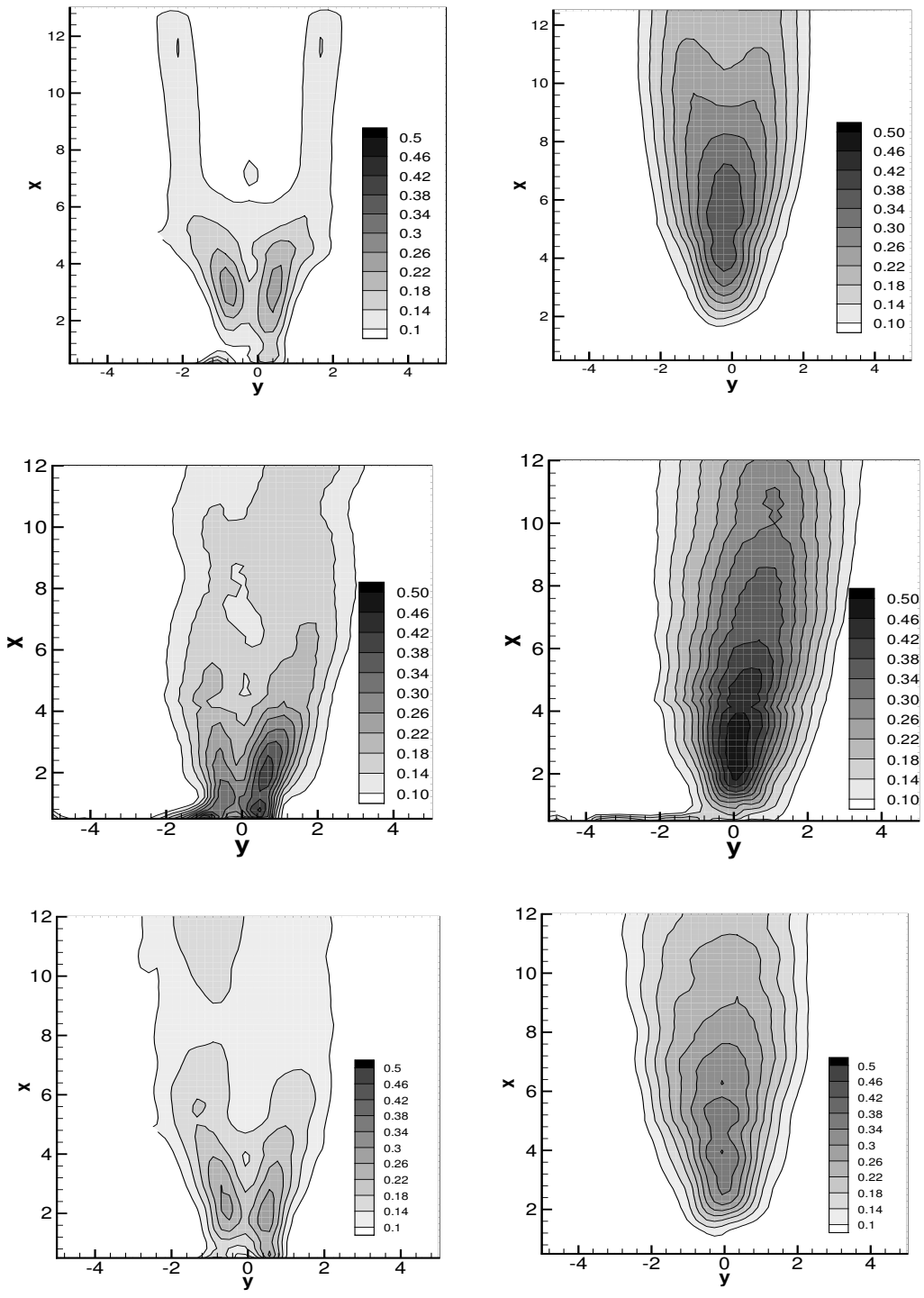

Figure A.9: Nondimensional u_{rms} (left) and v_{rms} (right) contours for stationary (top), open loop (middle) and closed loop (bottom) control.

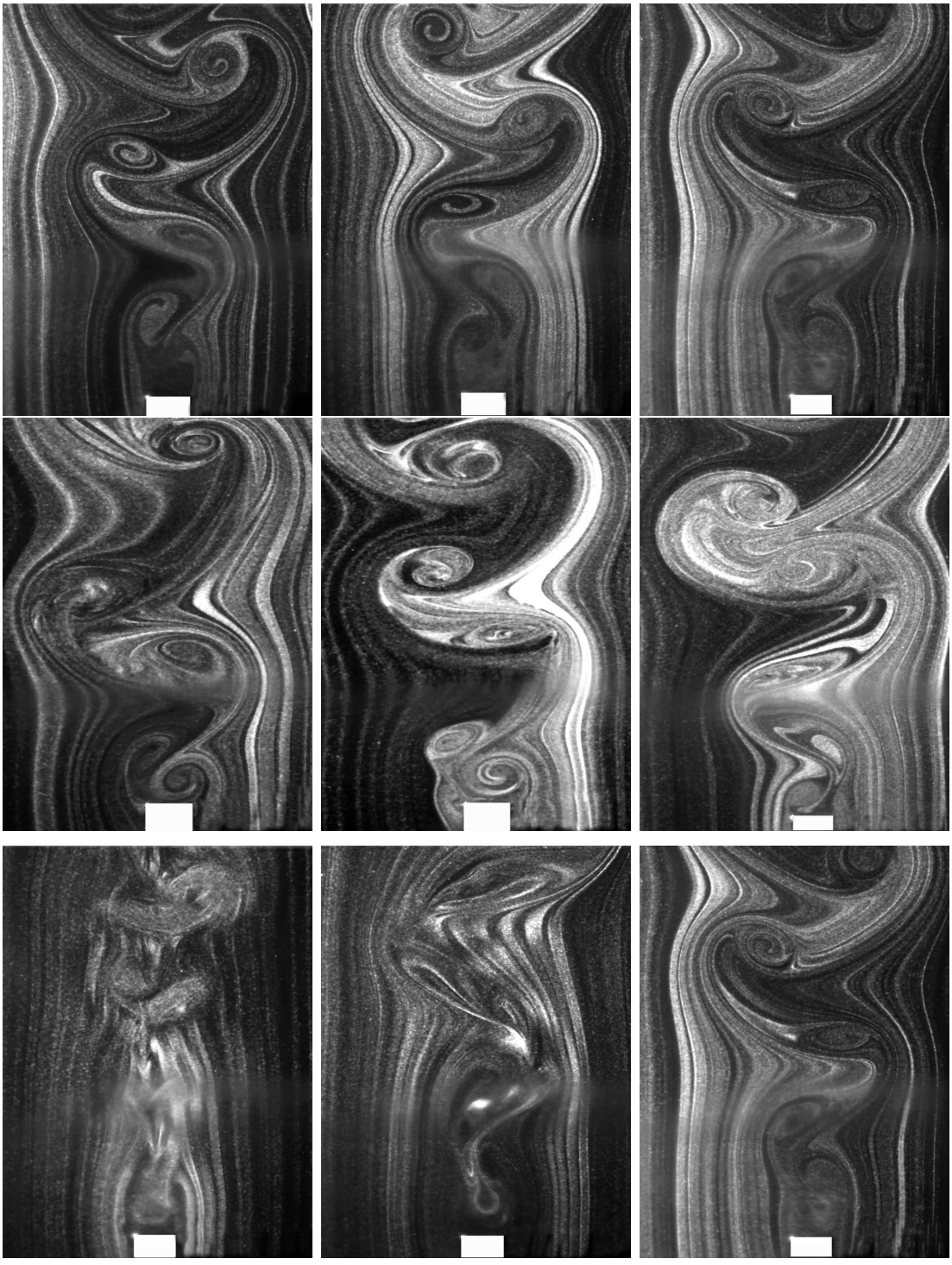

Figure A.10: Flow visualization images for stationary (top row), open loop (middle row) and closed loop oscillation (bottom row).

Closure

Experiments in which cylinder movement was driven by wake unsteadiness are reported. In the feedback mode, the cylinder was fed a 180^o phase shifted signal with respect to the velocity signal in the near wake. Keeping parameters such as amplitude and dominant frequency fixed, the time-averaged wake size was seen to increase with feedback. However, the instantaneous fluctuations were seen to be damped. Thus, the limited study did not result in definite conclusions. Extensive experiments on this subject are recommended.